

**MODELLING THE LOCAL ENVIRONMENTAL
IMPACT OF UNDERGROUND COAL GASIFICATION**

BENJAMIN DAVID ROULLIER, MA. MEng.

**Thesis submitted to the University of Nottingham
for the degree of Doctor of Engineering**

ABSTRACT

Underground coal gasification (UCG) has the potential to access vast resources of stored fossil energy in a safe, clean and environmentally sound manner. Previous experiments have however led to concerns around surface subsidence, groundwater pollution and water table lowering. These issues can be prevented through the use of appropriate site selection and an understanding of the processes which cause these effects. Numerical simulations provide a cost effective means of predicting these issues without the need for costly and publically opposed field trials.

This work uses a commercially available discrete element code to simulate the coupled thermal, hydraulic and mechanical phenomena which cause environmental damage. Surface subsidence is predicted through the displacements of fully deformable discrete elements separated by a network of fractures. The flow of groundwater through these fractures is simulated in order to predict the effects of water table lowering and the inflow of groundwater into the UCG cavity. Heat conduction from the cavity walls is simulated using an explicit finite difference algorithm which predicts both thermal expansion effects and the influence of temperature on rock material properties.

Comparison of results with experimental observations in the literature show good agreement for subsidence and groundwater behaviour, while initial predictions for a range of designs show clear relationships between environmental effects and operating conditions. Additional work is suggested to incorporate groundwater contaminant transport effects, and it is envisioned that the overall model will provide a valuable screening tool for the selection of appropriate site designs for the future development of UCG as an economically viable and environmentally sound source of energy.

LIST OF PUBLICATIONS

Roullier, B.D., Langston, P.A., Li, X. 2015: Effects of Joint Geometry on the Modelled Material Strengths of Rock Masses in the Distinct Element Method. In: Soga *et al* eds. *Geomechanics from Micro to Macro*. CRC Press. pp 431-436.

Roullier, B.D., Langston, P.A., Li, X. 2016: Modelling the Environmental Impact of Underground Coal Gasification. In: *Proceedings of the 1st International Conference on Energy Geotechnics*. Kiel, Germany, 29-31 August 2016.

Proposed Publications

Roullier, B.D., Langston, P.A., Li, X: Influence of Fracture Geometry on Simulated Rock Mass Material Behaviour.

This paper will present the theory, methodology and results of the simulated uniaxial and biaxial rock mass compression testing procedures presented in chapter 4 of this thesis. Additional discussions on the theory of interfacial behaviour and the process of rock mass compressive failure will also be presented.

ACKNOWLEDGEMENTS

I would like to take this opportunity to thank a number of people whose help, guidance, patience and support were invaluable in the creation of this work.

Firstly, to my academic supervisors, Dr Paul Langston and Dr Xia Li, whose continued support and guidance have been an inspiration throughout the creation of the thesis and without whom this would never have been possible.

Second, I'd like to thank those colleagues and friends who kept me sane through it all. In particular I'd like to thank Karen, Gary, Matt and Rachel for the endless discussions, helpful distractions, long lunch breaks and buckets of coffee that have got me through the past four years in one piece.

Finally, I'd like to thank those whose support and guidance over the past 27 years have led to this point. To my father David, for his continual encouragement and optimism on this and many other long journeys. To my grandfather Terry, for instilling in me the love of science that got me to this point. To my grandmother Margaret, for always taking an interest in my ramblings. Finally, and most importantly, to my wife Bethan, without whose love, patience, care and occasional chastisement I'd never have got this far in the first place. I love you, and I'm proud to call you my wife.

This thesis is dedicated to the memory of Tina Roullier.

TABLE OF CONTENTS

Abstract	i
List of Publications	ii
Acknowledgements	iii
Table of Contents	iv
Glossary of Terms	xii
Nomenclature	xv
1. INTRODUCTION	1
1.1. BACKGROUND	2
1.1.1. Global Energy Demands	2
1.1.2. Energy Sources	3
1.1.3. Fossil Energy Resources	4
1.2. UNDEGROUND COAL GASIFICATION	6
1.2.1. Process Description	6
1.3. ADVANTAGES AND CHALLENGES OF UCG	8
1.3.1. Political Issues	8
1.3.2. Economic Issues	8
1.3.3. Social Issues	10
1.3.4. Technical Issues	11
1.3.5. Legal Issues	11
1.3.6. Environmental Issues	12
1.3.6.1. Global Environmental Issues	13
1.3.6.2. Local Environmental Issues	14
1.3.7. Geographical Considerations	17
1.3.8. Competing Technologies	18
1.3.9. Principal Challenges to Development	19
1.4. ENVIRONMENTAL MODELLING	20
1.4.1. Modelling Overview	20
1.4.2. Model Aims	21
1.4.3. Proposed Use of Model	22
1.5. THESIS OUTLINE	23

2. LITERATURE REVIEW	25
2.1. UNDERGROUND COAL GASIFICATION TECHNOLOGY	26
2.1.1. Gasification Chemistry	26
2.1.2. Cavity Growth Mechanisms	29
2.1.3. Gasifier Designs	30
2.1.4. Coal Chemistry	33
2.1.5. Coal Geology	35
2.1.6. Gasifier Operating Conditions	36
2.2. LOCAL ENVIRONMENTAL ISSUES	40
2.2.1. Surface Subsidence	40
2.2.1.1. Subsidence Mechanisms	41
2.2.1.2. Preventing Subsidence	43
2.2.2. Groundwater Pollution	48
2.2.2.1. Common Pollutants	49
2.2.2.2. Pollution Mechanisms	50
2.2.2.3. Preventing pollution	51
2.2.3. Water Table Lowering	55
2.2.4. Preventing Environmental Damage	56
2.3. UNDERGROUND COAL GASIFICATION FIELD TRIALS	58
2.4. UNDERGROUND COAL GASIFICATION MODELLING	63
2.4.1. Modelled Phenomena	63
2.4.2. Previous Models	65
2.4.3. Modelling Methodologies	68
2.4.3.1. Finite Difference Methods	68
2.4.3.2. Finite Element Methods	69
2.4.3.3. Computational Fluid Dynamics	69
2.4.3.4. Discrete Element Methods	70
2.4.3.5. Compartment Modelling	71
2.4.3.6. Stochastic Methods	72
2.4.3.7. Empirical Modelling	73
2.4.3.8. Combined Methods	73
2.4.4. Future Modelling Developments	74
2.5. INITIAL MODELLING DECISIONS	75
2.5.1. Modelling Assumptions	75
2.5.2. Software and Hardware Considerations	77
2.6. CONCLUDING REMARKS	80

3. UNIVERSAL DISTINCT ELEMENT CODE METHODOLOGY	81
3.1. THE UNIVERSAL DISTINCT ELEMENT CODE	82
3.2. MECHANICAL CALCULATIONS	85
3.2.1. Mechanical Model Formulation	85
3.2.2. Mechanical Validation	90
3.2.2.1. Elastic Deflection Testing	90
3.2.2.2. Plastic Deflection Testing	92
3.2.2.3. Freefall Motion Test	93
3.3. HYDRAULIC CALCULATIONS	95
3.3.1. Hydraulic Model Formulation	95
3.3.2. Hydraulic Validation	98
3.3.2.1. Stress/Aperture Relationship Test	98
3.3.2.2. Flow/Pressure Relationship Test	100
3.4. THERMAL CALCULATIONS	102
3.4.1. Thermal Model Formulation	102
3.4.2. Thermal Validation	104
3.4.2.1. Fixed Temperature Conduction Test	104
3.4.2.2. Fixed Heat Flux Conduction Test	107
3.5. ADVANTAGES, CHALLENGES AND LIMITATIONS	109
3.5.1. Mechanical	109
3.5.2. Hydraulic	111
3.5.3. Thermal	114
3.6. CONCLUDING REMARKS	117

4. SIMULATED LABORATORY SCALE COMPRESSION TESTING	118
4.1. THEORY AND BACKGROUND	119
4.1.1. Representing Rock Masses in the discrete element method	119
4.1.2. Axial Compression Testing	120
4.1.3. Simulated Testing	123
4.2. METHODOLOGY OF SIMULATED TESTING	125
4.2.1. Model Design	125
4.2.2. Rock Mass Variations	128
4.2.3. Discrete Fracture Network Design	131
4.3. SIMULATED COMPRESSION TESTING RESULTS	134
4.3.1. Axisymmetric Results	134
4.3.1.1. Effects of Joint Pattern on Strength	135
4.3.1.2. Effects of Joint Pattern on Stiffness	139
4.3.1.3. Effects of Joint Pattern on Failure Criteria	139
4.3.1.4. Effects of Joint Pattern on Lateral Expansion	142
4.3.2. Plane Strain Results	146
4.3.2.1. Comparison of Axisymmetric and Plane Strain Results	146
4.3.2.2. Effects of Block Size on Mechanical Behaviour	149
4.3.2.3. Effects of Joint Material Properties on Mechanical Behaviour	152
4.4. MODEL VALIDATION	155
4.4.1. Comparison with Geological Strength Index	155
4.4.2. Comparison with Experiment	157
4.4.3. Repeatability Testing	158
4.4.4. Observations of Failure Behaviour	161
4.5. MODEL LIMITATIONS	163
4.6. PARAMETER SELECTION	165
4.7. CONCLUDING REMARKS	167

5. MODEL DEVELOPMENT	169
5.1. MODEL STRUCTURE	170
5.1.1. Order of Operations	170
5.1.2. Data Requirements	172
5.1.3. Data Produced	173
5.2. MODEL GEOMETRY	174
5.2.1. Site Geometry	174
5.2.2. Block Geometry	176
5.2.3. Zone Density	178
5.3. MODEL PROPERTIES	179
5.3.1. Mechanical Properties	179
5.3.2. Hydraulic Properties	181
5.3.3. Thermal Properties	183
5.4. BOUNDARY AND INITIAL CONDITIONS	187
5.4.1. Mechanical Boundary Conditions	187
5.4.2. Mechanical Initial Conditions	188
5.4.3. Hydraulic Boundary Conditions	189
5.4.4. Hydraulic Initial Conditions	190
5.4.5. Thermal Boundary Conditions	190
5.4.6. Thermal Initial Conditions	191
5.5. MECHANICAL AND HYDRAULIC LOGIC	192
5.5.1. Termination Criteria	194
5.6. THERMAL MODELLING	197
5.6.1. Underground Coal Gasification Thermal Behaviour	197
5.6.2. Thermal Algorithm	199
5.6.3. Thermal/Hydraulic Coupling	204
5.6.3.1. Fluid Thermal Energy Storage	204
5.6.3.2. Thermal Convection	206
5.6.3.3. Effects of Groundwater on Cavity Wall Temperature	207
5.6.3.4. Temperature Dependent Fluid Properties and Boiling Effects	209
5.7. CONCLUDING REMARKS	211

6.	INTERNAL PARAMETER EFFECTS	213
6.1.	INTRODUCTION	214
6.2.	STANDARD MODEL	215
6.3.	EFFECTS OF DISCRETE FRACTURE NETWORK DIMENSIONS	219
6.3.1.	Discrete Fracture Network Region Height	219
6.3.2.	Discrete Fracture Network Region Width	223
6.3.3.	Discrete Fracture Network Joint Density	225
6.3.4.	Discrete Fracture Network Joint Isotropy	227
6.4.	EFFECTS OF COARSE REGION DIMENSIONS	229
6.4.1.	Coarse Region Block Height	229
6.4.2.	Coarse Region Block Width	231
6.5.	EFFECTS OF MODEL WIDTH	234
6.6.	EFFECTS OF ZONE SIZE	237
6.7.	EFFECTS OF JOINT PROPERTIES	241
6.7.1.	Joint Normal Stiffness	241
6.7.2.	Joint Shear Stiffness	242
6.7.3.	Joint Friction Angle	243
6.7.4.	Joint Cohesion	245
6.7.5.	Joint Dilation Angle	247
6.8.	EFFECTS OF CONVERGENCE RATIO	249
6.9.	CONCLUDING REMARKS	253
7.	FIELD TRIAL STUDIES	254
7.1.	INTRODUCTION	255
7.2.	HOE CREEK 3 UNDERGROUND COAL GASIFICATION	259
7.3.	JINCHUAN NICKEL MINE	267
7.4.	ANGUS PLACE COLLIERY – SINGLE CAVITY	271
7.5.	ANGUS PLACE COLLIERY – MULTIPLE CAVITIES	274
7.6.	CONCLUDING REMARKS	278

8.	SITE DESIGN STUDIES	280
8.1.	INTRODUCTION	281
8.2.	EFFECTS OF CAVITY GEOMETRY	282
8.2.1.	Cavity Height	282
8.2.2.	Cavity Width	286
8.2.3.	Cavity Depth	289
8.2.4.	Combined Geometric Effects	293
8.3.	EFFECTS OF MECHANICAL PROPERTIES	295
8.3.1.	Rock Mass Stiffness	295
8.3.2.	Intact Rock Strength	297
8.3.3.	Lateral Earth Pressure	298
8.4.	EFFECTS OF HYDRAULIC PROPERTIES	298
8.4.1.	Water Table Depth	300
8.4.2.	Site Permeability	303
8.4.3.	Cavity Operating Pressure	307
8.5.	EFFECTS OF THERMAL PROPERTIES	309
8.5.1.	Thermal Conductivity	309
8.5.2.	Specific Heat Capacity	311
8.5.3.	Thermal Expansion Coefficient	313
8.6.	BEST PRACTICES GUIDELINES FOR SITE DESIGN	315
8.7.	CONCLUDING REMARKS	317
9.	CONCLUSIONS AND FURTHER WORK	319
9.1.	CONCLUSIONS	319
9.2.	SUGGESTIONS FOR FURTHER WORK	322
9.2.1.	Short Term Goals	322
9.2.2.	Long Term Goals	324
10.	REFERENCES	326

APPENDICES

A.	UNIVERSAL DISTINCT ELEMENT CODE THEORY	351
A.1.	MECHANICAL FORMULATION	351
A.1.1.	Mechanical Calculation Cycle	351
A.1.2.	Mechanical Timestep Determination	355
A.1.3.	Adaptive Local Damping	357
A.2.	HYDRAULIC FORMULATION	358
A.2.1.	Hydraulic Calculation Cycle	358
A.2.2.	Hydraulic Timestep Determination	363
A.3.	THERMAL FORMULATION	364
A.3.1.	Explicit Thermal Algorithm	364
A.3.2.	Implicit Thermal Algorithm	367
A.3.3.	Explicit Thermal Timestep Derivation	367
A.3.4.	Thermal Zone Generation	368
A.3.5.	Thermal Expansion	370
A.3.6.	Temperature Dependent Fluid Properties	371
B.	DERIVATIONS	372
B.1.	STRESS/DISPLACEMENT RELATIONSHIPS	372
B.2.	TEMPERATURE DEPENDENT MATERIAL PROPERTIES	375
B.2.1.	Friction Angle	376
B.2.2.	Cohesion	377
B.2.3.	Tensile Limit	377
B.2.4.	Normalised Properties	377
B.3.	CONDUCTIVE/CONVECTIVE HEAT TRANSFER RATIO	378
B.4.	CAVITY WALL TEMPERATURE DERIVATION	380
B.5.	THERMAL PENETRATION LENGTH	388
C.	GROUNDWATER CONTAMINATION MODELLING	390

GLOSSARY OF TERMS

Axisymmetric – Assumption that a body is identical for all angles of observation around a central rotational axis.

Block – Single, intact elements used to make up a rock mass in UDEC.

CBM – Coal Bed Methane. An unconventional fossil energy extraction technology which captures methane released from cleats in underground coal.

CFD – Computational Fluid Dynamics. A branch of the finite element method used to simulate fluid flow problems.

Chimneying – A form of subsidence in which a single cohesive pillar of earth undergoes rapid failure.

DEM – Discrete Element Method. Numerical method for simulating the motion and interaction of a number of independent particles which obey Newtonian mechanics.

DFN – Discrete Fracture Network. A method for stochastically producing sets of fractures within a material.

Distinct Element Method – A particular form of discrete element method which uses explicit time integration.

Domain – Discretised regions of fluid within UDEC.

Electrolinking – A method in which high voltages are used to break apart materials.

FDM – Finite Difference Method. Numerical method for simulating the behaviour of a system at a given point in space/time via numerical integration of differential equations.

FEM – Finite Element Method. Numerical method for representing the behaviour of a continuum by considering the forces and displacements on a number of mesh elements.

Fracking – Hydraulic fracturing. A method in which high pressure water is used to break apart solid materials.

Gasification – Reactions which produce gaseous products from solid reactants.

Gridpoint – The name given to nodes in UDEC.

GSI – Geological Strength Index. Empirical measure of how the strength of a rock mass relates to the strength of the individual rocks it contains.

Joint – Interfacial elements used to separate blocks and simulate sliding in UDEC.

Mesh – Representation of a continuous body as a number of small, interacting elements.

Mesh Element – The smallest individual region of a continuum model. State variables are assumed to be constant within a single element.

MODFLOW – MODular finite difference FLOW. Commercial software for modelling groundwater hydrogeology.

MT3DMS – Modular Transport, 3 Dimensional, Multi-Species Model. Commercial software for modelling contaminant transport in groundwater.

Node – The vertices of a mesh element. The displacements of nodes determine the deformation of a continuous body.

PFR – Plug flow reactor.

Plane Strain – Assumption that a material is identical at all points along its longest axis. Assumption of zero strain in the direction of this axis.

Pyrolysis – Thermal degradation of complex materials into simpler components.

Reserve – The amount of a material known to exist within a specified area which can be extracted in an economically viable manner.

Resource – The total amount of a material known to exist within a specified area.

Rock Mass – A large volume of a rocky material made up of a number of individual rock blocks separated by joints or fractures.

RNG – Random Number Generator.

Shale Gas – An unconventional source of oil. Commonly referred to as fracking.

Spalling – Thermally driven process of mechanical breakage and collapse.

Stoping – A form of subsidence in which voids in a material continuously move upwards through the material over time.

Syngas – An industrially useful mixture of gases, consisting mainly of carbon monoxide, carbon dioxide, hydrogen and methane.

UCG – Underground Coal Gasification. An industrial process for converting coal into syngas in-situ within an unmined coal seam

UCS – Uniaxial Compressive Strength.

UDEC – Universal Distinct Element Code. A commercially available two dimensional distinct element code for simulating the behaviour of heavily jointed rock masses.

Zone – The name given to mesh elements in UDEC.

NOMENCLATURE

A	Area	(m ²)
B	Zone Edge Length	(m)
C	Cohesion	(Pa)
C	Specific Heat Capacity	(Jkg ⁻¹ K ⁻¹)
D	Depth	(m)
D	Diffusivity	(m ² s ⁻¹)
E	Energy	(J)
E	Young's Modulus	(Pa)
F	Flow Rate	(mL/day)
F	Force	(N)
G	Shear Modulus	(Pa)
H	Enthalpy	(Jkg ⁻¹)
H	Height	(m)
K	Bulk Modulus	(Pa)
K ₀	Lateral Earth Pressure Coefficient	(-)
L	Length	(m)
N	Number	(-)
P	Perimeter	(m)
P	Pressure	(Pa)
Q	Specific Drawdown Rate	(-)
Q	Heat Flux in 2D	(Wm ⁻¹)
R	Rate of Consumption	(kgs ⁻¹)
R	Uniformly Distributed Random Number	(-)

S	Saturation	(-)
S	Subsidence (m)	(-)
T	Temperature	(K)
U	Heat Transfer Coefficient	(Wm ⁻² K ⁻¹)
V	Volume per unit depth into page	(m ²)
W	Width	(m)
a	Hydraulic Aperture	(m)
g	Acceleration due to gravity	(ms ⁻²)
k	Stiffness	(Nm ⁻¹)
k	Generic Proportionality Factor	(-)
m	Mass	(kg)
q	Flow Rate Per Unit Depth Into Page	(m ² s ⁻¹)
r	Radius	(m)
s	Separation	(m)
t	Time	(s/days)
u	Displacement	(m)
v	Velocity	(ms ⁻¹)
x	Horizontal Position	(m)
y	Vertical Position	(m)
Δ	Change/Increment	(-)
α	Linear Thermal Expansion Coefficient	(K ⁻¹)
α	Subsidence Factor	(-)

β	Contact Coefficient	(-)
β	Damping Factor	(-)
γ	Angle of Draw	($^{\circ}$)
γ	Poisson's Ratio	(-)
ε	Strain	(-)
θ	Friction Angle	($^{\circ}$)
κ	Permeability	(m^2)
λ	Multiplicative error factor	(-)
λ	Thermal Conductivity	($Wm^{-1}K^{-1}$)
μ	Dynamic Viscosity	(Pa s)
ρ	Density	(kgm^{-3})
σ	Normal Stress / Strength	(Pa)
τ	Shear Stress / Strength	(Pa)
ϕ	Joint Angle	($^{\circ}$)
ϕ	Porosity	(-)
ψ	Dilation Angle	($^{\circ}$)

SUBSCRIPTS

B	Block/Bottom
C	Compressive/Cavity/Coal
D	DFN
F	Fluid
G	Gridpoint
H	Hot

J	Joint
L	Lost
N	Normal
O	Oxidant
P	Product
R	Rock
S	Shear/Steam
T	Tensile/Thermal/Top
W	Water
Z	Zone
a	Axial
b	Background
c	Cavity
e	Extraction
f	Formation
l	Lateral
n	Number
p	Profile
r	Reaction
s	Surface
v	Volumetric
w	Wall
w	Width
x	Horizontal

y	Vertical
0	At Zero Stress/Initial
burn	Combustion Zone
crit	Critical
in	Net Inflow
max	Maximum
min	Minimum
sat	Saturated
tot	Total

SUPERSCRIPTS

C	Contact
D	Damped
L	External Load
P	Pressure
T	Thermal/Temperature
Z	Zone θ At Standard Conditions

ACCENTS

\hat{X}	Unit value of variable X.
\dot{X}	First time derivative of variable X.

1. INTRODUCTION

SUMMARY

Underground coal gasification (UCG) is an industrial process which converts coal into an economically valuable synthesis gas consisting mainly of hydrogen, carbon monoxide, carbon dioxide and methane in situ within an unmined coal seam. The product gas can be used as a fuel for electricity generation or as a precursor to synthetic liquid transport fuels and other chemicals. UCG is potentially safer, cheaper and less environmentally damaging than traditional methods of coal utilisation, and offers access to coal resources which would be uneconomical to extract using conventional means. As with any energy extraction technology however, UCG has the potential to cause environmental damage on both global and local scales.

The work presented in this thesis aims to further the understanding of the mechanisms behind the local environmental impact of UCG, with the goal of predicting and therefore preventing these issues in future operations. This chapter provides an introduction to both the UCG process and the numerical modelling of environmental issues. Information is given on the energy system as a whole, as well as the role of UCG in that system. Various advantages and disadvantages of UCG are presented, with a particular focus on local environmental issues. The application of numerical modelling to these issues is discussed and the principal aim, objectives and design considerations of the model produced in this project are outlined. Finally, this chapter concludes with a brief outline of the remainder of the thesis.

1.1. BACKGROUND

1.1.1. Global Energy Demands

As of the year 2016, global primary energy consumption is at a record high of 155 million GWh/yr, and is increasing at a rate of approximately 1.5% per year (BP, 2016). The upward trend in global energy demand is the product of three key factors: population, prosperity and energy efficiency. Prosperity has a strong effect on energy demand as more prosperous groups tend to consume more energy per capita. As global population and prosperity continue to grow, energy demands will continue to increase. Improvements in energy efficiency can offset this increase; however efficiency is ultimately limited by thermodynamic constraints. In order to meet increasing global energy demands, new sources of energy must therefore be found.

Any energy source must address three key issues, collectively referred to as the energy trilemma (World Energy Council, 2013a):

- Price – New energy sources must be cheap enough to ensure continued access at current levels, and allow for future increases in demand.
- Security – Energy sources must be able to cope with changes in demand, weather effects, fuel prices and national and international political issues.
- Sustainability – Sources must operate without causing environmental damage through greenhouse gas emissions, resource depletion etc.

Failure to meet any of the above issues can have severe economic, socio-political and environmental implications on global, national and local scales. A number of potential energy sources exist which can address these issues.

1.1.2. Energy Sources

All of the primary energy sources present on Earth can be classified either as renewable or exhaustible. Exhaustible sources include coal, oil and natural gas. Nuclear power is also exhaustible, however its use does not produce significant greenhouse gas emissions compared to fossil fuels. Renewable sources include wind, solar, geothermal and hydro power. Biomass is also considered renewable as the fuel used can be regrown and greenhouse gas emissions effectively offset by this growth. Table 1.1 highlights the key advantages and challenges of these sources with respect to the energy trilemma.

Table 1.1 – Advantages and challenges of various energy sources. + implies an advantage, - implies a challenge.

	Exhaustible	Renewable
Price	<ul style="list-style-type: none"> + Cheapest energy prices + Established technologies – Fuel price fluctuations 	<ul style="list-style-type: none"> + No fuel cost – Large infrastructure requirements – Currently very low capacity
Security	<ul style="list-style-type: none"> + Flexibility (transport or electricity) + Consistent power output – Dependence on international trade – Political uncertainty 	<ul style="list-style-type: none"> – Seasonal variability – Diurnal variability – Storage requirements – Geographically limited
Sustainability	<ul style="list-style-type: none"> – Greenhouse gas emissions – Air/water pollution – Resource depletion 	<ul style="list-style-type: none"> + Near zero emissions – Land usage

Table 1.1 shows that meeting the energy trilemma will be a considerable challenge, as no single energy source can reliably address all three concerns. While electricity grids may eventually run entirely on renewable sources, short term plans (i.e. those involving the current generation of power plants) must include fossil fuels in order to make up the shortfall in capacity while renewable sources are built. In addition, the use of renewable energy for transportation is problematic due to the geographical limitations of renewable energy sources. Renewable transport can be achieved through electrification, however this further increases electricity demands and the need for fossil fuels. In order to minimise the environmental impact of fossil fuel usage, new technologies are required which can extract this energy in an environmentally sound manner.

1.1.3. Fossil Energy Resources

This section gives a brief summary of global sources of fossil energy. Greater fuel abundance is beneficial as it keeps prices low. On the other hand, large stores of fossil fuels may promote the continued use of environmentally damaging sources of energy. Figure 1.1 shows the total extent of various fossil energy reserves. Coal and shale oil are seen to have greater reserves than other sources. It is of note that this figure lists reserves, rather than resources. Reserves are as sources which can be economically extracted using current technology, while resources are the total amount of fuel known to exist. Taking unrecoverable resources into account, coal is seen to be the most abundant fuel, with total resources of over 150 billion GWh (Self *et al*, 2012). By comparison, oil and gas resources are estimated as 11.6 and 5.8 billion GWh respectively (Brownfield *et al*, 2012; McGlade *et al*, 2012; Plummer *et al*, 2012).

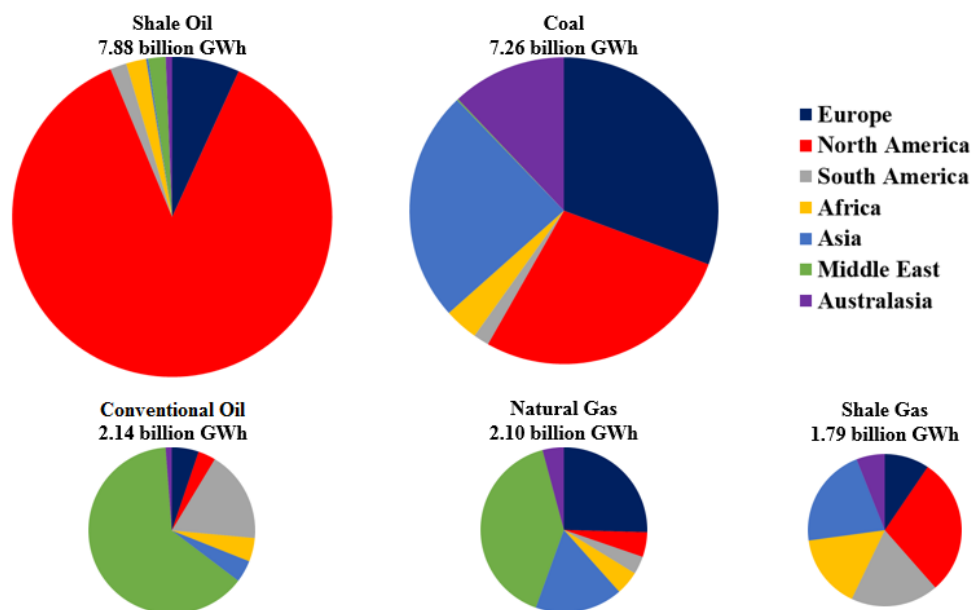


Figure 1.1 – Total economically recoverable fuel reserves by region. The area of each graph indicates the amount of energy available. After World Energy Council, 2013b.

As well as abundance, coal has a greater geographical diversity than other fuels. This is beneficial for both price and security as it helps keep costs low and reduces the impact of international politics on fuel supplies. On the other hand, coal has several environmental issues. Coal emits more CO₂ per unit energy than other fuels, as shown in Table 1.2. Coal also has higher sulphur and particulate contents and a greater number of inorganic contaminants than oil or gas (Kapusta & Stanczyk, 2011). Traditional coal use is therefore seen to cause a number of concerns which must be addressed in any future energy system. Underground coal gasification, especially in concert with carbon capture and storage (CCS), is a technology with the potential to address these concerns in a safe, cheap and environmentally sound manner.

Table 1.2 – CO₂ emissions by fuel (US Energy Information Administration, 2016).

Fuel	CO₂ Emissions (t/GWh thermal)
Coal	319 – 354
Oil	244 – 250
Natural Gas	181 – 215

1.2. UNDERGROUND COAL GASIFICATION

Underground coal gasification (UCG) is an industrial energy extraction technology with the potential to play an important role in future energy systems. UCG provides a means by which a great deal of the world's coal, including both proven reserves and currently unrecoverable resources, could be used in a safe and economically viable way. UCG presents a source of energy which is abundant, widely distributed, cost effective and secure from the external influences of international politics, market pressures and weather effects. Furthermore, the use of modern emissions reduction technologies, including CCS, allows UCG to operate in a much more environmentally friendly manner than traditional fossil energy technologies. Although coal is an inherently dirty fuel with finite reserves, UCG has the potential to utilise this resource in a way that many believe could provide an effective bridge to a future energy system based entirely on renewables (Roddy & Younger, 2010).

1.2.1. Process Description

The process of underground coal gasification involves the partial combustion and conversion of unmined coal within a coal seam into a synthesis gas (syngas) comprised mainly of carbon dioxide, carbon monoxide, methane, hydrogen and water vapour. Figure 1.2 depicts a typical UCG operation.

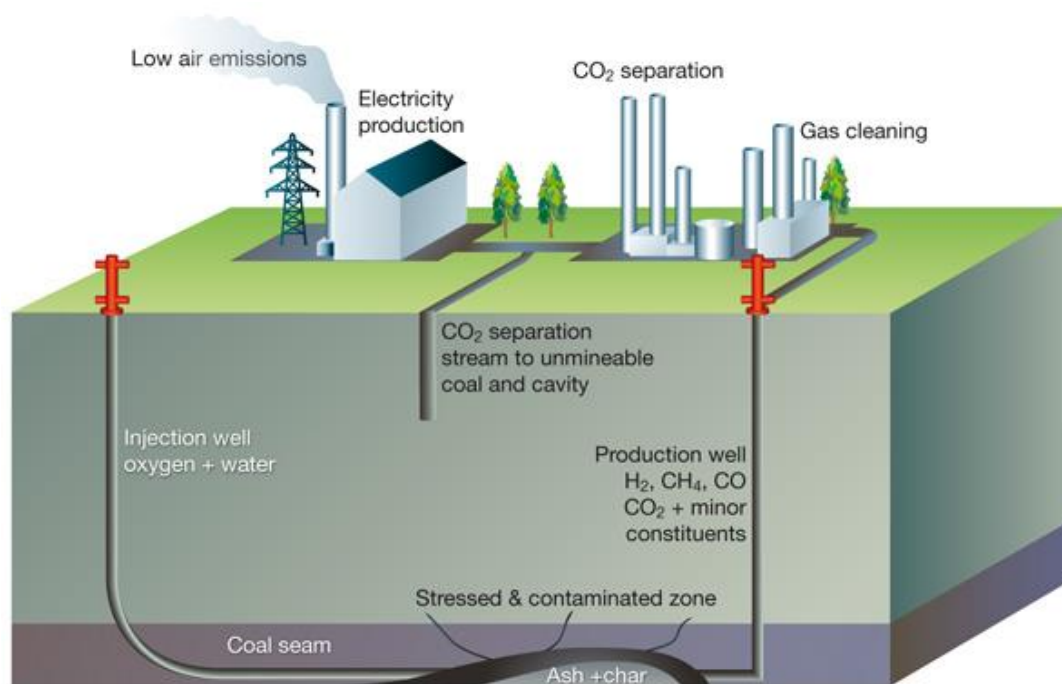


Figure 1.2 – Typical UCG operation. After Green, 2014.

UCG works by drilling two boreholes down into the coal seam and linking them together to form a gas circuit. One of the boreholes (the injection well) is used to supply air or oxygen and steam to the coal face, which is then ignited using a propane burner in the drillhead to begin the gasification reactions. These reactions consume the coal, converting it into a gaseous mixture of CO, CO₂, H₂ and CH₄, as well as a number of trace contaminants. The reaction set is autothermic and tends to occur at temperatures in the range of 800°C to 1800°C (Higman & Van der Burgt, 2008). Once this temperature is reached, the burner is shut off and the reaction becomes self-sustaining. The gaseous products then flow along the channel until they reach the second borehole (the production well) where they are extracted and processed for use in electricity generation or chemicals production (Couch, 2009). As the underground reaction proceeds, the coal on the inner wall of the cavity is consumed, causing the reactor to expand outwards through the coal seam, continually accessing fresh coal.

1.3. ADVANTAGES AND CHALLENGES OF UCG

1.3.1. Political Issues

The principal political issues around UCG relate to its status as a fossil fuel technology. In many developed countries, the continued development of fossil energy sources is politically unpopular due to their environmental impacts. This issue is less prevalent in developing countries as security of supply is often considered to be of greater importance. UCG is also often confused with shale gas extraction and hydraulic fracturing (fracking), which both have significant public opposition (Challener, 2013). The political advantages of UCG are mainly driven by increases in energy security. As shown in Figure 1.1, coal is by far the most geographically diverse fossil fuel. This diversity reduces dependence on trade and allows many nations a greater autonomy over their energy supply. This autonomy reduces the impact of international conflict on national economies and thus increases stability.

1.3.2. Economic Issues

A key economic benefit of UCG is its ability to access coal reserves which would be uneconomical using traditional means. UCG could potentially increase global coal reserves by a factor of up to twenty, greatly surpassing both shale oil and shale gas (Self *et al*, 2012). UCG is also an efficient method of extraction: Gasification efficiency (the fraction of the energy in the coal recovered in the syngas) exceeds 75% when oxygen is used as the injectant gas. Conversion efficiency (the proportion of the coal's mass converted to syngas) can be as high as 90% (Couch, 2009).

Other economic benefits of UCG arise because its simplicity reduces costs compared with traditional coal use: Surface infrastructure such as coal washing facilities and spoil tips are no longer necessary. Underground mine shafts are also not required, and surface based gasification equipment is eliminated entirely. Furthermore, the transport of gaseous fuels is easier and cheaper than that of coal, potentially allowing UCG syngas to displace solid coal imports to countries without indigenous resources. Because a UCG plant can be run by a small team of operators, overheads are considerably lower than those of coal mines employing hundreds of miners. Not only do these effects mean that UCG can generate larger profits for a given amount of coal, they also allow for the profitable extraction of previously unviable coal seams. This may allow UCG to operate in regions with large but uneconomically recoverable coal resources, such as the UK, however socio-political constraints may prevent this. The above effects suggest that UCG could provide electricity at a much lower cost than other potential clean energy sources, as shown in Figure 1.3.

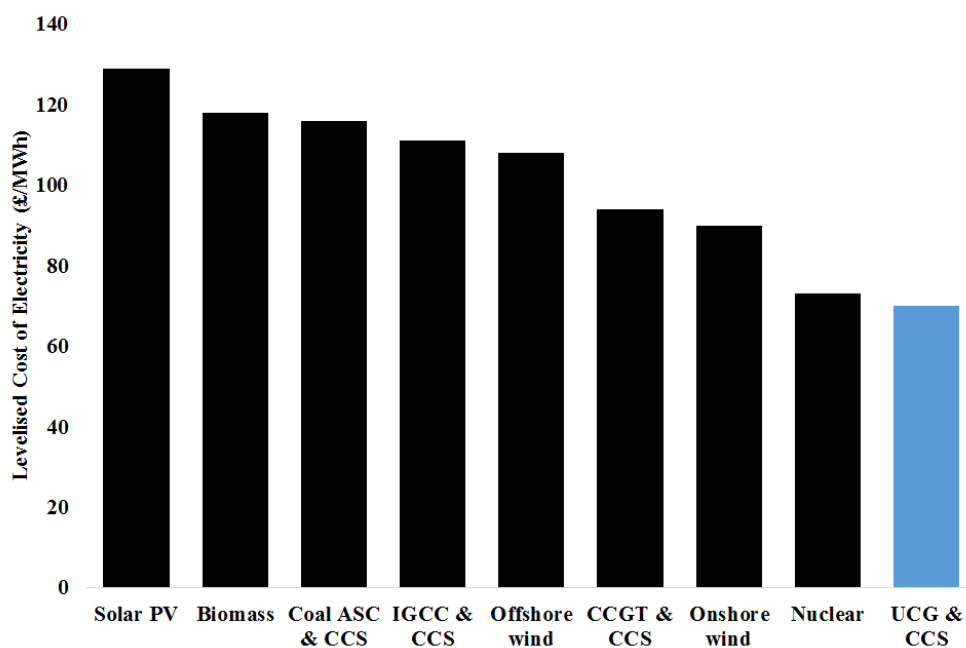


Figure 1.3 – Levelised cost of electricity in the UK for various clean energy technologies. (Department of Energy & Climate Change 2012; Ferguson, 2015).

1.3.3. Social Issues

UCG has several social advantages over other extraction technologies, the greatest of which is its safety compared with coal mining. In 2014, over 900 coal miners were killed in China alone due to accidents (Lelyveld, 2015). Many miners also suffer long term injuries and illnesses such as pneumoconiosis (black lung). Because UCG does not require any workers to be sent underground, these hazards are eliminated, potentially saving thousands of lives every year. These advantages also apply to other dangerous methods of energy extraction such as offshore oil and gas drilling.

Other social advantages of UCG include the creation of jobs for skilled workers and the potential economic benefits to economically deprived regions which previously depended on coal mining, such as the North East of England. Furthermore, the reduction in traffic, noise and dust compared with traditional coal mining can be seen as socially beneficial. On the other hand, in regions with existing coal mining industries, displacement by UCG could lead to the loss of a great number of jobs. Finally, the potential environmental impacts of UCG and perceived uncertainties around the technology may lead to reductions in property prices and considerable public opposition (Shackley *et al*, 2006).

1.3.4. Technical Issues

The majority of the technical challenges of UCG are caused by the novelty of the technology and the difficulty in understanding/monitoring the processes involved. Because of the underground nature of UCG as well as the extremes of temperature and pressure, much of what occurs in the reactor cavity is difficult and expensive to measure or observe (Britten & Thorsness, 1988). This not only introduces considerable difficulty in controlling the process but also makes it difficult to predict any impact the operation may have on the local environment. Future development of large scale commercial UCG may exacerbate this effect. Previous trials also had issues creating the initial connection between the injection and production wells, however modern operations solve this with the use of directional drilling techniques.

1.3.5. Legal Issues

Many of the legal issues of UCG relate to the novelty and uncertainties of the technology. Legal issues also tend to be specific to certain nations/regions and may have implications for international trade partners and countries bordering the target nation. One particular legal issue in a number of nations is the lack of coherent regulations regarding UCG. Due to the novelty of the technology, regulatory frameworks may not yet be present, or may be unclear. In the UK for example, UCG is overseen by the coal authority. Many of the technologies involved in UCG are overseen by the oil and gas authority however, leading to conflicting regulations (UK Oil and Gas Authority, 2015).

Other legal issues involve access rights to both the coal itself and the land above. These issues depend heavily on whether the mining industry in the target country is privatised or nationally owned. The legal implications of environmental damage also present a challenge to the development of UCG. For example, laws in the UK prevent the development of new coal fired power stations unless they are proved to be “CCS-ready” (Carrington, 2009). The effects of UCG on groundwater also have implications on local industries such as farms and mines, which depend on certain properties of the water table. This issue also applies to other nearby energy extraction methods such as hydraulic fracturing and coal bed methane (CBM) extraction, which both affect the local water table (Cuff, 2013). Because of these issues, the governments of Scotland, Wales and Queensland have each recently place moratoria on UCG (Queensland Government, 2016; Scottish Government, 2015; Welsh Government, 2015).

1.3.6. Environmental Issues

Many of the challenges of UCG relate to the environmental concerns of the technology. As with any energy extraction method, UCG has both local and global environmental impacts. In comparison with traditional extraction methods however, UCG also has several environmental advantages. These issues are summarised below.

1.3.6.1. Global Environmental Issues

The main environmental issues with coal are air pollution and greenhouse gas emissions. As shown in Table 1.2, coal emits more CO₂ per unit of thermal energy than any other fuel. Coal combustion also releases many other compounds, including sulphur and nitrogen oxides. These compounds both contribute to global warming and lead to other environmental effects such as acid rain. Compared with traditional extraction technologies however, UCG can greatly reduce these emissions for several reasons.

First, because the product of UCG is a combustible gas, it can be used with efficient combined cycle gas turbines (CCGTs). These turbines can have energy efficiencies of up to 60% (Seebregts, 2010) compared with values of less than 40% for traditional steam turbines (International Energy Agency, 2010). This greatly reduces CO₂ emissions per unit of electrical energy from UCG compared with traditional coal plants. Second, UCG reduces the need for many peripheral sources of CO₂ emissions associated with coal power. Because coal no longer needs to be transported, emissions from transport and shipping are eliminated. In addition, the smaller surface facilities of UCG reduce the emissions associated with construction.

Finally, UCG provides an ideal base for the development of CCS (Snape, 2013): The high CO₂ partial pressure of the syngas is beneficial for precombustion separation, while the existence of an air separation unit on site (to provide oxygen for gasification) greatly reduces the cost of oxyfuel capture (Thambimuthu *et al*, 2005). Additionally, the cavity itself may provide storage space for some of the captured CO₂. This process is known as reactor zone carbon storage (RZCS) (Burton *et al*, 2006). RZCS reduces the cost of CCS by eliminating transport costs and using the same wells that were used for gasification, reducing overall drilling costs. RZCS is not suitable for all sites however, as it requires a certain geology and a cavity depth of at least 800m to maintain CO₂ in a supercritical state. In addition, the volume of the CO₂ under these conditions would be 5 times greater than that of the gasified coal (Roddy & Younger, 2010), limiting the amount which can be stored. On the other hand, UCG suitable coal seams tend to be located in regions with suitable geology for CO₂ sequestration (Walter, 2007), allowing for storage in other nearby sites.

1.3.6.2. Local Environmental Issues

One of the principal advantages of UCG is its reduced effect on local pollution compared with traditional methods of coal utilisation. In addition to carbon and hydrogen, coal contains many environmentally damaging impurities, including sulphur, nitrogen, boron, lead and cadmium (Kapusta & Stanczyk, 2011). Traditional coal mining brings these to the surface where they are often released into the atmosphere or washed into rivers and lakes. By comparison, UCG leaves many of these impurities underground. This both reduces the environmental impact of UCG and the capital costs of ash clean up and storage.

As with any energy extraction method, UCG has a number of negative impacts on the local environment. While leaving coal impurities underground reduces air pollution, these impurities may instead migrate into local potable aquifers. This can contaminate local water sources and pose health risks to local residents, flora, and fauna. The conditions in the cavity also cause pyrolysis of coal, which produces additional contaminants (Humenick, 1984). Modern UCG operations aim to avoid this issue through good site selection. If possible, UCG operations are simply sited in coal seams which are isolated from any potable aquifers. While this eliminates the issue of contamination, it can have negative effects on the UCG process, as the presence of water helps to control gasification. Situation near saline aquifers solves this by supplying water that is already harmful to life, such that contamination is not an issue.

In cases where UCG operations must be sited near potable water sources, contamination is addressed using the technique of sub-hydrostatic operation. In this case, the cavity is operated at a pressure below the local hydrostatic pressure. This causes groundwater to flow into the cavity rather than allowing contaminants to flow out. This has been shown to greatly reduce contamination and has the additional benefit of forming a steam jacket around the cavity, preventing valuable heat and syngas from escaping into the overburden (Blinderman & Fidler, 2003). On the other hand, unpredictable groundwater inflow rates can affect gas quality and make process control difficult.

A second environmental issue, which may be caused by sub-hydrostatic operation, is water table lowering. If the rate of groundwater drawdown is greater than the local recharge rate, the level of the water table can be depressed. In some cases this can cause an increase in water table depth of up to 25m, which could lead to local wells and lakes drying out. (Lindblom & Smith, 1993). This may also exacerbate pollution if the lowering causes the phreatic surface of water table to enter the cavity, allowing pollutants to flow unimpeded into the vadose zone above the water table.

The final local environmental issue with UCG is surface subsidence. The removal of large areas of coal causes stress on the overburden above the cavity. This stress can cause the overburden to collapse, potentially damaging injection equipment and blocking the flow of gases. This collapse can propagate to the surface, damaging surface facilities and local buildings. In addition, the fracturing of rock strata can increase overburden permeability, potentially exacerbating groundwater effects. Figure 1.4 shows how these effects are interrelated.

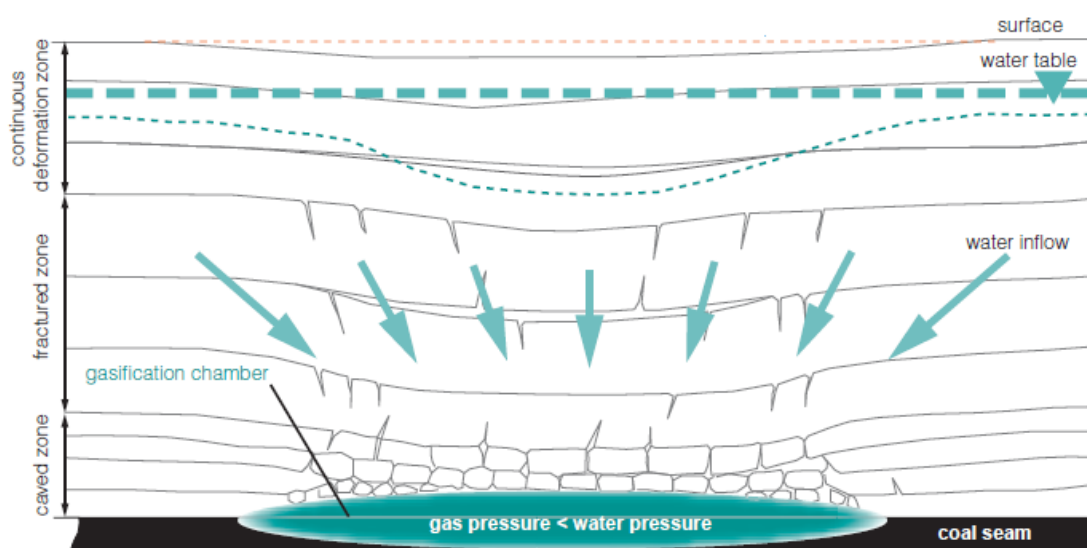


Figure 1.4 – Schematic description of subsidence and water table lowering effects caused by underground coal gasification. After Couch, 2009.

1.3.7. Geographical Considerations

As mentioned above, many of the issues of UCG are geographically specific. The suitability of a given region for UCG depends on a number of factors, including:

- The extent and quality of local coal resources.
- The demand for gas, electricity and chemical products.
- Political and public support/opposition to fossil fuel technologies.
- The history of the region with UCG and other unconventional energy sources.
- The main economic competitor for energy supply.
- Local competition for coal resources.
- Population density in targeted areas. Low populations greatly reduce the danger associated with local environmental damage.

These issues make the development of UCG easier in some nations than others. Many European nations, including the UK, have large coal reserves and high energy demands which currently depend on imported gas. On the other hand, these nations tend to have considerable public opposition to fossil energy sources. In addition, these countries tend to be densely populated with a politically active populace. By comparison, China and the USA have large coal reserves, high energy demands, large sparsely populated regions and supportive political climates. The USA also has extensive shale oil reserves however, which may be economically preferable to UCG. Given these issues, nations including China, India, Canada and the USA are prime targets for UCG. Australia was also considered a good target, however recent opposition (Queensland Government, 2016) has reduced this support somewhat.

1.3.8. Competing Technologies

The main competitors to UCG can be classified into two groups, depending on whether UCG is being considered for electricity generation or chemical production. If used as a source of electricity, UCG's main competitors are traditional fossil fuel plants, wind and nuclear power. These technologies are more mature than UCG and are currently much cheaper to operate. As the technology develops however, the price of UCG is expected to fall sharply, such that the cost of electricity approaches that shown in Figure 1.3. Although UCG will never compete environmentally with renewable energy, it still provides a very promising 'bridging' technology towards a renewable economy (Roddy and Younger, 2010). If UCG is used as a source of chemicals, its main competitors are oil and gas (traditional and unconventional). As mentioned in Section 1.3.7, UCG has a number of environmental advantages over both traditional and unconventional fossil fuel sources. These advantages can partly offset the increased cost of UCG in relation to these technologies. As such, the initial development of UCG may be easier as a source of chemicals rather than electricity.

A potential issue of UCG is the energy content of syngas. UCG syngas has a gross calorific value of $10 \pm 4 \text{ MJm}^{-3}$ compared with 37 ± 4 for natural gas (Blindermann & Fidler, 2003). As UCG would eventually be cheaper than natural gas per MWh this is not an issue for power generation, however it would affect the economics of syngas transport for export purposes. The continued development of unconventional oil and gas may also cause a reduction in the prices of these commodities, further reducing the relative economic benefit of UCG. Given the cost of long distance fuel transport, UCG may still be the best choice in regions with large coal and low oil/gas reserves.

A final advantage of UCG in comparison with other fossil energy sources is its reduced resource competition. UCG can operate on coals which are too remote to be recovered using traditional methods, and as such does not need to compete with other users for the same coal seam. Coal bed methane operations can conflict with UCG however, as this technology also targets deep coal seams. Resource competition between these technologies may also be exacerbated by the requirement of CBM to reduce groundwater pressure, potentially increasing the risk of contaminant escape from any nearby UCG activities (Moran et al, 2013).

1.3.9. Principal Challenges to Development

As seen above, UCG has the potential to be a key part of the future energy system or chemicals industry of many countries. It is seen however, that many challenges must be overcome before this can become a reality. Most of the greatest challenges relate to UCG's potential for environmental damage and its competition with unconventional oil and gas. Many of the political, social and legal issues are directly caused by these concerns. Technical and economic issues also relate to environmental damage because of the cost and difficulty in preventing these effects. As such, it is seen that reducing the environmental impact of UCG is the largest obstacle to its commercial development. While the global issues mentioned are serious problems, these are not specific to UCG itself. Greenhouse gas emissions and related effects are endemic to all fossil fuel technologies, and much research is currently underway to reduce these effects. As such, this thesis focuses only on local effects relevant to UCG. Given the difficulty in observing these effects, it is believed that gaining a better understanding of the processes involved is an important first step towards reducing their impact.

1.4. ENVIRONMENTAL MODELLING

1.4.1. Modelling Overview

As previously mentioned, the behaviour of a UCG operation is difficult to observe experimentally. The underground nature of the process makes direct observation impossible, while the high temperatures involved preclude the use of many in-situ monitoring techniques. In addition, the potential environmental impacts of UCG make experimental field trials politically and publically unpopular. Finally, the costs involved in performing trials prohibit their use in many studies. Because of these issues, much of the current work on UCG is performed using numerical modelling.

Numerical modelling has several advantages and disadvantages compared with experimentation. Modelling is considerably cheaper than experimentation and has no negative effects which could concern the public. Numerical modelling also allows for the evaluation of large numbers of potential sites with almost no increase in cost compared to that of a single site. On the other hand, the accuracy and usability of any numerical model is heavily limited by resources: Sufficient computational power, adequate physical understanding and large quantities of measured data are required to ensure model accuracy. In particular, a lack of relevant, accurate experimental data on which to base and verify the model can seriously reduce its usefulness. In effect, model accuracy is limited by the accuracy of the data used in its construction. Given the issues inherent in field trials however, numerical modelling is often greatly preferred for the analysis of UCG. The work presented in this thesis uses numerical modelling in an attempt to predict and therefore prevent the local environmental impacts of UCG, allowing for the safe design of future operations.

1.4.2. Model Aims

The principal aims of this model are to further the understanding of the local environmental impacts of underground coal gasification, and to provide simple, accurate and reliable predictions of these impacts for a range of potential gasifier designs. The model aims to produce a predictive model of the following highly coupled environmental concerns:

- Surface subsidence due to the removal of underground material.
- Contamination of groundwater by the products of gasifier operation.
- Water table lowering due to excessive groundwater consumption.

In addition, the model aims to be general, as opposed to site specific, and to produce results in under 24 hours when running on a standalone desktop PC. The runtime requirement is considered necessary as it allows the model to be tested against multiple potential site designs in a short time.

The environmental impacts above are driven by a combination of mechanical, hydraulic, thermal and chemical processes. These processes are highly coupled and occur over timescales ranging from milliseconds to days (Langland and Trent, 1981). Because of these issues, any fully realised model of environmental impact would be highly complex and would require a great deal of computational effort to simulate a single cavity design. Given the time and resources available, such a model is outside the scope of this project. In addition, this model would almost certainly fail to meet the target of sub 24 hour operation. As such, a greatly simplified model is required.

1.4.3. Proposed Use of Model

Given its short runtime, simplicity, and site-generic nature, it is envisioned that the model presented in this thesis will be used as a ‘first-pass’ screening tool for operators to choose between potential site designs. The completed model would be used to investigate the influence of a number of geological, design and operating conditions on the local environmental impacts of UCG. Trends in results could be used to inform site selection and operating procedures in order to prevent damage. Promising designs would then be further investigated using more detailed analyses before final decisions would be made.

1.5. THESIS OUTLINE

This thesis consists of nine chapters, including this introduction. The contents of the remaining chapters are summarised below:

Chapter 2 – Literature Review. Covers the relevant literature on both the UCG process and various aspects of environmental modelling. Outlines the choice of modelling methodology used in this work.

Chapter 3 – Introduction to UDEC. Covers the theory behind the mechanical, hydraulic and thermal modelling capabilities of the Universal Distinct Element Code, as well as the advantages, challenges and limitations of the software.

Chapter 4 – Simulated Lab Scale Testing. Introduces the method of simulated compression testing in UDEC. This novel methodology was used to help represent the overburden above UCG cavities using a reduced number of discrete elements.

Chapter 5 – UCG Model Development. Shows the design decisions and additional developments required to create the UCG model in UDEC. Initial validation of the UDEC software is also presented in this chapter.

Chapter 6 – Internal Parameter Effects. Gives the results of a large number of tests which were used to inform the selection of many internal (non-physical) parameters used in the final model.

Chapter 7 – Field Trial Validation. Presents the results of validation studies in which model results are compared to experimental observations from previous field trials. Discusses the validity of the model and its applicability as a predictive tool.

Chapter 8 – Site Design Studies. Gives the results of a number of simulations of UCG operations with varying geometric, geological and operating conditions. Identifies trends in environmental effects based on these conditions and provides guidelines for future operators.

Chapter 9 – Conclusions and Further Work. Summarises the work presented and highlights the key observations made during the modelling process. Suggests future developments in both the modelling and theoretical understanding of UCG.

2. LITERATURE REVIEW

SUMMARY

This chapter presents a review of the relevant literature published on the subjects of underground coal gasification (UCG) and environmental modelling. The chapter begins with an in-depth explanation of the UCG process, covering gasification chemistry, cavity growth mechanisms, gasifier designs and the effects of coal chemistry, site geology and operating conditions on UCG behaviour. The second part of the chapter presents a detailed explanation of the three main local environmental issues associated with UCG. The issues of surface subsidence, groundwater pollution and water table lowering are presented in terms of the mechanisms driving these processes, their effects on the local area, and the methods used to control and prevent these issues. A summary of recorded UCG field trials is then given, with a particular focus on the incidence of environmental damage caused by these trials.

The latter part of this chapter deals with the numerical modelling of the UCG process and the local environmental effects it can cause. The principal physical processes driving UCG are identified and the requirements for modelling these processes are considered. A number of modelling techniques are presented which may be used to simulate these issues and a summary of previous UCG modelling efforts is given. Notable gaps in the modelling of UCG are identified and recommendations are made for future efforts. Finally, the chapter concludes with a brief outline of the model produced in this work and the initial decisions on the software and assumptions used to create this model.

2.1. UNDERGROUND COAL GASIFICATION TECHNOLOGY

The basic principles of UCG are introduced in Section 1.2.1. This section gives a detailed overview of the mechanics of UCG, especially where issues relate to the potential for local scale environmental damage.

2.1.1. Gasification Chemistry

The process of coal gasification involves a complex, multi-step chemistry, as seen in Figure 2.1. The main chemical reactions involved are listed in Table 2.1. The first step of the process involves the drying of coal under the application of heat. Water trapped in the coal is boiled off and provides an important reactant in later stages. After continued heating, the process of pyrolysis begins. In this step volatile compounds are driven out of the coal matrix to leave a fixed carbon char (Seifi *et al*, 2011). The lighter compounds released are usually extracted with the syngas, while heavier compounds remain in the cavity and can potentially lead to groundwater pollution. The final three stages contain the reactions shown in Table 2.1. The combustion step depletes the injected oxygen in a series of exothermic reactions which provide the heat for the other stages. The gasification stage is largely endothermic and consists of a number of solid/gas reactions which produce the syngas. Finally, the refining stage alters the composition of the syngas. The final product composition can be set by controlling the equilibrium of this step, either in the cavity or in a separate reactor on the surface. Figures 2.2 and 2.3 show how syngas composition, temperature and calorific value vary along the cavity for an air fed gasifier.

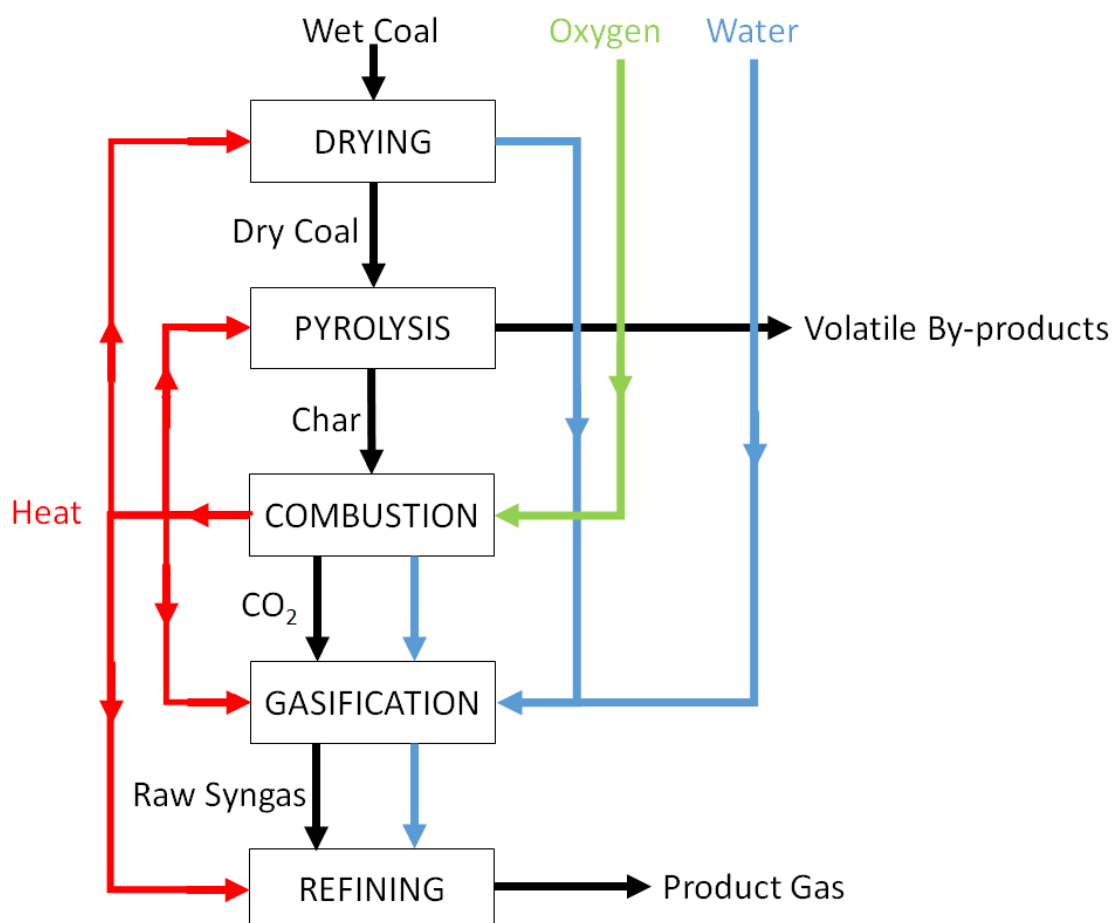


Figure 2.1 – Chemistry of the UCG Process.

Table 2.1 – Principal chemical reactions of UCG (Perkins & Sahajwalla, 2008)
Enthalpy values from Green & Perry, 2007.

No.	Reaction	Stage	Enthalpy Change at 1000K (kJmol ⁻¹)
1	$C + O_2 \rightarrow CO_2$	Combustion	-400
2	$CO + \frac{1}{2} O_2 \rightarrow CO_2$	Combustion	-288
3	$H_2 + \frac{1}{2} O_2 \rightarrow H_2O$	Combustion	-263
4	$CH_4 + 2 O_2 \rightarrow CO_2 + 2 H_2O$	Combustion	-825
5	$C + 2H_2 \rightarrow CH_4$	Gasification	-102
6	$C + CO_2 \rightarrow 2 CO$	Gasification	+176
7	$C + H_2O \rightarrow CO + H_2$	Gasification	+151
8	$CO + H_2O \leftrightarrow CO_2 + H_2$	Refining	-25
9	$CH_4 + H_2O \leftrightarrow CO + 3H_2$	Refining	+253

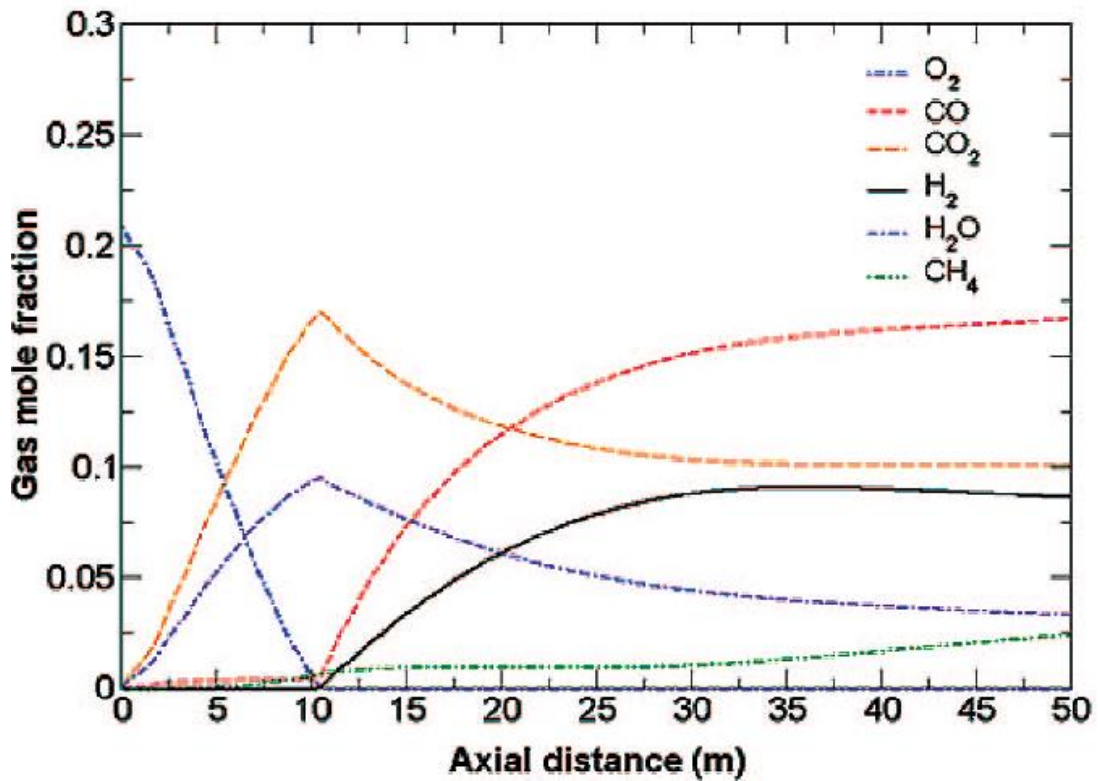


Figure 2.2 – Simulated variations in syngas composition as a function of length for an air blown gasifier. After Perkins & Sahajwalla, 2008.

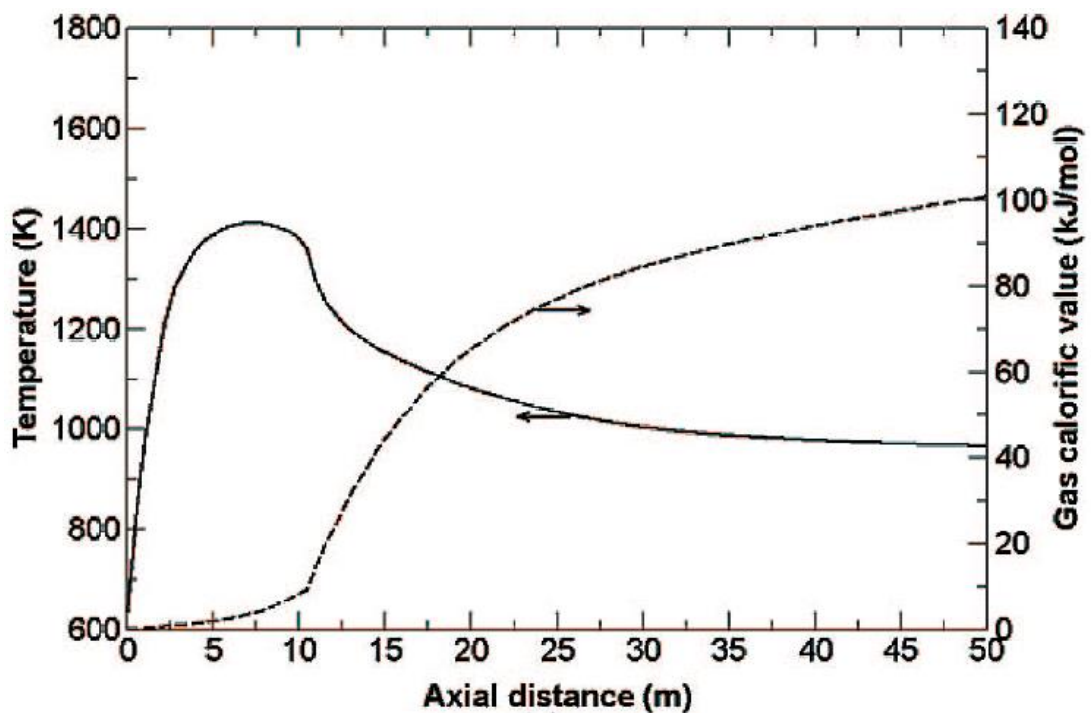


Figure 2.3 – Simulated variations in syngas temperature (solid line) and calorific value (dashed line) as a function of length for an air blown gasifier. After Perkins & Sahajwalla, 2008.

2.1.2. Cavity Growth Mechanisms

As gasification proceeds, material is continuously removed from the cavity wall as coal is converted into syngas and ash. This process constantly exposes fresh coal, driving gasification and increasing the size of the cavity. The rate at which growth occurs is fundamental to UCG as it controls both product gas quality and quantity throughout the life of the cavity. There are three principal mechanisms by which cavity growth occurs; reaction, thermo-mechanical spalling and large scale collapse:

Reaction is simply the process by which coal at the wall is converted to gas and ash which falls to the floor of the cavity and exposes fresh coal on the roof and walls. Reaction growth is a uniform process which causes the cavity wall to retreat at a rate of around 1cm/hr (Perkins, 2005). Spalling is a cyclic process in which the hot gases inside the cavity induce a steep temperature gradient in the cavity wall. This temperature gradient causes thermal stresses which lead to fracturing and cause pieces of coal to fall into the cavity. This exposes fresh coal to the hot gases, beginning the cycle again. Spalling is beneficial to UCG as it greatly increases the surface area available for gasification and promotes reaction within the rubble bed, however the spalling process itself is not well understood and spalling rates are often predicted using empirical models (Camp *et al*, 1980; Thorsness & Britten, 1986). Large scale collapse refers to roof and sidewall collapse caused by stresses in the coal near the cavity. The existence of a void where there was once solid coal, coupled with increased temperatures, causes large sections of coal/rock to fall into the cavity either as rubble or as coherent blocks. Large scale collapse is to be avoided, as the blocks of material can disrupt gas flow and their violent separation can exacerbate subsidence.

2.1.3. Gasifier Designs

Although the basic principle of UCG remain the same across all operations, factors such as local geology and the desired end use of syngas give rise to a number of gasifier designs, as shown in Figure 2.4.

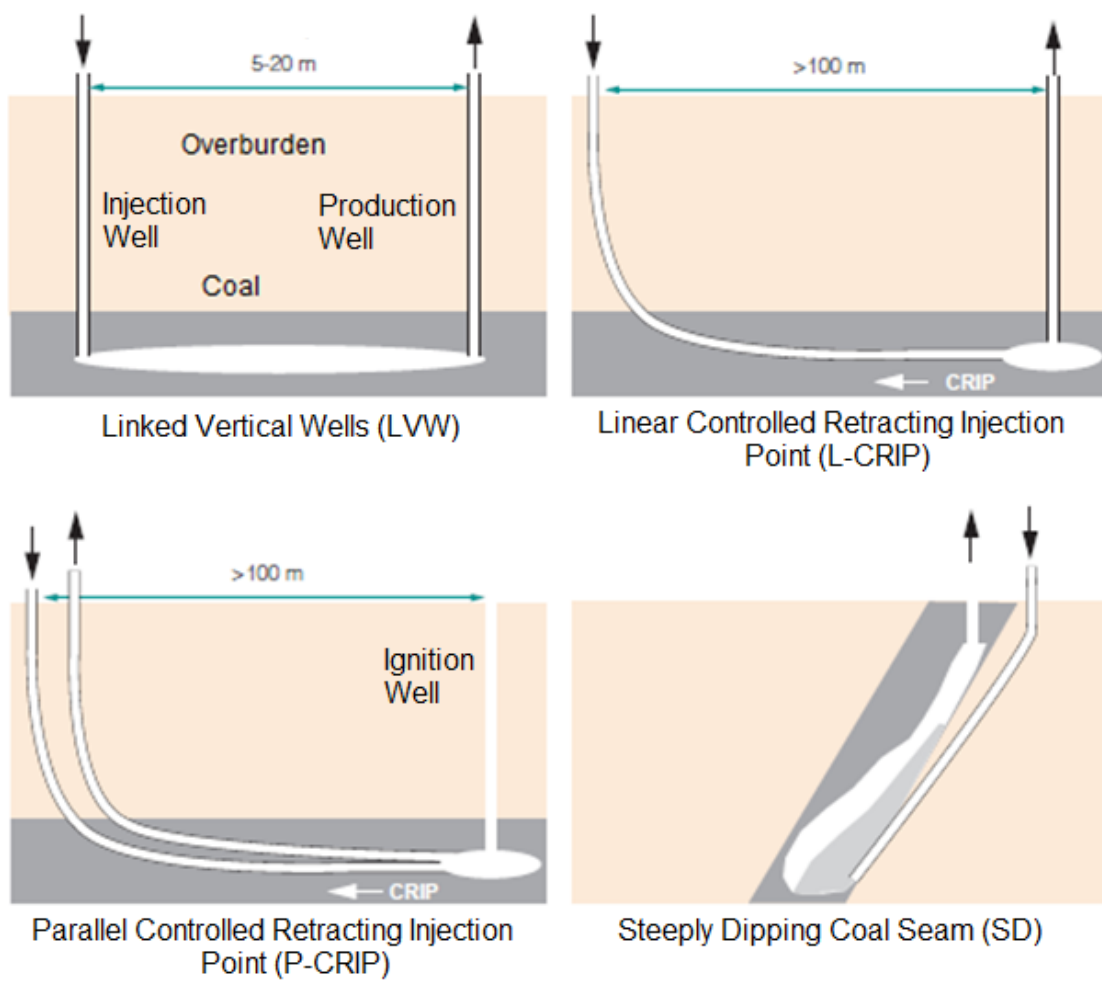


Figure 2.4 – Typical UCG cavity layouts. After Couch *et al*, 2009.

The simplest design of UCG reactor is the linked vertical well (LVW) layout, comprising a single pair of wells linked by a horizontal channel. Previous trials used a number of techniques to form this channel, including reverse combustion, hydraulic fracturing, explosive fracturing and electrolinking. Despite the high costs, modern operations tend to use directional drilling as this is much more controllable. Once the coal in the cavity is depleted, gasification ceases and a new pair of wells must be drilled in order to continue.

The controlled retracting injection point (CRIP) techniques allows access to much larger amounts of coal using only a single pair of wells (plus a vertical ignition well in the case of parallel CRIP). The linear CRIP (L-CRIP) technique works by drilling a single pair of wells several hundred metres apart. The injection well is deviated and drilled horizontally through the seam to intercept the production well at its base. Once the wells intersect, the injection point is retracted approximately 20m and gasification started. Once the coal in the vicinity of the cavity is depleted, gasification is stopped and the injection point is retracted a further 20m so that the process can be restarted in fresh coal. This process can be repeated a number of times, allowing for the creation of several UCG cavities from a single pair of wells (Thorsness & Britten, 1989). A successful trial of this technique was recently performed at the Swan Hills site in Canada (Green, 2015). In a commercial scale L-CRIP UCG facility, several CRIP channels would be bored in parallel so that multiple cavities could be operated simultaneously. As well as increasing production rates, this would give a tighter control over product composition through the blending of multiple product streams. A potential design for commercial scale L-CRIP UCG is shown in Figure 2.5.

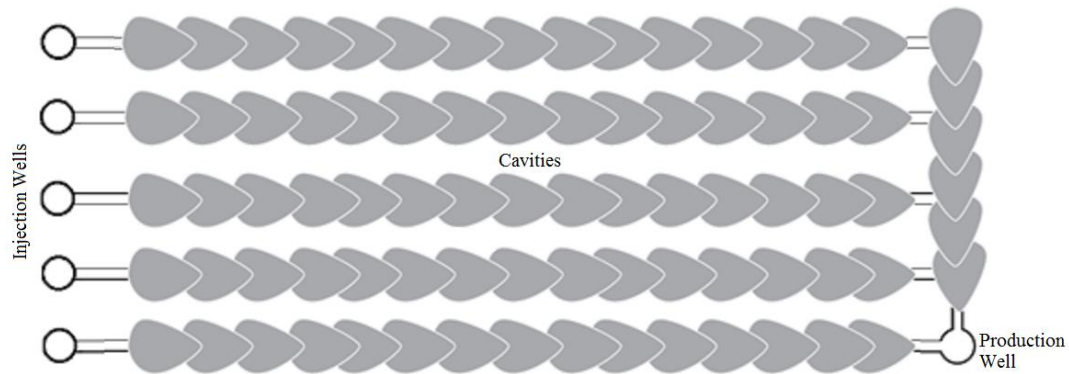


Figure 2.5 – Proposed layout of a commercial scale, multiple cavity L-CRIP UCG operation. After Couch *et al*, 2009.

Parallel CRIP (P-CRIP) is a similar method to L-CRIP, but in which two deviated wells are drilled in parallel along the coal seam and intercepted with a single vertical ignition well. Oxidant gases are injected along one of the wells and syngas withdrawn via the other. As gasification proceeds injection and production points retreat and the cavity grows in a similar shape to that of a traditional longwall mine. This method has recently been trialled at the Bloodwood Creek UCG pilot in Queensland (Mallett, 2013).

Steeply dipping coal seams (i.e. seams with an inclination to the horizontal of 60° or more) present an advantage in UCG operation in that the reaction's natural propensity to travel upwards causes the cavity to grow in the direction of further coal. In addition, heavy pollutants flow downwards, away from the production well. This technique also allows large deposits of coal to be gasified simply by using two wells spaced a short distance apart (Friedmann *et al*, 2007). Two key disadvantages of this design are its dependence on a certain geology and the potential to cause large amounts of subsidence due to the height of the cavity.

Given the above issues, many operators believe that the CRIP process provides the most viable technique for the commercial UCG (Couch, 2009). As such, the work in this thesis focuses on the use of this technique, in particular the L-CRIP configuration, and how the design and operation of the gasifier affects local environmental issues.

2.1.4. Coal Chemistry

One of the most important decisions in the design of a UCG operation is the location of the coal seam to be gasified. As well as the economic and political reasons for using a particular site, the chemistry and geology of the coal seam itself have a number of impacts on UCG performance. In terms of chemistry, the two main factors affecting UCG are the rank and grade of the coal.

Coal rank refers to the thermal maturity of the coal (the history of temperature and pressure which produced the coal). As coal increases in rank its moisture content decreases, while its carbon content and calorific value increase (Van Krevelen, 1993). Higher ranked coals contain more energy but also produce more CO₂. Low rank coals contain large amounts of moisture which must be evaporated, reducing their energy content. While conventional coal plants tend to use high rank coals, UCG can operate as well, if not better, on low rank coals. Although the moisture reduces the coal's calorific value, it also reduces the need to supply water for hydrogen production. The ability to use low rank coal allows UCG much greater economic flexibility than traditional methods, however there are efficiency issues. As shown in Figure 2.1, the energy for gasification is provided by combustion. Low rank coals provide less energy and thus reduce the conversion efficiency of UCG (Hebden & Stroud, 1981).

A particular issue of coal rank in UCG is swelling. When heated, coal undergoes processes which can lead to a change in density. During pyrolysis, reactions occur which produce a semi-fluid material called metaplast. Bubbles of volatile material form in the metaplast and cause the char to swell (Myongsook *et al*, 1989). Water present in the coal reduces this effect by promoting crosslinking reactions within the metaplast, leading to a smaller and more brittle char. As such, low rank coals tend to shrink, while high rank coals swell (Solomon & Serio, 1993). Shrinking is beneficial for UCG as swelling coals can block pores in the reactor, reducing efficiency. The increased brittleness of shrinking coals also promotes spalling, improving gasification rates (Anthony & Howard, 1976). The proclivity of a coal to shrink or swell is measured by the coal button profile, which ranges from 0 to 9. It is recommended that UCG should not be carried on coals with button profiles greater than 3 (Lavis, 2013).

Grade refers to the impurities present in the coal. These impurities are usually classed either as volatiles (e.g. hydrogen sulphide, ammonia, benzene) or ash (heavy metals, silicates, clay). Low grade coals have large amounts of impurities, increasing the risk of pollution from their use (Neavel, 1981). As UCG leaves much of the heavy contaminants underground, ash has less of an effect on UCG than on traditional coal uses. Though high ash contents affect calorific values by displacing carbon, the ash itself may act as a catalyst for gasification (Creedy *et al*, 2001). Volatiles may still present an issue with UCG, however these may be easier to deal with than under traditional combustion. As UCG predominantly takes place in a reducing atmosphere, sulphur and nitrogen are released as H_2S or NH_3 rather than SO_2 , NO or NO_2 . While these compounds still present environmental hazards, they are much easier to separate out of the syngas (Green, 2013a).

2.1.5. Coal Geology

While coal chemistry is an important factor in UCG design, the local geology of the coal seam and surrounding strata can be just as important. Table 2.2 shows how various local geological conditions affect the performance of UCG.

Table 2.2 – Effects of coal seam geology on UCG performance.

Coal Seam Characteristic	Advantages	Disadvantages
Increased Depth	<ul style="list-style-type: none"> - Higher operating pressures - Reduced risk of subsidence - Reduced resource competition - Allows RZCS if below 800m 	<ul style="list-style-type: none"> - Drilling costs - Oxygen compression costs
Increased Thickness	<ul style="list-style-type: none"> - Increased coal access - Increased conversion - Reduced heat loss 	<ul style="list-style-type: none"> - Increased risk of subsidence
Increased Dip Angle	<ul style="list-style-type: none"> - Enhanced cavity growth - Tars flow away from surface - Reduced resource competition 	<ul style="list-style-type: none"> - Variable cavity pressure - Difficult to control - Increased risk of subsidence - Usually found near faults
Increased Overburden Strength	<ul style="list-style-type: none"> - Reduced risk of subsidence - Reduced risk of pollution 	<ul style="list-style-type: none"> - Drilling costs
Increased Overburden Permeability	<ul style="list-style-type: none"> - Easier use of groundwater 	<ul style="list-style-type: none"> - Increased risk of pollution
Proximity to Aquifers (Potable)	<ul style="list-style-type: none"> - Allows use of groundwater 	<ul style="list-style-type: none"> - Risk of quenching reaction - Increased risk of pollution
Proximity to Aquifers (Saline)	<ul style="list-style-type: none"> - Allows use of groundwater - Reduced risk of pollution 	<ul style="list-style-type: none"> - Risk of quenching reaction
Proximity to Faults & Mine Workings	<ul style="list-style-type: none"> - None 	<ul style="list-style-type: none"> - Increased risk of subsidence - Increased risk of pollution

It can be seen that many factors affect the economics and safety of UCG. As such, legislators have produced guidelines for acceptable sites. In the UK, the Department of Trade and Industry (now the Department for Business, Energy and Industrial Strategy) sets the following criteria (Department of Trade and Industry, 2004):

- Coal seam depth between 600 and 1200m.
- Coal seam thickness greater than 2m.
- Good availability of rock material data.
- Horizontal distance of at least 500m from any faults or mine workings.
- Vertical distance of at least 100m from any potable groundwater resources.

In addition, the UK environment agency has stipulated that carbon capture and storage will be mandatory if UCG syngas is used for power generation, however this requirement is relaxed for other syngas uses such as chemicals production (Environment Agency, 2013).

2.1.6. Gasifier Operating Conditions

In addition to the properties of the coal seam itself, the economic and environmental performance of a UCG site also depends on a number of operating decisions. Essentially, there are six variables which can be controlled by the operator to affect gasification (Mostade, 2013): Well separation length, cavity operating pressure, oxidant composition, oxidant flow rate, oxidant/water ratio and channel spacing. The effects of each of these variables are outlined below.

With linked vertical wells or steeply dipping coal seams, well separation length is usually determined by geology. With CRIP UCG, separation length is a trade-off between the amount of coal that can be gasified, the pressure drop through the cavity, and the cost of drilling, which can be up to 70% of the total capital cost of UCG (Green, 2013b). While longer channels allow more cavities from each pair of wells, the increased length gives a greater risk of subsidence and higher compression costs.

The selection of an appropriate cavity operating pressure is often a trade-off between gasification efficiency and concerns over groundwater contamination. Operating pressure also has an effect on syngas composition through the equilibrium position of reaction 9 (see Table 2.1.). In modern UCG, operating pressures are limited to values below the local hydrostatic pressure in order to prevent contamination. Pressure is usually set at 75 – 80% of hydrostatic pressure at the cavity roof (Lavis, 2013). Excessively low pressures must be avoided however as they can cause considerable groundwater inflow which may quench the reaction or lead to water table lowering (Morris *et al*, 2009) The key risks and benefits of increased pressures are shown in Table 2.3.

Table 2.3 – Effects of operating pressure on UCG performance.

Pressure	Benefit	Risk
High	- Increased reaction rates - Increased syngas methane content	- Product escape - Groundwater contamination
Low	- Increase syngas hydrogen content - Reduced compression costs	- Quenching of reactions

Oxidant composition refers to the choice of using either air, enhanced air or oxygen to drive gasification. This choice is usually made on economic grounds and may vary based on the intended use of the product gas. Using oxygen rather than air increases the calorific value of the gas by eliminating diluent nitrogen. In addition, oxygen fuelled combustion occurs at higher temperatures, driving the endothermic gasification reactions and increasing syngas production rates. The elimination of nitrogen is also beneficial for CCS, both increasing CO₂ partial pressures and allowing for oxyfuel combustion. On the other hand, excessive amounts of oxygen can promote combustion over gasification, producing CO₂ and H₂O rather than CO and H₂. Finally, the capital and operating expenses of an air separation unit may considerably increase the cost of UCG.

Oxidant flow rates are much simpler to choose. Low flow rates promote gasification by more quickly providing a reducing atmosphere. On the other hand, low flow rates reduce temperatures by limiting the combustion process. Excessively high flow rates may simply cause the coal to combust rather than gasify. The rate of reaction in UCG is dominated by the natural convection of gases to and from the cavity wall (Perkins & Sahajwalla, 2008). As such, oxidant flow rate has little effect on the reaction beyond stoichiometry and temperature control. This was confirmed by experiments at the Centralia UCG trial (Burton *et al*, 2006). Given these considerations, the selection of an appropriate flow rate is predominantly a matter of stoichiometry and flow rates are generally selected in order to produce a desired syngas composition. The costs of compression and air separation (where oxygen is used) may also affect this decision.

The oxidant/water flow ratio is one of the most difficult variables to control. Where water is introduced artificially this can be achieved simply by altering flow rates. Where groundwater influx is significant however, this becomes more challenging. The rate of groundwater inflow is controlled by the operating pressure and as such these two conditions are intrinsically linked. The major effect of the O_2/H_2O ratio is its influence on product composition. Wetter ratios provide more hydrogen atoms, increasing concentrations of H_2 in the product. On the other hand, low ratios increase water flow rates, leading to a cooling effect and inhibiting the endothermic gasification reactions. Excessively high flowrates can quench gasification entirely, producing a CO_2 rich gas with low calorific value.

In commercial scale L-CRIP UCG, a number of cavities/channels would be drilled in parallel within the same coal seam, as in Figure 2.5. A key design factor is how many of these to drill, and how far apart to space them. The main factor determining the number of channels is economics. More channels imply more coal, increasing profitably and efficiency. On the other hand, drilling costs are one of the largest expenses of UCG and the more channels drilled, the greater the expense (Bhutto *et al*, 2013). The spacing of channels depends on the local stratigraphy and the strength of the coal and overburden rock. The sections of intact coal left between the channels are known as ‘coal pillars’ and these act to support the weight of the overburden. The size and location of these coal pillars, and hence the channels themselves, should be designed to reduce subsidence (Couch, 2009).

2.2. LOCAL ENVIRONMENTAL ISSUES

As mentioned in Section 1.3.7.2, the greatest environmental concerns of UCG on the local scale are surface subsidence, groundwater pollution and water table lowering. These issues are heavily coupled and highly dependent on the geological conditions of the gasifier. This section outlines the mechanisms behind these effects.

2.2.1. Surface Subsidence

Subsidence refers to a vertical movement of the ground's surface which can affect buildings, roads and utility pipes. Whenever a void is made in rock, the strata above the void will deform due to a lack of support from the removed material. In UCG, the strata are allowed to deform, leading to the collapse of the cavity and damage to the overburden. If this damage extends to the ground's surface, subsidence occurs. The extent of subsidence depends on the geometry of the cavity and the material properties of the overburden. The region of ground affected is called the subsidence trough. The height of the trough is ultimately limited by cavity height, which in turn depends on coal seam thickness. Trough width is defined by a constant angle of draw between the excavation and the surface. Subsidence occurs to some degree above almost all excavations, however disturbances of less than 20mm are generally considered to be harmless (Mine Subsidence Engineering Consultants, 2007). In addition to surface damage, the deformation of the overburden can also increase the permeability of the rock mass and connect previously separate groundwater resources, exacerbating groundwater pollution. This effect is explored in detail in Section 2.2.2.

2.2.1.1. Subsidence Mechanisms

While all cases of subsidence lead to vertical ground motion, there are four principal mechanisms by which this motion occurs (Friedmann *et al*, 2008; Gregg, 1977):

Stoping is the method of subsidence commonly seen where excavations are performed in brittle rocks with pre-existing fractures. As extraction continues, rocks fall into the cavity to fill up the space left behind by the removed material. This in turn creates a new void above the original which is later filled in by rubble from above. This process continues over time, causing the void to migrate upwards through the overburden (Hartman, 1992). Each successive void is smaller than the previous one however, because of the phenomenon of bulking. This refers to tendency of solid materials to expand in volume when they are broken up into rubble. The ratio of rubble to solid volume is known as the bulking factor, and has a value of approximately 1.25 for most rocks (Gregg, 1977). The void migration and bulking processes continue upwards until the current void is not large enough to cause roof collapse (Friedmann *et al*, 2008). Stopping subsidence can also be arrested when the void intersects a particularly strong stratigraphic layer known as a spanning unit (Keilich *et al*, 2006).

Chimneying is a severe form of stoping in which large vertical motion occurs with little or no bulking. This occurs either because the rock mass has a low bulking factor or because the rubble is removed from the cavity. Chimneying is common in block caving mines, where the rubble is intentionally removed in the mining process. Chimneys can have diameters as low as 3m, but can extend vertically by over 300m in a matter of days if the rubble is removed fast enough (Brady & Brown, 2005).

Bending subsidence is the mechanism seen most often where the overburden is ductile or where very little fracturing is present. In this mechanism, overburden strata simply bend under the weight of overlying rocks and sag into the cavity. Successive strata then continue to bend and fill the space below, causing the subsidence trough to migrate towards the surface. In many cases it is possible for several layered strata to bend in concert, causing considerable subsidence regardless of the depth of the initial void. Bending subsidence has little effect on rock fractures and is therefore unrelated to issues of groundwater pollution or water table lowering (Kratzsch, 1983).

The final subsidence mechanism is that of plug failure. This is an extreme form of subsidence in which the entire column of rock above a void fails en-masse and slides into the void, often in a sudden and violent manner. Almost no bulking occurs in this case, and the extent of surface subsidence is of a similar height to the initial void itself. Plug failure is usually caused by planes of weakness within the overburden and tends to occur in areas which have already undergone some degree of subsidence (Brady & Brown, 2005)

Figure 2.6 shows the typical overburden behaviour above a UCG cavity. Thin seams tend to subside via bending as gasification proceeds. Thicker seams tend to fail via stoping, with the failed region extending to more than twice the cavity height above the roof (Creedy *et al*, 2001). Chimneying and plug failure are observed in extreme cases, such as the Hoe Creek 3 trial. (Ganow, 1984). Significant subsidence is rare with UCG due to the typical geometry of the cavity. Where subsidence does occur, it is usually caused by a combination of the stoping and bending mechanisms. As shown in Chapter 5, it is these mechanisms that the proposed model attempts to simulate.

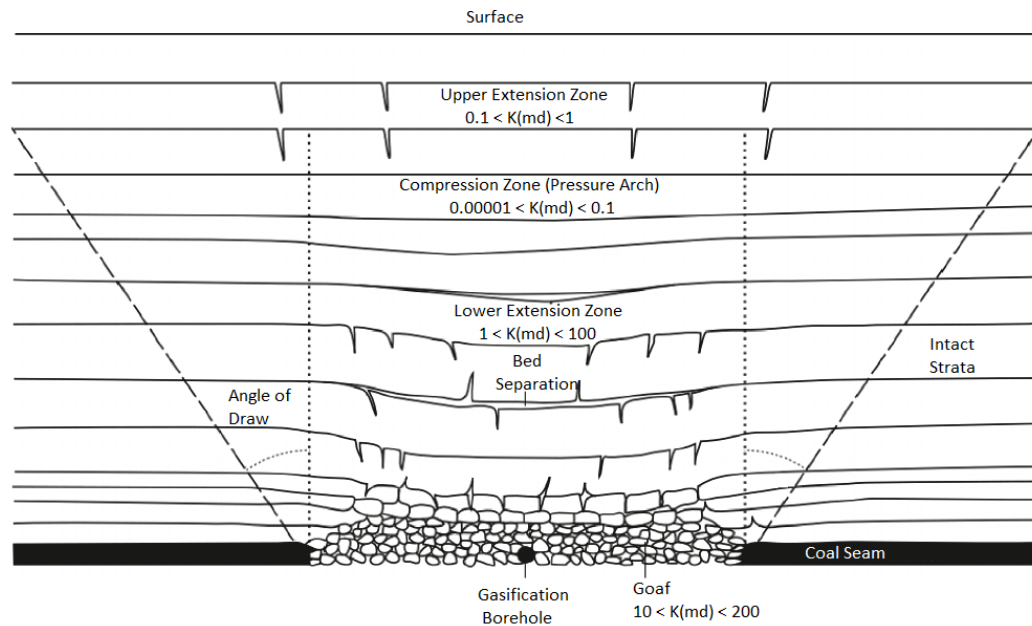


Figure 2.6 – Typical subsidence behaviour above a UCG cavity, including the effects on overburden hydraulic permeability. After Younger *et al*, 2011.

2.2.1.2. Preventing Subsidence

As mentioned above, the subsidence at a given site depends on cavity geometry and overburden strength. As such, the best way to control subsidence is to site the cavity appropriately. Artificial methods of support exist (e.g. rock bolting), however these are not appropriate for UCG. The extent of subsidence depends on six key factors:

- Extraction height
- Extraction depth
- Extraction length
- Extraction width
- Overburden stiffness
- Extent of fracturing of the overburden

Increases in extraction height cause greater surface subsidence by providing a larger initial void. The relationship between height and subsidence is usually linear, and is often expressed by means of a subsidence factor α . The subsidence factor is defined as the ratio of surface subsidence to extraction height for a theoretically infinite cavity (Brauner, 1973). Subsidence factors are measured experimentally and vary greatly from site to site. Factors for UCG are commonly found to be in the range of 0.7 to 0.9 (Gregg, 1977).

The depth of a cavity below the ground's surface has a strong influence over both the vertical and horizontal extents of subsidence. Increases in depth greatly reduce subsidence by introducing a larger amount of material above the cavity. This increases the chance of encountering spanning units before subsidence reaches the surface, and increases the effect of bulking. Increased depth also reduces the possibility of connection with potable groundwater sources, because deeper aquifers are more likely to be saline. Although greater depth reduces the magnitude of subsidence, it can increase the area over which subsidence is observed. As mentioned above, the horizontal extent of subsidence depends on the angle of draw γ . This is defined as the angle between the horizon and an imaginary line drawn between the edge of the cavity and the corresponding edge of the subsidence trough. The angle of draw for UCG is around 35° (Brown, 2012). Figure 2.7 shows the effects of the angle of draw on the subsidence trough.

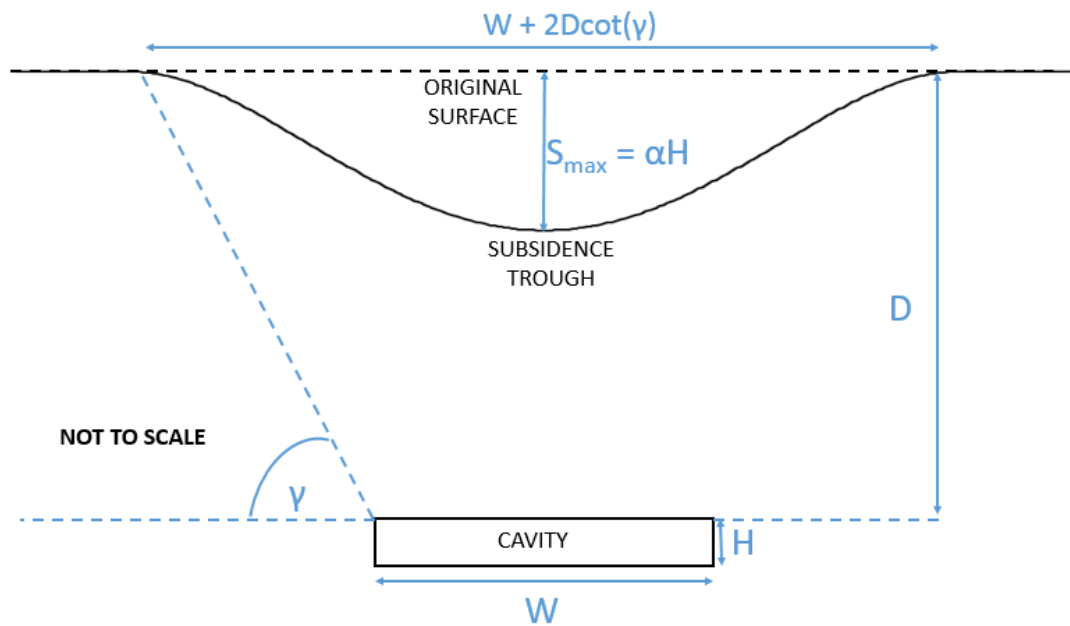


Figure 2.7 – Effects of cavity geometry on subsidence. After Brauner *et al*, 1973.

Extraction length and width have an effect on both the vertical and horizontal extent of subsidence. Due to the increased size of the void, larger cavities lead to more subsidence as more bulking is required to halt the stoping process. Larger voids also exacerbate bending subsidence by allowing larger sections of the overburden to sag into the cavity. These effects are often in opposition to those of increased depth. As such, many empirical methods relate the subsidence factor α to the ratio of W/D (Keilich *et al*, 2006; Langland & Trent, 1981).

Increasing cavity size also affects both the size and shape of the subsidence trough. As shown in Figure 2.7, the width of the trough depends directly on the width of the cavity. The shape of the trough however, depends on the relationship between cavity width W and the critical radius r_{crit} , given in Equation 2.1. The effect of the critical radius on trough shape is shown in Figure 2.8.

$$r_{crit} = 2D \cot(\gamma) \quad (2.1)$$

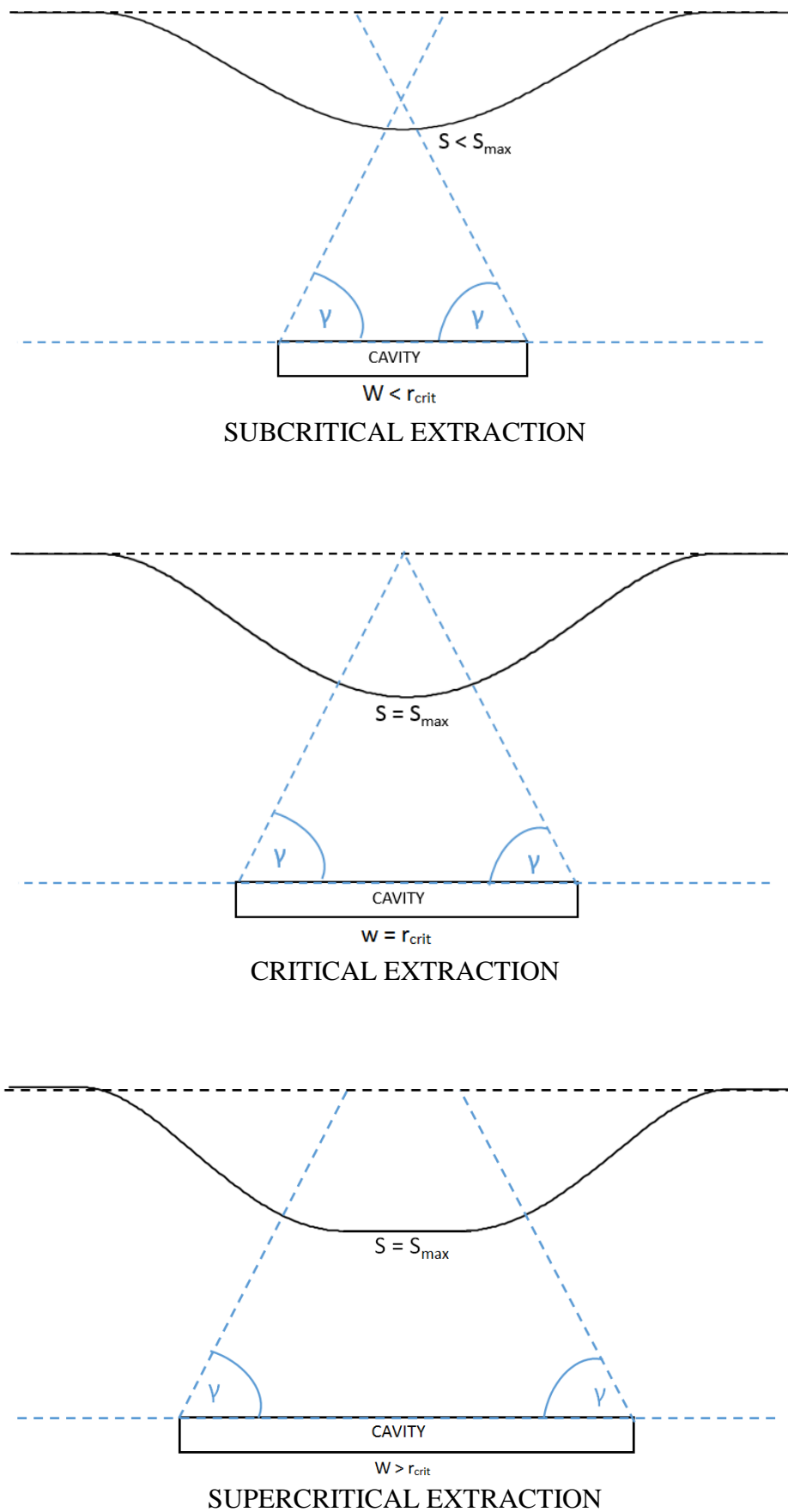


Figure 2.8 – Effects of cavity width on subsidence profile shape.

The effects of overburden material properties on subsidence are simpler to explain. The stiffness of the overburden is strongly related to the mechanism of bending subsidence. According to classical beam theory, stiffer strata (effectively acting as beams) deform to a lesser extent under a given force than softer beams. As such, stiffer strata lead to less subsidence for a given cavity geometry. Other material properties of the beam, such as cohesive strength, are irrelevant unless the force on the beam is large enough to cause brittle failure of the strata. Such a failure is usually pre-empted however, by failure along existing fractures which are much weaker than the rock matrix. As such, the degree of fracturing is an important parameter.

Heavily fractured strata contain more planes of weakness than lightly fractured strata. As such these are more prone to brittle failures, including the separation of discrete blocks of material from the overburden (i.e. stoping). Therefore the degree of overburden fracturing is seen to be strongly related to the mechanisms of stoping and chimney/plug failure. Unlike stiffness, the degree of fracturing of a rock mass is difficult to quantify. In many cases, empirical measures such as the disturbance factor (Hoek *et al*, 2002) are used to represent fracturing in a qualitative manner.

As shown in this section, subsidence above a UCG cavity depends greatly on the geometry and geology of the cavity. In all cases, these can only be realistically controlled by the selection of an appropriate site for UCG operation. This site must contain a coal seam deep enough that there is sufficient overburden to arrest the stoping and bending processes before they reach the surface. In the case of stoping, the depth must also be sufficient to ensure the process is stopped before it intersects any potable groundwater resources.

Modern operations suggest UCG should only be performed at depths greater than 300m, leaving at least 150m of undisturbed overburden between the surface and the roof of the caved zone (Mallett, 2006). The overburden must also be sufficiently stiff and undisturbed. The influence of cavity length, width and height must be considered, however the reduction of these dimensions is undesirable due to their influence on UCG economics.

Given these observations, it is clear that site selection is the most powerful tool for reducing surface subsidence above UCG cavities, but that the effects of site selection on other environmental and economic issues should also be considered. The effects of site geometry, geology and operating conditions on environmental issues are investigated in detail in Chapter 8. The effects of such properties on the economic performance of UCG have been considered by many authors, as shown in Table 2.2.

2.2.2. Groundwater Pollution

As previously mentioned, UCG has the potential to cause pollution of local groundwater resources. A number of pollutant species may be present in the coal seam, or may be generated by pyrolysis. Several mechanisms exist by which these species can migrate into groundwater and these may lead to a number of detrimental effects on local groundwater. This section outlines the common pollutants seen with UCG, their typical methods of groundwater entry and the effects of various geological and operating conditions on groundwater pollution.

2.2.2.1. Common Pollutants

The contaminants present in groundwater polluted by UCG can be broadly classified into two groups: coal impurities and pyrolysis products. Coal impurities represent the species present in the coal which are not converted by the gasification process. Common impurities include sulphates, ammonium salts, heavy metals and aluminosilicates. Many of these compounds are incombustible and therefore remain in the UCG cavity as ash after gasification ceases (Blinderman & Fidler, 2003). Pyrolysis products are organic compounds liberated by the thermal degradation of coal during the UCG process. These compounds may have been trapped in the pore spaces of the coal matrix or may have been produced through chemical reaction under heating (Seifi *et al*, 2011). Pyrolysis products include short chain hydrocarbons, phenols, polyaromatic hydrocarbons (PAHs), heavy hydrocarbon tars and BTEX compounds (benzene, toluene, ethylbenzene, xylenes) (Kapusta & Stanczyk, 2011).

The identities and concentrations of species present in UCG contaminated groundwater depend greatly on the rank and grade of the coal used, the composition of the groundwater and the operating temperature and pressure of UCG process (Humenick, 1984). The concentrations present also depend on the solubility of the compounds in water and the environmental persistence of the contaminant species. As well as affecting the amounts present, these factors can affect how long a contaminant stays in the groundwater and how far from the gasification cavity it travels in that time. These factors, along with human and environmental toxicity, determine the impact of groundwater contamination on the local environment.

2.2.2.2. Pollution Mechanisms

The pollutants released by UCG primarily enter groundwater resources through one of three mechanisms (Burton *et al*, 2008; Self *et al*, 2012). Firstly, high operating pressures and steep thermal gradients can drive product gases into the surroundings, where they later cool and condense within the pore spaces of the rock. Local groundwater flows can then dissolve the contaminants or wash them into nearby aquifers. Second, after UCG has finished, the cavity may fill with groundwater. Pollutants adsorbed on to the cavity wall and trapped within the pore spaces of the ash and rubble zones will then be leached out into this water. Over time the natural flows of the groundwater, coupled with the diffusion of the contaminants, can cause the pollutant species to migrate towards sources of potable water. The first mechanism tends to cause pollution in the short term (during or shortly after gasification), while the second occurs on a longer timescale (Blinderman & Fidler, 2003).

Finally, as mentioned in Section 2.2.1, the deformation of the overburden due to stoping and cavity collapse can exacerbate pollution. This occurs when the enhanced fracturing of the overburden creates a flow pathway between the cavity (the pollutant source) and a previously unconnected potable aquifer (the pollutant receptor). This method can cause considerable increases in pollutant concentrations in a very short time. This effect may also occur where production and injection wells are not correctly cased, allowing product gases to migrate up the sides of the well to impact aquifers several hundred metres above the cavity (Humenick, 1984).

Once contaminants have entered the groundwater, their concentrations vary with space and time. Contaminants are transported away from the cavity by diffusion and advection. Note that in the case of advection, net groundwater flow into the cavity acts to slow the spread of contamination rather than contributing to it. The effects of advection also vary depending on the stage of the gasification process due to changes in operating pressure (Lindblom, & Smith, 1993). Contaminant concentrations decrease over time due to the processes of adsorption, ion exchange, precipitation and biological conversion. Adsorption is a key mechanism in this process, as some species adsorb well enough on to the rock for the groundwater to be considered free from their presence (Stuermer *et al*, 1982). Biological conversion is the only process which destroys contaminants outright, however it can also provide a means for them to enter the food chain (Humenick, 1984). The efficacy of these processes varies between species, leading to considerable variations in contaminant persistence between sites.

2.2.2.3. Preventing Pollution

As seen above, groundwater pollution depends on the processes of contaminant generation, destruction and transport. The control of pollution can be achieved either by curtailing generation and transport, or by enhancing destruction. The control of contaminant generation is problematic, as the chemical processes which drive generation are the same as those which produce the syngas. As such, slowing these processes may be economically unviable. The use of high grade coals reduces contaminant generation somewhat, though the availability of these coals may restrict this approach. Coal rank may also affect contamination, as high ranked coals tend to produce more pyrolysis products than low ranked coals (Kapusta & Stanczyk, 2011).

Contaminant destruction processes are often difficult, if not impossible, to control during the gasification process. The mechanisms of destruction depend heavily on the local geology, geochemistry and geobiology of the UCG site. The only realistic method for enhancing these processes during gasification is simply to site the operation in a location with suitable properties. On the other hand, natural destruction processes occur on a much longer timescale than that of a typical UCG operation. Natural pollutant removal can take up to 30 years from the onset of contamination (Nathanail & Bardos, 2004), compared with UCG operating timescales on the order of months. Enhanced contaminant destruction processes such as air sparging and bioremediation could be applied after gasification has finished, however this would imply that pollution is initially allowed to happen. Such measures would therefore be politically, economically, ethically, socially and legally unpopular.

The most promising methods of pollutant control involve the alteration of contaminant transport processes. During gasification, trapping the contaminants within the cavity (e.g. by operating at sub-hydrostatic pressures) prevents their spread into the groundwater. Some species may then be destroyed by combustion within the cavity, or may be entrained in the syngas and brought to the surface where they can be treated. Heavy and incombustible species remain in the cavity during this process, but can later be removed through artificial means. The discussion of contaminant transport must therefore consider the control of groundwater flow both during and after gasification.

The control of contaminant transport during gasification is most easily achieved simply by locating the UCG cavity sufficiently far away from any potable groundwater sources. If the operation can be sited in a region which is completely dry, or in which groundwater sources are already unpotable, then the migration of contaminants poses no environmental danger. It is of note however that contamination of land, even in inhospitable locations, may still have political implications. Where a potable aquifer is present, transport can be avoided by ensuring that no flow pathways connect the aquifer to the coal seam. This is usually achieved by siting UCG in deep coal seams with aquitards present between the coal seam and the aquifer. It is important however that these aquitards are not compromised by the fracturing processes driven by UCG.

Where the above methods are not possible, contaminant transport can generally be controlled by reducing the operating pressure of the cavity. By operating below local hydrostatic pressure, a negative hydraulic gradient is formed, causing groundwater to flow into the cavity rather than allowing pollutants to flow out. This sub-hydrostatic operation can have unintended consequences on syngas production however, as explained in Section 2.1.6. In addition, sub-hydrostatic operation can lead to the depletion of local water resources, explained further in Section 2.2.3. Finally, because hydrostatic pressure increases with depth, operating pressure must be lower not only than that at the roof of the cavity but also that in any connected fractures within the overburden. As this is difficult to measure, many operators set an upper limit on operating pressure of 80% of hydrostatic pressure at the cavity roof (Lavis, 2013).

Control of contaminant transport after gasification ceases has the aim of removing pollutants from the cavity before they can spread into the overburden. This is most commonly achieved using the ‘clean cavern concept’ (Dennis, 2006). This involves flushing the cavity through with large quantities of injected steam, water and nitrogen to cool the cavity and halt pyrolysis. This cooling effect is required as, left unchecked, the UCG cavity could remain hot enough to drive pyrolysis for a number of years. This heat may also cause cavity pressures to increase above hydrostatic pressure through the evaporation of pore water (Sarhosis *et al*, 2013). While flushing proceeds, the cavity is allowed to vent continuously through the production well. This ensures cavity pressures remain sub-hydrostatic, and brings the contaminants trapped in the cavity to the surface where they can be processed. Once flushing is complete, the wells are sealed and the cavity may be filled with cement or drilling mud in order to prevent further groundwater motion (Burton *et al*, 2006). While this is effectively a remediation process (as opposed to prevention), in concert with sub-hydrostatic operation it is seen to greatly reduce the risks and extent of groundwater contamination (Blinderman & Fidler, 2003; Sarhosis *et al*, 2016).

As seen above, the main techniques for preventing groundwater pollution are sub-hydrostatic operation and the post gasification flushing of the cavity. Site selection is also important, as locating a UCG operation far from potable water sources is guaranteed to limit pollution. The influence of site selection on rock mass deformation also has a secondary effect on pollution through permeability enhancement. In summary, while operating conditions and processes may limit pollution, appropriate site selection to avoid potable groundwater resources and highly permeable overburden is still the best method for preventing it entirely.

2.2.3. Water Table Lowering

The final environmental concern of UCG is that of water table lowering. This refers to an increase in the depth of the water table in the region of the UCG cavity. This increase in depth may cause local wells to dry up and reduce water levels in lakes and streams. The greater depth of the water table also leads to a reduction in hydrostatic pressure at a given depth. This may exacerbate groundwater pollution issues unless operating pressures are also reduced to maintain sub-hydrostatic operation. This effect is greatly complicated by the presence of other nearby UCG cavities, as the reduction in pressure caused by one operation can cause unforeseen circumstances at another. Related extraction technologies such as coal bed methane may also contribute to this issue (Moran *et al*, 2012). Finally, the downward motion of groundwater caused by water table lowering can produce a suction force on the rock above, potentially contributing to surface subsidence (Vorobiev *et al*, 2008).

As mentioned in the previous section, water table lowering is caused by the sub-hydrostatic operation of UCG cavities. As such, the easiest way to combat this issue is to remove the need for such operation. Locating the cavity far from any groundwater resources is the most effective way of doing this. In many cases however, this is not practical. An alternative method would be to site the UCG operation near a saline aquifer, or a potable aquifer which is not currently being accessed by any other users. Unlike subsidence and pollution, the effects of water table lowering are reversed soon after gasification ceases (Lindblom & Smith, 1993). As such, provided that these issues do not occur, the long lasting effects of water table lowering are minimal. In cases where this is not possible, control of lowering can be difficult.

The rate of water table lowering is effectively a balance between the rate at which water is drawn into the cavity (drawdown rate) and the rate at which it is replenished by natural flows (recharge rate). As recharge rate cannot realistically be controlled, the only method to reduce water table lowering is to control the drawdown rate. Drawdown rate is primarily controlled through the operating pressure of the cavity.

The considerations of operating pressure on water table lowering are the same as those for groundwater contamination, however there is the added complication that both effects must be managed simultaneously. This effectively limits the range of pressures at which UCG can safely occur, as excessively high pressures will lead to contamination while excessively low pressures will lead to lowering of the water table. The actual value of the pressures allowed would depend on the current height of the water table above the cavity. This, coupled with the difficulty in measuring water table heights and composition in real time, would make the selection of operating pressure a highly complex matter. In addition, any increase in fracturing caused by UCG would further complicate this matter by increasing the permeability of the overburden. As such, site selection is seen to be the best way to combat drawdown effects, with pressure control providing a potential, if difficult, second option.

2.2.4. Preventing Environmental Damage

As seen above, the best way to prevent environmental damage in UCG is through appropriate selection of the operating site and cavity pressure. Any UCG site should meet the following criteria in order to prevent this damage:

- Cavity depth must be sufficient to reduce the effect of stoping and strata bending to prevent subsidence. Recent publications suggest a minimum depth of at least 300m (Mallett, 2006; Sarhosis *et al*, 2016). Other authors suggest ranges of 150-500m (Couch, 2009) or 600-1200m (Bhutto *et al*, 2013).
- Cavity overburden must be sufficiently strong to arrest subsidence, preventing surface deformations of more than 20mm (Mine Subsidence Engineering Consultants, 2007). Strata must be strong enough to provide at least 150m of undisturbed rock above the fractured zone (Mallett, 2006).
- Wherever possible, UCG operations should be located far from potable aquifers to prevent contamination. In cases where aquifers overlay the coal seam, the two strata should be separated by an aquitard layer. The minimum vertical separation between the strata has been suggested as 40-60m (Younger, 2011) or over 100m (Bhutto *et al*, 2013)
- Cavity operating pressures should be set at a value lower than the local hydrostatic pressure at the highest point in the fractured zone above the cavity (Lavis, 2013), but high enough to prevent excessive groundwater inflow.

As seen, the issues of local environmental damage are both complex and highly coupled. As such, modelling and experimental work is required to improve our understanding of these effects and ensure future operations do not cause damage. Despite these issues however, the majority of previous UCG trials have been shown to give little or no long term environmental damage, as shown in the following section.

2.3. UNDERGROUND COAL GASIFICATION FIELD TRIALS

The idea of UCG was first proposed in 1868 (Siemens, 1868), however the first trial did not take place until 1912. This trial was abandoned however, due to the outbreak of World War 1 (Klimenko, 2009). No further developments in UCG occurred until the Soviet Union began their own program in the 1930s. Eight trials were performed in the USSR between 1933 and 1961, culminating in the development of the Yerostigaz plant in Uzbekistan which is still operational today (Yerostigaz, 2014).

Much of the theory and technology of modern UCG was developed in the USA during the 1970s and 1980s at the Lawrence Livermore National Laboratory (LLNL) (Friedmann *et al*, 2006). LLNL continues to perform research into UCG in the modern day (Wampler, 2012). In the late 2000s a number of UCG trials were proposed in Europe, Australia, Canada and South Africa (Bhutto *et al*, 2013; Swan Hills Synfuels, 2012; Underground Coal Gasification Association, 2011). In recent years however, commercial secrecy, environmental issues, political uncertainty and a low oil price have reduced interest in UCG. These issues led to the cancellation of the Mecsek Hills trial (Dodson, 2014), the dissolution of the UCG association (Fergusson, 2015) and the liquidation of Linc Energy (Linc Energy, 2016).

Table 2.4 lists known UCG trials. Other trials exist, particularly in China, but little published information is available for these. Trials are currently planned in the UK (Green, 2015), South Africa (Brand, 2014) and China (ENN, 2014). Many of these trials have recently been cancelled however, due to the political, environmental and financial concerns mentioned above.

Table 2.4 – UCG Field trials to date.

Coal Ranks: L = Lignite, SB = Sub-Bituminous, B = Bituminous, A = Anthracite.

Cavity Designs: SB = Single Borehole, SD = Steeply Dipping, LVW = Linked Vertical Wells, CRIP = Controlled Retracting Injection Point.

Trial	Year	Country	Coal Rank	Coal Seam Depth (m)	Coal Seam Thickness (m)	Cavity Design	Injectant Gas	Syngas Calorific Value (MJ/m³)
Hett Hill	1912	UK	-	~ 40m	0.60	SB	Air	Cancelled
Shakhta	1933	USSR	A	-	0.38	-	Air	0.1 – 0.5
Leninskt	1933	USSR	B	30	4.85	-	Air	0.2 – 0.6
Lisichansk A	1934	USSR	B	24	0.75	SD	Air	3 - 4
Gorlovka	1935	USSR	-	40	1.9	SD	Air/O ₂	6 – 10
Podmoskova	1940	USSR	L	40 - 60	2 – 4	LVW	Air/O ₂	3.4 – 6
Lisichansk B	1943	USSR	B	400	0.4	LVW	Air	3.2 – 3.8
Bois-La-Dame	1948	Belgium	A	-	1	-	Air	-
Newman-Spinney	1949	UK	SB	75	1	SB	Air	2.6
Yuzhno-Abinsk	1955	USSR	B	138	2	SD	Air	9 – 12
Angren	1965	Uzbekistan	L	110 - 250	4 – 24	LVW	Air	3.6
Hanna 1	1973	USA	B	120	9.1	LVW	Air	4.2
Hanna 2	1975	USA	B	85	9.1	LVW	Air	5.3
Hoe Creek 1	1976	USA	B	40	8	LVW	Air	3.6
Hanna 3	1977	USA	B	85	9	LVW	Air	4.1
Hoe Creek 2A	1977	USA	B	40	8	LVW	Air	3.4
Hoe Creek 2B	1977	USA	B	40	8	LVW	O ₂ /H ₂ O	9.0
Hanna 4	1977	USA	B	100	9.1	LVW	Air	4.1
Hoe Creek 3A	1979	USA	B	40	8	LVW	Air	3.9
Hoe Creek 3B	1979	USA	B	40	8	LVW	O ₂ /H ₂ O	6.9
Pricetown	1979	USA	B	270	2	LVW	Air	6.1
Rawlins 1A	1979	USA	SB	105	18	SD	Air	5.6

Trial	Year	Country	Coal Rank	Coal Seam Depth (m)	Coal Seam Thickness (m)	Cavity Design	Injectant Gas	Syngas Calorific Value (MJ/m³)
Rawlins 1B	1979	USA	SB	105	18	SD	O ₂ /H ₂ O	8.1
Brauy-en-Artois	1981	France	A	1200	-	-	-	-
Centralia A	1984	USA	SB	75	6	CRIP	O ₂ /H ₂ O	9.7
Centralia B	1984	USA	SB	75	6	LVW	O ₂ /H ₂ O	8.4
Haute-Duele	1985	France	A	880	2	-	-	-
Thulin	1986	Belgium	A	860	6	LVW	Air	7.0
Rocky Mountain 1A	1987	USA	SB	110	7	CRIP	O ₂ /H ₂ O	9.5
Rocky Mountain 1B	1987	USA	SB	110	7	LVW	O ₂ /H ₂ O	8.8
Huntly	1994	New Zealand	-	350	-	-	-	-
El Tremedal	1997	Spain	SB	580	2	CRIP	O ₂ /H ₂ O	10.9
Chinchilla	2000	Australia	SB	140	10	LVW	Air	6.6
Barbara	2007	Poland	SB	30	1.5-2	-	O ₂	3.8
Majuba	2007	South Africa	-	300	3.5	-	-	-
Bloodwood Creek	2008	Australia	-	>200	8-10	CRIP	O ₂ /H ₂ O	6 – 7.5
Kingaroy	2009	Australia	-	130 – 300	5 – 17	-	-	-
Swan Hills	2009	Canada	B	1400	8	CRIP	O ₂ /H ₂ O	-
Mecsek Hills	2012	Hungary	-	-	-	-	-	Cancelled
Wieczorek	2014	Poland	B	430	5.5	-	Air/H ₂ O	3.5
Pingdingshan	2014	China	-	95	8	-	-	-

After Burton et al, 2006; Perkins, 2005; Underground Coal Gasification Association, 2011; Bhutto et al, 2013; Swan Hills Synfuels, 2012; Klimenko, 2009; Kapusta & Stanczyk, 2014; Mocek et al, 2016; Dodson, 2014.

Table 2.4 lists 41 known UCG field trials. Despite the lack of published data, it is also known that at least 15 field trials have also been performed in China (Yang *et al*, 2014). A number of other trials are known to exist which have not been included in the table due to a lack of available information, including several trials in the former USSR (Fergusson, 2011). As such, it is estimated that at least 60 UCG trials have taken place to date. It is of note that of all the trials mentioned above, only five (Brauy-en-Artois, Haute-Duele, Thulin, El Tremedal and Swan Hills) operated on coal seams which met the criteria for safe operation set out in Section 2.1.5. As such, it is suggested that a greater number of experimental trials which do meet these criteria are required before commercial scale UCG can become a reality. Additional field trials meeting these criteria were planned in Hungary (du Plooy *et al*, 2012) and Poland (Wildhorse Energy, 2013) however both of these trials have since been cancelled. Given the political, financial and environmental risks of UCG experiments, it is seen that these necessary field trials may be difficult to implement.

Finally it is of note that many of the trials above did not produce any environmental damage, and rarely was more than one issue seen at the same site. Only the Hoe Creek 3 trial showed any significant surface subsidence (Ganow, 1984) while water table lowering was not seen to notable extents at any of the above trials. On the other hand, groundwater pollution was observed at many of the Hoe Creek trials (Campbell *et al*, 1978) and the El Tremedal (Torres *et al*, 2014), Barbara (Kapusta *et al*, 2013), Chinchilla (Australian Broadcasting Corporation, 2016) and Kingaroy trials (Heger, 2010) as well as many of the early trials in the USSR (Klimentov, 1963).

It is of note that all of the trials which did see environmental damage, with the exception of El Tremedal, were sited in coal seams which would now be considered unsuitable for UCG. Much of the damage at the El Tremedal trial is believed to have been caused by an explosion within the coal seam after the gasifier pilot light went out (Creedy *et al*, 2001). Such an issue is avoidable using modern measuring and control techniques. Given these issues it is believed that while UCG could potentially be a clean source of energy, a much greater understanding of the mechanisms behind its associated environmental issues is required before this can be a reality. Given the risks inherent in the experimental study of UCG, numerical modelling may provide the safest means to obtain this understanding. As shown in the following section, modelling can be used to predict the processes of subsidence, groundwater contamination and water table lowering over a range of sites without the risk of causing environmental damage. As such, a great deal of numerical modelling of these issues is recommended for UCG.

2.4. UNDERGROUND COAL GASIFICATION MODELLING

As explained above, experimental studies of UCG are often difficult to justify given their cost and associated environmental, political and legal issues. In addition, the underground nature and extremes of temperature and pressure involved in UCG make it difficult to obtain physical observations of the process. Field trials can be useful for studying the chemistry of UCG, but generally cannot be used to study environmental effects without causing environmental damage. Because of these issues, much of the current work on UCG tends to focus on numerical modelling. Models have been produced to explain many aspects of UCG, including gasification kinetics, cavity growth mechanisms, groundwater effects and local rock mass deformation. This section summarises the models produced to date and the modelling techniques which can potentially be applied to UCG.

2.4.1. Modelled Phenomena

To effectively simulate the full nature of UCG would require a time dependent, three dimensional code capable of modelling a number of highly coupled thermal, hydraulic, chemical and mechanical processes (Nitao *et al*, 2011; Perkins, 2005). These processes include:

- Chemistry of pyrolysis, combustion and gasification reactions
- Kinetics of gas phase reactions within the cavity void
- Kinetics of gas/solid reactions at the cavity walls and in the rubble zone
- Two phase flow of syngas and groundwater both inside and outside the cavity
- Convective and radiative heat transfer within the cavity
- Cavity growth due to reaction, spallation and roof/sidewall collapse
- Calculation of ash, rubble and void volumes within the cavity
- Rock fracturing and subsidence caused by UCG
- Flow of groundwater around and into the UCG cavity
- Transport of UCG generated contaminants within local groundwater resources
- Long term effects of UCG on groundwater quality and quantity

The model would need to be accurate enough to provide useful results and stable enough to cope with changes to input parameters such as coal composition or oxidant flow rate. Computational efficiency is also a key factor to consider if the model is to be run on a low powered platform or is required to deliver results quickly. Models should be able to cope with arbitrary cavity shapes and geological factors such as faults and stratification. Validation of any model is very important as a model which gives anomalous results is useless, regardless of its complexity. As such, simulation results should be compared directly with field trial data and previous models to ensure the validity of the simulator and to avoid expensive or dangerous mistakes from basing field work on invalid computational results.

Such a model as described above would be highly complex and require a great deal of both computational resources and programming time. In many cases, where only a certain piece of information is required (such as syngas composition), many of these factors can be ignored or assumed and a simpler 1D or 2D model can be used instead. Because of computational constraints, the vast majority of models produced to date tend to be in this category.

2.4.2. Previous Models

Mathematical modelling of UCG has been performed since the late 1970s and has continued to grow in complexity and scope until the present day. Table 2.5 presents an overview of modelling efforts to date, with a focus on generic (non-site-specific) models. Because of the complexity involved, early efforts tended either to only model a certain aspect of the process (single physics models) or to greatly simplify their models with a large degree of assumption (multi physics models) (Reid *et al*, 2012a). While multi-physics models allow a user to simulate a wide range of processes, the computational time involved can be significant. Single-physics models can be faster and more accurate though they must be supplied with data or estimates of properties outside the scope of their own modelling. Single physics models can also be used to provide estimates for inputs to more complex models. Many existing UCG models are single-physics models focusing on cavity growth, product composition or single environmental effects. Many models also tend to be specific to a certain trial site.

Table 2.5 – Notable models of UCG produced to date.

Author	Focus	Geometry	Steady State	Aspects Modelled	Notes
Thorsness <i>et al</i> (1977)	Cavity growth	2D	Yes	Gas flow, chemistry	Qualitative Runtime on order of minutes
Langland and Trent (1981)	Subsidence	2D	No	Heat transfer, rock fracturing and subsidence	Underpredicts Subsidence Validated against HC3 Trial
Britten and Thorsness (1988)	Cavity growth Production rate	2D	Yes	Gas & groundwater flow, heat transfer, chemistry and kinetics	Highly idealised
Shirsat (1989)	Cavity growth Product composition	2D	No	Chemistry and kinetics, heat transfer, gas flow	Assumes cavity geometry Pseudo steady-state
Biezen <i>et al</i> (1996)	Cavity growth	3D	Yes	Chemistry, fluid flow	Assumes isothermal cavity Highly idealised
Yang (2005)	Heat transfer	2D	No	Heat transfer, gas flow, groundwater flow	Mostly theoretical Gives cavity temperature field
Perkins and Sahajwalla (2008)	Product composition	1D	No	Chemistry, kinetics, heat transport	Assumes cavity geometry No water influx
Vorobiev <i>et al</i> (2008)	Subsidence	2D	No	Rock fracturing and subsidence	Assumes cavity geometry No water influx
Yang and Zhang (2009)	Contamination	2D	Yes	Groundwater flow, contaminant transport, heat transport	Overpredicts extent of contamination

Author	Focus	Geometry	Steady State	Aspects Modelled	Notes
Morris <i>et al</i> (2009)	Cavity growth Subsidence	3D	Yes	Rock fracturing and subsidence, groundwater flow	Parallel code Mechanical/hydraulic coupling
Seifi <i>et al</i> (2011)	Product Composition	3D	Yes	Chemistry and kinetics, heat transport, groundwater inflow	Long runtime Part of a larger proposed model
Sarraf <i>et al</i> (2011)	Cavity growth	2D	Yes	Chemistry and kinetics, heat transfer, gas flow	Results agree well with experiment
Nitao <i>et al</i> (2011)	Multiple aspects	3D	Yes	Attempts to cover all of the issues mentioned in Section 2.4.1	Under development No updates since 2012
Daggupati <i>et al</i> (2012)	Product Composition	3D	No	Chemistry and kinetics, heat transfer, gas flow	Fast runtime Highly Idealised
Akbarzadeh and Chalaturnyk (2013)	Subsidence, Contamination	3D	No	Rock fracturing and subsidence, heat transfer, groundwater flow	Axisymmetric Investigates cavity pressure effects
Sarhosis <i>et al</i> (2013)	Heat transfer	3D	Yes	Groundwater flow, heat transport	Focuses on post gasification behaviour and decommissioning
Yang <i>et al</i> (2014)	Subsidence	3D	Yes	Rock fracturing and subsidence, heat transfer	Focuses on thermal behaviour Assumes constant cavity shape
Andrianopoulous <i>et al</i> (2015)	Product Composition	1D	No	Chemistry and kinetics, gas and groundwater flow, heat transport	Highly idealised Compares cavity design effects
Samdani <i>et al</i> (2016 a & b)	Cavity growth	2D	Yes	Heat transfer, chemistry and kinetics, gas flow	Assumes cavity geometry Highly idealised

2.4.3. Modelling Methodologies

Many techniques exist for modelling large scale problems such as UCG, several of which have been used in the models above. This section gives a brief overview of the most common methods and illustrates how they might be used in a UCG simulation.

2.4.3.1. Finite Difference Methods

The finite difference method (FDM) is a simple tool for solving complex problems, and forms the basis of many other methods. FDM uses Taylor series approximations to represent differential equations as finite difference equations, as in Equation 2.2:

$$y_{t+\Delta t} \cong y_t + \Delta t \frac{\delta y}{\delta t} \quad (2.2)$$

Where y can represent any continuous variable.

FDM discretises time into discrete elements of length Δt and iterates across each until the final time of the simulation is reached. FDM is relatively fast, though solution speeds depend upon the length of the timestep. Increasing Δt increases speed, but reduces accuracy and can cause instability. FDM can be applied to almost any problem which can be expressed using differential calculus, including chemical, mechanical, thermal and hydraulic systems. This led it to its use in many early UCG models, including those of Thorsness *et al.*, (1977), Langland and Trent (1981), Britten and Thorsness, (1988) and Akbarzadeh and Chalaturnyk (2013).

2.4.3.2. Finite Element Methods

The finite element method (FEM) is a powerful tool for modelling continuous systems with complex geometries. FEM discretises the problem into many small elements (the mesh) and then finds approximate solutions to characteristic equations in each element. The overall solution is found from the summation of the elemental solutions. FEM is numerically stable and allows for the simulation of geometries with moving boundaries, such as a growing UCG cavity. FEM can capture both local and global effects and can operate with variable mesh resolutions to improve accuracy in regions of interest without increasing runtime. FEM is the method of choice for structural mechanics and cavity growth models, though it is computationally expensive. FEM models are incapable of modelling brittle failure however, as continuum formulations preclude the separation of elements (Hammah *et al*, 2008). Previous UCG models based on FEM include those of Biezen *et al*, (1996), Vorobiev *et al*, (2008), Morris *et al* (2009), Yang and Zhang (2009), Sarraf *et al* (2011) and Yang *et al* (2014).

2.4.3.3. Computational Fluid Dynamics

Computational fluid dynamics (CFD) is a branch of FEM focused on the modelling of fluids. CFD solves the Navier Stokes equations over a finite element mesh. Modern CFD can approximate turbulent flows and additional effects including heat transfer and chemical reaction. CFD can be faster than FEM, though it is prone to numerical instabilities. CFD has recently been used in UCG simulations of both syngas and groundwater flows (Nitao *et al*, 2011; Sarhosis *et al*, 2013; Seifi *et al*, 2011).

2.4.3.4. Discrete Element Methods

Discrete element methods (DEM) model physical systems by simulating the position, velocity and forces acting on several small particles over successive time-steps. Unlike in FEM, the elements in DEM represent physical bodies and can move relative to each other. DEM is classified into particle or block based methods. Particle based methods treat elements as single bodies separated by space (or a fluid). Block based methods treat the entire domain as a single body which is then broken into smaller pieces by fractures. Particle based DEM is used to simulate sparse systems such as hopper flow (Cleary & Sawley, 2002; Li *et al*, 2004a), solids mixing (Bertrand *et al*, 2005; Xu *et al*, 2010), particle milling (Lee *et al*, 2010; Li *et al*, 2014; Sato *et al*, 2010) and heat transfer within granular materials (Chaudhuri *et al*, 2010; Tsory *et al*, 2013). Block based DEM is used to simulate cohesive systems such as rock masses (Barton *et al*, 1994; Bhasin and Hoeg, 1998; Boon *et al*, 2014; Coulthard, 1999; Keilich *et al*, 2006; Solak, 2009; Vardakos *et al*, 2007; Vyazmensky *et al*, 2007).

DEM can model a wide range of forces and particle sizes and shapes, though anything other than simple polyhedra can greatly increase runtimes. Modern DEM can also model thermal effects and fluid-mechanical coupling as well as the behaviour of fractures between elements. The generation of new fractures is problematic however, due to the need to conserve element volume. Fracturing in many DEM codes is therefore limited to the breakup of material along predefined planes of weakness (Lisjak and Grasselli, 2014). The main disadvantage of DEM is its high runtime, which is heavily dependent on the number of elements used. Large scale problems are often more easily modelled using continuous methods such as FEM.

The combination of particle motion (e.g. cavity collapse) and large scale deformation (e.g. strata bending) lead many geomechanical simulations to require a combination of continuum and discrete methods to accurately capture rock mass behaviour (Morris *et al*, 2006). Block based DEM codes achieve this by further discretising each discrete element with its own finite element mesh, allowing individual elements to deform and providing a means for adaptive mesh sizing in DEM. This is referred to as the combined finite-discrete element method (Munjiza & John, 2002). Vorobiev *et al* (2008) state that “Discrete methods are needed to capture the main features of cavity collapse. A combination of continuum (numerical or analytical) and discrete approaches is probably the best strategy in predicting surface subsidence due to UCG” Such methods are used by Vorobiev *et al* (2008), Morris *et al* (2009), Nitao *et al* (2011) and others.

2.4.3.5. Compartment Modelling

Compartment modelling is a method of abstracting complex problems as interlinked networks of simple processes. A common example is the approximation of any real chemical reactor as a series of perfectly stirred tanks. Complex chemical reaction and mass transfer problems can relatively easily be set up as compartment models using process simulation software such as Aspen Hysys (aspentech, 2016) and solved iteratively. Compartment models have been used in several UCG models to predict product gas flow rates and compositions (Andrianopoulous *et al*, 2015; Daggupati *et al*, 2012; Samdani *et al*, 2016a,b; Shirsat, 1989).

The main advantage of compartment models is their speed; however they can be less accurate than other models. Daggupati *et al* (2012) state that their model is over 6,000 times faster than CFD and produces results accurate to within 10% of those given by CFD. Figure 2.9 illustrates the comparison of a UCG cavity with Daggupati's model.

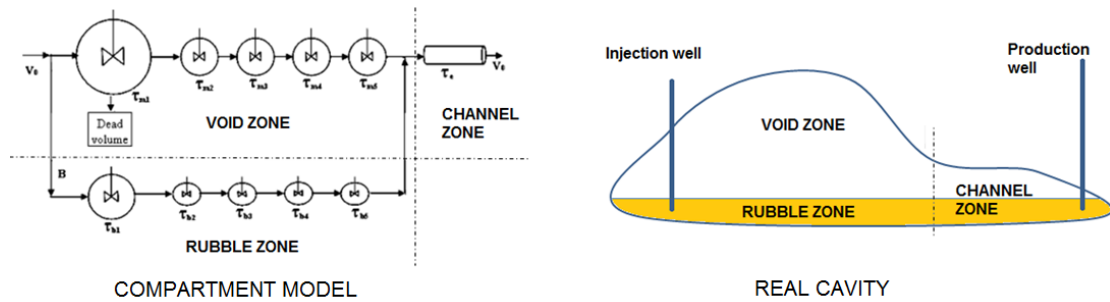


Figure 2.9 – Comparison of UCG compartment model with schematic of a typical UCG cavity. After Daggupati *et al*, 2012.

2.4.3.6. Stochastic Methods

Many processes in UCG contain random elements. The orientation of fractures in rock, chemical diffusion and thermomechanical spalling all contain randomness. Stochastic methods allow the incorporation of these elements using a random number generator. This allows for accurate simulation of these processes without the need to assume data, and simplifies model validation by allowing the user to see how these processes affect results. The use of the Monte-Carlo method allows the modelling of random processes a large number of times to give varying outputs. This requires much less computing power than simply modelling every possible outcome sequentially. Stochastic methods have been used with UCG to simulate spalling (Biezen, 1996) and have been used in related fields to generate fractured rock masses for geomechanical and hydrogeological simulations (Min *et al*, 2004; Vyazmensky *et al*, 2007).

2.4.3.7. Empirical Modelling

While many models have attempted to simulate their respective processes from first principles, some issues are either not well enough understood or require too much computing power to do so. In these cases, empirical models based on experimental results may be used. Common empirical methods include the many correlations used to model heat and mass transport processes. Empirical methods are simple, fast and often accurate, however they do not give any realistic physical explanation of the processes they simulate. As such, they are of limited use in research.

2.4.3.8. Combined Methods

While many of the methods above can simulate single aspects of UCG, few are capable of realistically simulating the entire process. While full simulation of UCG may be possible using combined DEM/FEM/CFD methods, the computational requirements of such a model would be incredibly high due to the varied length and timescales involved. Rather than attempting this, conventional models attempt to integrate the various aspects of UCG using submodels. The submodel concept involves the use of several smaller codes, each of which simulates a single aspect of UCG. These are linked together by a control model which passes data between submodels and calls them at appropriate time intervals. Combined models allow for the simulation of highly coupled processes by greatly simplifying each individual process. The use of submodel architecture can therefore greatly reduce CPU runtime by whilst retaining model accuracy.

2.4.4. Future Modelling Developments

As shown in Table 2.5, past models have produced a many useful results and helped improve the understanding of UCG. Much work still remains to be done in order to fully understand the processes involved however, especially those associated with local environmental damage. In addition, most of the models produced consider only a single UCG cavity. If commercial scale L-CRIP UCG is to become a reality, an understanding of the interaction of multiple cavities is required. Finally, few models focus on the long term effects of UCG. As mentioned in Section 2.2.2, groundwater pollution can occur months after gasification has ceased. As such, it is important that models cover the full lifetime of UCG, from drilling to decommissioning, which may take several years depending on the scale of the operation.

Some recent efforts aim to combine the modelling of various aspects of UCG into single integrated simulators which can predict the overall behaviour of UCG with little external input. The work of Nitao *et al*, (2011) attempts this, though no progress on this model has been reported since 2012 (Reid *et al*, 2012b). While integrated simulations would provide valuable tools for the development of UCG, there is still scope for the use of single physics models related to key areas of the technology. As mentioned above, the understanding of UCG induced environmental effects is still incomplete. Given the importance of these issues to the future commercial development of UCG, modelling efforts should focus on accurately predicting as many of these effects as possible. The work presented in this thesis therefore aims to produce a simple but accurate model of the key local environmental issues of UCG, including surface subsidence, groundwater contamination and water table lowering.

2.5. INITIAL MODELLING DECISIONS

The aim of this project is to produce a model which can predict the local environmental damage caused by UCG. As mentioned in Section 1.3.7.2, this involves the simulation of surface subsidence, groundwater pollution and water table lowering. The model is to be general, rather than site-specific, and aims to produce results in under 24 hours when executed on a standalone desktop PC. The proposed end use of the model is as a “first pass” screening tool used to compare the environmental impacts of a number of proposed UCG sites in order to quickly rule out those which are unsuitable. This section outlines the initial decisions made in the creation of this model.

2.5.1. Modelling Assumptions

In order to meet the aims of the project, a number of assumptions were used. The majority of these assumptions are required in order to keep the runtime of the model within reasonable limits, while others are needed to make up for a lack of data or physical understanding of the processes involved. The model therefore assumes:

- That a 3D cavity can be realistically simulated by a 2D, plane strain geometry.
- That the cavity forms instantaneously.
- That groundwater behaviour is constant over the time simulated (steady state).
- That induced rock fractures extend only a limited distance into the overburden.
- That cavity rubble, ash and rock provide no support to the cavity roof.

The assumption of 2D geometry is believed to be justified due to shape of an L-CRIP UCG cavity. As such cavities are often an order magnitude longer than they are wide or tall, end effects can safely be ignored and a 2D geometry used. The assumptions of instantaneous cavity formation and steady state groundwater flow effectively remove the dimension of time from the model, greatly reducing the amount of computational effort required. Although they limit the accuracy of the model, these assumptions would both lead to overprediction of environmental damage. As the aim of the model is to predict the negative consequences of UCG, this overprediction is deemed acceptable as it effectively acts as a safety factor in the model. The assumption of limited fracturing is used as a means of mesh refinement, providing a fine mesh near the cavity and a coarse mesh further away. This allows for reasonable accuracy whilst retaining a short runtime.

The assumption that ash and rubble provide no support to the roof is required, as modelling the formation of the ash and rubble zones would be too computationally expensive. This is also a necessary outcome of assuming steady state behaviour as ash formation is a time dependent process. Initial results suggest this assumption is valid however, as surface subsidence is seen to cease long before cavity collapse does. Though the assumptions reduces accuracy, results show good agreement between model results and field trial data, suggesting the assumptions are valid.

In many cases, the reductions in accuracy caused by these assumptions are smaller than those caused by uncertainty in material properties. As such, it is believed that the assumptions are valid. The use of stochastic modelling further alleviates this issue by introducing similar uncertainties in the model. This causes the model to give results with a similar degree of uncertainty to that seen in reality. This technique increases runtime however, as multiple executions are required to obtain the mean result.

Finally, one of the greatest challenges to model accuracy is the lack of available field data for use in validation. Commercial secrecy and the difficulty of measuring certain aspects of UCG severely reduces the volume of data available. This lack of data seriously affects both the accuracy and applicability of the model. Accuracy is affected as the potential for validation is greatly limited. Applicability is affected as validation can only cover a small number of experiments with similar geometry and geology, limiting the range over which model results can be safely extrapolated.

2.5.2. Software and Hardware Considerations

A number of potential methods were considered for the creation of the UCG model.

When comparing options, the following criteria were considered:

- Can the method used capture both discrete and continuous subsidence effects?
- Can it model large scale UCG in an accurate, fast and reliable manner?
- Can it represent coupled thermal, hydraulic, chemical and mechanical effects?
- How much does the required software cost?
- How easy is the method to learn and use?

A number of commercial software packages were considered, as was the option of creating a new in-house code. Table 2.6 compares the methods considered. Three dimensional codes were considered as initial plans involved the creation of a 3D model to better represent multiple cavity UCG.

Based on the information presented in Table 2.6, it was decided that the project would use a combination of the UDEC v4.01 (DEM) and MODFLOW/MT3DMS (FDM) codes. UDEC would be used to model the coupled mechanical, thermal and hydraulic behaviour of the rock mass and groundwater. The results from this model would then be passed to MODFLOW/MT3DMS to produce a more accurate hydraulic model incorporating the chemical effects of UCG. This second stage model was not completed however, due to time constraints. Appendix C shows initial considerations for how such a model could be produced, and it is envisioned that the production of such a model could be completed within approximately 6 months of work. Early modelling efforts also considered using ANSYS to extend the model into three dimensions but this was found to be incapable of accurately resolving the mechanical response of the overburden, as predicted by Morris *et al* (2009).

All of the modelling presented in this work was performed on a standalone 64 bit desktop PC containing a 3.6GHz Intel quad core processor and 16GB of random access memory. The processor has been hyper-threaded to produce 8 virtual cores, allowing up to 8 parallel executions of UDEC v4.01 to be executed simultaneously.

Table 2.6 – Comparison of software packages for use in the UCG model. Packages chosen for use are highlighted in bold.

Software	Method	Dimensions	Cost	Ease of Use	Capabilities			
					Thermal	Hydraulic	Chemical	Mechanical
3DEC	DEM	3D	£18,750 ¹	Difficult	Poor	Poor	None	Good
Abaqus	FEM & CFD	3D	Already Owned	Simple	Good	Good	None	Poor
Ansys	FEM & CFD	3D	£500 p.a. ²	Moderate	Good	Good	None	Poor
COMSOL Multiphysics	FEM & CFD	3D	£6,500 ³	Simple	Good	Good	Poor	Poor
FLAC	FDM	2D	£6,675 ¹	Moderate	Poor	Poor	None	Poor
FLAC3D	FDM	3D	£13,350 ¹	Moderate	Poor	Poor	None	Poor
MODFLOW & MT3DMS	FDM	3D	Free	Simple	Good	Good	Good	None
PFC	DEM	3D	Already Owned	Moderate	None	Poor	None	Poor
UDEC	DEM & FDM	2D	Already Owned	Moderate	Poor	Poor	None	Good
In-House	Various	2D	Free	Very Difficult	Unknown	Unknown	Unknown	Unknown

¹ Walker, 2013. ² Morvan, 2013. ³ COMSOL, 2013.

2.6. CONCLUDING REMARKS

This review has introduced the technology of UCG as a means to produce cheap, clean and safe chemical products and electricity. Extensive experimental and theoretical work has been carried out in the field over the past century, particularly in the last forty years. UCG technology has now developed to the point where commercialisation may be a reality within the next decade, however there are still several issues which must be addressed before this can happen. Predominant among these issues are the negative environmental impacts of surface subsidence, groundwater pollution and water table lowering. Much work is currently underway to understand these issues, however the legal and political ramifications of environmental damage limit the use of experiments in this area. Modelling of UCG is therefore the principal method by which this understanding must be gained.

While current efforts are beginning to prove useful in understanding UCG behaviour there are still many areas which require more attention. Predictive modelling of environmental impacts should continue to progress to the point where operators can say with certainty that their facility will not cause any of these issues. Models should be extended to cover commercial scale UCG facilities rather than just demonstration plants and consideration should be given to the movement of rocks, water and contaminant species in the time long after UCG reactions have ceased.

The following chapters describe how the UCG model was produced. It is hoped that this model will prove useful in furthering the understanding of UCG generated environmental damage, allowing for commercial development of the technology.

3. UNIVERSAL DISTINCT ELEMENT CODE METHODOLOGY

SUMMARY

This chapter presents an overview of the theory, numerical formulation and model set-up of a typical geomechanical model built using the universal distinct element code (UDEC). The discretisation and calculation cycles for the mechanical, hydraulic and thermal aspects of the model are presented in detail. The results of initial software validation tests are presented, showing that UDEC is capable of accurately predicting the principal physical processes occurring in UCG. Discussions on the advantages, disadvantages, and challenges of UDEC are given and comparisons are made with competing methodologies such as the particle based discrete element method and the finite element method. The limitations of the software are identified and methods for overcoming these limitations are discussed. UDEC is shown to be a powerful tool for use in the creation of the UCG model and recommendations are made for how best to apply the software to this problem.

3.1 THE UNIVERSAL DISTINCT ELEMENT CODE

The discrete/distinct element method (DEM) refers to a number of techniques for simulating the mechanical behaviour of systems comprised of large numbers of interacting particles. A number of software packages based on this method are compared in Section 2.5.2. The Universal Distinct Element Code (UDEC) is a commercially available, two dimensional DEM package which was developed specifically to model the behaviour of highly jointed rock masses (Itasca Consulting Group, 2004). UDEC models are comprised of many arbitrarily shaped elements separated by discontinuities (Cundall, 1980).

Given a full understanding of Newton's laws of motion and the interaction forces between the particles (e.g. gravity, friction, electrostatics etc.), UDEC can predict the motion of complex systems involving thousands of particles. By considering the position, velocity and forces of every particle in the system at time t , UDEC uses an explicit finite difference algorithm to find these values again at time $t + \Delta t$. Collisions between particles use linear springs to calculate reaction forces based on the interpenetration of the bodies involved. Individual particles used in a UDEC analysis can be either rigid or deformable and subject to combinations of static and dynamic external loads. A wide range of constitutive relationships can be simulated, including isotropic elastic, Mohr-Coulomb and strain softening/hardening behaviours. The value of the time increment Δt is kept small in order to minimise the influence of particle interpenetration on results and to ensure the stability of the simulation.

In addition to its mechanical capabilities, UDEC can simulate a range of hydraulic and thermal phenomena. Linking between these phenomena allows for the simulation of fully coupled thermal, hydraulic and mechanical systems within rock masses. Finally, new functionality can be developed using UDEC's built-in programming language FISH. Figure 3.1 shows a typical UDEC simulation in progress.

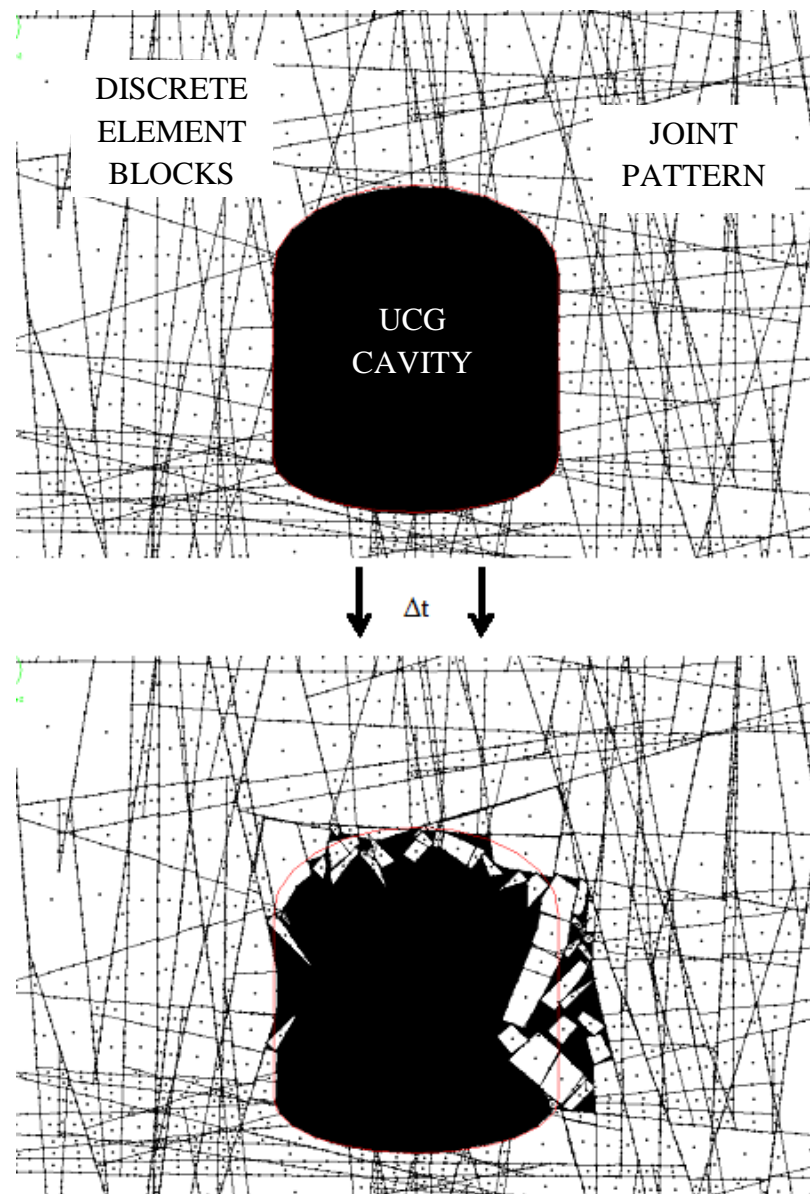


Figure 3.1 – A UDEC simulation before and during mechanical cycling showing the 2D cross section looking along the cavity. The red line shows the original cavity shape at time $t=0$.

A major disadvantage of DEM is its computational requirements. The CPU time required by a UDEC model is a product of the simulation time and the number of elements modelled. As such, the number of elements must be limited to preserve a reasonable runtime. This often precludes the ability of the method to fully resolve the behaviour of systems comprised of large numbers of particles or those in which physical effects manifest over long timescales. Scale up methodologies can be employed to represent assemblies of a large number of particles using fewer particles of larger sizes. Such methods can introduce inaccuracies into model results however, as the behaviour of particulate systems is often heavily scale dependent. Further discussions of these issues are given in Section 3.5, while Chapter 4 presents an investigation into the effects of block shape on model behaviour.

UDEC has successfully been applied to a number of issues across many scales and in several industries, including tunnelling (Boon *et al*, 2014; Solak, 2009; Vardakos *et al*, 2007), mining (Coulthard, 1999; Keilich *et al*, 2006; Vyazmensky *et al*, 2007), underground construction (Barton *et al*, 1994; Bhasin and Hoeg, 1998), carbon dioxide sequestration (Fang *et al*, 2013), hydroelectric dam construction (Bretas *et al*, 2014) and nuclear waste storage (Ahola *et al*, 1996; Blum *et al*, 2005, 2009).

3.2 MECHANICAL CALCULATIONS

3.2.1 Mechanical Model Formulation

The simplest simulations in UDEC consider only the mechanical behaviour of the rock mass. Ground deformation is predicted by altering the geometry of the rock mass (e.g. by excavating a cavity) and then allowing the system to come to mechanical equilibrium. This process can be repeated a number of times to simulate excavations occurring in multiple stages. Fully deformable mechanical simulations in UDEC consist of the following stages:

1. Select any appropriate model options (symmetry, fluid flow, thermal etc.)
2. Define the full extent of the model in 2D space
3. Define the geometry of discrete elements (blocks) and discontinuities (joints)
4. Discretise blocks into mesh elements (zones) to allow for deformation
5. Assign constitutive relationships to zones and joints
6. Assign material properties to zones, joints, fluids etc.
7. Assign boundary and initial conditions to the appropriate locations
8. Set any appropriate body forces (e.g. gravity)
9. Run the solver algorithm until an initial equilibrium state is reached
10. Perform any changes to the system (excavations, new thermal conditions etc.)
11. Rerun the solver to find the new equilibrium state
12. Repeat Steps 11 and 12 for problems involving multiple sequential stages
13. Analyse the results.

UDEC's calculation cycle for a deformable mechanical system is shown in Figure 3.2.

Technical detail on the formulation of Steps 1 through 6 is given in Appendix A.1.1.

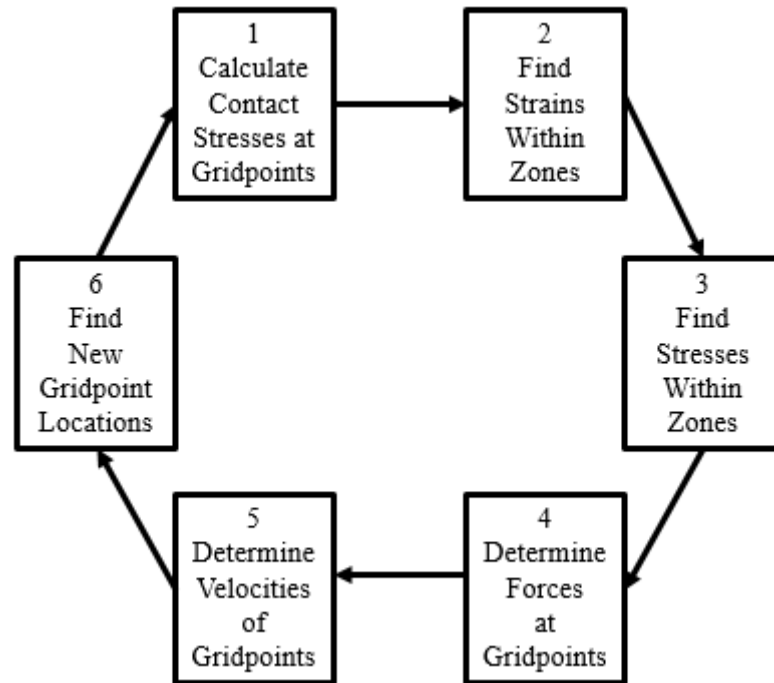


Figure 3.2 – UDEC calculation cycle for a mechanical analysis using deformable blocks. After Itasca Consulting Group, 2006

The individual elements within a UDEC model are defined below (Itasca Consulting Group, 2006). Figure 3.3 describes these definitions schematically:

- **Blocks** – Individual discrete elements which make up the model.
- **Joints** – Interfacial discontinuity elements between blocks. Joints allow for the relative motion of blocks, resisted by joint stiffnesses.
- **Zones** – Triangular finite difference mesh elements used to sub-discretise single blocks. Zones allow for the deformation of intact blocks.
- **Gridpoints** – Vertices of zones. Fundamental nodes of the geometry.
- **Contacts** – Formed when two or more gridpoints from different blocks are within a certain distance of each other. Used to transfer forces between blocks.

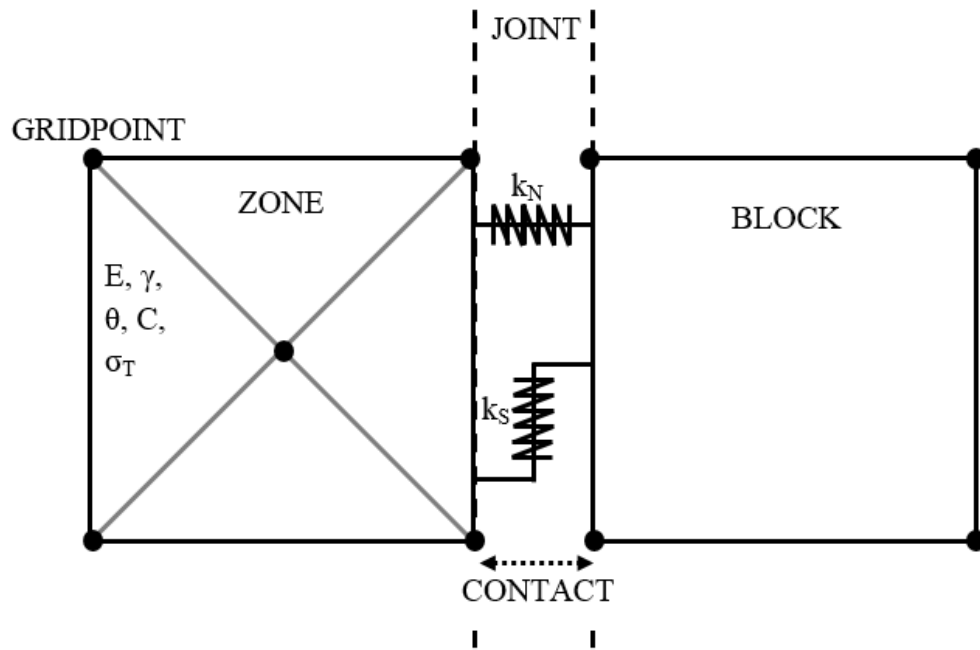


Figure 3.3 - Schematic representation of blocks, zones, joints, gridpoints and contacts used to represent rock masses in UDEC. After Itasca Consulting Group, 2006.

Where:

C	Cohesion	(Pa)
E	Young's Modulus	(Pa)
k	Stiffness	(Nm ⁻¹)
γ	Poisson's Ratio	(-)
θ	Friction Angle	(°)
σ _T	Tensile Strength	(Pa)

Subscripts:

N	Normal
S	Shear

Rather than being set by the user, the value of the timestep Δt is calculated by UDEC. This ensures the timestep is small enough to prevent excessive block interpenetration by limiting how far blocks can move within a single time step. The derivation of the timestep is given in Appendix A.1.2. Smaller timesteps lead to greater accuracy and stability, but can greatly increase the computational demands of the model. The following conditions lead to decreased values of Δt and therefore increased runtimes:

- Decreased block mass
- Increased joint stiffnesses
- Increased material stiffnesses
- Increased slenderness of zones

The above conditions apply to every block in the model, such that a single small block can cause a considerable reduction in the timestep. In order to prevent this, UDEC uses the process of mass scaling. As shown in Appendix A.1.2, timestep is proportional to the square root of density. For a static simulation in which gravity is the only external force, the actual value of density is irrelevant provided that gravitational acceleration remains the same. Using this observation, UDEC scales the density and gravitational acceleration of each block by a factor based on the average block mass throughout the entire model. This method can greatly speed up solution in non-uniform models and does not affect model results, provided that inertial forces are negligible (as they would be for a model with a stationary frame of reference). As with block size, a single overly stiff joint can also lead to a reduction in the model timestep. As joint stiffnesses are fully user defined however, this issue can be avoided by ensuring of uniformity of joint stiffnesses.

In addition to maintaining a low value of Δt , the stability of a numerical calculation can also be improved with the use of damping. UDEC uses the method of adaptive local damping to reduce the forces incident on gridpoints at every iteration of the mechanical cycle. Reduced forces lead to reduced gridpoint acceleration and velocity without the need to alter any modelled material properties. This effectively increases the number of timesteps required to generate a given amount of overlap, reducing the likelihood of overlap errors. The formulation of the damping scheme is given in Appendix A.1.3.

Zones and joints within a UDEC model can each be represented using many different constitutive models. These are summarised in Tables 3.1 and 3.2 respectively.

Table 3.1 – Zone constitutive models in UDEC. After Itasca Consulting Group, 2006.

Model	Behaviour Simulated	Example Uses
Null	Zero resistance to deformation. Zero density. Zero internal stresses.	Voids, holes, cavities.
Elastic Isotropic	Linear isotropic stress-strain relationship. No plastic failure.	Metals loaded below yield stress.
Drucker-Prager	Shear yield failure in low friction materials. No plastic flow rule.	Soft clays. Comparison with finite element programs.
Mohr-Coulomb	Shear yield failure in geological materials. No plastic flow rule.	Stress/stability calculations in soil, rock and concrete.
Strain softening Mohr-Coulomb	As Mohr-Coulomb, with strain dependent plastic behaviour.	Post failure analysis of rock. Tightly bedded rock strata.
Ubiquitous Joint	As Mohr-Coulomb, with planes of weakness at given orientations.	Geological materials with defined strength anisotropy.
Double Yield	As Mohr-Coulomb, with volumetric yield properties.	Compressible material, hydraulically placed sediment.

Table 3.2 – Joint constitutive models in UDEC. After Itasca Consulting Group, 2006.

Model	Behaviour simulated	Example Uses
Point contact Coulomb slip	Interaction between particles with small contact area.	Loosely packed granular material.
Area contact Coulomb slip	Interaction between tightly packed particles.	Joints, faults and bedding planes within rock masses.
Coulomb slip residual strength	As area contact Coulomb slip, with a distinct post-failure strength.	As area contact Coulomb slip for materials with residual strength.
Continuously yielding	Joints subject to continuous progressive damage and hysteresis.	Cyclic loading with hysteresis. Dynamic behaviour (e.g. earthquakes).
Barton-Bandis*	Highly accurate joint hydraulic behaviour.	Simulation of purely hydraulic phenomena.

*The Barton Bandis model is an optional extra not included in UDEC by default and not currently licensed by the University of Nottingham.

3.2.2 Mechanical Validation

This section outlines simple tests performed to verify the use of UDEC in simulating mechanical phenomena. A number of tests have been performed and their results have been compared with analytical solutions. Similar tests for hydraulic and thermal phenomena are presented in Sections 3.3.2 and 3.4.2 respectively.

3.2.2.1 Elastic Deflection Testing

This test verifies the mechanical behaviour of deformable bodies in UDEC. An isotropic elastic cantilever is fixed in place at one end and allowed to deform under gravity. The vertical displacement at the free end is given by Equation 3.1:

$$u_y = -\frac{3\rho g L^4}{2EH^2} \quad (3.1)$$

Where:

E	Young's modulus	(Pa)
H	Height	(m)
L	Length	(m)
g	Acceleration due to gravity	(ms ⁻²)
u	Displacement	(m)
ρ	Density	(kgm ⁻³)

The properties of the beam used are given in Table 3.3:

Table 3.3 – Properties of cantilever used in beam deflection test.

Density (kgm ⁻³)	3000
Height (m)	1.0
Length (m)	10.0
Young's Modulus (Pa)	2×10 ¹⁰

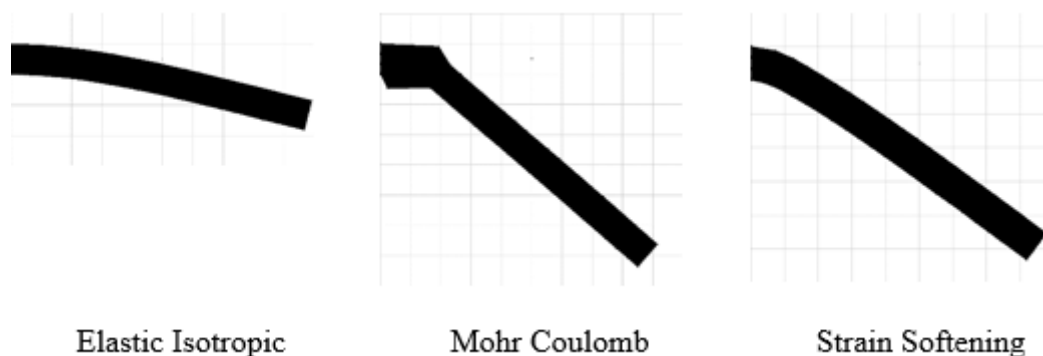
Table 3.4 compares the deflection seen in several models with that given by Equation 3.1. As seen, the deflection predicted by UDEC asymptotically approaches the analytical value as zone density increases. This suggests that high zone densities are required to give accurate results. Such high densities would greatly increase model runtime however. Further testing of the effects of zone density on model behaviour is presented in Section 6.6.

Table 3.4 – Results of simulated cantilever bending test.

Zone Edge Length (m)	Zone Density (m⁻²)	Displacement (m)
1.00	8.80	0.0146
0.50	25.2	0.0190
0.20	122	0.0212
0.10	444	0.0214
0.05	1690	0.0220
Analytical Result	N/A	0.0225

3.2.2.2 Plastic Deflection Testing

In addition to the elastic test above, a test was performed to examine the plastic deformation of a beam using different constitutive models. Only the isotropic elastic, Mohr-Coulomb and strain softening models were tested as the others were considered unsuitable for UCG based on the considerations in Table 3.1. Figure 3.4 shows the deformation of each cantilever after 5 seconds of simulated time. All models used a friction angle of 30° and a cohesion of 100kPa. Strain softening parameters were set at zero as the constitutive model was used to simulate perfectly plastic behaviour.

**Figure 3.4** – Plastic deflection of a cantilever under different constitutive models.

As seen, the relationship used has a strong effect on behaviour. While the isotropic model is shown to be valid for the elastic regime, it does not consider plastic strains. The Mohr Coulomb model does show plastic behaviour, however the predicted shape of the beam is physically unrealistic. As mentioned in Table 3.1, this model does not contain a plastic flow rule, leading to an unrealistic failure shape. As such, the model is seen to be unsuitable when large plastic strains are expected. Finally, the strain softening Mohr Coulomb model is seen to give realistic behaviour. Although this model causes a slight increase in runtime, the accuracy of its results justify its use.

3.2.2.3 Freefall Motion Test

This test of UDEC's mechanical behaviour involves the motion of a single block under freefall, and its interaction with the ground upon impact. This test was performed by dropping a 1x1m deformable block from a height of 2m onto a fixed base 5m wide by 1m high. The velocity of the block's centroid is tracked for 3 seconds after the initial release of the block and compared with expected behaviour. All materials in the test were modelled using the isotropic elastic constitutive model with arbitrarily high Young's modulus and density of 3000kgm^{-3} . Gravitational acceleration was set at 9.81ms^{-2} . Figure 3.5 shows the results of this test.

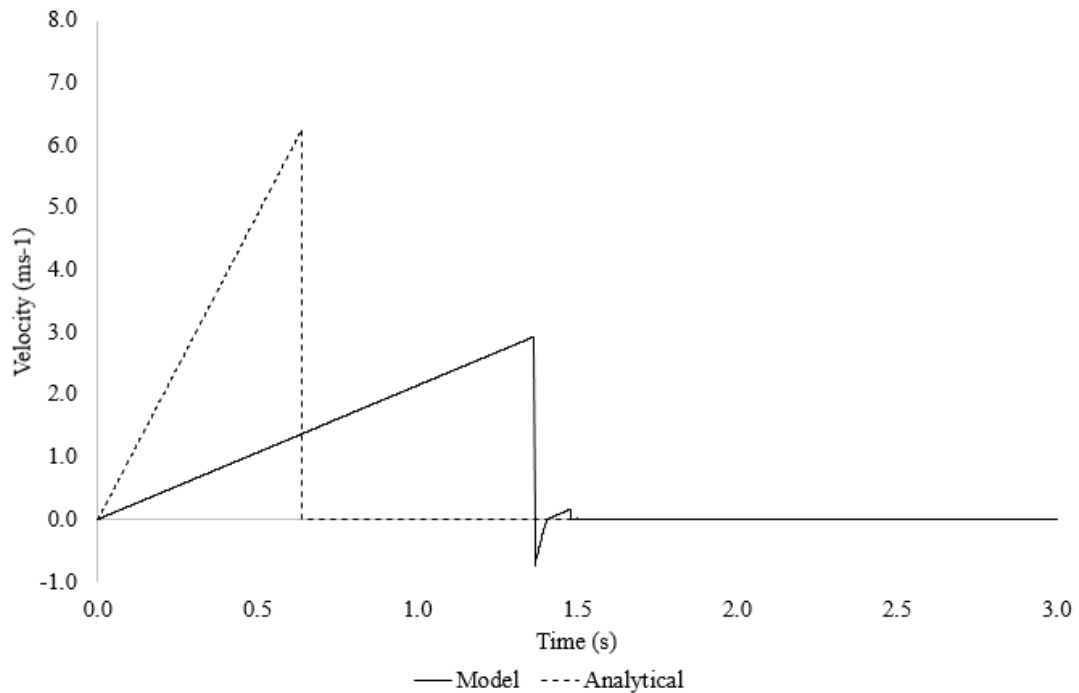


Figure 3.5 – Freefall velocity profiles calculated in UDEC and via kinematics.

As seen, the velocity profile given by UDEC is considerably different to the analytical profile. Firstly, the acceleration of the modelled profile is approximately 2.1ms^{-2} , whereas the analytical profile gives 9.8ms^{-2} . This discrepancy is due to damping. As mentioned in Appendix A.1.3, the force on each gridpoint at every calculation cycle is effectively reduced by a factor of 5. As the only force present in this test is gravity, the acceleration seen is also reduced by a factor of approximately 5. The factor of reduction is not exactly 5 due to rounding errors in the calculation process. The second discrepancy is the brief velocity reversal seen after approximately 1.4 seconds. This is simply caused by the temporary overlap of the falling block with the base of the model and the action of the restorative force to remove this overlap. Despite these discrepancies, the total displacement of the block reaches the expected value of 2m and then becomes steady for the remaining time, as expected. As such, the use of UDEC in modelling blocks under freefall is justified.

3.3 HYDRAULIC CALCULATIONS

3.3.1 Hydraulic Model Formulation

The UDEC hydraulic algorithm assumes fluids within a rock mass exist entirely within the joints between blocks. The blocks themselves are assumed to be dry and impermeable. Two way coupling links the aperture (and hence flow volume) of joints to both the mechanical stresses of the blocks and the pore pressure of the fluid. Fully coupled hydraulic/mechanical UDEC models have the capability to simulate a range of hydraulic effects, including:

- The effect of pore pressure on rock blocks
- The effect of mechanical stress on fluid volumes and flow behaviour
- Pressure driven flow of fluids along joints
- Changes in pressure due to inflow/outflow of fluids from joints and/or voids
- Flow within fully saturated and partially saturated (vadose) regions

The above effects are added to the mechanical calculation cycle (Figure 3.2) to form a fully coupled hydraulic/mechanical model. Figure 3.6 shows the additions and how they connect to the mechanical cycle. The details of the individual steps in the hydraulic cycle are examined in Appendix A.2.1.

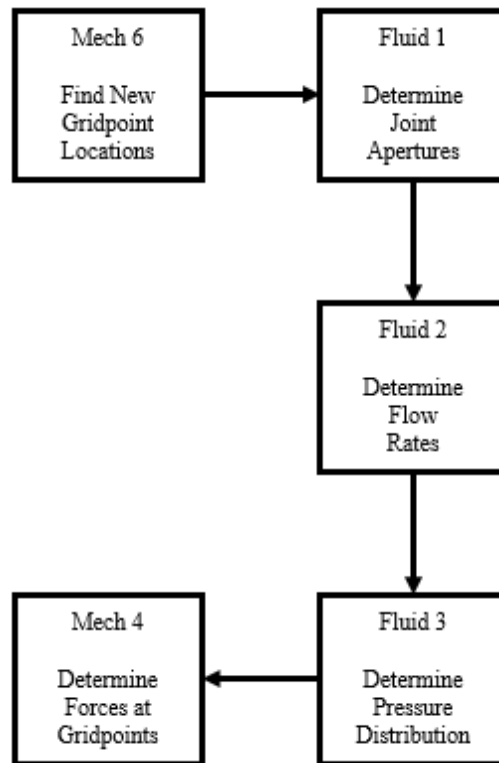


Figure 3.6 – Hydraulic calculation cycle for a coupled hydraulic/mechanical model. The three fluid steps are calculated independently of mechanical Steps 1 through 3. After Itasca Consulting Group, 2006.

Volumes of fluid within UDEC are discretised into regions known as *domains*. A domain is created wherever two or more zones meet, provided these zones are from different blocks. Domains are defined within joints, voids, and intersections between joints. Voids are defined as joints with an aperture greater than a predefined maximum value. Fluid properties are assumed to be constant throughout a domain, with the notable exception of hydrostatic pressure. When gravity is present, the fluid pressure within each domain varies linearly with the hydrostatic gradient. Figure 3.7 shows the discretisation of a model into blocks, zones and domains.

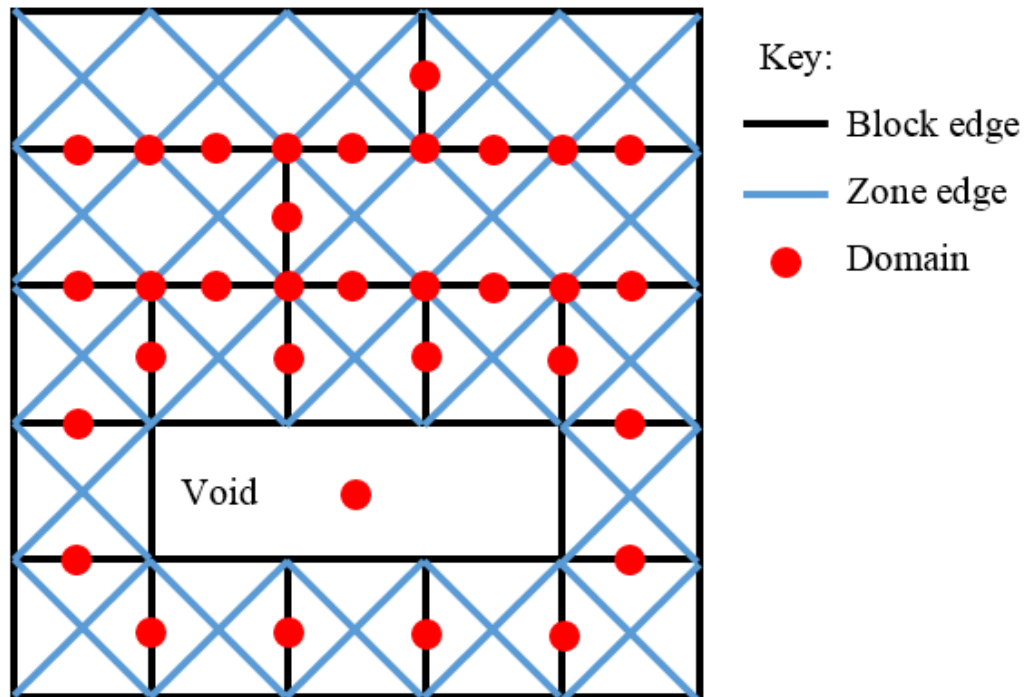


Figure 3.7 – Schematic representation of domains used to discretise hydraulic problems. After Itasca Consulting Group, 2006.

As with the mechanical calculation, the timestep used in the hydraulic model is automatically determined in order to maintain the stability of the model. The definition of the timestep is given in Appendix A.2.2. In coupled hydraulic/mechanical models, the value of the overall timestep is chosen as the smaller of the mechanical or hydraulic timesteps. The hydraulic timestep can be severely limited in cases with large contact apertures or small domain volumes. In many cases however, only the steady state solution to the hydraulic problem is of interest. In this case a simplified steady state algorithm can be used, which greatly improves computational efficiency.

The steady state algorithm works by assuming the volume of each domain is roughly constant throughout the runtime of the model. As such the actual values of the domain volumes are irrelevant, as is the fluid bulk modulus. The volumes and bulk moduli can then be scaled so that each domain gives the same timestep. This method is analogous to the process of mass scaling mentioned in Section 3.2.1. Assuming domain volume changes remain low throughout the model, this algorithm greatly speeds solution. In addition, as the model approaches solution, the pressure variation in each timestep becomes very small. This allows several fluid steps to be executed for every mechanical step, further speeding solution. In this method, mechanical steps are triggered whenever the change in pressure of any domain exceeds a given fraction of the original pressure in that domain. This method can greatly speed coupled models, but can lead to inaccuracies if any large scale collapse behaviour is present.

3.3.2 Hydraulic Validation

3.3.2.1 Stress/Aperture Relationship Test

This test verifies UDEC's hydraulic logic by testing the relationship between stress, pressure and joint aperture. Consider a single horizontal joint between two rigid blocks, as shown in Figure 3.8. The only relevant forces in the system are those of gravity and fluid pressure. By considering these forces, an analytical expression can be derived for the aperture of the joint. This is given in Equation 3.2.

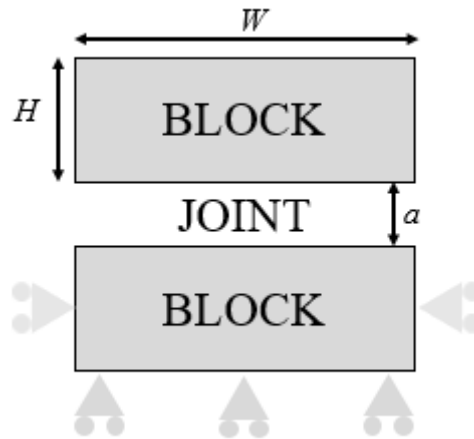


Figure 3.8 – Simple joint geometry used for stress/aperture verification.

$$a = a_0 + \frac{1}{k_N} [2P\hat{L}^2 - \rho gWH\hat{L}] \quad \forall \quad a_{min} < a < a_{max} \quad (3.2)$$

Where:

\hat{L}	Unit length	(m)
P	Pressure	(Pa)
W	Width	(m)
a	Hydraulic Aperture	(m)

The above system was created in UDEC using the properties listed in Table 3.5. The modelled aperture is found to agree with the analytical value to within an error of 0.8%, verifying the relationship as sufficiently accurate for use in the UCG model.

Table 3.5 – Verification of UDEC’s stress/aperture relationship.

Input Values	
Aperture at Zero Stress a_0 (mm)	1.00
Normal Stiffness k_N (Nm ⁻¹)	1×10 ⁸
Pore Pressure P (Pa)	100,000
Block Density (kgm ⁻³)	2,500
Gravitational Acceleration g (ms ⁻²)	10.0
Block Width W (m)	2.0
Block Height H (m)	1.0
Output Apertures (mm)	
Analytical	2.50
UDEC	2.48

3.3.2.2 Flow/Pressure Relationship Test

Fluid flow in UDEC is governed by the cubic flow law, given by Equation 3.3. The verification of UDEC’s flow logic was performed by applying a pressure gradient across the joint in Figure 3.8 and measuring the flow rate observed. Table 3.6 shows the results of this test. The model and theory are again seen to agree to within an error of 0.8%, verifying the use of the steady state flow algorithm in UDEC.

$$q = -\frac{1}{12\mu} a^3 \frac{\Delta P}{L} \quad (3.3)$$

Where:

q = Flow rate per unit depth into page (m^2s^{-1})

μ = Dynamic viscosity (Pa s)

Table 3.6 – Verification of UDEC’s fluid flow logic.

Input Values	
Fluid Viscosity μ (Pa s)	0.001
Joint Aperture a (mm)	2.50
Pressure Difference ΔP (Pa)	100,000
Joint Length L (m)	2.0
Output Flow Rates (m^2s^{-1})	
Analytical	0.0650
UDEC	0.0645

3.4 THERMAL CALCULATIONS

3.4.1 Thermal Model Formulation

UDEC's thermal modelling capabilities include heat conduction, thermal expansion of intact rocks and the modelling of temperature dependent fluid density and viscosity. Heat sources and sinks can be included at model boundaries and within the bulk of the rock mass. Heat sources can have constant magnitudes or can vary with time. Convective and radiative heat transfer can be simulated as boundary conditions (by specifying heat transfer coefficient and background temperature), but cannot be included within the bulk of the model. Due to a number of differences between the thermal model and the hydraulic/mechanical models, thermal aspects of coupled simulations must be cycled separately. In most cases the thermal model is run to completion in between stages of the hydraulic/mechanical model. The temperature profile found in the thermal model can then influence hydraulic or mechanical effects via temperature dependent fluid properties and/or thermal expansion.

Thermal modelling in UDEC can be achieved with either an explicitly or implicitly time stepped algorithm. The calculation cycle for the explicit algorithm is shown in Figure 3.9. The implicit algorithm works by iteratively finding the solution to a set of simultaneous equations for the temperature of each zone in the model at the desired time(s). The full formulations of the explicit and implicit algorithms are given in Appendices A.3.1 and A.3.2 respectively. A comparison between the methods is given in Table 3.7. The long timestep means the implicit method can be faster for simple models, but unsuitable for models with complex geometries, non-linear phenomena or high accuracy requirements.

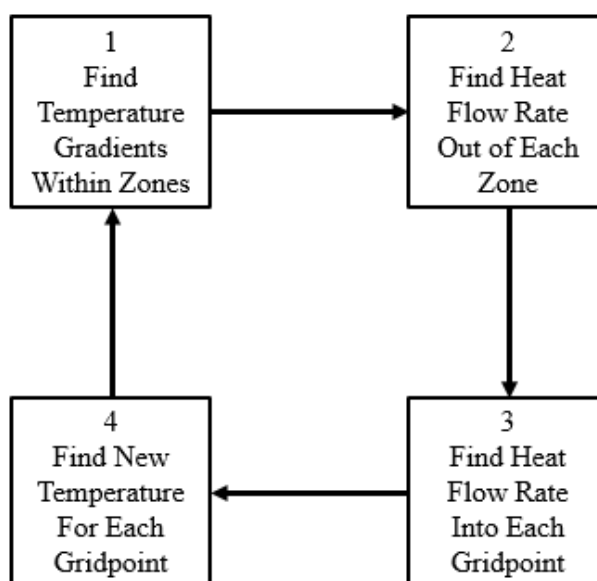


Figure 3.9 – Calculation cycle for the explicit thermal algorithm. After Itasca Consulting Group, 2006.

Table 3.7 – Comparison between explicit and implicit thermal algorithms in UDEC.

Consideration	Explicit Algorithm	Implicit Algorithm
Timestep determination	Automatic	User controlled
Timestep length	Short	Long
Cycles per timestep	One	Many
Stability	Depends on timestep	Unconditionally stable
Accuracy	Depends on timestep	Depends on timestep
Non-linear Solutions	Possible	Not possible

Thermal conduction in UDEC is modelled entirely through the intact rock blocks. Joints are defined as be perfectly conducting while voids are perfectly insulating. Thermal discretisation is based on the zones used in the mechanical model, however extra thermal zones must often be created to ensure conservation of energy between misaligned blocks. The need to generate these zones precludes thermal/mechanical coupling as new zones would need to be created after every thermal step. This would greatly increase the complexity and runtime of the model as well as introducing a large source of error through the need to conserve energy between the meshes. A full description of thermal zone generation is given in Appendix A.3.4.

In addition to heat transfer, UDEC's thermal algorithm can also simulate thermal expansion and the temperature dependent density and viscosity of fluids. The formulation of these effects is shown in Appendices A.3.5 and A.3.6 respectively. As shown in Section 3.5.2 however, the temperature dependence of fluid properties breaks down near the boiling point of the fluid.

3.4.2 Thermal Validation

3.4.2.1 Fixed Temperature Conduction Test

This test verifies UDEC's thermal logic by modelling temperature conduction along an insulated rod. This is one of very few transient heat transfer problems which can be solved analytically. Consider a rod of length L , with initial temperature T_0 throughout. One end of the rod is fixed at a higher temperature of T_H . The other edges are perfectly insulated. It can be shown (e.g. Coulson *et al*, 2004) that the temperature T at any given time t and location x along the length of rod is given by Equation 3.4.

$$T = T_0 + \sum_{n=0}^{\infty} (-1)^n (T_H - T_0) \left[\operatorname{erfc} \left(\frac{2nL+x}{2\sqrt{D_T t}} \right) + \operatorname{erfc} \left(\frac{2(n+1)L-x}{2\sqrt{D_T t}} \right) \right] \quad (3.4)$$

Where:

T = Temperature (K)

t = Time (s)

x = Length along rod (m)

D_T = Thermal diffusivity (m^2s^{-1})

Subscripts:

0 = Initial

H = Hot end.

erfc is the complementary error function:

$$\operatorname{erfc}(\varphi) = \frac{2}{\sqrt{\pi}} \int_x^{\infty} e^{-t^2} dt$$

Consider a rod with the properties given in Table 3.8. The temperature profile of the rod has been found at a number of times using Equation 3.4. A UDEC model has been created to analyse the same problem. A comparison between the UDEC results and the analytical solution is shown in Figure 3.10. It is seen that the accuracy of the UDEC result decreases with distance from the hot end, with a maximum temperature error of 22K seen after 12 months. UDEC is also seen to consistently overestimate temperatures. Given the reasonably small degree of error however, the thermal algorithm in UDEC is considered to be accurate enough for use in the UCG model.

Table 3.3 – Physical properties of 1D beam used in UDEC thermal verification.

Height H (m)	1.0
Length L (m)	10.0
Initial Temperature T_0 (K)	300
Hot End Temperature T_H (K)	500
Thermal Diffusivity D_T (m^2s^{-1})	1×10^{-6}

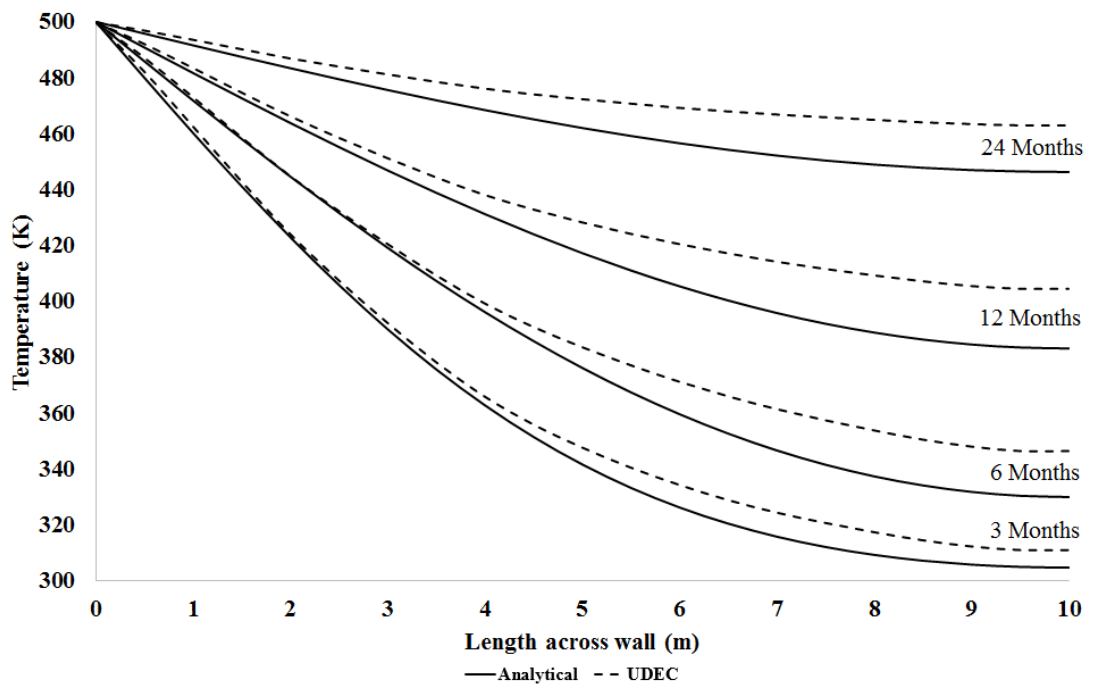


Figure 3.4 – Temperature profiles along a 10m rod as a function of time found from UDEC and analytical calculation. All UDEC models used identical physical properties and therefore identical timesteps. Analytical calculation used the first three terms of the Taylor expansion in Equation 3.4.

3.4.2.2 Fixed Heat Flux Conduction Test

This test verifies the thermal algorithm by modelling how a transient heat transfer problem reaches steady state. The geometry and material properties used are the same as those in Section 3.4.2.1, with the exception of thermal diffusivity. This is set to a value of $1 \times 10^{-3} \text{ m}^2\text{s}^{-1}$ to speed the establishment of the steady state. Heat is applied to the left hand end of the rod at a constant rate and is removed from the right hand end by convection to the surroundings. The model runs for 1 week (modelled time) to ensure the steady state has been reached. The average temperature of the rod at steady state can be found by Equation 3.5. Table 3.9 lists the physical properties used in this calculation alongside the results of the UDEC model and analytical calculation. As with the previous test, UDEC is seen to slightly overestimate the final temperature. The thermal model is still considered valid however, as this error is reasonably small.

$$T = T_b + \frac{Q}{UH} \quad (3.5)$$

Where:

Q = Heat flux (Wm^{-1})

T_b = Background temperature (K)

U = Convective heat transfer coefficient ($\text{Wm}^{-2}\text{K}^{-1}$)

Table 3.4 – Input properties and output temperatures of fixed heat flux test.

Input Variables	
Background Temperature T_b (K)	300
Heat Flow Rate Q (Wm^{-1})	10,000
Convective Heat Transfer Coefficient U ($\text{Wm}^{-2}\text{K}^{-1}$)	100
Output Temperature (K)	
Analytical	400
UDEC	406

3.5 ADVANTAGES, CHALLENGES AND LIMITATIONS

3.5.1 Mechanical

UDEC simulates rock masses using a combined finite-discrete element representation. Table 3.10 compares the relative advantages, disadvantages and capabilities of UDEC in comparison with both fully discrete (e.g. particle based DEM) and fully continuous (e.g. FEM) methods.

Table 3.5 – Advantages, disadvantages and capabilities of UDEC relative to continuum methods and particle based discrete methods of mechanical simulation.

Issue	UDEC	Discrete Methods	Continuum Methods
Rock separation	Possible	Possible	Not Possible ¹
New Fracture Generation	Not Possible	Possible	Not Possible ¹
Goafing/Collapse Prediction	Possible	Possible	Not Possible ¹
Bending Behaviour	Possible	Not Possible	Possible
Solution Speed	Moderate	Slow	Fast
Solution Stability	Moderate	Moderate	High
Mesh Dependence	High	High	Low
Material Property Selection	Very Difficult	Simple	Difficult

1 – These issues can be modelled with continuum methods, but doing so is difficult and computationally expensive (Hammah *et al*, 2008).

The ability of UDEC to model both discrete (rock separation and collapse) and continuum (bending) effects allows for a closer representation of reality than that given by either fully continuum or fully discrete methods. As such, UDEC is often used in the modelling of complex behaviours of highly jointed rock masses (Coulthard & Dutton, 1988; Coulthard, 1999; Lisjak & Grasselli, 2014; Morris *et al*, 2006; Morris *et al*, 2009; Vorobiev *et al*, 2008; Wei & Hudson, 1998).

One of the greatest challenges in designing a UDEC model is the selection of an appropriate joint pattern, which in turn determines block size and shape parameters. Increased numbers of blocks decrease both solution speed and stability. In addition, block size and shape can have profound effects on model results, complicating the selection of appropriate material properties. This issue is referred to as mesh dependence. The problem is further compounded by the impossibility of creating new fractures within an existing rock mass. Lorig & Cundall (1987) suggest a method in which this can be approximated, however this greatly increases model runtimes with little advantage. Figure 3.11 highlights the effect of block size on model performance. The influence of block morphology on model results is further examined in Chapter 4. Despite these issues, UDEC is seen to be a useful tool for modelling the local environmental impact of UCG.

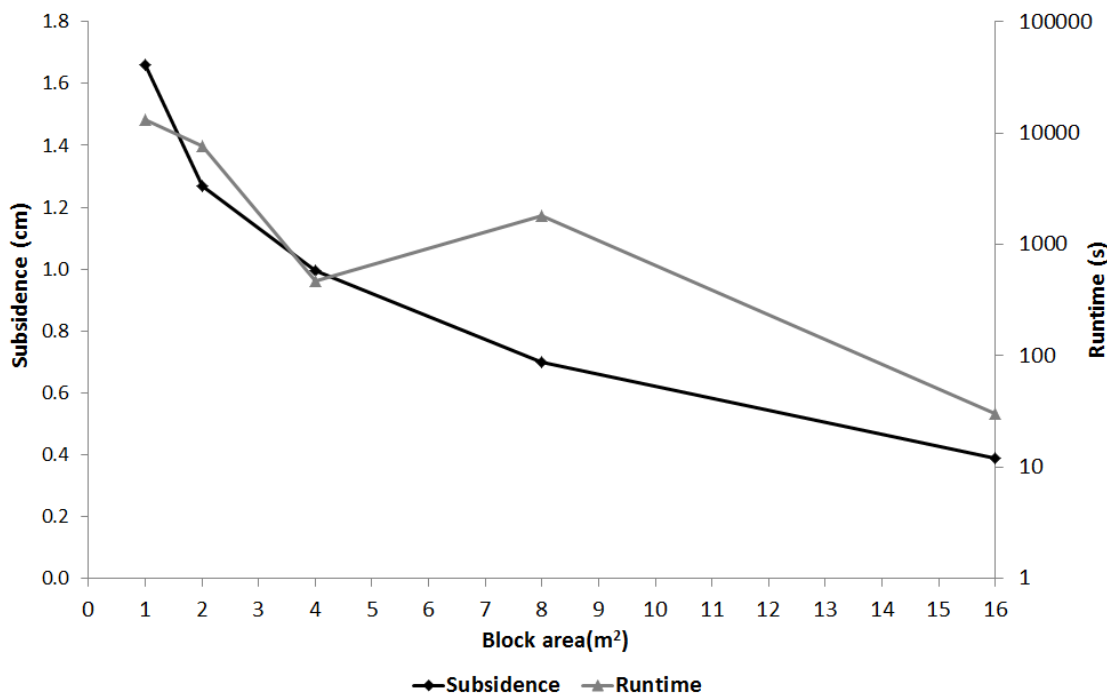


Figure 3.5 – Effects of block size on model behaviour. Results taken from preliminary designs for a UCG model.

3.5.2 Hydraulic

Hydraulic effects contribute greatly to the environmental impacts of UCG, both in terms of groundwater issues and their coupling with mechanical effects. Given that the UDEC model will need to predict both subsidence and groundwater flow rates, it is essential that the methods used in the model are able to realistically simulate hydraulic behaviour. Table 3.11 highlights the principal advantages and disadvantages of UDEC's hydraulic capability in comparison with continuum methods such as CFD. Particle based DEM is more suited to modelling fluid dominant systems (i.e. those in which small solid elements exist surrounded by fluid) than solid dominant systems. As such, it will not be considered further for this model.

Table 3.6 – Advantages, disadvantages and capabilities of UDEC compared with continuum methods of hydraulic simulation.

Issue	UDEC	Continuum Methods
Variable Permeability	Spatial & Temporal	Spatial ¹
Stress/Pressure Coupling	Possible	Possible
Stress/Aperture Coupling	Simple	Difficult
Fluid Phase Change	Not Possible	Possible
Solution Speed	Moderate	Fast
Solution Stability	Moderate	High
Mesh Dependence	High	Low

1 – Temporal variations in permeability can be modelled with continuum methods, but doing so is difficult and computationally expensive.

The modelling of hydraulic problems using fluid filled fractures gives UDEC a considerable advantage over continuum methods, in that the coupled temporal variations of mechanical stress, hydraulic aperture and fluid pressure are simple to consider. In comparison, continuum methods tend to assume constant permeabilities and calculate flow rates using a variant of Darcy's law (Köhne *et al*, 2009). A potential disadvantage with the UDEC representation is the dependence of the hydraulic model on the joint pattern, further complicating the issues presented in Section 3.5.1. Fracture patterns must contain enough joints to ensure sufficient connection of fluid filled regions, and these joints must be oriented in such a way that any permeability anisotropy is retained. Note that the absolute permeability of a system can be controlled by altering the aperture of joints, such that the total number of joints present is not significant. The effects of fracturing on mechanical and hydraulic results are investigated in detail in Chapters 4 and 6.

The principal disadvantage of UDEC's hydraulic model is the inability to model fluid phase changes and dissolution. This precludes the modelling of several important hydrological effects including:

- Boiling of groundwater as it enters the UCG cavity
- The effects of water inflow rates on cavity heat generation
- Thermal convection
- Solution, adsorption, diffusion and advection of dissolved species

While some of these issues can be approximated using FISH functions, doing so greatly increases the computational demands of the model (Tomac & Gutierrez, 2015). As such, full modelling of groundwater contamination is not possible with UDEC alone. In order to include these effects, alternative modelling methodologies are required. Another limitation of UDEC's hydraulic model is the simplistic definition of joints. The stress/aperture relationship is assumed to be linear (though cut-offs are used at extreme values) and neither joint roughness nor tortuosity is considered. Tortuosity can be considered simply by including more complex joint patterns. Joint roughness and non-linear stress/aperture relationships can be included by using the Barton-Bandis joint model (Bandis *et al*, 1985). Both methods can greatly increase computational runtimes however. Simpler methods involve the use of corrective factors in the cubic flow law, however these can reduce the overall accuracy of the model.

The final limiting assumption of the hydraulic model applies only where the steady state approximation is used. Considering the increase in solution speed given by this approximation, this applies to the majority of large scale models. The assumption of constant domain volumes is problematic for models containing large amounts of separation or those considering the formation or collapse of voids. Care should be taken that pressures in such regions are adequately defined in the event of predictable void volume changes. Despite the inclusion of void collapse, this assumption is not considered a problem with UCG, as cavity pressure is controlled by the operator.

Given the above considerations, it is believed that UDEC is more than capable of simulating the coupled mechanical and hydraulic behaviour of UCG. Full groundwater contamination modelling will need to be performed using alternative software however, due to the lack of fluid phase partitioning in UDEC. Appendix C suggests how this may be possible using the USGS MODFLOW/MT3DMS codes.

3.5.3 Thermal

Table 3.12 compares the thermal modelling capabilities of UDEC with continuum methods. As seen, UDEC suffers a number of limitations. Initial results show however that thermal effects have a relatively minor impact on environmental damage compared with mechanical or hydraulic effects. As such, UDEC is still suggested to be appropriate for use in a coupled thermal/hydraulic/mechanical UCG model.

Table 3.7 – Comparison of the capability of various techniques for modelling thermal phenomena within a rock mass.

Issue	UDEC	Continuum Methods
Thermal Conduction	Yes	Yes
Thermal Convection	No	Yes
Thermal Radiation	No	Yes
Thermal Expansion	Yes	Yes
Temperature Dependent Solids	No	Yes
Temperature Dependent Fluids	ρ, μ Only	Yes
Thermal/Mechanical Coupling	Partial	Full
Thermal/Hydraulic Coupling	Partial	Full
Solution Speed	Moderate	Fast
Solution Stability	Low	High
Mesh Dependence	Moderate	Low

The main limitations of UDEC's thermal model are the lack of thermal/hydraulic coupling and the separation of thermal and mechanical/hydraulic runtimes. These issues preclude the modelling of coupled thermal effects such as convection and thermal spalling (Biezen, 1996), as well as the simulation of temperature dependent thermal properties such as heat capacity and conductivity. Previous attempts to include these effects have been moderately successful, but tend to greatly increase model runtimes (Tomac & Gutierrez, 2015). More realistic thermal modelling can be achieved by alternating the thermal and mechanical/hydraulic algorithms, though this also increases runtime. The modelling of temperature dependent rock mechanical properties can be included using FISH functions, as shown in Section 5.5.

As shown in Table 3.12, UDEC is capable of modelling temperature dependent fluid density and viscosity, however this can cause serious instabilities if the fluid approaches boiling temperature. In UCG, groundwater can exist either as liquid water or superheated steam. Given the low flow rates involved, UDEC's thermal algorithm assumes fluid temperature equals rock temperature at all times. As such the fluid in the joints surrounding a rock will instantly boil as soon as the temperature of the rock exceeds the boiling point of water. This boiling causes fluid density to suddenly reduce by a factor of approximately 1,000, leading to a sudden change in stress which causes the rock mass to break apart and the model to crash. In addition, changes in density can produce a buoyant force which alters fluid flow rates, affecting the hydraulic model and introducing uncertainty into model results.

Given the above considerations, UDEC is seen to be a poor choice for thermal modelling. Several attempts to improve the thermal model are presented in Section 5.6.3, however these were seen to be generally unsuccessful. Given that thermal effects are observed to be relatively unimportant however, these issues are not considered to be significant to the overall performance of the model. Given its advantages in hydraulic and mechanical modelling, UDEC is therefore considered to be the appropriate choice for modelling the local environmental impacts of underground coal gasification. It is suggested however, that future more detailed work should use some form of 3D modelling which can accurately couple mechanical, hydraulic and thermal effects. Such a formulation is currently difficult to achieve with either discrete or continuum methods however, suggesting that new techniques may need to be developed.

3.6 CONCLUDING REMARKS

This chapter has outlined the capabilities, advantages, challenges and limitations of UDEC with respect to its use as a tool for modelling the local environmental impacts of UCG. The combined finite/discrete representation provided by modern DEM codes such as UDEC has been shown to be a very useful tool for the prediction of subsidence on a number of occasions. The inclusion of fully coupled hydraulic modelling based on joint apertures also provides a key advantage in comparison with many continuum methods. Finally, despite a number of shortcomings, the thermal algorithm within UDEC adds to the capabilities of the software for predicting the local effects of UCG.

A number of limitations of the software have been identified, including the strong influence of joint geometry on results, the dependence of result accuracy and runtime on zone density and the lack of full thermal/mechanical coupling. Many of these issues have been overcome somewhat through the use of novel modelling techniques. Chapter 4 introduces a new methodology for representing the effects of unknown fracture patterns on rock mass behaviours, while further investigations of zone density effects are presented in Chapter 6. Chapter 5 presents a number of attempts to include full thermal modelling in UDEC, though these were met with limited success. Despite these issues, it is believed that the advantages of UDEC over other modelling methods lead to it being the best tool for modelling the local environmental impacts of UCG. It is believed that with a greater understanding of the limitations of the software, UDEC should prove capable of producing fast, accurate and reliable predictions of subsidence and groundwater issues associated with underground coal gasification.

4. SIMULATED LABORATORY SCALE COMPRESSION TESTING

SUMMARY

When modelling heavily jointed rock masses in the discrete element method, particular attention must be paid to the selection of appropriate material properties and joint patterns to give a realistic representation of rock mass behaviour. This chapter presents a new methodology for choosing these parameters, based on the results of simulated laboratory scale compression testing. Investigations into the effects of joint patterns, block geometry and joint properties on rock mass mechanical behaviour are presented and used to derive sets of rock mass material properties. Validation studies and a discussion of the limitations of the new methodology are presented to justify its use in further modelling. Decisions on the joint pattern and material properties to be used in the underground coal gasification (UCG) model are given based on the results of the tests performed in this chapter. The chapter concludes with suggestions for further validation of the method and its potential application to a wider range of rock materials and modelling scenarios.

4.1 THEORY AND BACKGROUND

4.1.1 Representing Rock Masses in the Discrete Element Method

As mentioned in Section 3.5.1, the joint pattern used within model based on the distinct element method (DEM) can have profound effects on the mechanical behaviour of that model. The mechanical properties of the blocks within the model are often altered to take account of these effects. Methods such as the Hoek & Brown failure criterion and geological strength index (GSI) (Hoek *et al*, 2002; Marinos *et al*, 2007) can be used to select these properties based on empirical measurements of real joint patterns. Such methods tend not to consider the effects of particle shape, variability and anisotropy on rock mass behaviour however. In order to gain a better understanding of how joint patterns affect material properties, a number of simulated laboratory scale compression tests have been performed on rock masses with varying joint geometries. In addition, a new methodology has been developed in which the results of such simulations are scaled up to provide material properties for a larger engineering scale rock mass. Effectively, the entire laboratory scale geometry represents an assembly of rocks which constitute a single rock block in the engineering scale model. Figure 4.1 highlights this concept. The remainder of this section outlines the methodology used to select the rock mass material properties.

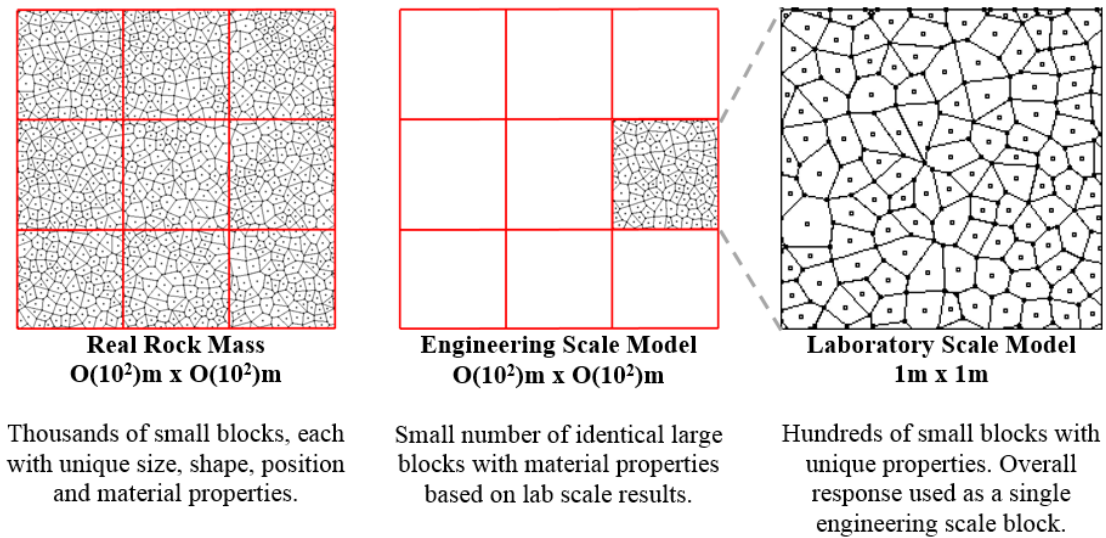


Figure 4.1 – Representation of a real rock mass as an assembly of large particles, where each particle has properties based on laboratory scale simulation results.

4.1.2 Axial Compression Testing

Axial compression testing refers to two common laboratory techniques used to determine the material properties of intact rock specimens. Core samples from the site of interest are cut down to produce cylindrical test sections with dimensions on the order of centimetres. These sections are then loaded into a test apparatus, such as that illustrated in Figure 4.2. The sample is contained within a flexible membrane and is held between two stiff plates inside a sealed container of hydraulic fluid. Lateral confining stress σ_L is applied by controlling the hydrostatic pressure of the fluid. Axial compressive stress σ_A is applied to the sample via the upper plate. The total axial strain of the sample can be derived from measurements of the displacement of the upper plate. Strain gauges are also often applied to the sample to measure stresses in the transverse direction (British Standards Institute, 1990).

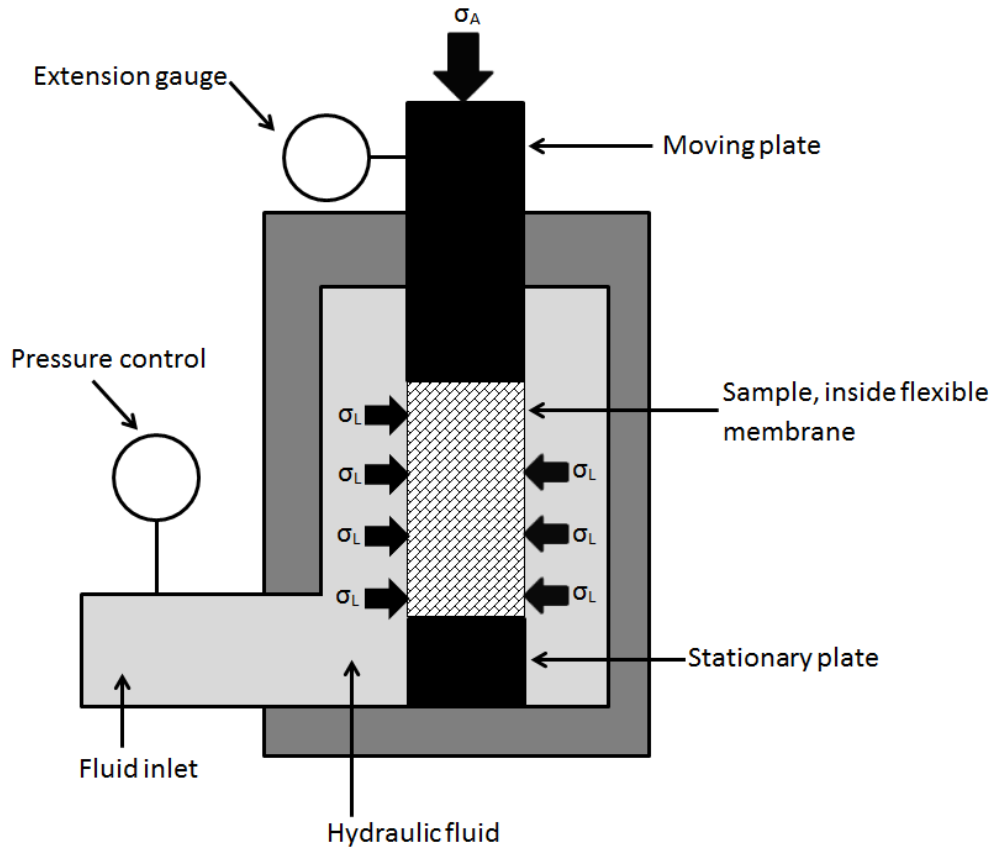


Figure 4.2 – Typical apparatus used for a triaxial compression test.

In cases where zero confining pressure is applied, this technique is referred to as uniaxial compression. For cases with nonzero confining pressure, the term biaxial compression is used. In uniaxial compression, the axial stress-strain response of the sample can be analysed to determine the material Young's modulus E and axial compressive strength σ_C . Measurement of transverse strains gives information on the material Poisson's ratio γ and dilation angle ψ . By measuring yield stress over a range of confining pressures in the biaxial test, it is possible to derive the Mohr-Coulomb parameters of friction angle θ and cohesion C . Finally, the maximum tensile strength of the rock mass $\sigma_{T,max}$ can be estimated from the cohesion and friction angle. Figures 4.3 through 4.5 show how these results are derived.

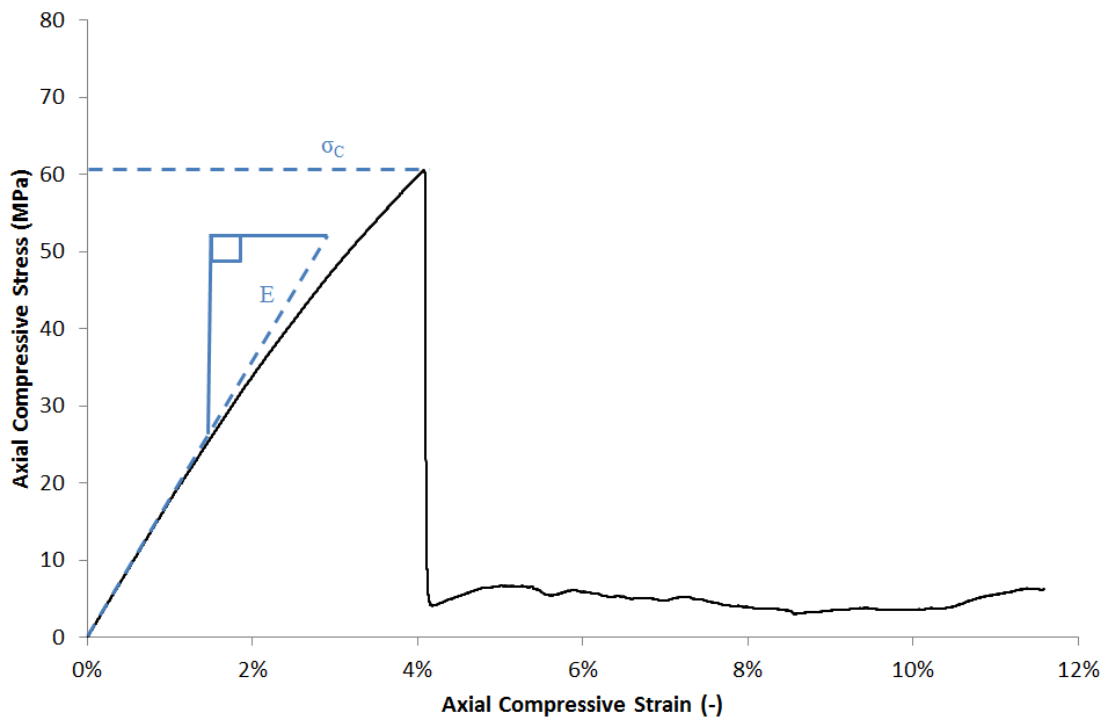


Figure 4.3 – Derivation of Young's modulus E and compressive yield stress σ_c from uniaxial/biaxial compression test results.

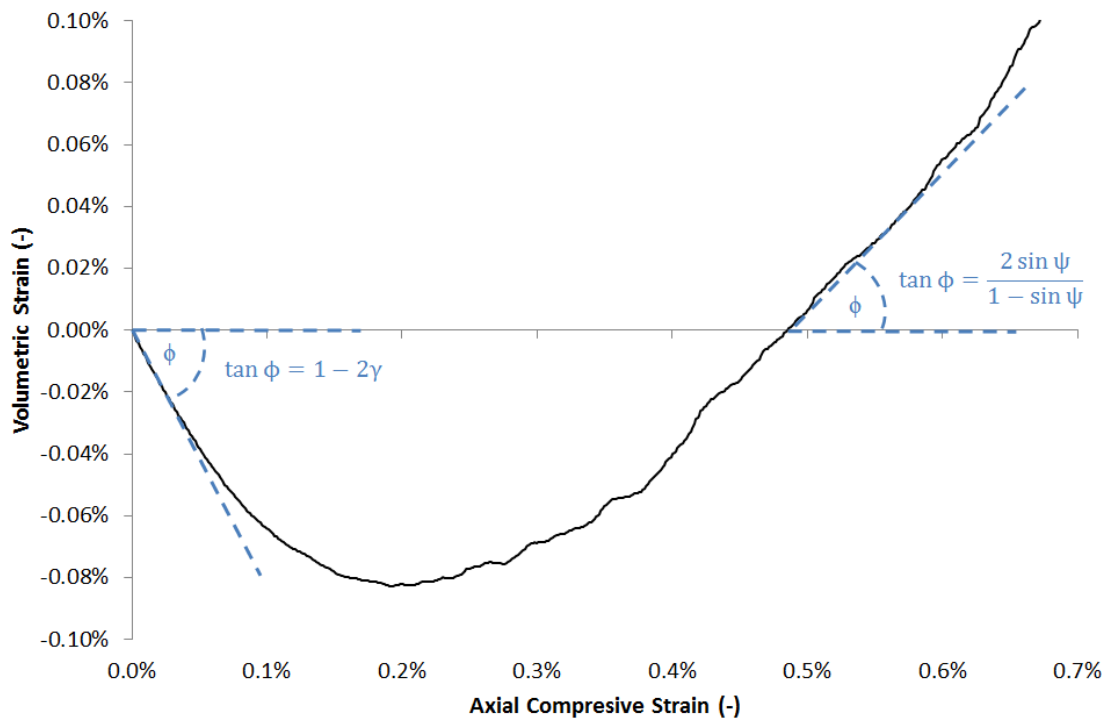


Figure 4.4 – Derivation of Poisson's ratio γ and dilation angle ψ from uniaxial compression test results. Volumetric strain is found as $\mathbf{1 + \epsilon_v = (1 + \epsilon_l)^2(1 + \epsilon_a)}$.

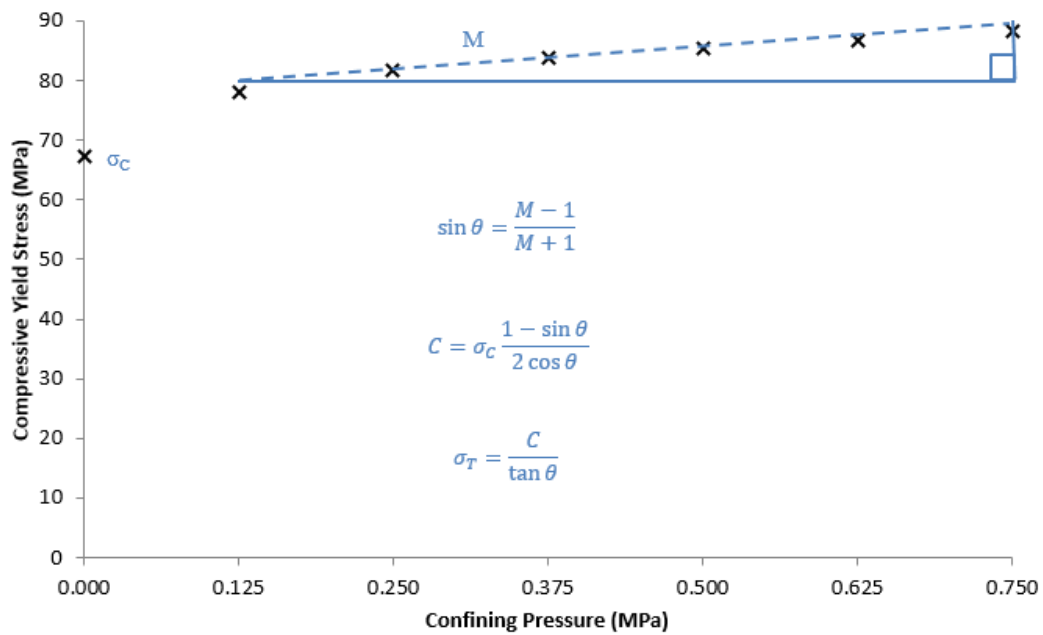


Figure 4.5 – Derivation of friction angle θ , cohesion C and maximum tensile strength σ_T from biaxial compression testing results over a range of confining pressures.

4.1.3 Simulated Testing

While axial compression tests are a common tool for determining the material properties of intact rocks and small particle assemblies (e.g. soil), they are rarely applied to large rock masses. The principal reason for this is the inherent difficulty in transporting the rock mass to a laboratory without disturbing the in-situ state of the constituent rocks. While in-situ testing of rock masses is possible, the costs involved make it impractical in most cases. Given these difficulties, numerical simulation of compression testing is a viable alternative. Simulated compression tests can resolve inter-particle effects over a range of scales, and studies into the transmission of forces through granular media can provide information on material behaviour that would be difficult or impossible to obtain through experimental means (Barreto & O’Sullivan, 2012; Ng, 2004; O’Sullivan, 2015).

The work presented in this chapter aims to use simulated axial compression testing to achieve a greater understanding of the effects of element morphology on the material properties of rock masses in DEM. Simulated testing has been performed on rock masses with varying block geometries and joint mechanical properties. The work aims to produce a methodology for the selection of material properties to be used in representing assemblies of small rocks as single large blocks. These properties will then be applied to the blocks used in the UCG model. It is hoped that the new property selection methodology will retain both mechanical and hydraulic accuracy without the need for excessively large numbers of joints and correspondingly large runtimes. It is also suggested that a successful methodology may be applied to increase the accuracy of future models of jointed rock masses, including both DEM models and continuum based simulations.

4.2 METHODOLOGY OF SIMULATED TESTING

4.2.1 Model Design

The commercially available Universal Distinct Element Code (UDEC) 4.01 has been used to simulate uniaxial and biaxial compression of a number of large scale rock masses with varying joint geometries and material properties. Two methods have been used to represent the 3D rock mass using the 2D software. The axisymmetric method assumes a line of rotational symmetry about the left hand edge of the model. This represents a cylindrical rock mass similar to those used in laboratory tests, with a radius of 1m and height 5m. The plane strain method represents a geometry extending an infinite distance into the page, with a square cross section of side length 5m. While physically unrealistic for a laboratory test, this geometry was chosen for similarity with the UCG model presented in Chapter 5.

Both models contain rock blocks of average side length 10cm, chosen to represent single intact rocks on a similar scale to those found at the Rocky Mountain 1 field trial site (Oliver, 1987). This set up gives approximately 500 blocks in the axisymmetric model and 2,500 in the plane strain model. The size of the models is sufficient to exceed the representative elementary volume (REV) (Min *et al*, 2004) of the system. Stiff metal plates 1m thick are placed along the top and bottom edges of the rock mass to ensure even transmission of axial strains. Lateral confining stresses are applied directly to the side walls of the rock mass to approximate the behaviour of a flexible membrane. Figure 4.6 shows the two model geometries.

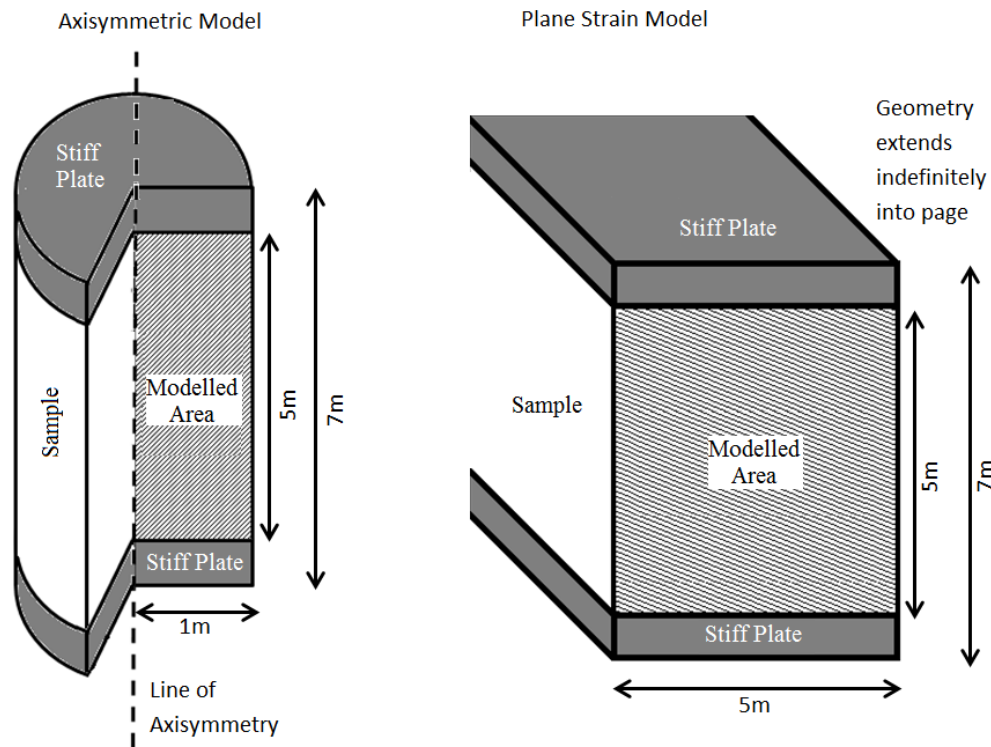


Figure 4.6 - Test geometries of the axisymmetric and plane strain models.

Intact rock blocks are simulated using a strain softening Mohr Coulomb constitutive relationship. As shown in Section 3.2.1, this constitutive relationship is required to reliably predict plastic strain effects. The stiff plates are modelled as an isotropic elastic material for simplicity. Joint behaviour is simulated using an area contact Coulomb slip model as this gives reliable predictions of tightly packed geological materials. Mechanical properties of the rocks, joints and stiff plates are given in Table 4.1. Rock and joint values were chosen from UDEC's internal database entry for sandstone. Sandstone was chosen as it was the predominant rock in the overburden of the Rocky Mountain 1 UCG field trial, used as a benchmark for the UCG model presented in Chapter 5 (Lindblom *et al*, 1990). The stiff plates have Poisson's ratio and density equivalent to that of mild steel and an arbitrarily high Young's modulus. This was selected to minimise the effects of plate deformation on model results.

Table 4.1 - Mechanical Properties for the intact rock material, rock joints and stiff plates in the laboratory scale models.

Mechanical Property	Intact Rock	Rock Joints	Stiff Plates
Density ρ (kgm^{-3})	2700	-	7000
Young's Modulus E (Pa)	1.93×10^{10}	-	1.00×10^{12}
Poisson's Ratio γ (-)	0.38	-	0.30
Friction Angle ϕ ($^{\circ}$)	27.8	30.0	-
Cohesion C (Pa)	2.72×10^7	1.00×10^5	-
Tensile Limit σ_T (Pa)	1.17×10^6	0.00	-
Dilation Angle φ ($^{\circ}$)	0.00	5.00	-
Shear Stiffness k_S (Nm^{-1})	-	1.00×10^9	-
Normal Stiffness k_N (Nm^{-1})	-	1.00×10^{10}	-

Testing is performed by holding the lower plate in place while the upper plate moves downwards at a constant velocity of 0.01ms^{-1} . The models are found to have timesteps on the order of 1×10^{-6} s, giving very low strain rates of approximately 1×10^{-8} per iteration. This helps to maintain a minimal unbalanced force whilst ensuring a reasonable model runtime. Simulations run to an axial strain of 12%, or until block contact overlap tolerances are exceeded. Axial stress is measured at the base of the upper plate. Lateral displacement is measured at nine equally spaced locations along each side of the rock mass. Young's modulus, yield stress, Poisson's ratio and dilation angle were determined from unconfined results. Young's modulus and Poisson's ratio were determined over an axial strain range of 0.01% to 0.03%. Dilation angle is determined from the point of zero volumetric strain to an axial strain 0.02% greater than this.

4.2.2 Rock Mass Variations

Eight joint patterns have been tested throughout this work, including an intact jointless pattern, 4 periodic patterns and 3 stochastically varying patterns. Sample geometries are shown in Figure 4.7. The Voronoi pattern is generated using UDEC's inbuilt Voronoi tessellation algorithm. Further details on the two patterns based on the discrete fracture network (DFN, Figures 4.7g and 4.7h) are given in Section 4.2.4. Across all models, the representative edge length L is 10cm unless otherwise stated. For the Voronoi and DFN patterns, L is the mean edge length across the entire model. H and W refer to block height and width respectively. All of the DFN models used a consistent random seed to eliminate random variation from results.

A total of 76 models have been tested under simulated laboratory conditions, including 53 axisymmetric models and 23 plane strain models. The axisymmetric tests investigated the behaviour of each of the joint patterns under a range of confining stresses to determine rock mass material parameters. The plane strain models investigate the effect of varying geometry, including the effects of changing geometric parameters of the nominally perpendicular (N-DFN) joint pattern. Further plane strain models examine the effects of joint mechanical properties on behaviour. Variations in joint friction angle, dilation angle and normal and shear stiffness were tested under identical conditions in an attempt to verify relationships between joint and rock mass properties. Two tests on intact patterns were also performed to compare model results with experimental data. Finally, repeatability studies of both axisymmetric and plane strain N-DFN models are performed to investigate the stochastic variability of the results. The full list of models tested is given in Table 4.2.

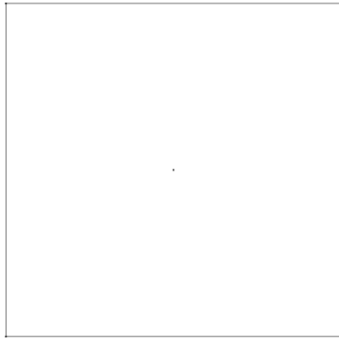


Figure 4.7a – Intact

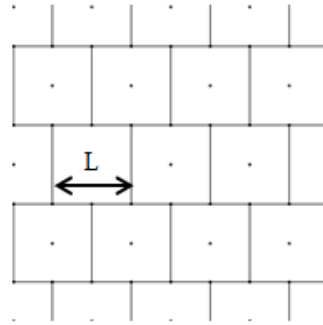


Figure 4.7b – Brickwork

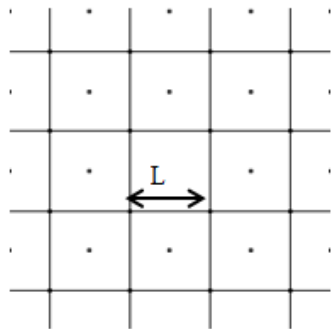


Figure 4.7c – Grid

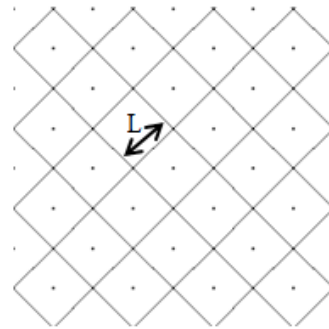


Figure 4.7d – Diamond

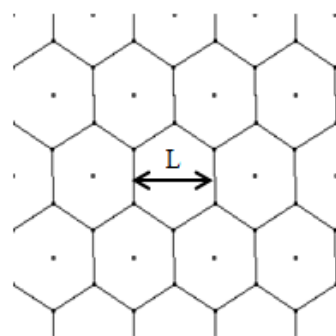


Figure 4.7e – Hexagon

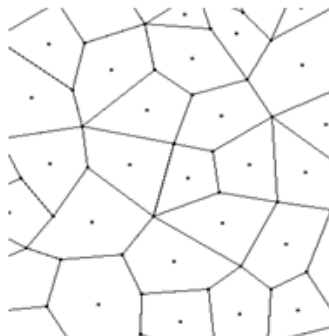


Figure 4.7f – Voronoi

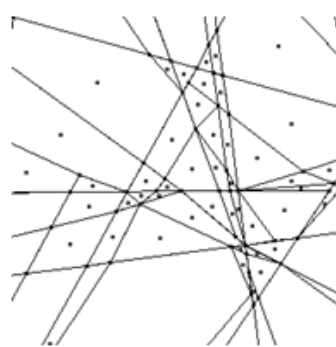


Figure 4.7g – Isotropic Discrete Fracture Network (I-DFN)

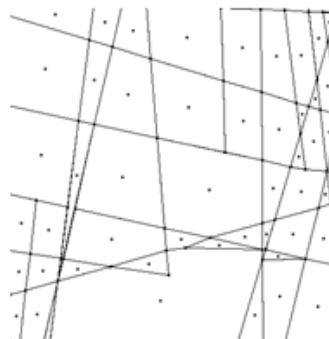


Figure 4.7h – Nominally Perpendicular Discrete Fracture Network (N-DFN)

Table 4.2 – Full list of modelled axial compression tests.

Model(s)	Name	Geometry	Pattern	Material parameters
1 – 7	Brickwork biaxial	Axisymmetric	Brickwork	As Table 4.1
8 – 14	Grid biaxial	Axisymmetric	Square	As Table 4.1
15 – 21	Diamond biaxial	Axisymmetric	Diamond	As Table 4.1
22 – 28	Hexagon biaxial	Axisymmetric	Hexagon	As Table 4.1
29 – 35	Voronoi biaxial	Axisymmetric	Voronoi	As Table 4.1
36 – 42	I-DFN biaxial	Axisymmetric	I-DFN	As Table 4.1
43 – 49	N-DFN biaxial	Axisymmetric	N-DFN	As Table 4.1
50	Brickwork uniaxial	Plane Strain	Brickwork	As Table 4.1
51	Grid uniaxial	Plane Strain	Square	As Table 4.1
52	Diamond uniaxial	Plane Strain	Diamond	As Table 4.1
53	Hexagon uniaxial	Plane Strain	Hexagon	As Table 4.1
54	Voronoi uniaxial	Plane Strain	Voronoi	As Table 4.1
55	I-DFN uniaxial	Plane Strain	I-DFN	As Table 4.1
56	N-DFN uniaxial	Plane Strain	N-DFN	As Table 4.1
57	Small blocks	Plane Strain	N-DFN	L = 7.07cm
58	Large blocks	Plane Strain	N-DFN	L = 14.14cm
59	Tall blocks	Plane Strain	N-DFN	H/W = 2
60	Wide blocks	Plane Strain	N-DFN	H/W = 0.5
61	Low joint friction	Plane Strain	N-DFN	$\theta = 20.0^\circ$
62	High joint friction	Plane Strain	N-DFN	$\theta = 40.0^\circ$
63	Low joint dilation	Plane Strain	N-DFN	$\psi = 0.0^\circ$
64	High joint dilation	Plane Strain	N-DFN	$\psi = 10.0^\circ$
65	Low normal stiffness	Plane Strain	N-DFN	$k_N = 1 \times 10^9 \text{ Nm}^{-1}$
66	High normal stiffness	Plane Strain	N-DFN	$k_N = 1 \times 10^{11} \text{ Nm}^{-1}$
67	Low shear stiffness	Plane Strain	N-DFN	$k_S = 1 \times 10^8 \text{ Nm}^{-1}$
68	High shear stiffness	Plane Strain	N-DFN	$k_S = 1 \times 10^{10} \text{ Nm}^{-1}$
69	Intact biaxial	Axisymmetric	Intact	As Table 4.1
70	Intact uniaxial	Plane Strain	Intact	As Table 4.1
71 – 73	Repeatability tests	Axisymmetric	N-DFN	As Table 4.1
74 – 76	Repeatability tests	Plane Strain	N-DFN	As Table 4.1

4.2.3 Discrete Fracture Network Design

The discrete fracture network (DFN) patterns (Figures 4.7g, 4.7h) are generated using a method based on the work of Min *et al* (2004). DFNs have been used in a number of successful mechanical and hydraulic models of rock masses (Baghbanan & Jing, 2007; Bidgoli *et al*, 2013; Bidgoli & Jing, 2014; Blum *et al*, 2005).

The N-DFN pattern contains two joint sets with normally distributed orientations; one with a mean angle of 0° and one with mean angle 90° . The isotropic I-DFN pattern contains a single joint set with a uniformly distributed angle between 0° and 180° . The position of the centre point of each joint is distributed in a uniformly random manner within the rock mass. The number of joints within each set is determined by a user defined joint density. The length of each joint follows a power law distribution with minimum and maximum cut-offs: The number N of fractures larger than length L is given as: $N = 4L^{-k}$, where k is an empirically derived constant with value 2.2 (Min *et al*, 2004). The input parameters used in the two DFNs are given in Table 4.3. Parameters were chosen to give a mean block edge length of 10cm. Block edge length is a complex function of the density, orientation and length of joints, so choosing input parameters is often a process of trial and error.

Table 4.3 – Geometric parameters for the two joint patterns based on discrete fracture networks.

Parameter	N-DFN		I-DFN
	Joint Set 1	Joint Set 2	
Joint Mean Angle (°)	0	90	90
Standard Deviation in Angle (°)	10	10	180
Joint Minimum Length (m)	1.70	1.70	1.70
Joint Maximum Length (m)	5.00	5.00	5.00
Joint Density (m ⁻²)	5.0	5.0	9.0

The random numbers used to generate the DFN patterns are found using a Poisson process, as shown in equation 4.1. This gives a good approximation of a uniform distribution and allows any model to be repeated, provided that the initial random seed is preserved. The initial seed R_I for the process is determined from the system clock. This is accurate to 1/100th of a second and covers a 24 hour period, making it extremely unlikely that two separate models would ever share the same seed.

$$R_{n+1} = 27R_n - \text{int}(27R_n) \quad (4.1)$$

In order to verify the randomness of the Poisson process, a simple test has been performed. Ten sets of 1,000 consecutive random numbers between zero and one were generated using the process. Table 4.4 compares the mean and variance of these sets with those of the ideal uniform distribution. In addition, the coefficient of determination (COD) for the plot of R_n against n is given for each set.

The results show that the Poisson process is a sufficient method for generating sets of uniformly distributed random numbers for use in the DFNs. In all cases the mean and variance of the sets are well within 10% of the ideal value, and the largest coefficient of determination is well below 1%. The use of the system clock is seen to be a valid method for generating the random seed, with over 8 million unique values obtainable in any 24 hour period.

Table 4.4 – Statistical data on random number sets generated using the Poisson process.

Set	Mean	Variance	COD
1	0.500	0.085	0.00023
2	0.516	0.082	0.00422
3	0.500	0.088	0.00070
4	0.496	0.085	0.00111
5	0.500	0.084	0.00155
6	0.495	0.081	0.00064
7	0.502	0.083	0.00006
8	0.518	0.080	0.00257
9	0.504	0.080	0.00002
10	0.513	0.082	0.00353
Ideal	0.500	0.083	0.00000

4.3 SIMULATED COMPRESSION TESTING RESULTS

4.3.1 Axisymmetric Results

Models 1 through 49 used biaxial testing to investigate the effects of joint pattern on rock mass material properties. Considerable differences in compressive yield strength and rock mass dilation angle were seen between different geometries. The brickwork and grid patterns in particular showed very different behaviour to other patterns, with order of magnitude differences in yield strength and Poisson effect. Material properties derived from these tests are given in Table 4.5. As shown in Figure 4.8, the mechanical behaviour of the rock mass depends heavily on the proportion of joints oriented normally, tangentially or obliquely to the applied strain. Sections 4.3.1.1 through 4.3.1.4 explore this effect in detail for each of the derived material properties.

Table 4.5 – Rock mass material properties derived from simulated triaxial testing.

Geometry	E (Pa)	σ_c (Pa)	θ (°)	C (Pa)	$\sigma_{T,max}$ (Pa)	γ (-)	ψ (°)
Brickwork	1.58×10^9	6.74×10^7	61.6	8.54×10^6	4.63×10^6	0.019	55.2
Grid	1.72×10^9	2.57×10^7	65.1	2.83×10^6	1.31×10^6	0.020	77.5
Diamond	1.07×10^9	1.01×10^6	54.6	1.61×10^5	1.15×10^5	0.112	38.8
Hexagon	1.37×10^9	8.56×10^6	67.7	8.43×10^5	3.46×10^5	0.100	59.3
Voronoi	1.23×10^9	1.34×10^6	61.0	1.73×10^5	9.58×10^4	0.110	54.2
I-DFN	1.48×10^9	8.03×10^5	52.6	1.36×10^5	1.04×10^5	0.100	38.0
N-DFN	2.68×10^9	2.02×10^6	57.5	2.94×10^5	1.87×10^5	0.075	53.3

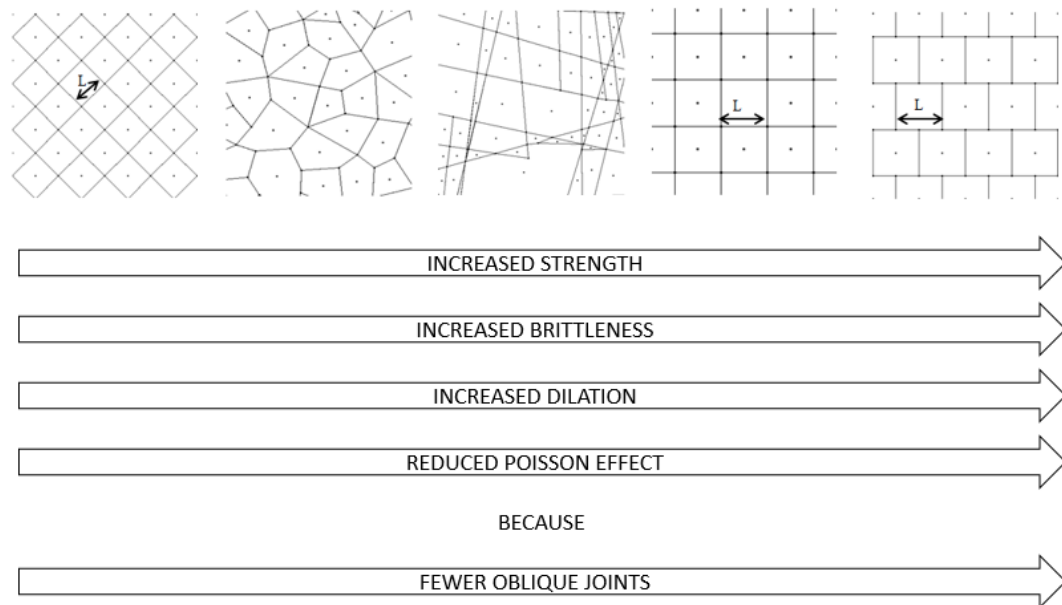


Figure 4.8 – Key effects of joint orientation on mechanical properties derived via axisymmetric compression testing.

4.3.1.1 Effects of Joint Pattern on Strength

Figures 4.9 and 4.10 show the stress/strain relationships for joint patterns with high and low compressive strength. Note the considerable difference in compressive strength between the two figures. The majority of the patterns are seen to behave in the expected manner for a brittle material such as rock under low confining pressure: Initial elastic behaviour at low strain is followed by sudden brittle failure and a considerable reduction in stress. In some models however, strain continues to accumulate after failure under a reduced value of stiffness to give an overall strain softening behaviour.

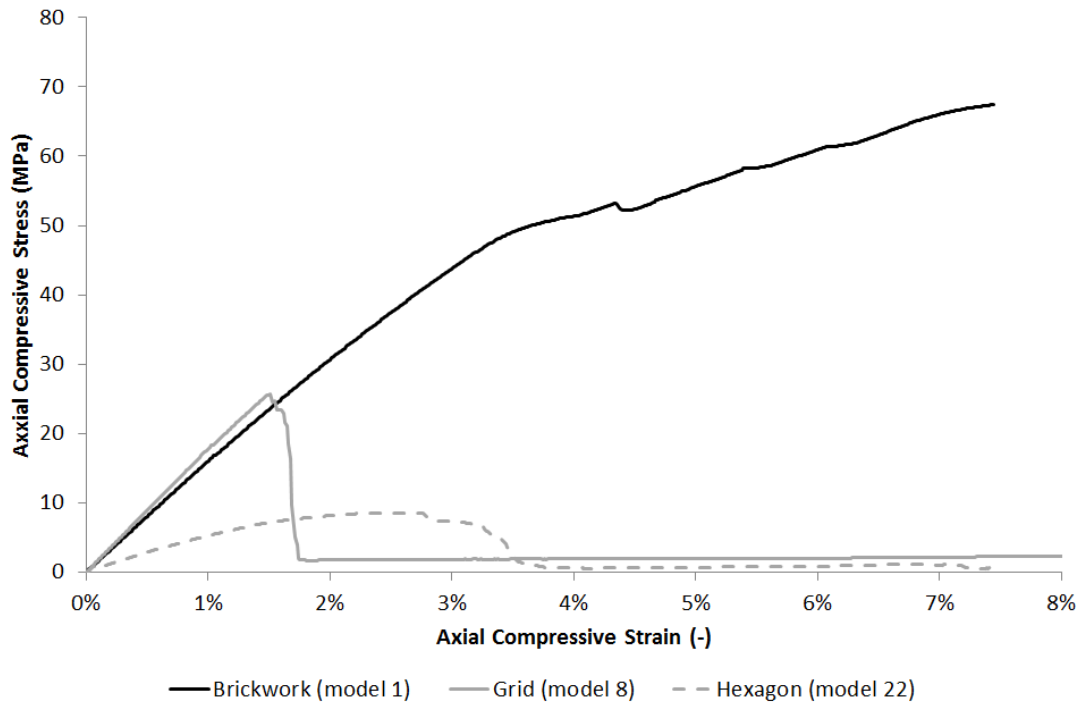


Figure 4.9 – Stress/strain relationships seen under axisymmetric testing for patterns with high yield strength.

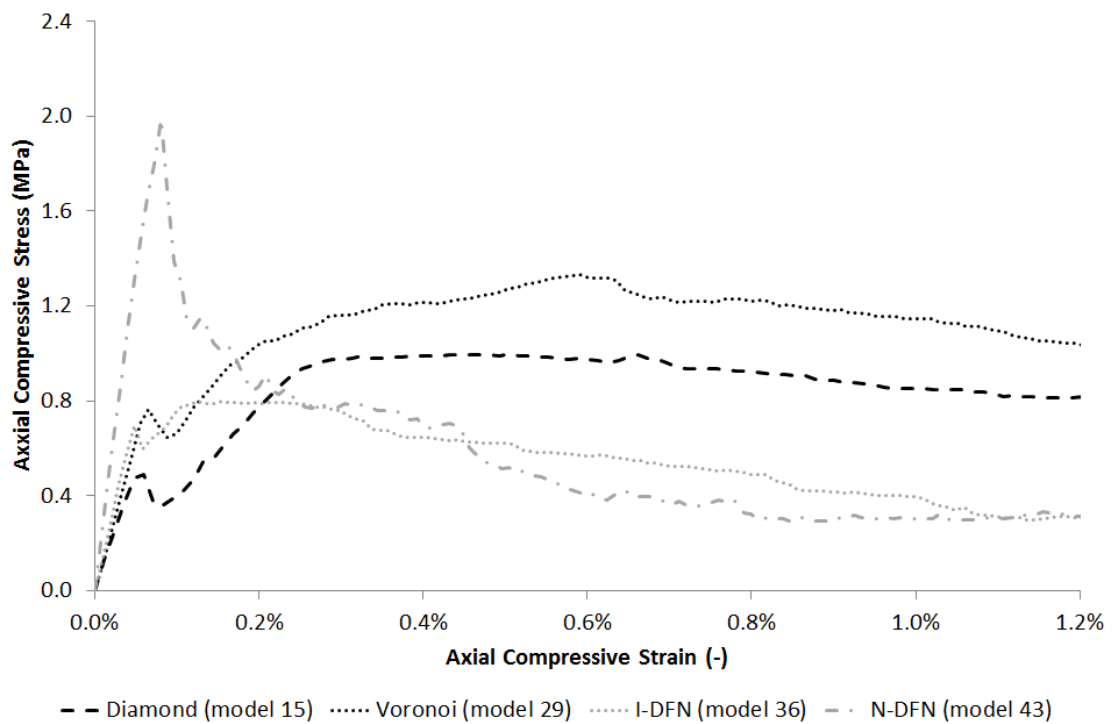


Figure 4.10 – Stress/strain relationships seen under axisymmetric testing for patterns with low yield strength.

A strong correlation can be seen between yield strength and joint angle. Patterns consisting solely of purely horizontal and vertical joints (i.e. the brickwork and grid models) have considerably higher yield strengths than all other patterns. The hexagon pattern, in which every third joint is vertical, is also seen to be notably stronger than the remaining patterns. Of the remaining geometries, the N-DFN pattern (containing predominantly perpendicular joints) is seen to be the strongest. It is therefore seen that the presence of normally oriented joints (i.e. those at 0° and 90° angles to the applied force) considerably strengthens the rock mass, for the following reason:

In all tests, strain is applied in the vertical direction. In the majority of cases failure occurs by separation along vertical or obliquely angled joints, as seen in Figure 4.11. Given that all joints have identical material properties, compressive strength must be a function of joint orientation. It is thought that the principal mechanism behind this effect is that of strain transfer from the vertical to the horizontal direction.

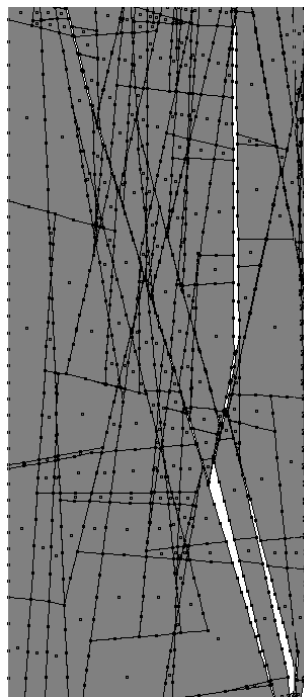


Figure 4.11 – Failure state of an axisymmetric model using the N-DFN joint pattern.

Consider a single joint, at an angle ϕ to the horizontal. This joint is part of a rock mass subjected to an axially applied strain ε_a . It can be shown that the total displacement of this joint in the horizontal (x) and vertical (y) directions are given by Equations 4.2 and 4.3 respectively. The full derivation of these equations is given in Appendix B.1.

$$u_x = \frac{E\varepsilon_a A}{2} \left(\frac{1}{k_s} - \frac{1}{k_n} \right) \sin(2\phi) \quad (4.2)$$

$$u_y = E\varepsilon_a A \left(\frac{\cos^2(\phi)}{k_n} + \frac{\sin^2(\phi)}{k_s} \right) \quad (4.3)$$

Where A is the surface area of the joint.

The $\sin(2\phi)$ term in Equation 4.2 predicts a maximum horizontal displacement when joint angle $\phi = 45^\circ$, and zero horizontal displacement when $\phi = 0$ or 90° . Given that the majority of models fail by horizontal movement, this explains why patterns containing normally oriented joints tend to be stronger than those with many oblique joints. This suggests that the diamond and I-DFN patterns should be the weakest geometries and the grid/brickwork patterns should be strongest, agreeing with the results seen in Figures 4.9 and 4.10. Given the difference between the grid and brickwork results (which have identical joint orientations), some other factor must also control failure however.

4.3.1.2 Effects of Joint Pattern on Stiffness

Rock mass Young's modulus is seen to vary considerably less with joint orientation than rock mass strength, suggesting that the fracture pattern has a minor effect on material stiffness. Definite trends can be observed however, as square based patterns tend to have the highest stiffnesses, while those with many oblique joints are softer. It is of note that the N-DFN pattern has a substantially higher stiffness than all other patterns, including the grid and brickwork geometries. Given that this pattern contains fewer normally orientated joints than these models, some other effect must be influencing stiffness. Block interlocking may be a factor, as the N-DFN pattern produces a number of points at which this may occur. Further investigation is thus recommended to determine the cause of the trend in rock mass Young's modulus.

4.3.1.3 Effects of Joint Pattern on Failure Criteria

Figures 4.12 and 4.13 show the relationship between yield strength and confining pressure for each joint pattern. These relationships are used to examine the effects of geometry on friction angle, cohesion and maximum tensile strength of the rock mass. It is of note that the I-DFN and N-DFN curves show a more variable gradient than the other patterns. This is simply due to the stochastic nature of these patterns increasing the amount of uncertainty in model results. Interesting behaviour is also seen with the grid pattern, as an apparent discontinuity in strength occurs at low confining pressures. As with unconfined failure behaviour, it is interesting to note that this is not observed with the brickwork pattern.

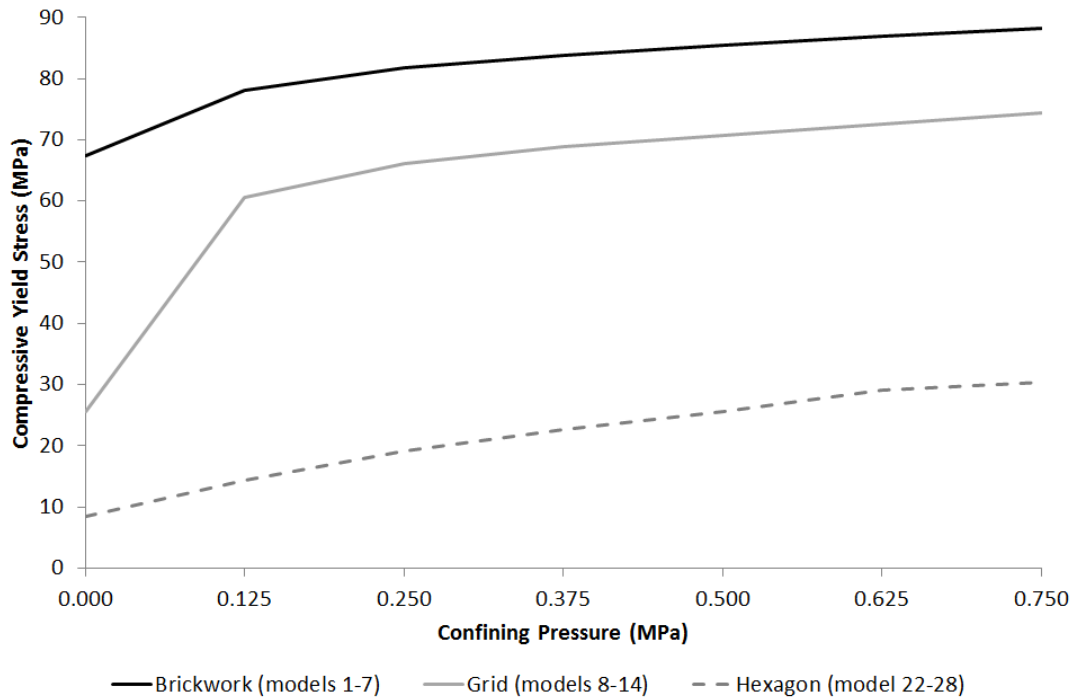


Figure 4.12 – Compressive yield stress as a function of confining pressure under axisymmetric testing for patterns with high yield strength.

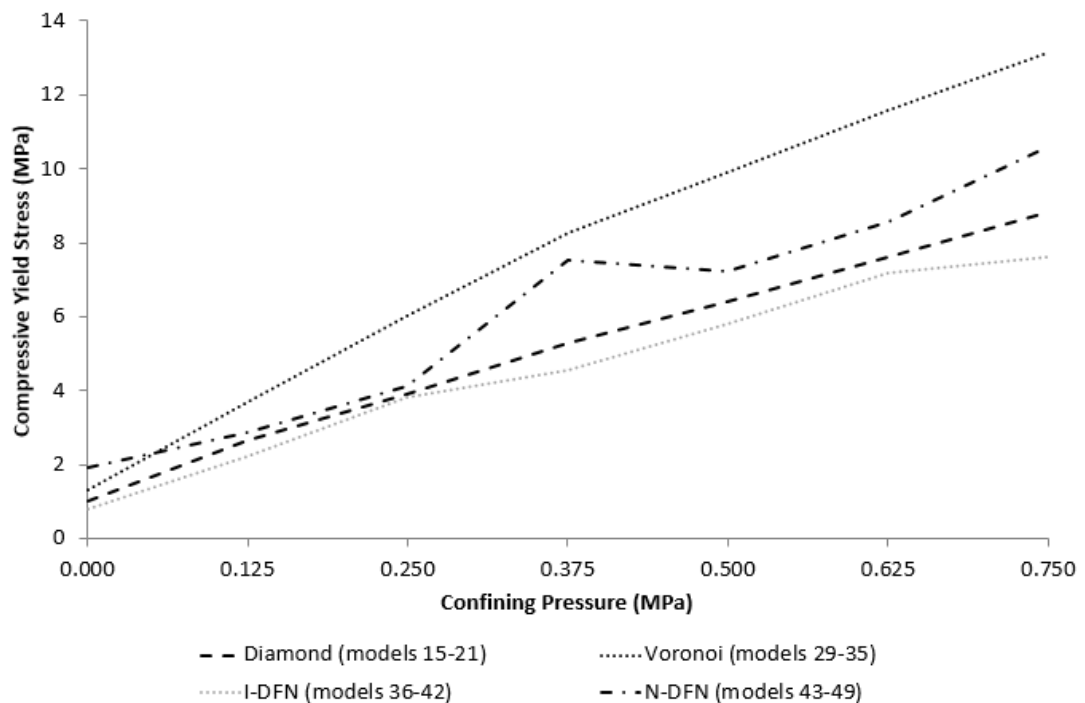


Figure 4.13 – Compressive yield stress as a function of confining pressure under axisymmetric testing for patterns with low yield strength.

Across all geometries, rock mass friction angle is seen to be much greater than that given by either the intact rocks or joints (as given in Table 4.1). Values given for the rock masses tend to be of an order similar to the sum of the rock and joint values (57.8°), suggesting that the frictional resistance of the rock mass may be found through some additive function based on these component values.

Trends in rock mass friction angle are harder to define than those for other material parameters. As with unconfined compressive strength, patterns consisting of mainly horizontal and vertical joints tend to have higher values of friction angle than those containing many oblique joints. It is of note however that the hexagonal pattern shows the highest value of friction angle, despite only one in three joints meeting this criterion. This observation suggests that the presence of vertical joints may be the deciding factor in rock mass friction. This may be explained by considering how confining pressure relates to the geometry of the rock mass:

In the biaxial tests, confining pressure is applied in the horizontal direction. As such, the force is applied most effectively against vertical joints. Because this force acts against the failure of the rock mass, vertical joints effectively contribute the most to the strengthening effect of confining pressure. As friction angle relates the yield strength of a material to an applied confining stress, vertical joints are therefore seen to give the greatest increase in rock mass friction angles.

Cohesion refers to the yield strength of a material under unconfined conditions. As mentioned in Section 4.3.1.1, it is the yield strength of the normally oriented joints that gives the largest contribution to rock mass compressive strength. As such, discussions of the effect of joint pattern on cohesion are identical to those for unconfined compressive strength. Given that the maximum tensile strength σ_T is found as a function of friction angle and cohesion, discussions of the effects of geometry on this property are also covered in this section.

4.3.1.4. Effects of Joint Pattern on Lateral Expansion

The lateral expansion behaviour of a material under compression depends on the values of material Poisson's ratio and dilation angle. These properties predict the extents of lateral expansion in the elastic and plastic regimes respectively. Figures 4.14 and 4.15 plot the volumetric/axial strain relationships for the patterns showing high and low extents of peak strain. As with other properties, square based geometries are seen to give extremes of expansion behaviour.

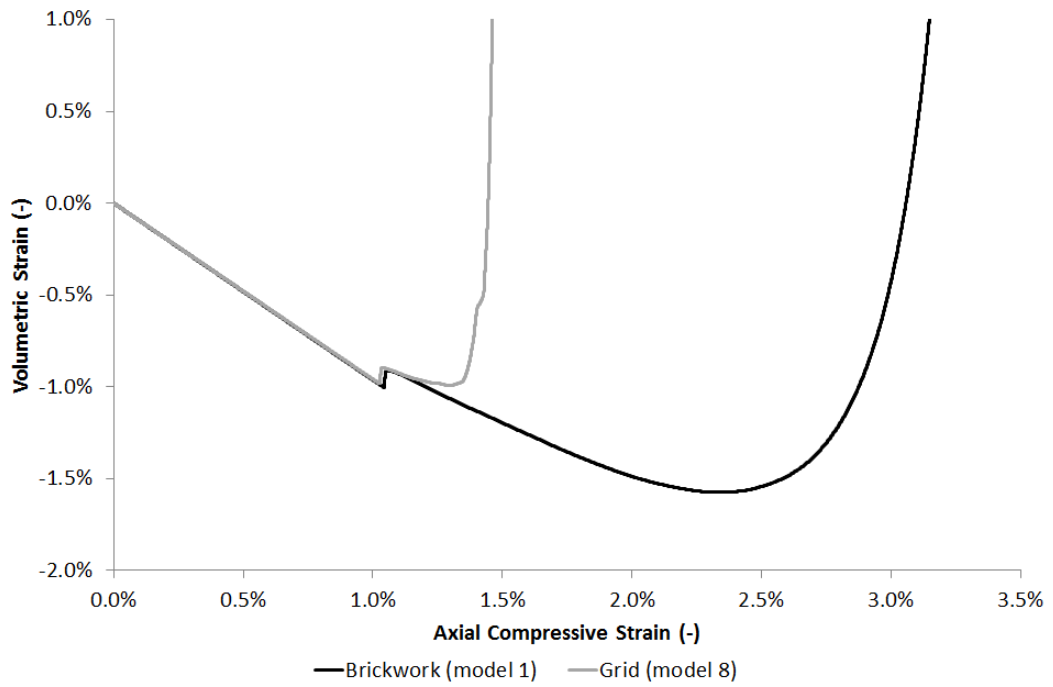


Figure 4.14 – Volumetric/axial strain relationship under axisymmetric testing for patterns showing high axial yield strains.

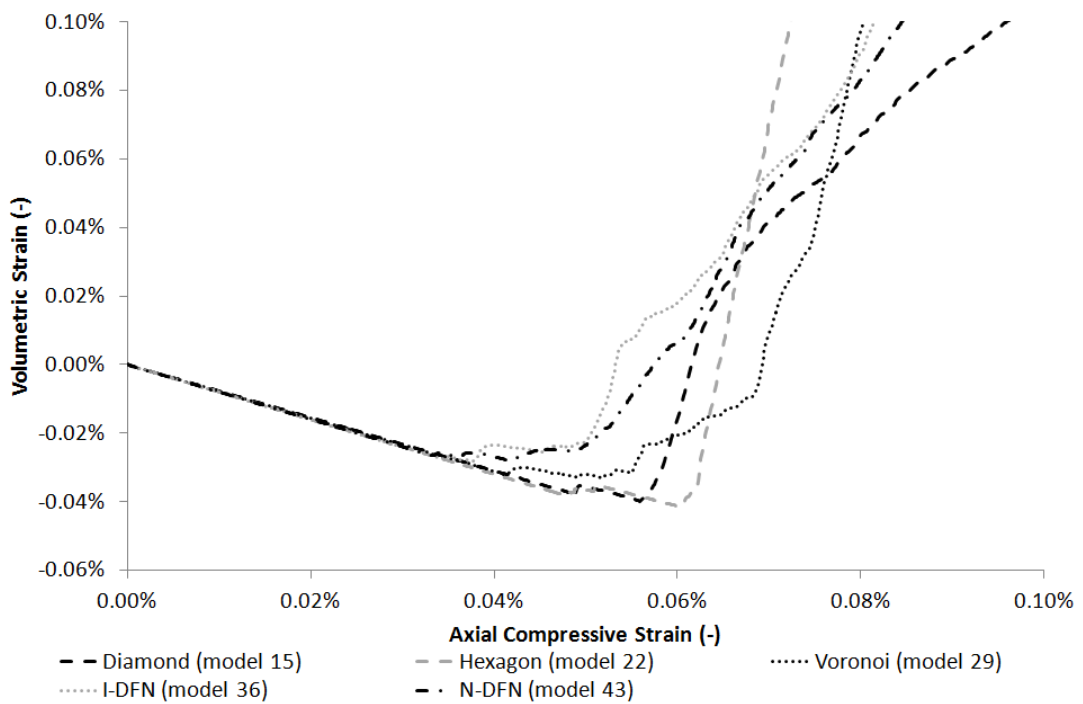


Figure 4.15 - Volumetric/axial strain relationship under axisymmetric testing for patterns showing high axial yield strains.

Poisson's ratio represents the amount of lateral strain observed per unit elastic axial strain, as shown in Equation 4.4:

$$\gamma = -\frac{\delta \varepsilon_L}{\delta \varepsilon_A} \quad (4.4)$$

In all of the rock masses tested, the measured Poisson's ratio is considerably lower than that of the intact rock elements. This can be explained by considering the axial strain of the entire rock mass compared with that of the intact blocks. For a rock mass, the total axial strain is found from the contributions of blocks and joints, as shown in Equation 4.5. Note that this assumes joints have negligible thickness.

$$\varepsilon_{a,tot} = \frac{1}{\sum_B H_B} [\sum_B (H_B \varepsilon_{a,B}) + \sum_J U_{a,J}] \quad (4.5)$$

Where:

H Height (m)

U Displacement (m)

ε Strain (-)

Subscripts:

B = Blocks

J = Joints

a = Axial

In effect, Equation 4.5 states that the total strain on the rock mass $\varepsilon_{a,tot}$, is greater than the sum of the strains on the intact blocks. This difference becomes greater as the degree of jointing increases. This increase in the value of ε_a gives a corresponding decrease in the value of γ (as calculated by Equation 4.4), compared with that for the intact rocks. In essence, much of the axial strain applied to the rock mass is taken up by the joints as opposed to the rocks. As such, the Poisson's ratio of any given rock mass will always be smaller than that of its constituent particles. This is true for real rock masses as well as those simulated in DEM (Hoek, 2001).

While all geometries show low values of Poisson's ratio, the grid and brickwork patterns are seen to be particularly incompressible. This can be explained by Equation 4.2, which suggests that models containing purely horizontal and vertical joints would not show elastic horizontal expansion. The expansion that is seen in these models is primarily caused by the Poisson effect of the blocks themselves. The N-DFN pattern shows the lowest Poisson's ratio of the remaining geometries. This is expected given the prevalence of horizontal and vertical joints in this pattern. The diamond pattern, containing purely oblique joints, shows the highest value. With the exception of the grid and brickwork geometries, Poisson's ratio was similar across all geometries. This suggests that joint orientation only has an effect on this value up to a certain point, after which other effects dominate.

Rock mass dilation refers to the increase in volume of the rock mass under plastic strain. In all of the models tested, dilation is observed in the sudden transition from volumetric contraction to expansion at the point of shear yielding. For all joint patterns, dilation angle is seen to be much greater than that of the individual joints, as given in Table 4.1. Measured values of dilation angle are also seen to be greatest for those patterns containing few oblique joints. The high levels of dilation in such models are caused by the complete separation of the outermost rock blocks from the main rock mass. These blocks tend to have a horizontal velocity after failure, such that their displacement from the rock mass increases over time. The motion of these blocks quickly comes to dominate the dilation process, contributing a much greater volume increase than simple shear dilation along joints. A more precise understanding of rock mass dilation is difficult to achieve due to difficulties in accurately measuring volumetric expansion using only a small number of displacement measuring points.

4.3.2 Plane Strain Results

4.3.2.1 Comparison of Axisymmetric and Plane Strain Results

Models 50 through 56 repeated the unconfined compression tests of various joint patterns using a plane strain geometry. The plane strain assumption was chosen as it is required for the UCG model, while the axisymmetric model is a more realistic representation of an actual lab scale test. Stress/strain and volumetric/axial strain behaviours were qualitatively similar to those seen under axisymmetric compression, however a number of quantitative differences are observed. Table 4.6 lists the derived material properties for the joint patterns tested.

Table 4.6 - Derived material properties from plane strain compression testing for models with varying joint patterns.

Geometry	E (Pa)	σ_c (Pa)	γ (-)	ψ (°)
Brickwork	6.69×10^8	Not Reached	0.010	Not Reached
Square	8.33×10^8	1.77×10^7	0.012	67.6
Diamond	4.65×10^8	9.99×10^5	0.254	3.23
Hexagon	6.57×10^8	1.08×10^7	0.246	4.58
Voronoi	6.72×10^8	3.53×10^6	0.258	12.7
I-DFN	5.91×10^8	8.85×10^5	0.253	4.99
N-DFN	9.06×10^8	3.14×10^6	0.114	9.24

While yield strength appears to be unaffected by the method of compression, rock mass stiffness is observed to be approximately half as large under plane strain testing for all patterns. Conversely, Poisson's ratio is twice as large under plane strain testing, though the square based patterns still show incompressible behaviour. The difference seen with Poisson's ratio can be explained with reference to the plane strain assumption. In an axisymmetric model, the lateral expansion of the rock mass can occur in both dimensions orthogonal to the vertical axis. In the plane strain model, it is assumed that no motion occurs into the plane of the page. As such, in order to maintain the same degree of volumetric expansion, Poisson's ratio must be twice as large in the plane strain model as in the axisymmetric model. The reduction in Young's modulus is believed to be caused by a similar effect, as the lateral forces resisting axial strain in the rock mass would only be half as strong for similar reasons. Although the plane strain assumption is less, it is sufficient for use in the UCG model, and therefore is acceptable in tests related to this model. Given the differences in results, it is recommended that the mechanical properties of the UCG model should be based on axisymmetric results to avoid a doubling of the plane strain effect.

Dilation angle is also seen to be considerably smaller under plane strain testing than under axisymmetric testing, though square based patterns still show extreme values. Dilation angles measured under plane strain compression were seen to be of an order similar to that given for the joints. This suggests that large scale horizontal block motion is rare under plane strain conditions, with rock mass volumetric expansion being driven principally by the dilation of the joints. In many cases it was seen that plane strain models did not undergo the same extent of horizontal separation as the comparative axisymmetric model, confirming this suggestion.

Finally, it is of note that the brickwork pattern never reached failure under plane strain testing. This model encountered overlap errors after approximately 9.5% axial strain. Increasing the value of overlap tolerance was not seen to solve this issue. As such, distinct values for compressive strength and dilation angle cannot be derived for this pattern. Due to their simplicity, square based joint patterns are often used in discrete element models (Coulthard and Dutton, 1988; Keilich *et al*, 2006). Given the results above however, it is suggested that such patterns should not be used within regions of high stress, as they are incapable of fully realising plastic behaviours, calling the results of many previous models into question.

Despite the above limitations, the general similarity between plane strain and axisymmetric results suggests that the methodology of incorporating material properties derived from axisymmetric testing into plane strain geomechanical models is justified. The appropriate selection of material properties for the UCG model is discussed further in Section 4.6.

4.3.2.2 Effects of Block Size on Mechanical Behaviour

In addition to shape, the size and aspect ratio of distinct element blocks are shown to have a strong effect on the mechanical behaviour of the rock mass. Models 57 through 60 investigated these effects by varying the densities of nominally horizontal and vertical joints in the N-DFN pattern under plane strain compression testing. This geometry was chosen as it gave good results in previous tests and has geometric properties which are easy to adjust.

In the case of the small and large block models, joint density was doubled or halved in order to produce blocks with average areas equal to half or twice that of the base case. In the case of the tall and wide models, one density was increased while the other was decreased by a factor of $\sqrt{2}$. This produces blocks with an average area equal to that of the base case models, but in which the ratio of block height to block width is increased or decreased by a factor of two. Table 4.7 lists the derived material properties for these rock masses.

Table 4.7 - Derived material properties from plane strain compression testing for models with varying block size and aspect ratio

Geometry	E (Pa)	σ_c (Pa)	γ (-)	ψ (°)
Base Case	9.06×10^8	3.14×10^6	0.114	9.24
Small Blocks	6.73×10^8	1.78×10^6	0.113	9.07
Large Blocks	1.10×10^9	4.47×10^6	0.144	9.94
Tall Blocks	9.77×10^8	1.99×10^6	0.172	6.83
Wide Blocks	5.63×10^8	5.26×10^6	0.194	29.85

Block size and aspect ratio are seen to affect rock mass strength and stiffness in predictable ways. Increased block size increases both Young's modulus and compressive strength. This is to be expected, as larger blocks reduce the total number of joints in the rock mass. As such, behaviour depends more on the blocks (strong, stiff) than the joints (weak, soft).

Increasing block width increases rock mass strength but decreases stiffness. The increase in strength can be explained by Equation 4.2. As blocks get shorter and wider, the number of horizontal joints (under normal stress) increases while the number of vertical joints (under shear stress) decreases, as shown in Figure 4.16. Due to the ratio of joint normal to shear strength (10:1), the increased number of horizontal joints increases the overall strength of the rock mass.

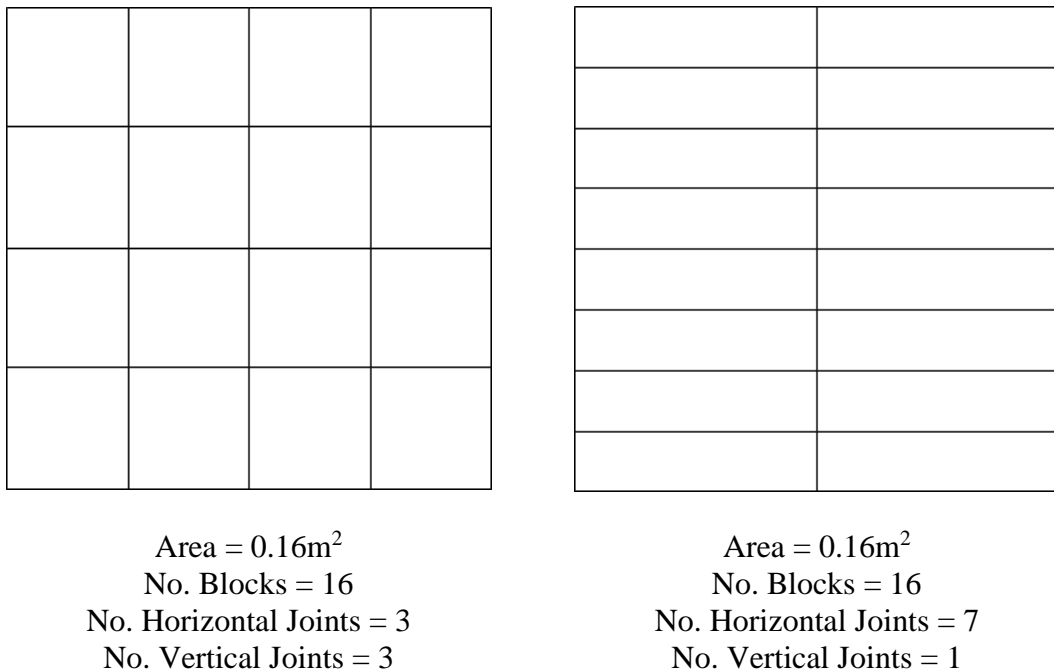


Figure 4.16 – Effect of varying block aspect ratio on the numbers of horizontal and vertical joints in the model. Greater numbers of vertical joints increase the horizontal motion of the rock mass, promoting failure and thus reducing rock mass strength.

The decrease in stiffness with block width is more difficult to understand, but is predominantly caused by the increased number of horizontal joints causing the rock mass to depend more on joint behaviour than block behaviour. Although Equation 4.3 suggests the shearing of vertical joints contributes the most to vertical motion, shearing may not yet have begun at the low values of strain under which Young's modulus is derived. In addition, the reduced potential for block interlocking with short wide blocks also contributes to the reduction in stiffness.

Table 4.7 suggests that rock mass Poisson's ratio is not greatly affected by block size. Block aspect ratio is seen to alter the recorded values, but the lack of a clear trend suggests these differences are simply due to random variations. These results suggest that the Poisson effect within a rock mass depends entirely on the orientation of the joints (as in Equation 4.2) and is not affected by their number or length. Dilation angle appears to be very weakly related to block size, however there is a strong relationship between block aspect ratio and rock mass dilation angle. Short, wide blocks are seen to give a much greater extent of dilation than tall, thin blocks. This effect can be explained with reference to the conservation of block area. Assuming equal values of Poisson's ratio, short, wide blocks undergo much greater lateral expansion than tall, thin blocks when both are compressed by the same height increment. As such, wide blocks contribute more to the post-failure expansion of the rock mass than tall blocks, therefore increasing rock mass dilation angle.

4.3.2.3 Effects of Joint Material Properties on Mechanical Behaviour

Models 61 through 68 investigated the effects of joint material properties on the mechanical response of the rock mass. The influence of joint friction angle, dilation angle and normal and shear stiffnesses were tested under plane strain compression of the N-DFN geometry. Table 4.8 lists the mechanical properties derived from these models.

Table 4.8 - Derived material properties from plane strain compression testing for models with varied joint mechanical properties.

Model	E (Pa)	σ_c (Pa)	γ (-)	ψ (°)
Base Case	9.06×10^8	3.14×10^6	0.114	9.24
Low Friction	8.08×10^8	1.23×10^6	0.127	18.08
High Friction	8.46×10^8	4.26×10^6	0.151	11.42
Low Dilation	8.33×10^8	2.70×10^6	0.138	6.62
High Dilation	8.13×10^8	2.24×10^6	0.127	12.31
Low Normal Stiffness	1.38×10^8	1.07×10^6	0.021	16.51
High Normal Stiffness	1.99×10^9	2.78×10^6	0.380*	6.94
Low Shear Stiffness	4.99×10^8	1.31×10^6	0.346	8.94
High Shear Stiffness	9.88×10^8	2.96×10^6	0.028	13.13

*Due to this model reaching the volumetric turning point at very low axial strain, Poisson's ratio has to be measured at lower strains than in other models.

These results suggest that joint friction and dilation angles have little effect on rock mass behaviour, with two exceptions: Firstly, joint friction angle is correlated with rock mass compressive strength. As mentioned previously, friction angle relates to the shear yield strength of a joint under a given normal stress. Given that many joints within the model fail in shear, this explains the observed correlation. Second, there is a correlation between the dilation angle of the joints and the rock mass. This is to be expected, as the dilation of single joints promotes that of the rock mass.

Unlike joint friction and dilation angles, joint stiffnesses have a considerable effect on rock mass behaviour. Both normal and shear stiffnesses have a strong positive effect on rock mass Young's modulus. This is explained with reference to Equation 4.3: As both stiffnesses are denominators in the calculation of vertical displacement, increases in stiffness reduce axial displacement and hence increase Young's modulus. The relative importance of the two stiffnesses depends on the prevalence of joints at near horizontal and near vertical angles, based on the \cos^2 and \sin^2 terms in the equation.

Both stiffnesses are also seen to have a positive effect on rock mass compressive strength, though it is of note that the strongest rock mass appears to be that given in the base case model. Given the inherent randomness of the N-DFN geometry, this discrepancy is seen to be predominantly due to random variations in the deformation of the joint pattern. The overall effect can be explained with reference to Equation 4.2. Increased stiffnesses reduce the extent of horizontal motion, in turn leading to a reduction in joint separation and an increased material strength. As with Young's modulus, the relative importance of the stiffness depends on the prevalence of near horizontal (failing in shear) and near vertical (failing in tension) joints.

Joint normal and shear stiffnesses appear to have opposing effects on the lateral expansion behaviour of rock masses. Increasing joint normal stiffness causes an increase in rock mass Poisson's ratio and a decrease in rock mass dilation angle. The reverse is seen with joint shear stiffness. The influence of joint stiffnesses on the Poisson effect is explained by Equation 4.2: An increase in k_s causes a decrease in the reciprocal term, which in turn causes an decrease in the total elastic lateral expansion and hence Poisson's ratio. Conversely, the negative sign in front of the normal stiffness term causes the opposite effect, as observed.

Effects of stiffness on dilation appear to oppose those of the Poisson effect. This opposition can also be observed in the results based on joint pattern, as given in Tables 4.4 and 4.5. This observation suggests some kind of causal link between the mechanisms of elastic and plastic lateral expansion, in which reductions in expansion during the elastic phase lead to increased expansion after failure. It is believed that this effect is predominantly caused by the storage of strain energy in the rock mass. Models which undergo less elastic expansion are seen to reach higher levels of stress at failure. This stress then manifests as a greater extent of lateral motion in the post-failure stage of compression, leading to an increase in rock mass dilation.

4.4 MODEL VALIDATION

The observations and trends discussed in the previous sections relate only to rock masses simulated with UDEC (i.e. not real rock masses). In order to obtain confidence in this methodology when related to real rock material, validation against real world data and other techniques must be performed. Results of similar compression studies using different numerical methods agree well with both reality and the results given in this work (Rong *et al*, 2013; Tan *et al*, 2015). Given the highly variable behaviour of geologic materials under different conditions however; it is essential that any geotechnical model is proved to be internally valid before its results can be trusted. In order to ensure the validity of this model, a number of comparative tests have been performed.

4.4.1 Comparison with Geological Strength Index

Firstly, material properties derived by the axisymmetric simulations are compared with those obtained by the empirical geological strength index (GSI). Rock mass Young's modulus, friction angle and cohesion are calculated according to the method of Hoek *et al* (2002), using GSI parameters given in Marinos *et al* (2007). Results of the comparison are given in Table 4.9.

Table 4.9 – Comparison of axisymmetric results with empirical predictions from Geological Strength index.

Geometry	E (Pa)	θ (°)	C (Pa)
Brickwork	1.58×10^9	61.6	8.54×10^6
Grid	1.72×10^9	65.1	2.83×10^6
Diamond	1.07×10^9	54.6	1.61×10^5
Hexagon	1.37×10^9	67.7	8.43×10^5
Voronoi	1.23×10^9	61.0	1.73×10^5
I-DFN	1.48×10^9	52.6	1.36×10^5
N-DFN	2.75×10^9	57.5	2.78×10^5
GSI	1.40×10^9	41.0	6.01×10^6

Good agreement is seen between the GSI predictions and model results for rock mass Young's modulus and cohesion, especially with the square based patterns. This is to be expected, given that many real rock masses contain predominantly horizontal joints. As such, the brickwork pattern is believed to give the most realistic material properties for a rock mass, although the use of the pattern itself in models under high stress is not recommended.

It is of note that a considerable difference is seen between UDEC and GSI in terms of friction angle. This difference may be caused by the kinematic constraints of the axisymmetric model compared with a real (i.e. 3D) rock mass. As the UDEC model assumes identical behaviour in the two lateral dimensions, the effects of planes of weakness in certain directions may be ignored. In reality, these will weaken the rock mass somewhat at high confining pressures leading to a reduced friction angle compared with that predicted by UDEC. Considering the inaccuracies of the geological strength index and the inherent variability of real rock masses however, model results are considered to be accurate enough for all practical purposes.

4.4.2 Comparison with Experiment

Two jointless models (69 and 70) have been tested and compared with experimental results from a triaxial test performed on Stanton Moor sandstone at the Nottingham Centre for Geomechanics. Stanton Moor sandstone is a fine to medium grained carboniferous millstone grit (Building Research Establishment, 2000) typical to the overburden above coal seams in the north of England. The results of this comparison are shown in Figure 4.17.

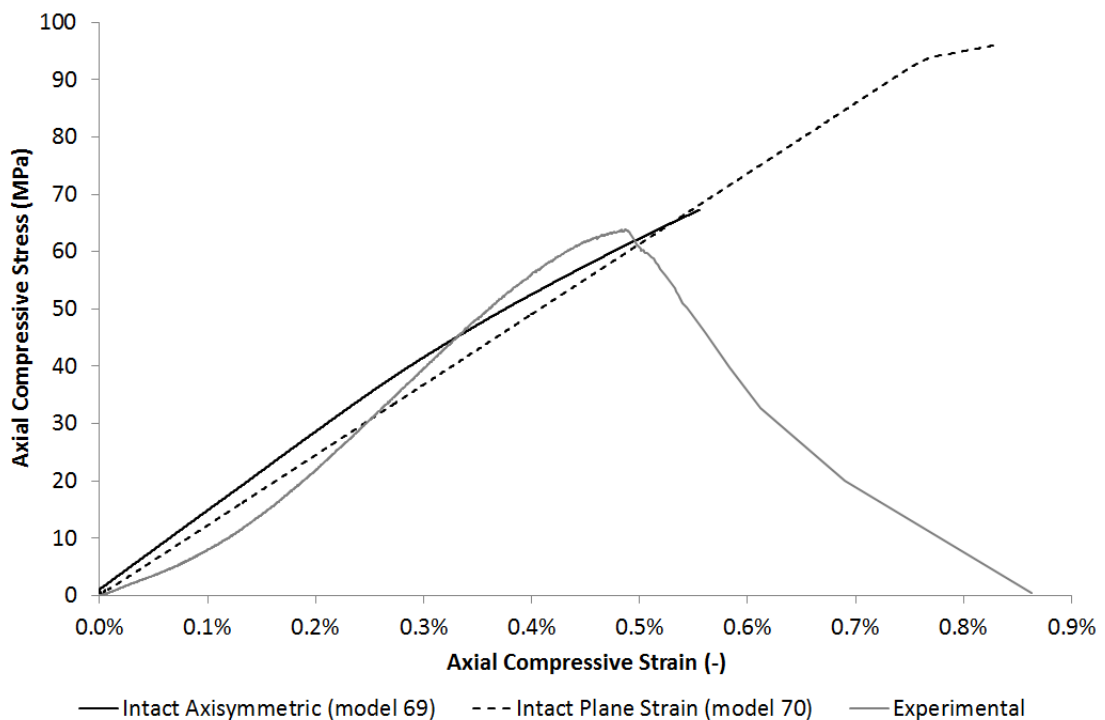


Figure 4.17 – Comparison of stress/strain response between models and experiment.

It can be seen that the axisymmetric model agrees well with experiment in terms of failure prediction. Errors of 5.4% and 14.0% are seen for failure stress and strain respectively, well within the expected error margins for a geologic material (Cai, 2011). The axisymmetric model is seen to somewhat overpredict stiffness however. It is believed that the lack of resolution of the rock microstructure (cracks, grain boundaries etc.) is the main reason for this difference. Given the high variability of real rocks however, the inaccuracies of the model are considered minor.

The results of the intact plane strain model show considerably less agreement with experiment. Although model stiffness is reasonable in comparison with the axisymmetric case, the plane strain model greatly overpredicts the failure strength of the rock mass. Given the considerable differences in geometry however, close agreement between the plane strain model and reality was not expected.

4.4.3 Repeatability Testing

In order to better understand the variability of the model, a number of repeats of the N-DFN models have been performed. Models 71-73 repeated the axisymmetric test (model 43) while models 74-76 repeated the plane strain test (model 56). Tables 4.10 and 4.11 show the variability in derived material parameters for each of these models.

Table 4.10 – Derived material properties and variability statistics for the axisymmetric repeatability study.

Model	E (Pa)	σ_c (Pa)	γ (-)	ψ (°)
Base case (model 43)	2.68×10^9	2.02×10^6	0.075	53.3
Repeat 1 (model 71)	2.74×10^9	2.03×10^6	0.093	60.4
Repeat 2 (model 72)	2.45×10^9	1.88×10^6	0.078	56.4
Repeat 3 (model 73)	2.59×10^9	1.87×10^6	0.089	36.6
Average	2.59×10^9	1.95×10^6	0.084	51.7
Standard Deviation	1.47×10^8	8.68×10^4	0.009	10.5
COV	5.7%	4.5%	10.7%	20.3%

Table 4.11 – Derived material properties and variability statistics for the plane strain repeatability study.

Model	E (Pa)	σ_c (Pa)	γ (-)	ψ (°)
Base case (model 56)	9.06×10^8	3.14×10^6	0.114	9.24
Repeat 1 (model 74)	8.32×10^8	2.43×10^6	0.143	13.57
Repeat 2 (model 75)	8.77×10^8	3.66×10^6	0.139	13.98
Repeat 3 (model 76)	7.88×10^8	3.34×10^6	0.129	11.58
Average	8.51×10^8	3.14×10^6	0.131	12.09
Standard Deviation	5.17×10^7	5.21×10^5	0.013	2.17
COV	6.1%	16.6%	9.9%	18.0%

In both cases it is seen that the variability in results is reasonably small, and generally within the range of variation expected for a geological material (Cai, 2011). The small number of repeats performed does reduce the reliability of these statistics however. As such, it is suggested that the results of further modelling work based on this pattern should be repeated a number of times to ensure reliable reporting.

Variations in Young's modulus and Poisson's ratio are seen to be reasonably small and unrelated to the geometric assumption used. Given that both of these properties are determined at low values of axial strain, this suggests that variations in the N-DFN geometry have little effect on the elastic behaviour of the material. Dilation angle is also seen to have a variability unrelated to the geometric assumption used, however the magnitude of this variability is considerably larger.

Variability in dilation is partly due to differences in individual DFN patterns causing more or less horizontal motion at key locations in the rock mass. As mentioned in Section 4.3.1.4, accurate derivation of dilation angle is difficult using only a small number of displacement measuring points. This difficulty exacerbates the measured variability of dilation angle as the measurement points may or may not be nearest to the blocks which are undergoing the most dilation. The final parameter considered is the rock mass compressive strength. This is seen to vary considerably more under plane strain testing than axisymmetric testing. It is believed that this variation may be linked to the more ductile behaviour commonly seen in plane strain models (as evidenced by an increased Poisson's ratio and reduced dilation angle), as this makes accurate determination of yield stress more difficult.

Despite the above considerations, the methodology of simulated triaxial testing to determine material properties is believed to be valid, given the inherent difficulties and variability seen with any method for the prediction of rock mass strength. The N-DFN pattern is also seen to provide a reasonable means to account for this inherent uncertainty in modelling geological materials. Considerable reductions in variability for the axisymmetric model compared with the plane strain model suggest this geometry should be used for future determinations of rock mass properties. As such, material properties derived from axisymmetric simulations will be used in all future UCG models, and the N-DFN pattern will be used within the model to incorporate a random element into the results.

4.4.4 Observations of Failure Behaviour

In addition to its use in determining material properties, simulated compression testing allows us to gain a better understanding of the failure mechanisms of granular materials. Such tests are commonly performed using particle based DEM methods (Chen *et al*, 2016; Hadda *et al*, 2015; Liu *et al*, 2015), as these are more suited to investigating fracture and failure behaviour. Comparisons of the behaviour seen between the UDEC compression models and reality can be used as a means of validating UDEC results however. Andreev (1995) states that compressive failure of rock occurs in 6 distinct phases:

1. Microscopic cracks in the rock close, giving an increase in strain at low stress.
2. Grains begin to deform elastically, giving an approximately linear stress/strain relationship.
3. Fractures begin to propagate and dilation begins to occur, causing instabilities in the stress/strain curve.
4. Fracture propagation accelerates, causing the stress/strain curve to level off.
5. Brittle failure of the rock causes a sudden decrease in stress.
6. Strain accumulates rapidly post-failure, with stress given by the residual strength of the rock.

Figure 4.18 shows the stress/strain relationship for the axisymmetric N-DFN model (model 43). The close agreement between model results and expectations provides further evidence for the validity of simulated compression testing in UDEC.

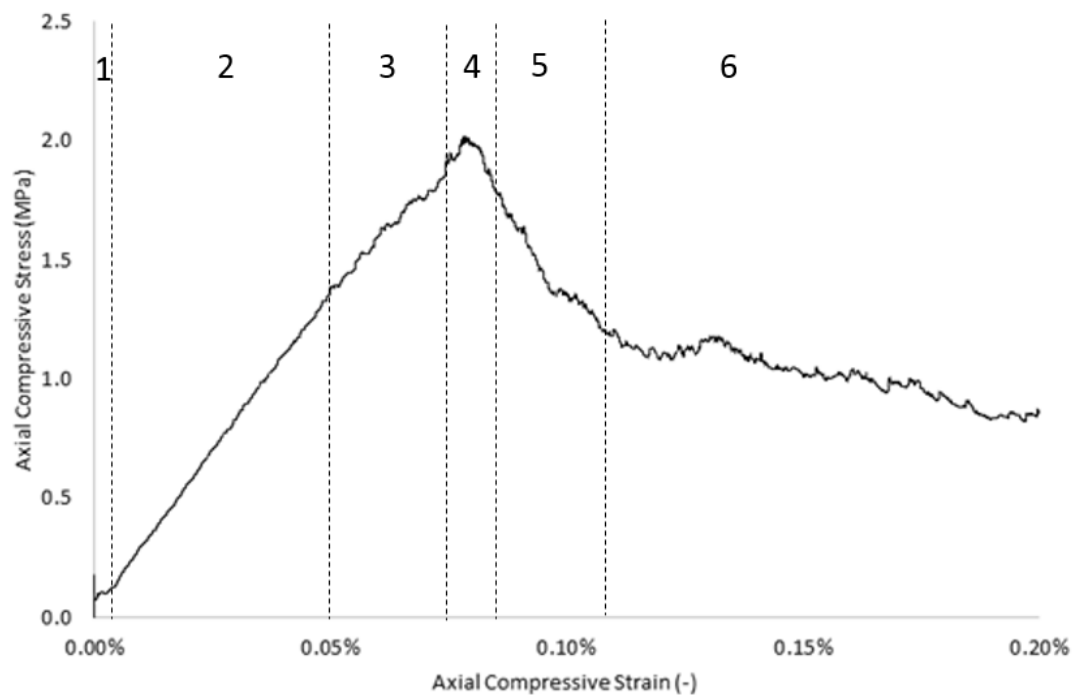


Figure 4.18 – Comparison of model results with the six stages of rock failure (Andreev, 1995).

4.5 MODEL LIMITATIONS

While the overall result of the new model methodology appears to be a success, a number of limitations must be discussed: Firstly, it is seen that the choice of assumption used to represent a 3D material in 2D space has a profound effect on material behaviour, especially with regards to plastic lateral expansion. Although the axisymmetric assumption more closely resembles reality, care should be taken applying results obtained using this method to large scale models represented by the plane strain assumption. Second, the reported results of all tests are seen to be highly sensitive to random perturbations of the model. This is especially notable with the stochastically based I-DFN and N-DFN geometries, but effects are also observed in the stress/strain response of fully deterministic patterns due to the semi-random nature of failure mechanics.

Finally, considerable uncertainty is introduced into the derived material properties by the method of their calculation from stress/strain and volumetric/axial strain graphs. The turning points and gradients of these graphs can be difficult to accurately determine, and the uncertainty this causes is often amplified by their conversion into material properties. The difficulty in calculating accurate material properties is also greatly affected by the inherent randomness of the model behaviour. These inaccuracies are similar to the variability seen in reality however, such that the simulated results are often of an accuracy comparable to that achievable by experiment.

It is important to note that errors inherent in this methodology have the potential to introduce even larger errors into the results of any model based on this work, including the UCG model detailed in the remainder of this thesis. Conversely, currently used empirical models also show very high degrees of variation and low accuracy, often due to their user based decision making requirements. In addition, real world rock masses can often vary considerably over short distances, such that accurate depictions of material properties are not possible without fully representing every individual rock within the assembly. As previously mentioned, the inaccuracies of the model are comparable to real world variability (Cai, 2011). Given these considerations, it is believed that the accuracy of these simulations are appropriate for the end use of the methodology. Some random variability in model results is desired, as this reflects the inherent variability of real rock masses. The use of the N-DFN pattern in future modes should be sufficient to achieve this degree of variability.

4.6 PARAMETER SELECTION

Results of both axisymmetric and plane strain simulations have been used to inform the selection of rock mass material properties and block geometry for use in the UCG model. This section explains and justifies the decisions made in this regard.

In order to maintain accuracy whilst limiting runtime, the UCG model geometry is broken into two distinct regions. The region near the cavity must have a high joint density and a degree of randomness to account for the largely unknown fracturing behaviour caused by the UCG process. Less resolution is needed further away from the cavity, therefore the joint pattern in this region can be simplified. Both regions should still show an appropriately brittle response and give a realistic depiction of geomechanical behaviour. For these regions the final model uses an N-DFN pattern within the highly fractured region near the cavity, while a brickwork pattern with a considerable reduction in joint density is used in the region far from the cavity.

The N-DFN pattern was chosen for four principal reasons: Firstly, the geometry is somewhat representative of real rock mass stratification. Secondly, the material behaviour of the pattern, while generally weaker than square based geometries, still gives an appropriately brittle rock mass response. Third, the stochastic nature of the N-DFN pattern allows for relatively simple fine-tuning of the random elements of rock mass behaviour. Finally, the inherent randomness of the N-DFN pattern provides a simple means to simulate the variability observed in real rock materials.

The brickwork pattern was chosen for the coarse region of the model as this geometry tends to show behaviour closest to that expected for a real rock mass. As mentioned in Section 4.3.2.1, the use of the brickwork pattern is not recommended in any regions undergoing large stresses. Given that the coarse region is a low stress area, it is believed that the use of this pattern is justified in this case.

In both regions of the model, rock mass properties were based on the axisymmetric result for the brickwork pattern. Identical properties were used in both regions to maintain the stability of the model. Axisymmetric brickwork properties were chosen as they most closely resemble the behaviour of a real rock mass. The agreement shown between the brickwork results and the predictions of the GSI method are taken as a justification for this decision. Axisymmetric results were used as these models more closely resembled a realistic test geometry. In addition, given that the UCG model uses the plane strain assumption, axisymmetric results were chosen to avoid the doubling of the weakening effect seen in Section 4.3.2.1.

The only exception to the above decision is the rock mass dilation angle. Given the extreme values reported for the axisymmetric models, a plane strain result was chosen. As both of the square based patterns showed unphysically high dilation angles, the result for the N-DFN pattern was used. This pattern was chosen as it is geometrically similar to the square based patterns but does not show an extreme result. The full set of material properties for the UCG model are given in Table 4.12.

Table 4.12 – Derived material properties to be used in the full UCG model.

ρ (kgm ⁻³)	E (Pa)	θ (°)	C (Pa)	σ_T (Pa)	γ (-)	ψ (°)
2700	1.58×10^9	61.6	8.54×10^6	4.63×10^6	0.019	9.24

4.7 CONCLUDING REMARKS

This work aimed to investigate the effect of joint patterns on rock mass material properties and develop a methodology for the selection of these properties and patterns for use in DEM models. Validation studies comparing simulation results with experiment verify the methodology, while similarities between model results and empirical correlations show that the method produces usable material parameters. Although a number of issues limit the accuracy of the methodology, this is considered reasonable in comparison with the inherent variability of rock mass properties in reality.

Model results show that the mechanical properties of a rock mass depend heavily on the ratio of fractures oriented normally, tangentially and obliquely to the direction of applied strain. The ratio of joint shear to normal stiffness also has a profound effect on behaviour which is intrinsically linked to geometric properties. Joint dilation angles are also shown to have a notable influence on the overall mechanical response of rock masses. The mechanisms behind these effects have been explored and simple relationships have been drawn which allow for the prediction of rock mass displacements based on the orientation and stiffness of the joints contained. These relationships also allow for a qualitative understanding of how these parameters control the strength, brittleness and lateral expansion behaviour of the rock mass.

In addition to the determination of material properties, this work proposes a new joint pattern based on the discrete fracture network. This geometry allows for the realistic modelling of fractured rock masses without the need for excessive numbers of fractures. The stochastic nature of the pattern allows models to be based on available statistical site data and can account for local variations across a site. The random nature of the pattern also allows for a realistic representation of the variability inherent in real rock masses. The use of both the N-DFN geometry and the new material properties should allow for greater confidence in the modelling of highly fractured rock masses where the exact pattern of fracturing is unknown. Chapter 5 shows how these principles are applied to the modelling of UCG.

It is suggested that further work in the modelling of simulated compression tests should be performed in order to improve the accuracy of the method and further prove its validity. Investigations into the effects of other properties, such as fracture cohesion, the variability of joint angles and the choice of constitutive model could provide greater insight into the behaviour of rock masses simulated using DEM. An extension of this work to cover investigations into the hydraulic behaviour of rock masses is also suggested. Finally, the application of this methodology to other rock materials (as opposed to sandstone as used in this work) could be performed in order to develop a database of reduced material properties or empirical correlations for various rock types. Such a database could be very useful for future efforts to model the behaviour of heavily jointed rock masses.

5. MODEL DEVELOPMENT

SUMMARY

This chapter discusses the development of the coupled mechanical, hydraulic and thermal aspects of the underground coal gasification (UCG) model created with the Universal Distinct Element Code (UDEC). Discussions cover the decisions made with regards to model geometry, material properties, boundary and initial conditions and the development of new functionality within UDEC for both mechanical and thermal simulations. A number of limitations of the software are presented, and methods for overcoming these are discussed. Throughout the chapter, the conflicting issues of model accuracy, stability and runtime are analysed and conclusions are drawn about how these issues should be addressed. With careful model design and the inclusion of new functionality, UDEC is shown to be more than capable of modelling the complexities of UCG's impact on the local environment.

5.1 MODEL STRUCTURE

5.1.1 Order of Operations

As mentioned in Section 3.2.1, mechanical simulations in UDEC work by finding the equilibrium state of the rock mass both before and after excavation. Ground movements are then determined as the difference in the displacements found at these states. In the UCG model, the rock mass is simulated at 3 distinct stages:

1. Before – the initial equilibrium stage, before gasification begins.
2. After – the state of the model after gasification ceases.
3. Final – the state of the model after the rock mass has cooled down and groundwater pressures have reverted to their initial values.

This formulation allows the model to simulate the environmental damage caused by the UCG operation over the full life cycle of the process, including decommissioning. Results can be analysed at each of the three stages, and comparisons drawn between any two points in time. In addition to the three calculation stages, a number of auxiliary steps are required. Figure 5.1 shows the individual steps involved in the entire model. Numbers in brackets refer to the section of the thesis in which further details on the relevant step are given.

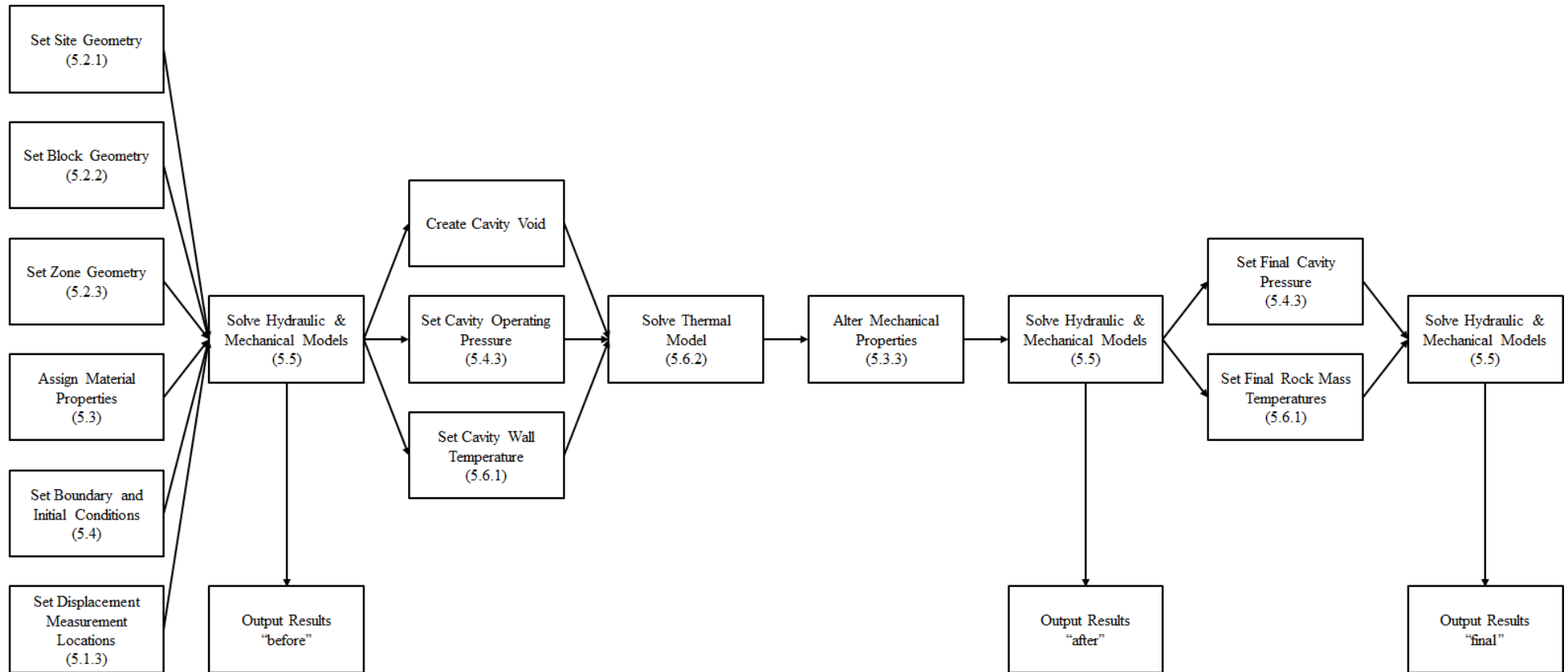


Figure 5.1 – Schematic description of the calculation steps involved in the fully coupled thermal/hydraulic/mechanical UCG model.

5.1.2 Data Requirements

In order to produce results a great deal of input data are required by the model, however the accuracy of the model is limited by uncertainties in this data. In order to minimise the risks of erroneous calculations from incorrect data, the number of user entered values has been minimised. Wherever possible, modelling parameters are derived from their relationship with other properties, rather than being entered by the operator. In other cases, constant values have been chosen to give appropriate results. For a simple, single cavity UCG model, the variables which must be entered by the user are shown in Table 5.1. The base case values were chosen based on field measurements from the Rocky Mountain 1 field trial site (Lindblom *et al*, 1990; Mason *et al*, 1987). This site was chosen as a benchmark case for the UCG model as a considerable amount of published geological and geometric data are available from this trial.

Table 5.1 – Required input variables for fully coupled UCG model.

Variable	Value (base case)
Cavity Height (m) ¹	14.2
Cavity Width (m) ¹	12.4
Cavity Depth (m) ¹	98.4
Water Table Depth (m) ²	27.6
Site Permeability (mD) ²	5.29

1 – Lindblom *et al*, 1990. 2 – Mason *et al*, 1987. Site permeability data are geometrically averaged.

5.1.3 Data Produced

The fully coupled UDEC model produces a large quantity of data at each of the three stages mentioned in Section 5.1.1. Table 5.2 lists the important outputs produced and the locations at which they are measured. Many more properties can also be extracted from the model and used in analysing rock mass behaviour, including forces, stresses, displacements, flow rates, pressures and joint apertures.

Table 5.2 – Important output data obtained from the coupled UDEC model of UCG.

Output	Locations
Surface Displacement	50 equally spaced points along the top edge of the model
Groundwater Pressure	At every domain within the model
Rock Mass Temperature	At every intact block within the model

5.2 MODEL GEOMETRY

5.2.1 Site Geometry

Site geometry refers to the large scale features of the model, including its total width and height. These properties are derived from the cavity geometry given in Table 5.1. As mentioned in Section 4.6, the model is broken into ‘coarse’ and ‘fine’ mesh regions in order to reduce runtime whilst retaining accuracy. Figure 5.2 shows the model geometry. Numbers in brackets refer to those from the Rocky Mountain 1 model (Lindblom *et al*, 1990). The effects of variations in these geometric properties are investigated in Chapter 8. The overall shape of the cavity is assumed to be identical in all models, though the dimensions of height, width and depth may vary.

The dimensions of the model varied throughout the creation process. The final values used were chosen in an attempt to give as accurate a model as possible whilst retaining a runtime under 24 hours. Model width is set at 2.5 times the predicted width of the subsidence trough (as given by the angle of draw) to avoid the influence of boundary conditions on results. Determining model width in this manner allows the model to operate on cavities of any given depth. The factor of 2.5 was chosen based on the results of initial parametric studies presented in Chapter 6. Model height is determined by the depth and height of the cavity, however the distance between the cavity floor and the model base must be manually defined. The model uses a separation equal to the cavity height, as this is seen to be sufficient to realise the extent of heaving below the cavity. The height and width of the discrete fracture network (DFN) region are set at 4 and 3 times the cavity dimensions. Investigations into the effect of varying these dimensions are presented in Section 6.3

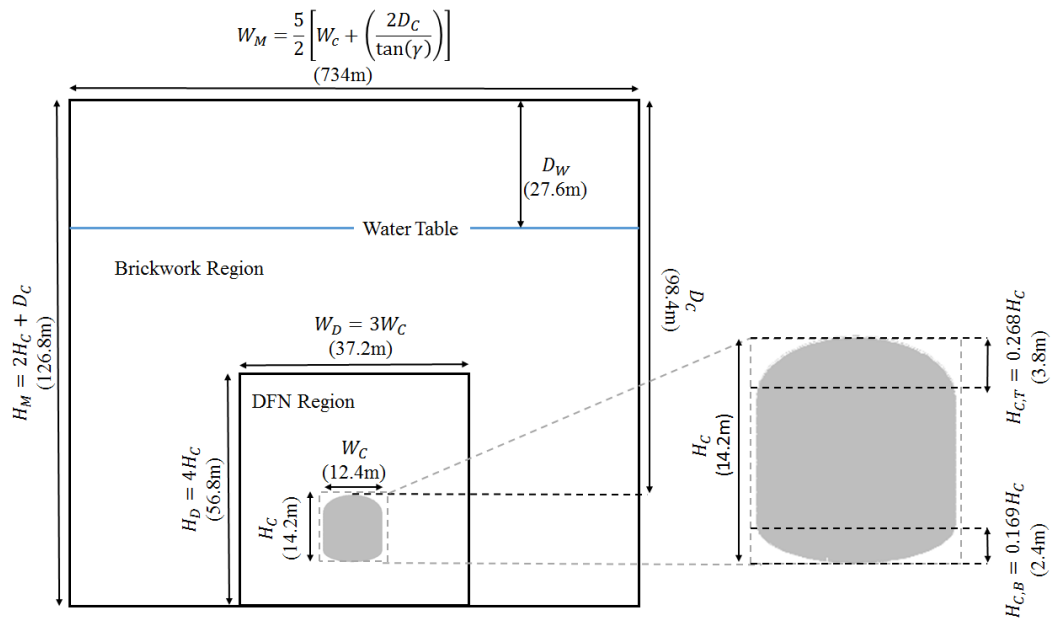


Figure 5.2 – Site geometry calculations for the base case UCG model.

Where:

D	Depth	(m)
H	Height	(m)
W	Width	(m)
γ	Angle of Draw	($^{\circ}$)

Subscripts:

B	Bottom
C	Cavity
D	Discrete Fracture Network
M	Model
T	Top
W	Water Table

5.2.2 Block Geometry

As shown in Chapter 4, the size and shape of the individual blocks within the UDEC model can greatly affect results. A discussion of the selection of appropriate block shapes is given in Section 4.6. In order to maintain consistency between sites, block sizes in both regions of the model are defined as functions of cavity geometry. Regardless of the size or depth of the cavity, all models are designed to contain approximately 2,000 blocks in the fine (N-DFN) region and 200 blocks in the coarse (brickwork) region. These values were chosen as a compromise between runtime and accuracy. Smaller blocks allow for more accurate temperature and pressure distributions, however they also give a considerable increase in runtime. Smaller blocks are also seen to affect subsidence results as model behaviour becomes more dependent on joints (weak) rather than blocks (strong). The use of deterministic (rather than arbitrary) geometry greatly reduces the effect of model design on results, increasing confidence that observed trends are due to changes in cavity shape rather than properties such as joint density, which are not based on measured quantities of the site. Table 5.3 shows how block geometry is determined in the model. Further investigations into the effects of block size are given in Section 6.4.

Table 5.3 – Determination of block geometric parameters in the UDEC model.

Fine region property	Calculation	Base case value
Joint density (m ⁻²)	$\rho_J = \frac{2\sqrt{2000}}{(W_D H_D)^{1.012}}$	0.077
Joint maximum length (m)	$L_{max} = \max(H_D, W_D)$	56.8
Joint minimum length (m)	$L_{min} = L_{max}/3$	18.9
Joint set angles (°)	Fixed	0 ± 10; 90 ± 10
Coarse region property	Calculation	Base case value
Block height (m)	$H_B = H_M/20$	6.34
Block width (m)	$W_B = W_M/10$	73.4

The calculations used to determine the DFN joint geometry were chosen based on experience and recommendations from the literature. As mentioned in Section 4.2.4, the N-DFN pattern contains two sets of joints oriented perpendicular to each other. The standard deviation of both sets is set at 10° as this was seen to give appropriate behaviour. Maximum and minimum lengths are based on the suggestions of Min *et al*, (2004). Joint density is designed to give a constant number of joints across all models and depends on a number of factors. The factor of 2 represents the fact that each block has an average of 4 joints (2 of each joint set). 2000 is the target number of blocks in the DFN. The square root is required to convert the number of blocks (2D) into edges (1D). Initially the area of the DFN was used as the denominator, however this caused larger models to produce too many joints. The exponent 1.012 was found to give stable behaviour over a wide range of DFN sizes. The sizes of coarse blocks were chosen to give appropriate behaviour without increasing runtime. Investigations into the effects of DFN and coarse region block geometry are given in Chapter 6.

5.2.3 Zone Density

In a fully deformable analysis, zones act as the fundamental unit of model geometry. As shown in Section 3.2.2.1, zone density can have a considerable effect on model behaviour. UDEC automatically generates zones within each block and attempts to keep zone sizes approximately uniform throughout each region of the model. In UDEC, zones are defined by their average edge length. Shorter edges increase zone density and lead to more accurate models. On the other hand, shorter edges increase runtime and can lead to overlap errors and model instability. As seen with continuum methods, there exists a minimum edge length below which further reductions have no effect on accuracy. Given these considerations, edge lengths are chosen to give accurate results without excessive runtimes. As with blocks, the model aims to produce a roughly constant number of zones across all site geometries, with an average of 10 zones per block. This is achieved by basing zone edge lengths on block sizes, which are in turn a function of site geometry. Table 5.4 lists the edge lengths used in each region of the UCG model. Further investigations into the effects of zone edge length are given in Section 6.6.

Table 5.4 – Zone edge lengths used in the base case UCG model.

Region	Calculation	Base case value (m)
Fine	$L_{z,F} = \frac{\sqrt{W_D H_D}}{2000}$	0.023
Coarse	$L_{z,C} = \sqrt{\frac{W_B H_B}{2}}$	15.3

5.3 MODEL PROPERTIES

Simulation results depend greatly on the properties of the materials modelled within the simulation. Some of these properties represent measurable quantities, for example thermal conductivities, which can be obtained from experiments or literature sources. These are referred to as physical properties. Other properties, such as joint stiffnesses, relate only to the way in which the system is represented by the UDEC model. These are referred to as internal properties. This section outlines how the mechanical, hydraulic and thermal properties used in the UDEC model were selected and discusses their importance.

5.3.1 Mechanical Properties

Mechanical properties refer to the parameters controlling stress, strain and displacement relationships for both intact rocks and joints. Blocks in the UCG model are simulated using a strain-softening Mohr-Coulomb constitutive relationship. This relationship was chosen as it is the most suitable for the analysis of geomechanical problems involving collapse behaviour. Joints are modelled using an area contact Coulomb slip model. This model was chosen as it gives an effective representation of joint behaviour in heavily jointed rock masses. Discussions on the selection of block and joint constitutive models are given in Section 3.2.1. Table 5.5 lists the block and joint mechanical properties used in the model.

Table 5.5 – Mechanical properties of base case UCG model.

Property	Value	Type	Source
Intact Rock Properties			
Density (kgm ⁻³)	2700	Physical	See Chapter 4
Young's Modulus (Pa)	1.58×10 ⁹	Physical	See Chapter 4
Poisson's Ratio (-)	0.019	Physical	See Chapter 4
Friction Angle (°)	61.6	Physical	See Chapter 4
Cohesion (Pa)	8.54×10 ⁶	Physical	See Chapter 4
Tensile Limit (Pa)	4.63×10 ⁶	Physical	See Chapter 4
Dilation Angle (°)	9.24	Physical	See Chapter 4
Joint Properties			
Normal Stiffness (Nm ⁻¹)	1.00×10 ¹⁰	Internal	UDEC database
Shear Stiffness (Nm ⁻¹)	1.00×10 ⁹	Internal	UDEC database
Friction Angle (°)	30.0	Internal	UDEC database
Cohesion (Pa)	1.00×10 ⁵	Internal	UDEC database
Tensile Limit (Pa)	0.0	Internal	UDEC database
Dilation Angle (°)	5.0	Internal	UDEC database

The intact rock properties used in the model are based on the results of the simulated laboratory scale compression tests presented in Chapter 4. Joint properties were chosen from the sandstone entry of UDEC's internal property database. Investigations into the effects of joint properties are presented in Section 6.7.

5.3.2 Hydraulic Properties

Hydraulic properties relate joint aperture with groundwater flow velocity and pore pressure. Flow in the UCG model is simulated using the steady state flow approximation presented in Section 3.3.1. This approximation is considered necessary due to the complexity of the joint pattern in the DFN region. Inaccuracies caused by the approximation are considered to be reasonable, given that the UCG process occurs over sufficiently long timescales to approach a pseudo-steady state at the times of interest. Table 5.6 lists the hydraulic properties used in the base case model. In all cases the fluid simulated was water. The properties used are those of pure water at standard temperature and pressure. In reality, the groundwater around a UCG cavity would exist under a range of temperatures and pressures, and would almost certainly contain high levels of dissolved solids. While this difference would affect the hydraulic properties of the fluid, the expected scale of the variation was not considered great enough to justify the extra modelling effort required to simulate it.

Table 5.6 – Hydraulic properties used in the base case UCG model.

Property	Value	Type	Source
Fluid Density (kgm^{-3})	998	Physical	Green & Perry, 2007
Fluid Viscosity (Pas)	1×10^{-3}	Physical	Green & Perry, 2007
Site Permeability (mD)	52.9	Physical	Mason <i>et al</i> , 1987
Joint Aperture at Zero Stress (m)	2.50×10^{-7}	Internal	Equation 5.1
Minimum Joint Aperture (m)	2.50×10^{-8}	Internal	Equation 5.2
Maximum Joint Aperture (m)	2.50×10^{-5}	Internal	Equation 5.3

As shown in Section 3.3, the hydraulic response of the model relies heavily on joint aperture. In order to give accurate flow behaviour, joint aperture is based on the measured permeability of the Rocky Mountain 1 trial site, as shown in Equation 5.1. The derivation of this equation is given in Appendix A.2.1. Permeability in the model can be altered to simulate different sites, as shown in Section 8.4.2.

$$a_0 = \sqrt{12\kappa} \quad (5.1)$$

Where:

a_0 Aperture at zero stress (m)

κ Permeability (m^2)

Note that permeability in Equation 5.1 is in units of m^2 , whereas most results use units of millidarcy for convenience. Minimum and maximum apertures are set according to Equations 5.2 and 5.3. Maximum aperture is set further from zero than minimum aperture because of the large number of completely separated joints in the model.

$$a_{min} = 0.1a_0 \quad (5.2)$$

$$a_{max} = 100a_0 \quad (5.3)$$

The calibration of joint apertures against site measurements allows for increased confidence in hydraulic model results. Model accuracy is expected to be less than that which could be achieved using CFD, however the full mechanical/hydraulic coupling capabilities of UDEC are considered to be more beneficial to the overall model.

5.3.3 Thermal Properties

Thermal properties refer not only to parameters which control heat transport, but also to those which link mechanical properties to temperature. These properties are given in Table 5.7.

Table 5.7 – Thermal properties used in the base case UCG model.

Property	Value	Type	Source
Thermal Conductivity ($\text{Wm}^{-1}\text{K}^{-1}$)	1.39	Physical	Robertson, 1988
Specific Heat Capacity ($\text{Jkg}^{-1}\text{K}^{-1}$)	920	Physical	Robertson, 1988
Linear Thermal Expansion Coefficient (K^{-1})	1.16×10^{-5}	Physical	Robertson, 1988
Temperature Dependent			
Young's Modulus	See Fig 5.4	Physical	Ranjith <i>et al</i> , 2012
Friction Angle	See Fig 5.4	Physical	Ranjith <i>et al</i> , 2012
Cohesion	See Fig 5.4	Physical	Ranjith <i>et al</i> , 2012
Tensile Limit	See Fig 5.4	Physical	Ranjith <i>et al</i> , 2012

The first three properties in Table 5.7 can be found from literature sources or experimental studies and as such are considered sufficiently accurate. A potential issue with these properties however, is their temperature dependence. For reasons outlined in Section 3.5.3, simulations of temperature dependent thermal properties are not possible without a considerable increase in computational runtime. In order to minimise inaccuracies whilst avoiding this problem, the values of these properties are set at their mean value over the expected range of temperatures within the model. Given that the influence of temperature on environmental issues is reasonably minor, it is believed that this simplification will not greatly affect model accuracy. Tests of the effects of various thermal properties on results are presented in Section 8.5.

The influence of temperature on the mechanical properties of rocks is difficult to define. Because of the difficulties in performing compression tests at elevated temperatures, data on temperature dependent strength and stiffness are rare. Ranjith *et al* (2012) present a review of results in this field, in addition to their own results. This paper highlights the vast differences seen between the results of previous authors, as shown in Figure 5.3. These differences call into question the validity of the results, and introduce a large source of uncertainty into any models in which they are used. As mentioned above however, the relatively low influence of thermal effects on environmental issues suggest that these uncertainties should not adversely affect the overall behaviour of the model to a significant degree.

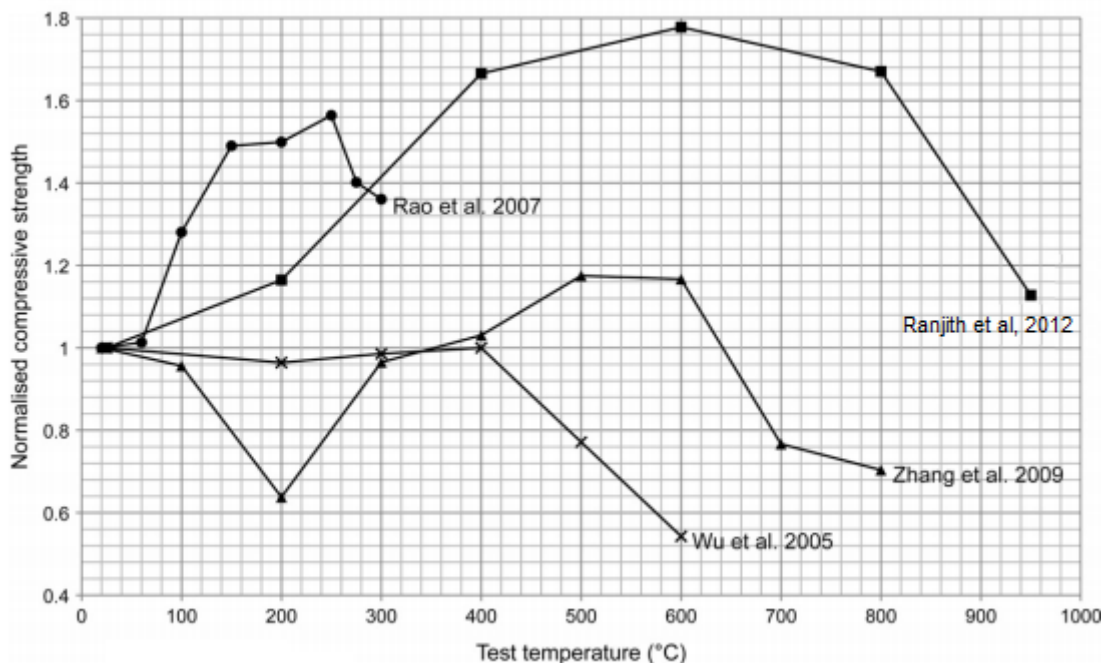


Figure 5.3 – Results of a number of studies on the temperature dependence of compressive strength for sandstone. After Ranjith *et al*, 2012.

The properties used in this model are based on Ranjith’s own results as these cover the broadest range of temperature. Values for temperature dependent Young’s modulus are extracted directly from the paper. Values for temperature dependent friction angle, cohesion and tensile limit must be derived from the paper’s results for uniaxial compressive strength. The methods for the above calculations are given in Appendix B.2. No data are available for temperature dependent Poisson’s ratio or dilation angle and these are therefore assumed to be constant with temperature. Figure 5.4 presents the final derived parameters. Temperature dependent fluid properties are not included in the model due to the problems of boiling, as shown in Section 3.5.2.

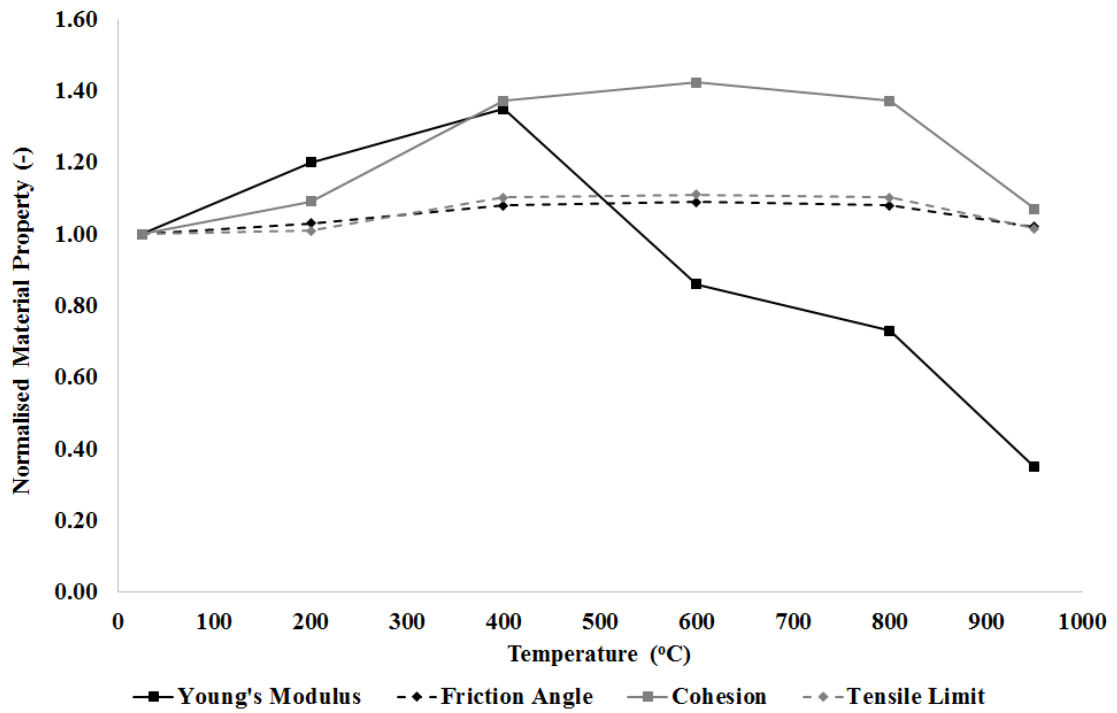


Figure 5.4 – Effects of temperature on various mechanical properties used in the UCG model.

5.4 BOUNDARY AND INITIAL CONDITIONS

Boundary conditions in the UCG model are specified along the side and bottom edges of the model, as well as at the cavity wall in the case of thermal conditions. Initial conditions are set prior to the first stage of model cycling, however some hydraulic and thermal conditions are altered before the second (after) or third (final) stage.

5.4.1 Mechanical Boundary Conditions

Mechanical boundary conditions are applied primarily to hold the model in place and ensure that internal forces do not cause rigid body motion of the entire model. The conditions applied are listed below:

- Zero horizontal motion along the left and right hand edges of the model.
- Zero vertical motion along the bottom edge of model.

These conditions allow full motion over the rest of the model, including the surface. The lack of a vertical condition on the side boundaries also allows for heave or subsidence at the model edges, reducing the effect of the boundary conditions on model results.

5.4.2 Mechanical Initial Conditions

Initial conditions in the mechanical model relate to the in-situ stress state of the site. The normal stress in the vertical (y) direction is given by Equation 5.4. Normal stresses in the horizontal (x) and out of plane (z) directions are equal, and are given by Equation 5.5. Shear stresses are initially set at zero throughout the model.

$$\sigma_y = -\rho_R g D \quad (5.4)$$

$$\sigma_x = \sigma_z = K_0 \sigma_y \quad (5.5)$$

Where:

D	Depth below ground's surface	(m)
K ₀	Lateral earth pressure coefficient	(-)

The application of these stresses speeds solution of the “before” stage by giving an initial guess of in-situ stresses at that time. The lateral earth pressure coefficient K_0 is set at 0.5 in all models, as this is a commonly used value when measurements are not available. A sensitivity analysis of the influence of K_0 on model results is presented in Section 8.3.3. Gravitational acceleration is set at 9.81ms^{-2} directly downwards at all stages of the model.

5.4.3 Hydraulic Boundary Conditions

Hydraulic boundary conditions represent groundwater pressures at great distances from the cavity. These pressures are set equal to the local hydrostatic pressure on the side and bottom edges of the model. As with the mechanical model, it is important to ensure that boundaries are located far enough from the region of interest to prevent them adversely affecting results. Local hydrostatic pressures are found according to Equation 5.6.

$$P = \rho_F g (D - D_W) \quad (5.6)$$

Where:

D	Depth	(m)
D _W	Water Table Depth	(m)
P	Pressure	(Pa)
ρ_F	Fluid Density	(kgm ⁻³)

Cavity pressure is set as a hydraulic boundary condition at various stages to simulate the effects of UCG on groundwater. Pressures are set as fractions of the local hydrostatic pressure at the roof of the cavity. Table 5.8 lists the pressures set at each stage of the model. The fraction set during the “after” stage represents the cavity operating pressure. The value used was suggested based on previous industrial experience (Lavis, 2013).

Table 5.8 – Cavity pressure conditions at various stages of the model.

Stage	Pressure Fraction (-)	Reason
Before	1.0	Undisturbed water table
After	0.8	UCG operating pressure (see Section 2.1.6)
Final	1.0	Site returned to background conditions

5.4.4 Hydraulic Initial Conditions

The initial hydraulic state of the site is a flat water table D_W metres below the ground's surface. The hydraulic initial condition applies Equation 5.6 to set pressures at all points within the model.

5.4.5 Thermal Boundary Conditions

Thermal boundary conditions are required to ensure conservation of energy over long timescales, and to provide heat sources. Boundaries are set as constant temperature conditions with associated heat transfer coefficients. The cavity wall temperature varies throughout the model to simulate various stages of the gasification process.

Table 5.9 lists the thermal boundary conditions used within the model.

Table 5.9 – Thermal boundary conditions used in base case UCG model.

Location	Heat Transfer Coefficient ($\text{Wm}^{-2}\text{K}^{-1}$)	Temperature (K)
Side edges	1.39 (rock to rock)	300
Bottom Edge	1.39 (rock to rock)	300
Top Edge	10.0 (rock to air)	300
Cavity Wall	1.39 (rock to rock)	Varies. See Section 5.6.1

5.4.6 Thermal Initial Conditions

Thermal initial conditions simply set the temperature of the rock mass to 300K before the thermal model runs (i.e. at the start of model cycling), and then reset temperatures again after gasification ceases (i.e. before the “final” stage).

5.5 MECHANICAL AND HYDRAULIC LOGIC

As shown in Figure 5.1, there are three distinct stages at which the coupled mechanical and hydraulic models are solved. While the technical details of how these models are cycled is given in Chapter 3, additional logic is required to ensure the accuracy and speed of these models. Each “solve hydraulic & mechanical models” step in Figure 5.1 actually consists of a number of sub-steps used to control cycling and check for convergence. The overall mechanism of the solution step is shown in Figure 5.5.

As seen in Figure 5.5, the cycle repeats after every 1,000 iterations. This is done in order to minimise runtime. Repeating more frequently causes the computationally intensive termination criterion check to be called more often. Repeating less frequently can allow the model to cycle for a long time after convergence is reached, wasting computational resources. The initial 10,000 cycles are performed to ensure that sufficient motion occurs before the convergence check is called for the first time, preventing false positives. The maximum number of iterations is set at 2,000,000 to limit model runtime. Models are generally seen to solve in between 200,000 and 500,000 cycles, so this limit is considered sufficient to avoid causing premature termination. In general, if a model does not solve within 2,000,000 cycles, it indicates that there is a problem with this particular execution. An error report is output from models which reach this limit to allow operators to identify problems.

5.5.1 Termination Criteria

In order to check whether a model has reached completion, a termination criterion (or criteria) must be defined. This may be performed manually (i.e. by the operator looking to see if the model has changed significantly since the last inspection), but automatic criteria allow the model to produce results much faster by preventing unnecessary cycling. Automatic criteria check for completion by comparing some measurable quantity of the model against a predefined limit. A number of criteria were considered during the creation of the model, these are briefly outlined below.

The first criterion considered compared the maximum unbalanced force in the model with a user defined limit. Under this criterion, the model was considered to be solved if no single block in the model was subject to a net force greater than 0.01% of the weight of a rectangular column of overburden with unit width and a height equal to the cavity depth. This value was somewhat arbitrary, however the dependence on cavity depth ensured that the limit was still appropriate for use in models with extreme geometries. This criterion was abandoned however, due to issues with oscillating blocks. Because the criterion is based on an instantaneous measurement of force taken at every thousandth iteration, small oscillations of single blocks can prevent it from ever returning a true result. These oscillations are often seen in models with considerable failure behaviour. As such, the criterion often caused models to fail to reach convergence and was therefore abandoned.

The second attempt at a termination criterion considered the change in displacement of all the blocks in the model. The criterion calculated the ratio of the change in displacement of a block over the previous 1,000 iterations (i.e. block velocity) to its total displacement over the current model stage (before, after or final). The model was considered converged if no single block had a ratio greater than 0.01%. The averaging of displacement over 1,000 steps solves the issue of oscillating blocks as their average velocity over 1,000 iterations tends to zero. This criterion also failed however, due to the motion of very slowly moving blocks at the model edges. These blocks move slowly enough to be considered stationary, however their total displacement over a stage may still be large enough to register. The issue arises when 0.01% of this velocity is small enough to round to zero when stored as a floating point number, while 100% of it is not. This gives a convergence limit of zero, preventing the model from ever finishing. This could be avoided by applying a minimum displacement limit to the criterion, however this was seen to cause premature termination, as the model would sometimes report convergence while blocks were still accelerating.

The third attempt at a termination criterion considered only the motion of the ground's surface (i.e. the subsidence trough itself). This criterion used the same logic as the displacement criterion, but rather than applying it to every block in the model, it was only applied to the 50 surface displacement points defined in Table 5.2. The cessation of subsidence was considered an acceptable criterion, as subsidence is the main result of interest from the model. Although this criterion considers only a small area of the model, it is seen to be both computationally efficient and more reliable than simple manual inspection. The criterion however does have the potential to cause premature termination of cycling, as explained below.

With some model geometries, it is possible that ground motion may appear to cease while cavity collapse is ongoing. This collapse can lead to a weakening of the overburden which may later lead to further subsidence. Under the subsidence criterion, the model may terminate before this secondary subsidence occurs, leading to erroneous results. This can only be prevented by ensuring that the model simulates the full process of cavity collapse from start to finish. Achieving this would require the model to contain a highly fractured joint pattern (e.g. the fine region) throughout the entire modelled domain. In addition, the time dependent nature of cavity collapse would require a fully dynamic simulation of cavity collapse. Incorporating either of these would lead to order of magnitude increases in model runtime, precluding the ability to consider the results of several sites in a short timescale. As such, this method of solution is not appropriate for the envisioned end use of this model.

Despite the above issue it is seen that the subsidence criterion is sufficient to capture the behaviour of the majority of UCG sites. Chapters 6 through 8 show results both proving this suitability and highlighting cases in which the model may not be appropriate. In particular, Section 6.8 shows the results of investigations into the effect of varying the target convergence ratio (0.01% in the standard case). Given that the criterion works well in the vast majority of models tested, it is considered to be more than sufficient for use in the UCG model.

5.6 THERMAL MODELLING

The UCG process depends heavily on thermal effects. Heat transfer within the cavity drives many aspects of UCG, including coal conversion, thermal spalling, groundwater evaporation and coal shrinking/swelling processes. Temperature effects are also seen to be heavily coupled with mechanical and hydraulic phenomena. As such, it is important that thermal effects are considered in the UCG model. Note however, that the thermal influence of UCG is rarely seen to extend far from the cavity, with no temperature deviation seen at distances greater than approximately 15m from the cavity wall (Sarhosis *et al*, 2013; Yang, 2005). As such, the effects of temperature on environmental issues are minor, and thermal effects are often considered less important than mechanical or hydraulic effects. Nevertheless, thermal issues do affect rock mass behaviour, and as such, attempts were made to incorporate detailed thermal modelling within the UCG model.

5.6.1 Underground Coal Gasification Thermal Behaviour

The thermal evolution of UCG can be broken into four distinct phases:

1. Pre-ignition – the coal seam is at the local background temperature.
2. Combustion – exothermic.
3. Gasification – endothermic.
4. Shutdown – the cavity is artificially cooled back to the initial background temperature.

As the gases flow through the cavity, their temperatures change with position. Over short timescales (hours), the temperature at a given point is approximately constant. In effect, the channel acts as a plug flow reactor (PFR). Over longer timescales (days), the temperature profile moves as the flame front advances towards the injection well. The rate of movement varies, with values from 0.5 to 1.1 mday⁻¹ being reported for oxygen blown gasification, with an average of 0.73 mday⁻¹ (Sarraff *et al*, 2011; Seifi *et al*, 2011; Shafirovich & Varma, 2009). Because of the inherent difficulties in measuring cavity wall temperatures during operation, experimental temperature profiles are not available. Profiles can be approximated from simulations however, such as those of Perkins and Sahajwalla (2008). The typical UCG temperature profile is shown in Figure 5.6. Once operation has ceased, the entire cavity is rapidly cooled to the initial background temperature of 300K (not shown in this figure).

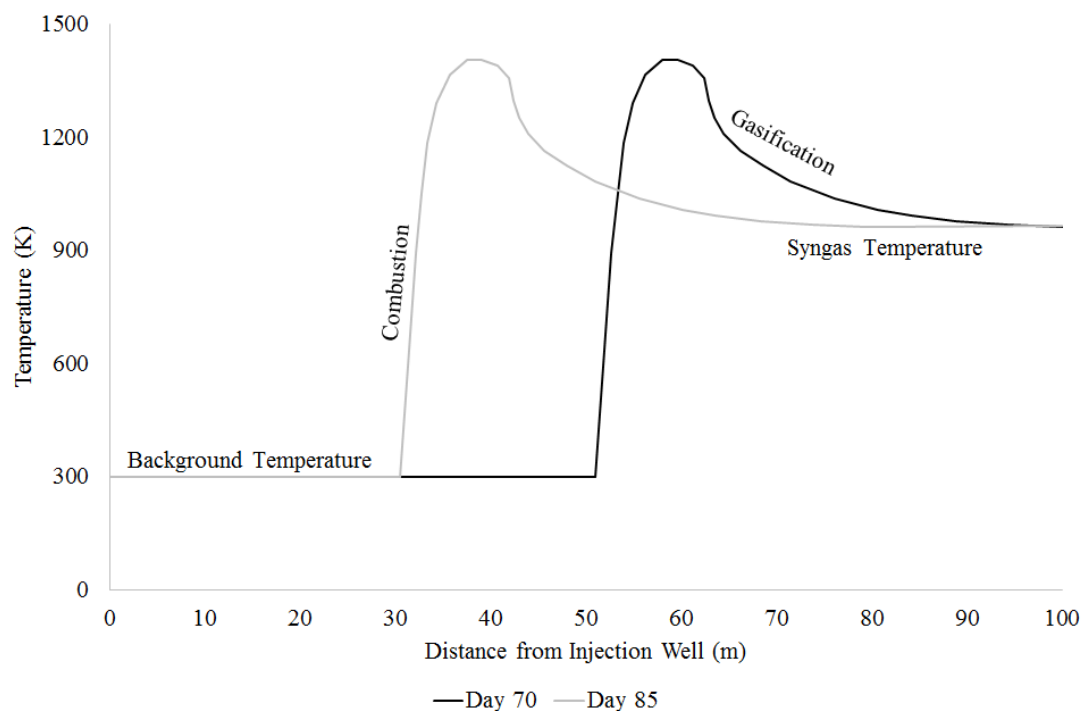


Figure 5.6 – Temperature profiles within the UCG cavity as a function of time.

During operation, heat is transferred away from the cavity, increasing local rock mass temperatures. This leads to a number of coupled thermal/hydraulic/mechanical phenomena. Three particular issues are of interest in the environmental model:

- Thermally generated stresses in the rock mass.
- The effects of increased temperature on the mechanical properties of rock.
- The effects of increased temperature on inflowing groundwater.

The first two issues can be simulated using the thermal modelling logic available in UDEC. The application of UDEC to these issues is discussed in Section 5.6.2. As mentioned in Section 3.5.2, UDEC is incapable of simulating coupled thermal/hydraulic phenomena such as convection. A number of attempts have been made to approximate these effects, however this has proven to be highly impractical within a model of this complexity. Section 5.6.3 discusses these attempts in detail.

5.6.2 Thermal Algorithm

As shown in Figure 5.1, the thermal model is called prior to the “after” stage of the model. This ensures that the mechanical response at this stage includes the entire thermal history of the operation. As mentioned above, the temperature profile in the cavity moves towards the injection well as gasification proceeds. For a given slice through the reactor (i.e. the model geometry), cavity wall temperature is therefore seen to vary with time. The temporal temperature profile can be found by dividing the spatial profile by the flame front velocity. Figure 5.7 shows this profile, as well as the stepwise profile used as an approximation in the model. The profile continues to a time of 100 days after ignition in order to capture the full thermal history of the slice.

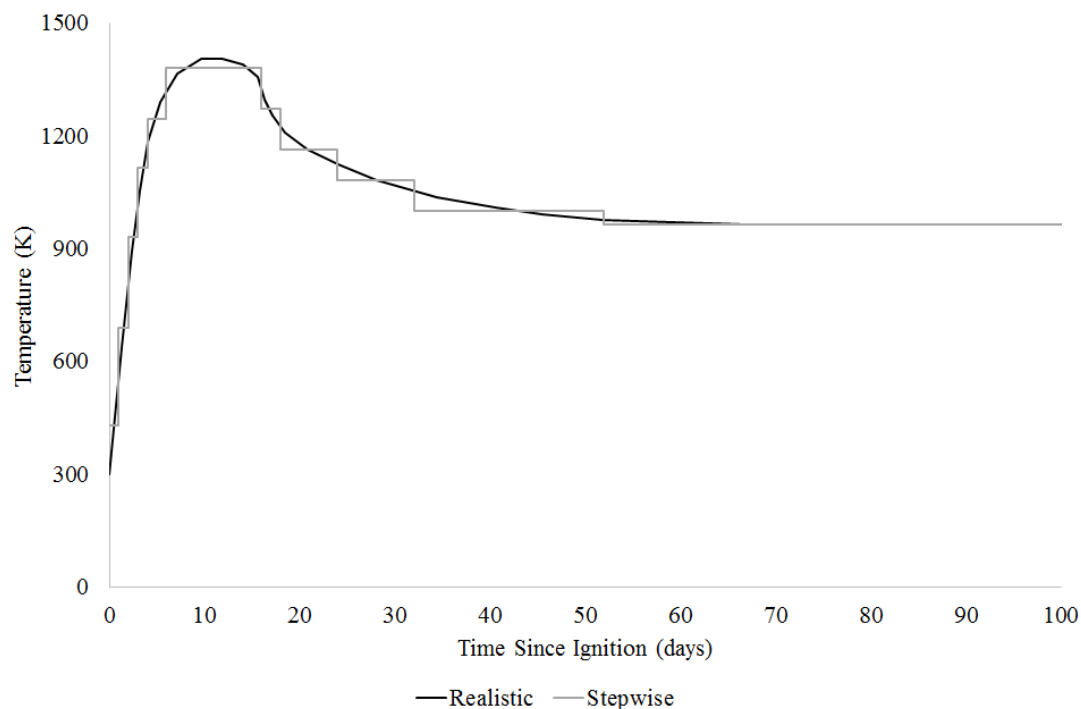


Figure 5.7 – Cavity wall temperature as a function of time in the thermal model. After Perkins & Sahajwalla, 2008.

In the case of thermally generated stresses, the temperature of interest is that at the end of thermal cycling. As such, these stresses can be simulated simply by applying a thermal expansion coefficient to each block after cycling terminates. In the case of temperature dependent rock properties however, the physical and chemical changes to the rock remain after the rock mass cools. As such, it is the historic maximum temperature of a block that is important, rather than its current temperature. As such, the model must be able to record the temperature of each block over time and store the maximum value experienced. The data are then used to assign altered material properties to the affected blocks. This is achieved by running the thermal algorithm in discrete sections of one day and recording temperatures at the end of each day. This formulation also allows for the use of varying cavity wall temperatures. Figure 5.8 describes the full mechanism of the thermal calculation step. The nomenclature for Figure 5.8 is given on the following page.

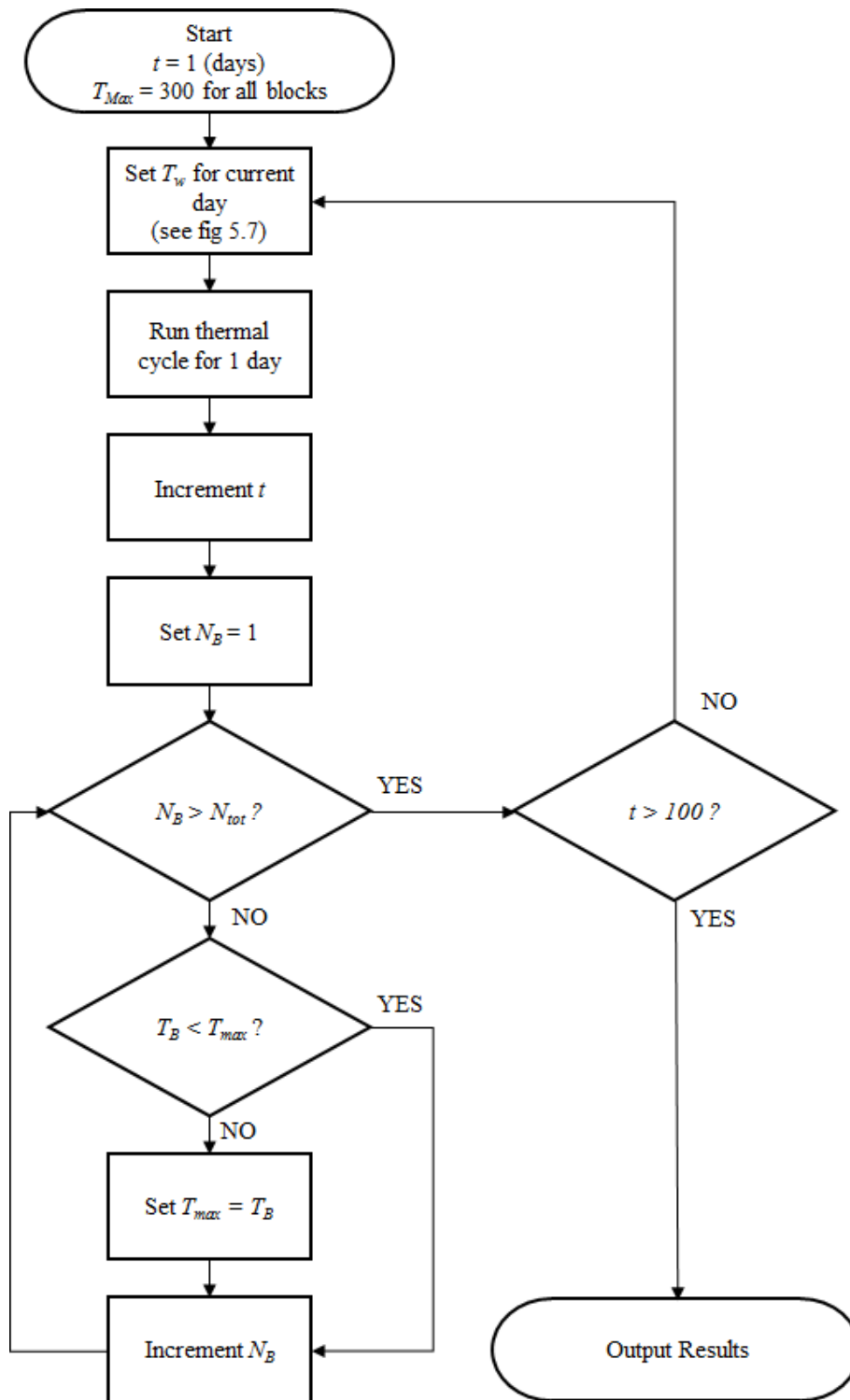


Figure 5.8 – Thermal solution algorithm.

Where:

N	Number	(-)
T	Temperature	(K)
t	time	(days)

Subscripts:

B	Block
max	Maximum
tot	Total
w	Cavity Wall

The value of T_{wall} is found by interrogating the stepwise temperature profile (Figure 5.7) for the current day. This temperature is applied as a boundary condition to every block which makes up the cavity wall. Because of the complex cavity and joint geometry, it is difficult to exactly specify which blocks constitute the cavity wall. An approximation is therefore required to allow the model to operate with varied cavity geometries. A block is assumed to be part of the cavity wall if its centroid is contained within a rectangle extending a given distance around the cavity itself. The distance used is equal to the average zone edge length in the fine zone region. As this tends to capture only the nearest block to the cavity edge, this is seen to be a reasonable approximation, though there are some issues:

Firstly, especially long blocks near the cavity may have their centroids outside the specified region, preventing their selection, while especially thin blocks may sit so close to the cavity that the next block out is also close enough to be selected. Second, the cavity wall must be defined within a rectangular area as UDEC's initial condition logic is incapable of using more complex shapes. This leads to a minor distortion of the temperature profile, causing an extension of the wall region above the curved regions of the cavity. These issues are considered acceptable however, as the thermal model runs for a long enough time to smooth out any inaccuracies. In addition, the minor influence of the thermal model on overall results reduces the importance of thermal inaccuracies compared with those from other sources.

Once the thermal modelling stage is completed, thermally altered material properties are assigned to blocks with increased temperatures. The maximum temperature experienced by a given block is determined by the thermal model and material properties are set according to the values given in Figure 5.4. In order to simplify this process, material properties are assigned at a temperature equal to the closest data point on the graph. This greatly reduces the computational demands of the model by eliminating the need for interpolation and is considered to be accurate enough for use in the UCG model.

5.6.3 Thermal/Hydraulic Coupling

As mentioned in Section 5.6.1, the thermal algorithm within UDEC cannot reliably simulate the coupled thermal/hydraulic phenomena occurring near the cavity. As groundwater flows towards the cavity, it passes through the hot cavity wall. In reality heat would transfer between the rocks and the fluid, giving rise to a number of effects which may influence the thermal, hydraulic or mechanical behaviour of the overburden. The most important effects include:

- Storage of thermal energy in the fluid
- Heat transfer via convection.
- Effects of groundwater on cavity temperature.
- Boiling of groundwater within the pore space between rocks.

The influence of each effect is explained below. Attempts to incorporate these issues into the model and suggestions for future additions to the model are also discussed.

5.6.3.1 Fluid Thermal Energy Storage

In a real rock mass, the pore spaces within rocks are often filled with water. In UDEC, intact rocks are assumed to be completely dry, with all the fluid existing in the joints. This is a reasonable approximation for hydraulic effects, but it can under-represent the total amount of fluid present in a rock mass. Because of the high degree of fluid/rock contact, this fluid is often assumed to be at the same temperature as the rock material.

While this is a valid assumption given the low groundwater flow rates, it does not consider the heat required to raise the fluid to this temperature. As such, UDEC may overpredict rock mass temperatures by assigning all of the transferred heat to the solid material. This overprediction can be accounted for by altering the specific heat capacity of the rock to include the effect of the fluid, as shown in Equation 5.7:

$$C_p = \phi C_F + (1 - \phi)C_R \quad (5.7)$$

Where ϕ is rock mass porosity.

Carboniferous sandstones tend to have a porosity of around 0.15 (Building Research Establishment, 2000), giving a corrected heat capacity of $1410 \text{ Jkg}^{-1}\text{K}^{-1}$ compared with $920 \text{ Jkg}^{-1}\text{K}^{-1}$ for the intact rock, assuming a fully saturated rock mass. In addition, this does not consider the contribution from the latent heat of vaporisation, which may be considerably greater than that of sensible heat. Unlike with sensible heat however, latent heat cannot be included in the heat capacity of the rock mass, as its existence depends on temperature. Latent heat could be included with the use of a temperature dependent heat capacity, though this is impossible due to the separation of thermal cycling and material property designation, as outlined in Section 3.5.3.

As shown in Section 8.5.2, increases in heat capacity have little effect on mechanical or hydraulic results. Given this observation, coupled with the increases in complexity and runtime required to accurately model changing heat capacities, it has been decided to maintain rock mass heat capacity at $920 \text{ Jkg}^{-1}\text{K}^{-1}$. While this decision will overestimate temperatures, this is considered to be justified for two reasons:

Firstly, the higher temperatures represent a “worst case scenario” for environmental damage. As the aim of the model is to predict such damage, overestimation is generally considered to be preferable to underestimation. Second, this avoids the complication arising from needing to set heat capacities based on water table height. In cases where water table lowering is significant, this could greatly increase runtime. The additional complexity and runtime required to reduce this inaccuracy is therefore considered too great in comparison to the minor effect this would have on results.

5.6.3.2 Thermal Convection

As well as storing heat, the existence of groundwater greatly affects heat transfer mechanisms within the rock mass. The only mechanism modelled in UDEC is conduction through the rocks. In reality, heat is also transferred via convection within the pore fluid. Convection not only alters the rate of heat transfer through the rock mass, but causes this rate to be dependent upon the flow rate of groundwater. Because groundwater tends to flow towards the cavity (i.e. against the direction of conduction), convection acts to reduce the heat loss to the rock mass and shorten the thermal penetration length. The relative importance of rock and fluid heat transfer is estimated by Equation 5.8. The derivation of this equation is given in Appendix B.3.

$$\frac{Q_R}{Q_F} = -\frac{\lambda H}{\rho a v C} \quad (5.8)$$

Where:

C	Fluid heat capacity	(Jkg ⁻¹ K ⁻¹)
H	Average rock height	(m)
Q	Heat flux	(Wm ⁻¹)
a	Joint aperture	(m)
v	Fluid velocity	(ms ⁻¹)
λ	Rock thermal conductivity	(Wm ⁻² K ⁻¹)
ρ	Fluid density	(kgm ⁻³)

Initial model results give groundwater flow rates of approximately 28 mL/day. Assuming a cavity length of 600m, this corresponds to a velocity of approximately $4 \times 10^{-14} \text{ ms}^{-1}$ at the cavity wall. Assuming the maximum joint aperture of $2.50 \times 10^{-5} \text{ m}$ and using previously defined values of the other constants, conduction is shown to have a magnitude approximately 1×10^{12} times greater than that of convection. As such, the assumption that convective heat transfer is negligible is easily justified.

5.6.3.3 Effects of Groundwater on Cavity Wall Temperature

In addition to the above effects, the inflow of groundwater into the cavity also influences cavity wall temperatures in UCG. This can be explained by considering the energy balance over the entire UCG process, as shown in Figure 5.9.

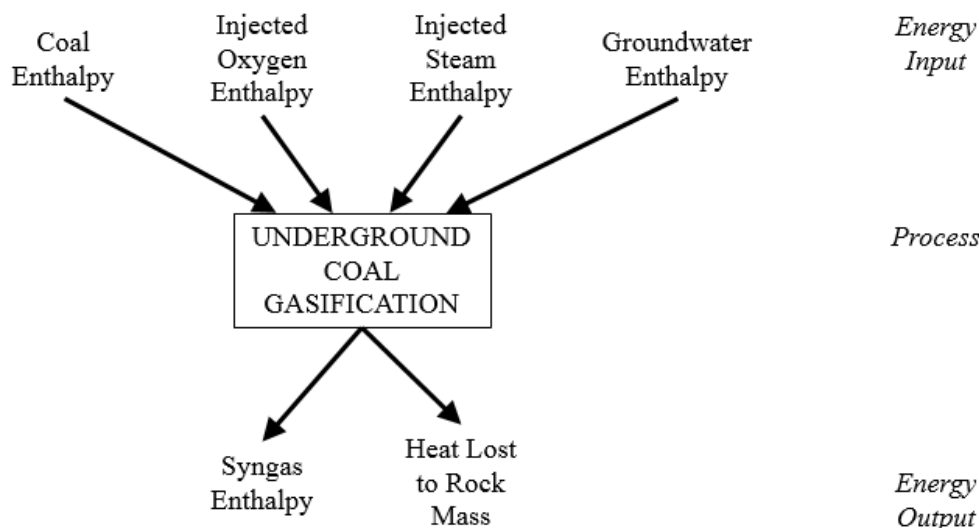


Figure 5.9 – Principal sources and sinks of thermal energy over the entire underground coal gasification process.

Knowing the flow rate and composition of the syngas, as well as the elemental composition of the coal, it is possible to calculate the amounts of water and oxygen required by the UCG process. This water is supplied by both injected steam and inflowing groundwater. The amount contributed by groundwater can be found from the UDEC hydraulic model, allowing the amount supplied by steam to be found through subtraction. Because groundwater has a lower specific enthalpy than steam, the total amount of energy in the system decreases as groundwater flow rate increases. As the enthalpy of the syngas is fixed, this reduction in energy manifests as a reduction in the heat lost to the rock mass. This is expressed in the UDEC model as a reduction in cavity wall temperature.

Working through the above energy balance gives a linear relationship between flow rate and temperature, as shown in Equation 5.12. The full derivation for this equation is given in Appendix B.4.

$$T_w = 1153 - 4.1 \times 10^6 q \quad (5.12)$$

Where:

q is the total flowrate of groundwater into the modelled cavity $(\text{m}^2\text{s}^{-1})$.

T_w is cavity wall temperature (K)

Initial model results give a value for q of approximately $5.4 \times 10^{-13} \text{ m}^2\text{s}^{-1}$ during operation. As such, groundwater inflow is seen to have a negligible effect on cavity wall temperature and the assumption of a flow rate independent wall temperature is seen to be justified. It is of note that Equation 5.12 gives a lower wall temperature than that used in the model (given by Perkins and Sahajwalla, 2008). It is believed that this discrepancy is due to oversimplification in the derivation of Equation 5.12. For this reason, the UCG model continues use the temperature suggested by Perkins and Sahajwalla. Given the very low influence of flow rate on wall temperature, this decision is believed to be justified.

5.6.3.4 Temperature Dependent Fluid Properties and Boiling Effects

As mentioned in Section 3.5.2, UDEC has the capability to set fluid density and viscosity as functions of temperature, however these capabilities fail for temperatures near the boiling point of the fluid. A number of attempts have been made to solve this issue, though none have been successful.

The simplest method to approximate boiling is to replace the discontinuity in density with a gradual change. While this reduces stresses in some locations, it has no effect in regions where temperature changes suddenly. Another method would be to insert coupled mechanical/hydraulic steps within the thermal model. This would allow pressure and density to redistribute, reducing the chances of failure. The addition of these steps would greatly increase runtime however, given how often would they need to be called. In addition, this method will still fail close to boundary conditions, as sudden spatial temperature changes will still give sudden temporal density changes.

The final method for incorporating fluid/thermal coupling uses a semi-analytical relationship between temperature and flow rate. Deriving such a relationship is a complex matter however. Assuming the temperature profile is known for the fluid, groundwater behaviour depends on three unknown variables; velocity, pressure and density. These three variables are interdependent and all are discontinuous at the interface between water and steam. As such, any relationship between the three cannot be solved analytically. While it may be possible to solve the relationship numerically, doing so is difficult due to the the discrepancy between hydraulic and thermal timescales. In order to accurately capture fluid behaviour, any model would have to use very small length elements and run for a large number of timesteps (Abdallah *et al*, 1995; Jing & Stephansson, 2007; Tomac & Gutierrez, 2015). Given the minor influence of thermal behaviour on results, the complications of creating such a model are not considered to be justified in the context of this work. It is assumed that boiling is a slow enough process that it does not affect UCG induced environmental effects, however this is not known. As such, it is suggested that further work should be performed in order to better understand this process.

5.7 CONCLUDING REMARKS

The model presented in this chapter is believed to provide a good representation of the local environmental effects of underground coal gasification. The accuracy and repeatability of the model are considered to be sufficient for the model's intended end use as a first pass screening tool, however there are some limitations to the model.

A termination criterion based on subsidence behaviour has been developed to identify when the model has converged, however this can lead to inaccurate results. Initial results suggest that this issue is rare however, and can usually be identified if and when it occurs. The criterion is generally seen to be sufficient for the degree of accuracy required by the model, however further development may be required if the model is to be used for in depth investigations over longer timescales.

A second drawback of the model is the relative inaccuracy of the thermal simulation. Given the minor influence of thermal effects on environmental issues however, this is not considered to be an important area for consideration. In addition, many of the thermal effects present in UCG cannot be realistically modelled in UDEC without greatly increasing the runtime of the model. While the simplification of thermal effects is considered to be justified with respects to this model, further developments are suggested which could improve the usefulness of environmental models and increase our understanding of the coupled thermal, hydraulic and mechanical behaviour of UCG overburden. While such developments are outside the scope of this project they may be very important in the design of future models, particularly those used to provide in-depth environmental assessments of single sites.

In conclusion, the coupled model developed in UDEC is deemed to be sufficient for its intended use as a first pass screening tool for assessment of large numbers of potential UCG site designs. While further developments may increase model accuracy, these should instead be applied to more specialised models dealing with single sites, in which practical simulation runtimes can be much longer. The validity of this model for its use as an assessment tool is discussed further in Chapters 6 and 7, while its application to a wide range of sites is presented in Chapter 8.

6. INTERNAL PARAMETER EFFECTS

SUMMARY

This chapter investigates the effects of various internal parameters on the results and behaviour of the underground coal gasification (UCG) model presented in Chapter 5. Internal parameters are defined as those model variables which are arbitrarily chosen, rather than being based on site design considerations. Many of these parameters are shown to have a considerable influence on the results, runtime and stability of the model. Given that these parameters have little or no basis in reality, these effects must be understood in order to ensure that predictive results are not skewed by their influence. As such, these tests act as a form of model validation, ensuring that trends in predictive results are caused by site design and operating conditions, rather than arbitrary internal parameters.

The results in this chapter show that internal geometric parameters have the greatest effect on model behaviour. The dimensions of the discrete fracture network (DFN), zone density and joint material properties are seen to have a considerable influence on results. It is for this reason that the final model bases as many of these parameters as possible on cavity geometry and reliably sourced literature data.

In addition to the above effect, results in this chapter highlight a number of limitations of the model. In all cases, the reason behind these limitations is identified and solutions are put forward. As such, the model is considered to be valid for use in future predictive modelling efforts.

6.1. INTRODUCTION

As shown in Chapter 5, the behaviour of the Universal Distinct Element Code (UDEC) model depends on a large number of parameters which have little or no basis in real, physical measurements. This chapter aims to examine how these parameters affect model behaviour. In this work, internal parameters are defined as those model properties which are neither based on site design (e.g. cavity geometry) nor previous results (e.g. rock mass properties). Internal parameters were initially chosen arbitrarily, based on experience from the literature or the default settings in UDEC. Further developments then adjusted these parameters to give desirable behaviour in the final model. Once this behaviour was achieved, structured testing was performed to identify trends in how these parameters affect behaviour and better understand the operation of the model.

The results presented in this chapter are based on a number of tests in which the final model has been altered in various ways. These alterations generally involve changing one or more internal parameters. The influence of these parameters on model results, are analysed in order to further prove the validity of the model and identify any important limitations in its application.

6.2. STANDARD MODEL

In order to determine the effects of various parameters on results, it is essential to have a standard case against which variations can be compared. This model is identical to that presented in Chapter 5, and represents the final model design used in Chapters 7 and 8. The model has been run 10 times in order to obtain information on the variability of results. The model with results closest to the mean value is chosen as a benchmark. Wherever possible, studies have used the same random seed as the benchmark model in order to eliminate random variation. In cases where this is not possible, models are repeated 3 times and mean results presented.

Figures 6.1 through 6.3 show the subsidence profile, pore pressure and temperature distribution for the model. A summary of these results is given in Table 6.1. Results are reported as the mean and standard deviation over 10 trials. The arithmetic mean is used for the runtime, mechanical and thermal results, while the geometric mean is used for the hydraulic results due to the increased variability seen in these results. Hydraulic errors are therefore given as multiplicative, rather than additive, indicated by prefixing with an “x”. For example, a value of $28.2 \pm x2.8$ mL/day implies a range of results from 10.1 to 79.0 mL/day. Flowrates are produced by the model in units of m^2s^{-1} and are converted to mL/day to aid in comprehension. This conversion assumes that flow rate is constant along the length of a 600m long channel. This length was chosen to be equal to that of the Bloodwood Creek field trial (Mark & Mallett, 2008).

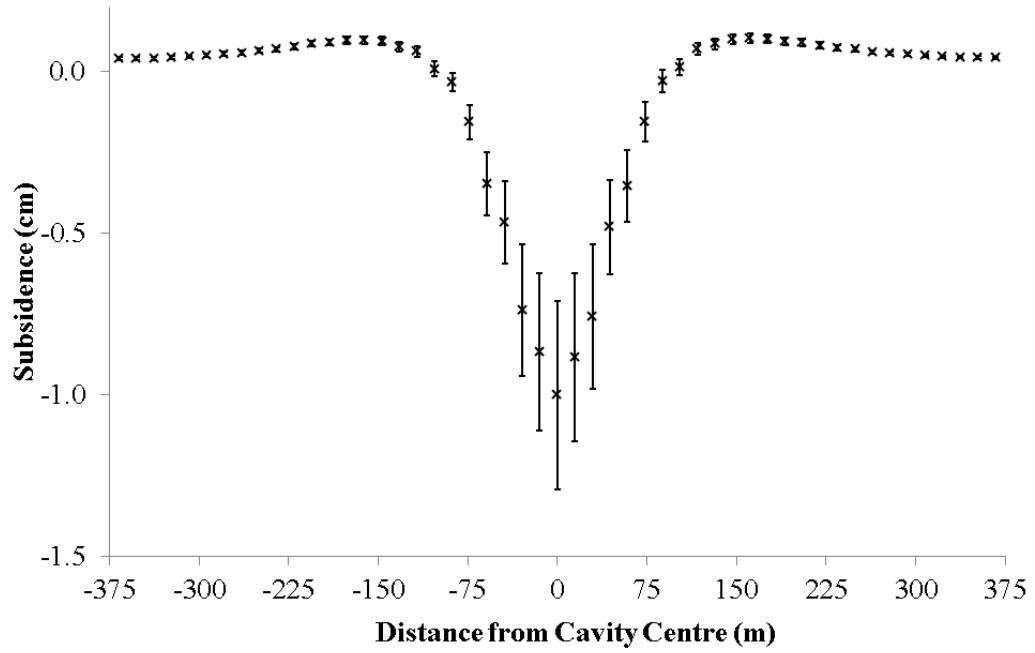


Figure 6.1 – Simulated subsidence profile for the initial UCG model.

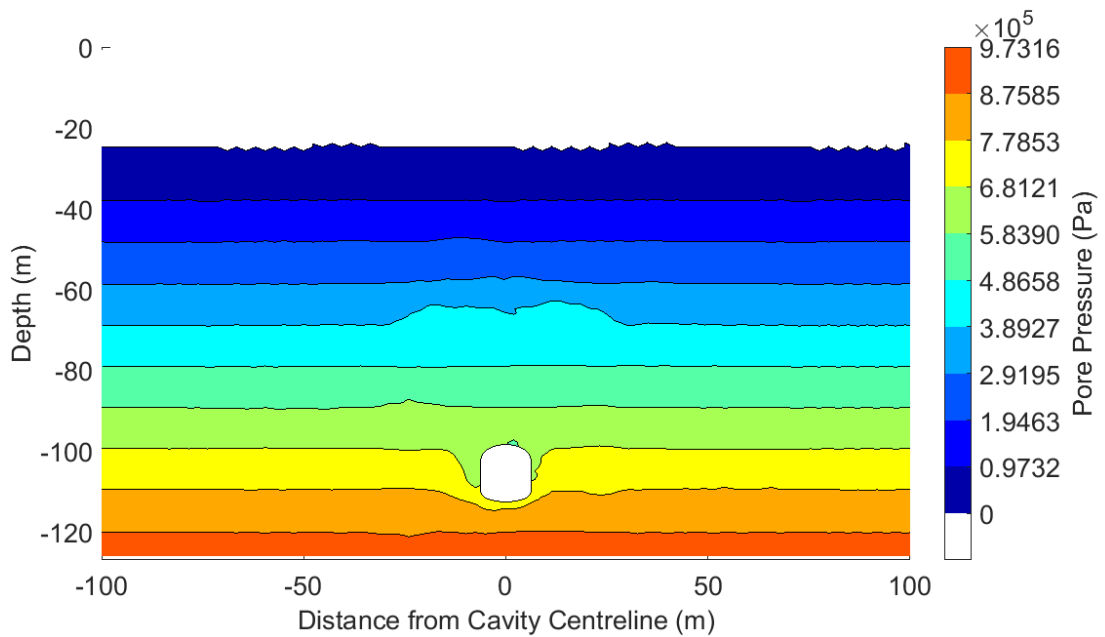


Figure 6.2 – Simulated pore pressure distribution for the initial UCG model.

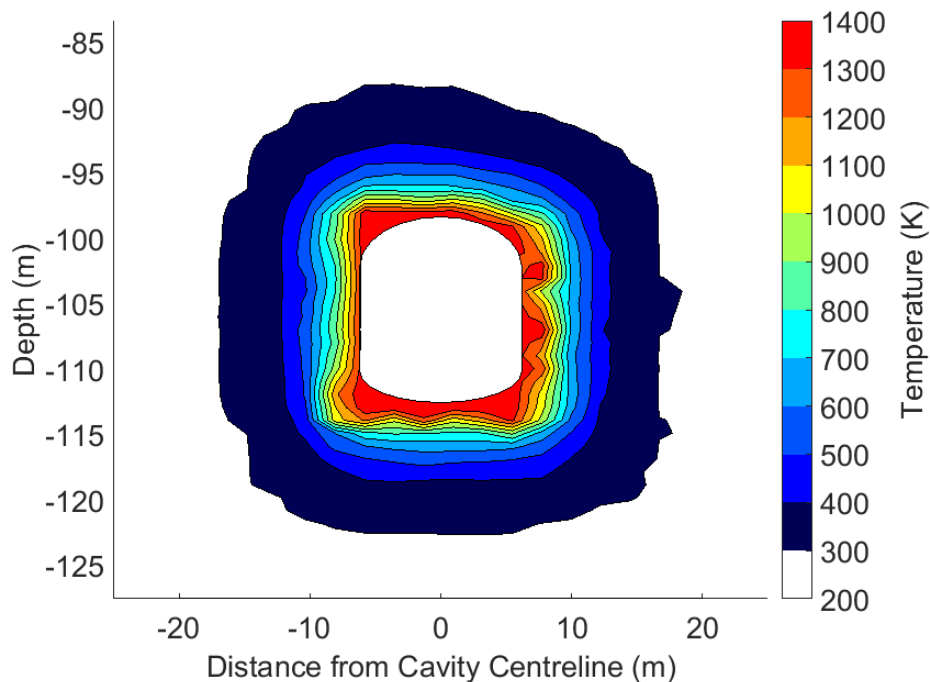


Figure 6.3 – Simulated temperature distribution for initial UCG model.

Table 6.1 – Selected results from base case UCG model.

Property	Value
Runtime (hrs)	37 ± 7
Maximum Subsidence (cm)	1.00 ± 0.29
Water Table Lowering (m)	Negligible
Groundwater Inflow Rate (mL/day)	$28.2 \pm x2.8$
Thermal Penetration Length (m)	9.62 ± 1.36

As seen above, the model usually takes around 1.5 days to solve. Throughout this chapter, reported runtimes were measured when the model was one of seven simultaneous executions. As such, the average time taken to obtain a single result is found as 5.3 ± 1.0 hours. This is well within the model aim of producing results within 24 hours, as outlined in Section 1.4.2.

The subsidence profile predicted by the model gives the expected shape for a small shallow cavity. The profile is found to have an angle of draw of 44° and a subsidence factor of 0.59, notably different to those suggested by the literature (Brown, 2012; Gregg, 1977). The variability shown over the 10 trials is considered acceptable in comparison with that seen in reality for a highly fractured rock mass. It is of note that a small amount of heave is observed at the model edges. Heave refers to the upward movement of the rock mass relative to its initial location. The small amounts of heave seen in these results are principally caused by rounding errors. Given the relative extents of heave and maximum subsidence, this error is considered acceptable.

Hydraulic results show that although groundwater flow is present at the site, the effect of UCG on the water table is negligible. Spatial variations in water table height are caused by the semi-random nature of the joint pattern. Despite a large variability, the groundwater flow rate into the cavity is low enough to be replenished by natural flows in all but the driest of sites. The large variability in results is caused by the random nature of the DFN affecting local permeability. This variability somewhat reduces the reliability of the hydraulic model, however the results are considered accurate enough for the intended end use of the model, especially given the intent to produce further hydraulic models at a later date.

The thermal penetration length of the model is well within the range expected from the literature (Yang, 2005), and produces results with reasonably low variability. This suggests that the thermal model is sufficiently accurate for use, despite the large number of assumptions and simplifications involved.

6.3. EFFECTS OF DISCRETE FRACTURE NETWORK DIMENSIONS

The size, number and orientation of the blocks which comprise a discrete element model have a profound impact on the overall behaviour of that model. This has already been demonstrated in Chapter 4. Within the UCG model, geometry depends on the size of both the fine region itself and the blocks within it. Block geometry is in turn dependent on the density and isotropy of the joints which delineate the blocks themselves.

6.3.1 Discrete Fracture Network Region Height

As mentioned in Section 5.2.1, the dimensions of the DFN region are defined as multiples of cavity dimension. In the base case, the height of the DFN region is given as four times the maximum height of the cavity. In this study, models were produced with varying ratios of DFN to cavity height. Table 6.2 shows the results of these tests.

Table 6.2 – Effects of DFN height on UCG model results. The standard case is highlighted in bold

DFN/Cavity Height Ratio (-)	Model Runtime (hrs)	Maximum Subsidence (cm)	Groundwater Inflow Rate (mL/day)	Thermal Penetration Length (m)
2.00	31 ± 10	0.66 ± 0.14	117.2 ± x2.3	9.34 ± 1.69
2.83	38 ± 14	0.79 ± 0.05	154.7 ± x1.6	9.51 ± 1.17
4.00	37 ± 7	1.00 ± 0.29	28.2 ± x2.8	9.62 ± 1.36
5.66	43 ± 6	1.07 ± 0.21	42.6 ± x17.2	9.13 ± 1.50
8.00	89 ± 29	4.65 ± 2.29	25.9 ± x1.3	11.21 ± 1.09

As seen above, variations in the height of the DFN have a considerable influence on many aspects of the model. Increases in height tend to have little effect on solution speed, however a large jump in runtime is seen between the two tallest models. Runtime should be independent of DFN height, due to the size dependent joint density explained in Section 5.2.2. It is seen however, that the density function fails somewhat for extreme values of height. The models with the tallest DFNs were seen to have up to 50% more blocks than the initial model, leading to the observed increases in both the magnitude and variability of model runtimes.

In addition to runtime, the increased number of blocks in the models with the tallest DFNs leads to an increase in subsidence as the relative area of joints (weak) to blocks (strong) increases. This effect is seen at all values of DFN height and is exacerbated by the increase in the relative size of the DFN compared with the coarse region of the model. The dependence of subsidence on DFN height is problematic, as it may mask the influence of the site geometry on results. For example, because DFN height changes with cavity height, it is difficult to know how much of the effect of changing cavity height is due to physical changes, and how much is due to DFN geometry. It is hoped that maintaining a constant cavity to DFN height ratio will alleviate this problem somewhat, allowing the model to produce reliable results across a range of designs. It is suggested however, that further investigations and validation work should be performed to ensure this reliability.

The relationship between DFN height and groundwater flow rate is seen to be complex. Flow rates are seen to decrease with increasing DFN height, however the scale of errors in the hydraulic results are large. As such, it is unknown whether the effects of DFN height on flow rate are caused by a defined relationship between the two quantities or whether they are simply the result of random variations. The fact that flowrates appear to decrease with DFN height is also unexpected, as the increased number of joints in the taller DFNs should increase permeability and therefore flowrate. As with the effects on subsidence, it is therefore seen that hydraulic results may be detrimentally affected by DFN height

Finally, it is of note that thermal results are generally unaffected by DFN geometry, with mean results seen to be within error for all values of height. It is important to note however, that in the shortest case, the thermal penetration length extends above the DFN and into the coarse zone of the model. As seen in Figure 6.4, this distorts the temperature profile around the cavity as heat enters the much larger blocks of the coarse zone. In order to account for this issue, the thermal penetration length in these models is not measured in this direction. This issue may be resolved by specifying a minimum height for DFNs, however this was not implemented in the UCG model due to the complex effects of DFN height on the other results of the model.

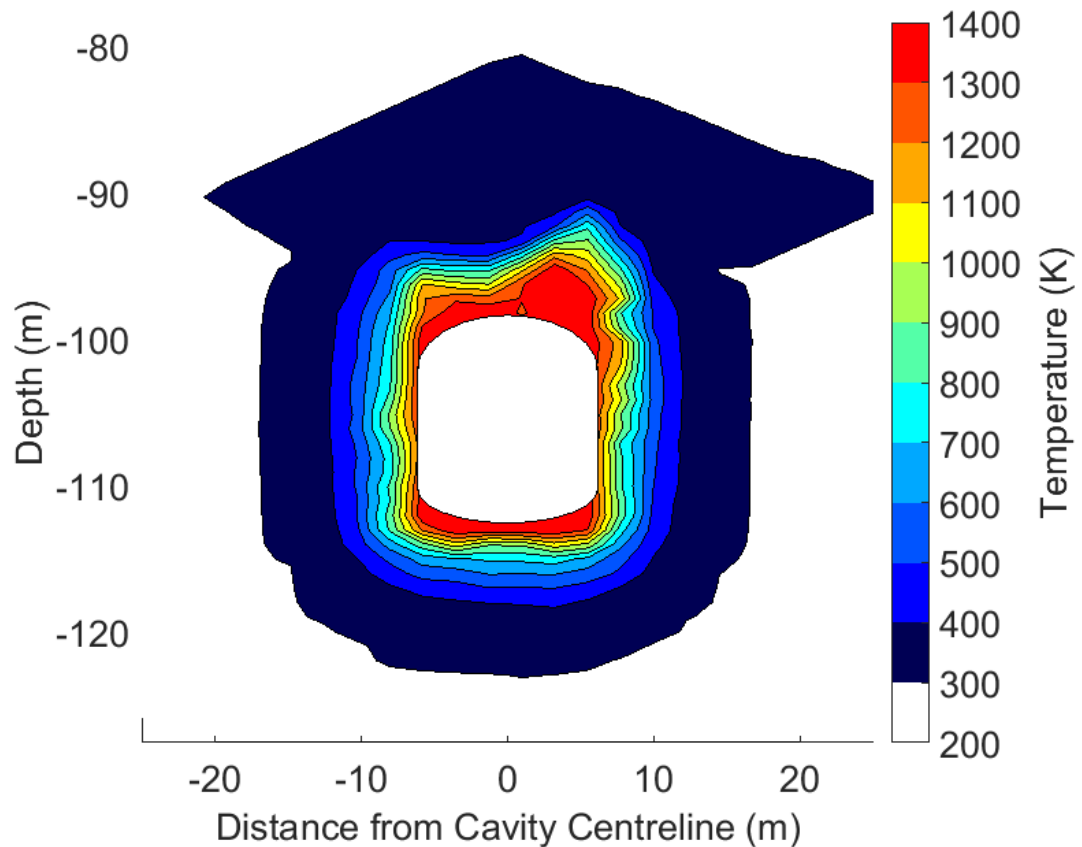


Figure 6.4 - Temperature profile for a model with a DFN/cavity height ratio of 2.0.

The results in this section show that DFN height has a powerful and detrimental effect on the behaviour of the UCG model. For this reason all future models will ensure a constant ratio of DFN height to cavity height, in an attempt to reduce these effects. As such, all future models will use a constant height ratio of 4.00, including both the field trial validation studies in Chapter 7 and the initial predictive results in Chapter 8. It is hoped that the results of these tests will show that the use of a constant DFN geometry leads to a reliable and accurate predictive model.

6.3.2. Discrete Fracture Network Region Width

The effects of DFN width on model results are shown in Table 6.3.

Table 6.3 – Effects of DFN/cavity width ratio on UCG model results. The standard case is highlighted in bold.

DFN/Cavity	Model	Maximum	Groundwater	Thermal
Width Ratio	Runtime	Subsidence	Inflow Rate	Penetration
(-)	(hrs)	(cm)	(mL/day)	Length (m)
1.50	46 ± 11	0.57 ± 0.04	1824.3 ± x2.4	8.44 ± 1.11
2.12	49 ± 12	0.83 ± 0.05	63.5 ± x1.6	9.03 ± 0.90
3.00	37 ± 7	1.00 ± 0.29	28.2 ± x2.8	9.62 ± 1.36
4.24	25 ± 3	1.05 ± 0.13	16.7 ± x1.2	10.72 ± 1.12
6.00	46 ± 19	1.51 ± 0.42	9.00 ± x2.8	10.19 ± 1.26

The effects of DFN width are seen to follow similar trends to those seen for DFN height. Subsidence is seen to increase with DFN width as the relative size of the highly fractured region increases. The effect is considerably weaker than that seen with height however. The influence of height is found to be stronger because of the way in which DFN joint length is defined. As shown in Table 5.3, the length of joints in the DFN depends on the maximum dimension of the DFN. In all but two cases (width ratio 6.00 and height ratio 2.00), DFN height is greater than DFN width. As such, changing DFN height has a greater impact on joint pattern than changing DFN width, leading to a greater influence on the mechanical results of the model.

Unlike with height, changing DFN width is seen to have little effect on runtime. Although changes are observed, the variations are usually within error, and no discernible trend is seen. In comparison with height, it is found that altering DFN width has no effect on the total number of blocks in the model. This is primarily caused by the dependence of joint length on DFN height, as mentioned above. These observations suggest that both the total number of blocks and the overall behaviour of the model depends greatly on whichever of the two DFN dimensions is the largest. This is not considered a problem however, unless the dimensions of the cavity (and thus the DFN) are very different from each other. Given the nature of the process, this is not expected to occur for UCG. As such, the issue is not considered to be important.

As with DFN height, groundwater flow rates are found to decrease as DFN width is increased. Again this is unexpected, given that larger DFNs correspond to larger areas with high permeability. The trends in flowrate seen with DFN size therefore suggest that some other factor has a greater influence on flowrate than the number of joints near the cavity. It is seen that models with smaller DFNs tend to have larger joint apertures in the DFN region. In the models with the smallest DFNs, a discontinuity in flowrate is seen at the boundary between the DFN and coarse regions of the model. As the coarse region contains fewer joints, the apertures in this region must increase in order to maintain flow. In models with small DFNs, the apertures inside the DFN are also increased due to the influence of the boundary with the coarse region. This effect increases permeability in the small DFNs and therefore increases flowrate. While this effect may reduce the accuracy of the hydraulic model, it is considered to be valid, provided that the ratios of DFN to cavity dimensions are held constant. As such, all further models will use a height ratio of 4.00 and a width ratio of 3.00.

Finally, thermal penetration length is seen to increase with width. This is expected, given that wider DFNs contain wider blocks. As the maximum temperature profile is discretised to the level of the blocks, wider DFNs stretch the temperature profile in the horizontal dimension. It is of note that while a trend in length is observed, many of the results are within the expected level of error from the standard case. As such, part of this trend is found to be caused simply by random variations in results. As seen in Section 6.3.1, temperature profiles for the narrowest DFNs are seen to extend into the coarse zone of the model. To prevent distortion of results, temperature profile lengths are therefore not measured in the horizontal direction. As with the effects of height, this may be resolved with the use of a minimum DFN width, however this has not been carried out in order to reduce the other effects of DFN geometry on results.

6.3.3. Discrete Fracture Network Joint Density

Table 6.4 shows the effects of joint density on model results. Density was varied by altering the value of the intended number of blocks N in Equation 6.1.

$$\rho_J = \frac{2\sqrt{N}}{(W_D H_D)^{1.012}} \quad (6.1)$$

Where:

H_D	Height of DFN region	(m)
N	Intended number of blocks	(-)
W_D	Width of DFN region	(m)
ρ_J	Joint Density	(m ⁻²)

Table 6.4 – Effects of DFN joint density on model results. The standard case is highlighted in bold.

Intended number of blocks (-)	Model Runtime (hrs)	Maximum Subsidence (cm)	Groundwater Inflow Rate (mL/day)	Thermal Penetration Length (m)
500	17 ± 4	0.79 ± 0.14	38.7 ± x1.4	10.51 ± 1.40
1000	35 ± 25	0.85 ± 0.39	14.5 ± x1.3	9.32 ± 2.20
2000	37 ± 7	1.00 ± 0.29	28.2 ± x2.8	9.62 ± 1.36
4000	58 ± 7	0.97 ± 0.10	76.0 ± x1.6	8.63 ± 1.31
8000	Model failed to generate joint pattern.			

Many of the trends seen in Table 6.4 are to be expected. Increased densities lead to greater runtimes due to the larger number of blocks in the model. Groundwater flow rates are generally seen to increase with density, as permeability in the DFN is improved. The effect of density on flow rate is seen to be much less than that of DFN width or height however, suggesting that the proximity of the coarse region is a more important factor in results. Furthermore, the scale of variability in the hydraulic results suggests that these observations are in part due to random variations. Thermal penetration length is seen to gradually decrease with density, however the decrease is dwarfed by the uncertainty in results. This decrease is to be expected given that the maximum temperature profile is found on a block by block basis, and higher densities produce smaller blocks.

Finally, increased joint density is seen to lead to increased subsidence. This is to be expected, as higher densities imply greater fracturing and a behaviour which is more dependent on joints than blocks. Overall, the weak dependence of results on DFN density is beneficial, as it shows that model behaviour is more dependent on physical (cavity) than nonphysical (DFN) geometry. In addition, these results give further evidence that maintaining constant DFN size is beneficial to model accuracy. As such, an intended block number of 2,000 is used in all future models.

6.3.4. Discrete Fracture Network Joint Isotropy

Joint isotropy refers to the standard deviation of joint angles in the DFN. Low isotropy produces patterns with joints aligned close to parallel with the horizontal or vertical axes, while high deviations lead to patterns with more randomly distributed joint orientations. Table 6.5 shows the effect of joint isotropy on model results.

Table 6.5 – Effects of joint angle variance on model results. The standard case is highlighted in bold.

Joint Angle	Model	Maximum	Groundwater	Thermal
Standard	Runtime	Subsidence	Inflow Rate	Penetration
Deviation (°)	(hrs)	(cm)	(mL/day)	Length (m)
5.00	36 ± 4	0.83 ± 0.11	15.7 ± x4.4	8.89 ± 1.10
7.07	37 ± 9	0.97 ± 0.04	89.3 ± x1.2	10.14 ± 0.98
10.00	37 ± 7	1.00 ± 0.29	28.2 ± x2.8	9.62 ± 1.36
14.14	66 ± 14	0.99 ± 0.62	24.0 ± x8.1	9.15 ± 2.22
20.00	71 ± 19	1.14 ± 0.35	7.59 ± x17.6	10.61 ± 0.56

As seen above, joint isotropy has little effect on thermal model results. Although penetration length is seen to vary considerably between tests, neither the magnitude nor variability has any direct correlation with isotropy. Groundwater inflow rates are also seen to be generally unaffected by isotropy, however the variability in these results increases greatly with joint standard deviation. This is to be expected, given that flow behaviour depends heavily on joint orientation, and that increasing isotropy effectively increases the randomness of the joint pattern.

The magnitude and variability of both runtime and subsidence are also seen to increase with isotropy. The effect on subsidence is to be expected, as Section 4.3.1 shows that isotropic rock masses are weaker than those with perpendicular joints. The effects on runtime and result variability are caused by an increase in the number of blocks as the DFN becomes more isotropic. A more uniform distribution of joint orientation is seen to give greater numbers of blocks as the likelihood of joints intersecting each other increases with isotropy. Overall, these results show that maintaining a reasonably low level of joint isotropy is an important step in designing a realistic model of highly fractured rock masses. A deviation of 10 degrees is considered low enough to achieve this while still ensuring a reasonable degree of variability in results.

6.4. EFFECTS OF COARSE REGION DIMENSIONS

As with the blocks in the DFN, the dimensions of the blocks in the coarse region of the model may affect results. This section investigates these effects. Unlike the DFN region, the blocks in the coarse region follow a completely deterministic pattern. As such, all tests were performed only once, using the same random seed in all cases.

6.4.1 Coarse Region Block Height

The height of the blocks in the coarse region is expressed as a fraction of cavity depth. The effects of this height on results were tested, and the results of these tests are shown in Table 6.6.

Table 6.6 – Effects of coarse region block height on UCG model results. The standard case is highlighted in bold.

Block Height / Cavity Depth Fraction (-)	Model Runtime (hrs)	Maximum Subsidence (cm)	Groundwater Inflow Rate (mL/day)	Thermal Penetration Length (m)
2.50%	Model failed due to block overlap errors.			
3.54%	38	0.92	27.4	10.64
5.00%	31	0.82	26.3	10.36
7.07%	23	0.87	29.0	10.29
10.0%	19	0.86	25.2	10.38

As seen above, the height of blocks in the coarse region of the model has little influence on results, though runtime is affected to a noticeable degree. The effect on runtime is expected as the increase in height corresponds to a reduction in the total number of blocks in the model. It is interesting to note that the variation in runtime is of a similar order to that given by varying DFN joint density. This is unexpected, given that the model contains approximately 10 times as many blocks in the DFN as in the coarse region. As such, changes in the size of coarse blocks would be expected to have a much smaller effect on runtime. This suggests that it is actually the number of zones which has the greatest effect on runtime, as this is considerably reduced in models with larger coarse blocks.

The apparent independence of results on coarse block geometry is beneficial, as it suggests that model behaviour is unaffected by this semi-physical parameter. One aspect of model results which is affected however, is the accuracy of the pore pressure distribution. As smaller blocks reduce the number of zones in the model, they also reduce the resolution of the hydraulic result. This produces a pore pressure distribution with a much greater degree of spatial variability, as seen in Figure 6.5. As this result is important for the determination of water table lowering effects, such a reduction in accuracy is unacceptable. As such, the final model will continue to use a block height equal to 5% of cavity depth. It is believed that the increase in runtime caused by this decision is justified, given the increase in accuracy and the fact that many results can still be produced within a single day.

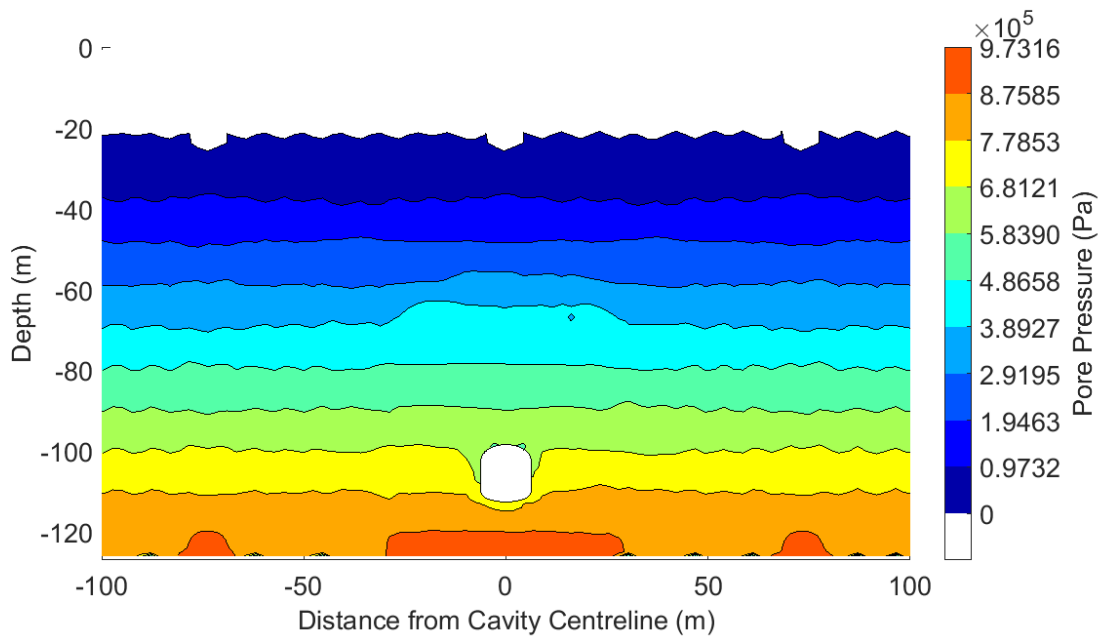


Figure 6.5 – Pore pressure distribution for a model with a coarse block height equal to 10% of cavity depth, showing considerable spatial variability.

6.4.2. Coarse Region Block Width

The influence of block width on model behaviour is seen to be stronger than that of block height. As with height, block width is expressed as a fraction of total model width. The results of investigations into the effect of block width are presented in Table 6.7.

Table 6.7 – Effects of coarse region block width on UCG model results. The standard case is highlighted in bold.

Block/Model	Model	Maximum	Groundwater	Thermal
Width	Runtime	Subsidence	Inflow Rate	Penetration
Fraction (-)	(hrs)	(cm)	(mL/day)	Length (m)
2.5%	56	0.97	61.0	10.76
5.0%	41	0.81	56.0	9.56
10.0%	31	0.82	26.3	10.36
20.0%	18	0.85	25.3	Failed
33.3%	Model failed due to block overlap errors			

Block width is seen to have a similar influence on runtime to block height, further suggesting that zone geometry has a more important effect on runtime than block geometry. Mechanical results are seen to be mostly unaffected by block width, though the thinnest model gave increased subsidence. This error is within the expected level of variation however, suggesting there is no relationship between these properties.

Although the change is relatively minor, coarse region width produces a defined trend in hydraulic behaviour, with thinner blocks giving increased flow rates. This effect is due to a reduction in tortuosity. As blocks get thinner, the path of a fluid travelling vertically through a brickwork pattern gets shorter. This reduces flow path length and therefore increases the flow rate achieved from a given pressure gradient. The small increase in flow rate compared with the difference in width suggests that this effect has only a minor influence on behaviour. Given the considerably reduced number of joints in the coarse region compared with the fine region, this is expected.

Thermal penetration lengths are seen to have no discernible trend with block width. This is to be expected given that the thermally altered region of the rock mass is entirely within the DFN. It is of note however, that the thermal model failed to solve for the 20.0% model. It is believed that this occurred because of the increased size of the zones in the coarse region. As shown in Appendix A.3, the thermal algorithm depends heavily on the size of the zones within the model. The greater difference in zone size between the two regions is therefore believed to have destabilised the thermal algorithm. Given the above results, it is therefore suggested that block widths should be limited to no more than 10% of model width in all future trials.

6.5. EFFECTS OF MODEL WIDTH

Model width affects behaviour by providing a separation between the region of interest (i.e. the cavity) and the applied boundary conditions. Decreases in width can negatively affect behaviour by imposing boundary effects close to the cavity. Increases in width should have no effects on behaviour above a critical value at which the cavity is sufficiently far from the boundary conditions. Model width is defined as given in Equation 6.2. Tests were performed by altering the value of the width factor k_W . Table 6.8 shows the results of these tests.

$$W_M = k_W \left[W_C + \frac{2D_C}{\tan(\gamma)} \right] \quad (6.2)$$

Where:

D	Depth	(m)
k_W	Width factor	(-)
W	Width	(m)
γ	Angle of Draw	(35°)

Subscripts:

C	Cavity
M	Model

Table 6.8 – Effects of model width factor on model results. The standard case is highlighted in bold.

Width Factor	Model Runtime (-) (hrs)	Maximum Subsidence (cm)	Groundwater Inflow Rate (mL/day)	Thermal Penetration Length (m)
1.0	27	0.56	29.6	8.98
1.5	34	0.85	33.4	10.51
2.0	29	0.89	56.2	10.58
2.5	31	0.82	26.3	10.36
3.0	30	0.87	36.8	11.08

As seen above, model width has little influence on behaviour. Results for runtime, subsidence, flow rate and thermal penetration length are seen to be constant within error across all width ratios greater than 1.0. The considerable reductions in subsidence and penetration length for the thinnest model show that edge effects are affecting results for this model. The above observations therefore suggest that the minimum required width ratio for the model is somewhere between 1.0 and 1.5. These observations do not take into account the behaviour away from the cavity however.

Figure 6.6 shows the subsidence profiles for the models with varying widths. Only one half of each profile is shown to more clearly demonstrate model behaviour at the boundaries. It is clearly seen that as width increases, heave at model edges decreases, before stabilising at a ratio of 2.5. The heave at this ratio is small enough to be considered negligible, and as such, a width ratio of 2.5 is considered sufficient for use in all further models.

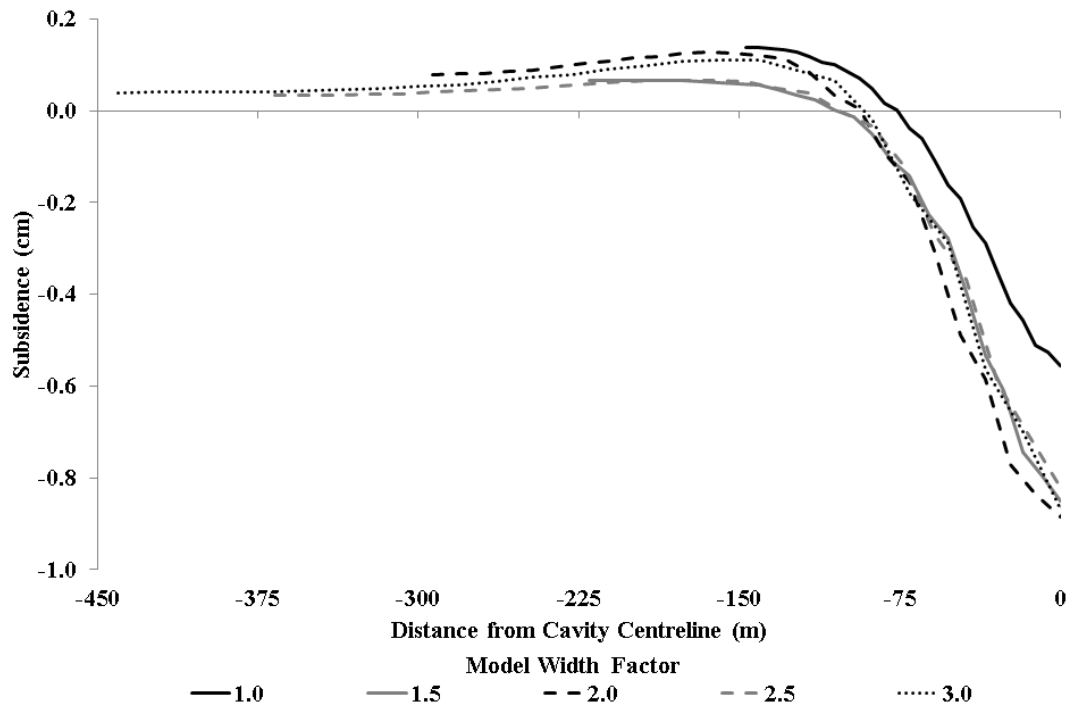


Figure 6.6 – Effects of model with on the behaviour of subsidence profiles.

6.6. EFFECTS OF ZONE SIZE

As previously mentioned, the behaviour of a UDEC model depends on the number of finite difference zones within that model. Rather than being set directly, the number of zones is determined by their average edge length. In the UCG model, the average edge lengths in the fine and coarse zones are based on other aspects of model geometry, as shown in Section 5.2.2. In order to maintain consistency throughout the following tests, edge lengths in both regions were multiplied by the same scaling factor. Table 6.9 shows the effects of these tests. Zone densities are reported for both the fine and coarse regions of each model.

Table 6.9 – Effects of zone edge lengths on model results. The standard case is highlighted in bold.

Zone Edge Length Scaling Factor (-)	Zone Density (fine / coarse) (m⁻²)	Model Runtime (hrs)	Maximum Subsidence (cm)	Groundwater Inflow Rate (mL/day)	Thermal Penetration Length (m)
0.500	3.79 / 0.022	112	1.31	554.4	10.28
0.707	1.89 / 0.011	46	0.96	69.6	9.33
1.000	0.95 / 0.006	31	0.82	26.3	10.36
1.414	0.47 / 0.003	23	0.81	17.4	9.02
2.000	0.24 / 0.001	18	0.91	29.2	10.39

As shown above, zone density has little effect on model results for scaling factors greater than 0.707. Zone density is seen to have a strong effect on runtime however, with an approximately exponential relationship between the two. This is the single greatest contributor to the computational demands of the model and explains the lack of influence seen with block geometry. These results therefore suggest that in order to produce fast model results, zone density should be set at the lowest possible value which still ensures accurate results.

The lack of influence on model results at high scaling factors is an interesting observation, as it suggests that density is high enough even in these models to avoid mesh dependency. It is therefore counterintuitive that results appear to diverge for low scaling factors and high densities. In theory, results should be approximately constant between high density models, with low density tests producing erroneous behaviour. This discrepancy between theory and observation suggests that some previously undetected scale dependent behaviour is occurring within the model. As with the effect of model width, the influence of zone density on results can be further explored by considering the full subsidence profiles predicted by the models tested. Figure 6.7 shows these subsidence profiles. In order to highlight the different behaviours observed, the profiles have been cropped to show only half of the full subsidence profile.

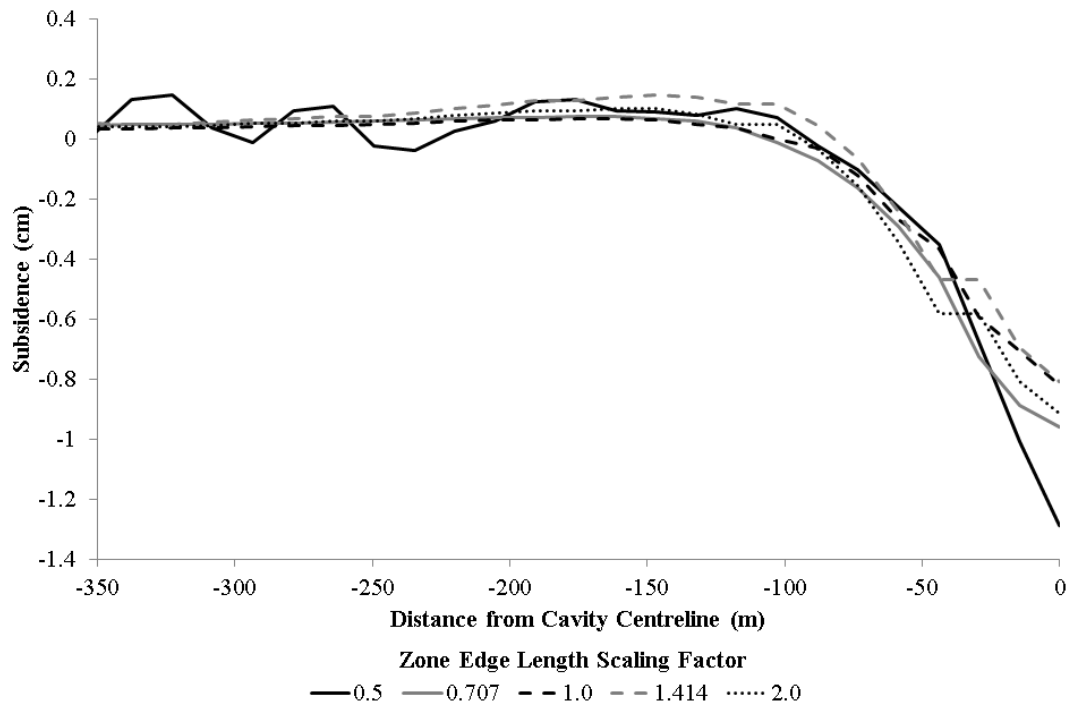


Figure 6.7 – Half subsidence profiles for models with varying zone edge lengths.

It can clearly be seen that a scaling factor of 0.5 produces a subsidence profile with an incorrect shape. This, coupled with the high groundwater flow rate and extreme runtime, show that this model has failed to solve correctly. As such, scaling factors less than 0.707 should not be used in further models. Results for scaling factors of 1.414 and 2.0 show appropriate behaviour at the centreline and edges, but are seen to give a discontinuity in subsidence approximately 40m from the cavity centre. This discontinuity is physically unrealistic and is caused by a lack of adequate resolution in the coarse region of the model at low zone densities. Based on these results, it is suggested that an upper limit of 1.0 should be set on the zone scaling factor.

Results for scaling factors of 0.707 and 1.0 are seen to give the expected profile shape. As seen in Table 6.9 however, the high density model gives a distinct increase in groundwater flow rate. Given the constant (within error) flowrates seen at lower zone densities, it is believed that this effect is the beginning of the considerable increase in flowrate seen with the 0.5 model. As seen in Table 6.9, the reduction of the scaling factor from 1.0 to 0.707 also leads to a notable increase in runtime. For these reasons, as well as that of simplicity, it was decided that future models should continue to use a scaling factor of 1.0. It is of note however that the results of both the 1.0 and 0.707 models are within expected values for all measurements. Given that increasing zone density should theoretically increase accuracy, it may be that future models use the lower version of edge scaling factor. It is therefore suggested that further testing of these effects should be performed to better understand how zone densities within this range affect model results.

6.7. EFFECTS OF JOINT PROPERTIES

Unlike those of the intact rocks, the mechanical properties of the modelled joints are not based on physical measurements. The following sections investigate the effects of these properties on model results.

6.7.1. Joint Normal Stiffness

Joint normal stiffness relates the normal stress on a joint to the normal displacement of the joint. This is important for mechanical and hydraulic behaviour as it controls both overburden collapse and the stress/aperture relationship. Table 6.10 shows how normal stiffness affects model results.

Table 6.10 – Effects of joint normal stiffness on UCG model results. The standard case is highlighted in bold.

Joint Normal Stiffness (Nm ⁻¹)	Mechanical Timestep (μs)	Model Runtime (hrs)	Maximum Subsidence (cm)	Groundwater Inflow Rate (mL/day)	Thermal Penetration Length (m)
1×10 ⁸		Model failed due to block overlap error			
1×10 ⁹		Model failed due to block overlap error			
1×10¹⁰	180	31	0.82	26.3	10.36
1×10 ¹¹	86	57	0.79	37.8	10.44
1×10 ¹²	42	89	0.98	90.5	10.53

As expected, joint normal stiffness has a strong influence over model runtime. Increases in stiffness lead to a considerable reduction in timestep, as given by Equation A.11. Joint normal stiffness is seen to have little effect on the thermal behaviour of the model, however mechanical and hydraulic results are affected. Groundwater flow rates are seen to increase with normal stiffness. This shows that the majority of joints tend to close under normal stress, rather than open, as increased stiffnesses prevent this motion and thus give greater flow rates. Maximum subsidence is seen to be approximately constant for small increases in stiffness, while larger changes are seen to give an increase in deformation. This observation is counterintuitive, as increases in stiffness should act to increase the strength of the rock mass and therefore reduce subsidence. It is of note however, that the difference in subsidence is well within the expected level of statistical error for the model. As such, the increase in subsidence is predominantly caused by random perturbations in the model, which are in turn exacerbated by the increase in runtime.

6.7.2. Joint Shear Stiffness

Joint shear stiffness has much less of an effect on results than joint normal stiffness, as seen in Table 6.11. Thermal and hydraulic results are seen to be generally unaffected by shear stiffness, as is model runtime. Maximum subsidence is seen to decrease with shear stiffness. This is to be expected, given that increased stiffness reduces the amount of shearing along fractures in the rock mass. The strong trend seen with shear stiffness compared with normal stiffness suggests that shearing is the predominant failure mechanism of the rock mass. This suggestion is further corroborated by the results for joint friction angle and cohesion.

Table 6.11 – Effects of joint shear stiffness on UCG model results. The standard case is highlighted in bold.

Joint Shear Stiffness (Nm ⁻¹)	Model Runtime (hrs)	Maximum Subsidence (cm)	Groundwater Inflow Rate (mL/day)	Thermal Penetration Length (m)
1×10 ⁷	Model failed due to block overlap errors.			
1×10 ⁸	22	0.98	42.2	10.38
1×10⁹	31	0.82	26.3	10.36
1×10 ¹⁰	25	0.58	31.1	10.29
1×10 ¹¹	Model failed due to block overlap errors.			

6.7.3. Joint Friction Angle

Joint friction angle controls the relationship between the normal stress on a joint and the shear strength of that joint. As such, it is expected to affect subsidence results by altering the shear stress at which joints fail. The effects of joint friction were tested at angles chosen such that their tangents were multiples of 0.1, 0.5, 1.0, 2.0 and 10.0 times the standard value. Table 6.12 shows the results of these tests.

Table 6.12 – Effects of joint friction angle on UCG model behaviour. The standard case is highlighted in bold.

Joint Friction Angle (°)	Model Runtime (hrs)	Maximum Subsidence (cm)	Groundwater Inflow Rate (mL/day)	Thermal Penetration Length (m)
3.3	Model failed due to block overlap errors.			
16.1	29	2.56	2.74	10.55
30.0	31	0.82	26.3	10.36
49.1	31	0.60	122.6	10.67
80.2	19	0.68	16.9	10.66

As seen above, joint friction angle appears to have little effect on the thermal results of the model. Solution speed is also seen to be generally unaffected by joint friction, although the highest friction angle gives a notable decrease in runtime. This is caused by a reduction in the extent of joint failure in this model, as explained below.

The friction angle of a joint is directly related to the shear yield strength of that joint. As friction angle increases, strength increases, preventing the onset of shear failure and leading to a reduction in overburden collapse. This in turn leads to a reduction in subsidence and runtime, which is observed in the model results. Variations in friction angle are seen to have an effect on flow rate, however no discernible trend can be observed. As such, the effect of friction angle on groundwater flow are seen to be masked by random effects.

Given that friction angle is arbitrarily defined, these observations introduce considerable uncertainty into model results. In reality, friction angles of rock discontinuities often take values from less than 10° to over 40° (Hoek, 2007). Such a range is shown by Table 6.12 to lead to variations in subsidence of a factor of 3 or greater. As such, joint friction is seen to be a key parameter in subsidence prediction. It is therefore suggested that future models should endeavour to obtain experimental data on joint friction wherever possible, rather than relying on arbitrary values.

6.7.4. Joint Cohesion

Joint cohesion controls the shear strengths of unconfined joints. The ratio of frictional to cohesive forces on a given joint increases with depth, as friction is dependent on the normal stress on a joint, which in turn depends on lithostatic pressure. As such, cohesion is of greater importance for joints closer to the ground's surface. Table 6.13 shows how varying cohesion affects results.

Table 6.13 – Effects of joint cohesive strength on UCG model results. The standard case is highlighted in bold.

Joint Cohesion (Pa)	Model Runtime (hrs)	Maximum Subsidence (cm)	Groundwater Inflow Rate (mL/day)	Thermal Penetration Length (m)
1×10^3	68	1.43	211.1	10.36
1×10^4	48	0.97	149.7	10.10
1×10^5	31	0.82	26.3	10.36
1×10^6	29	0.76	0.105	10.24
1×10^7	20	0.76	0.065	10.32

As shown above, joint cohesion has little effect on thermal results, as expected. All other results are seen to be greatly affected however. Model runtime is seen to decrease with increasing cohesion. This is to be expected as the increased strength of the joints prevents large scale motion and hence reduces the computational demands of solution.

Groundwater flowrates are seen to decrease considerably with increasing cohesion as joints remain closed. In comparison with the effects of shear stiffness, this suggests that hydraulic behaviour depends much more on the plastic (cohesion dependent) than elastic (stiffness dependent) behaviour of joints. This suggests that it is the total failure of joints, rather than their partial opening, that has the greatest effect on groundwater flow behaviour.

As expected, maximum subsidence decreases with cohesion. The rate of decrease is slower than that seen with friction however, suggesting that friction is the principal force preventing the shear failure of joints. As mentioned above, the ratio of frictional to cohesive strength increases with depth. Given that the majority of joint failures occur near the cavity (at considerable depths), this is to be expected. These results suggest that both joint friction and cohesion are important parameters controlling the behaviour of UCG overburden. Further models in this work will continue to use a cohesion of 100kPa for consistency. It is recommended however that future work should consider friction and cohesion as site dependent properties, and endeavour to acquire experimental data for these properties rather than relying on arbitrary values.

6.7.5. Joint Dilation Angle

Dilation is the process by which the shear displacement along a joint causes a change in the normal separation (aperture) of the joint. Greater dilation angles imply a faster change under shear yielding, which in turn leads to changes in the strength and permeability of the rock mass. Table 6.14 shows the results of a number of tests using rock masses with varying joint dilation angles.

Table 6.14 – Effects of joint dilation angle on UCG model results. The standard case is highlighted in bold.

Joint Dilation Angle (°)	Model Runtime (hrs)	Maximum Subsidence (cm)	Groundwater Inflow Rate (mL/day)	Thermal Penetration Length (m)
0.0	27	0.62	239.2	10.69
2.5	31	0.83	386.2	10.67
5.0	31	0.82	26.3	10.36
10.0	36	1.18	23.2	10.20
20.0	Model failed due to block overlap errors.			

Joint dilation is seen to have little effect on thermal results, as expected. Increases in dilation are seen to give a corresponding increase in subsidence as joints separate and weaken the rock mass. Runtime is also increases as a greater degree of motion must be simulated. Groundwater flow rate is seen to decrease with increasing dilation. This is counterintuitive, as increases in separation should increase flow rates. This disagreement suggests that the influence of joint dilation on hydraulic results is more complex than initially thought. It is also of note that the result for an angle of 2.5° does not follow the general trend. Given the scale of errors in hydraulic results, it may therefore be the effect of dilation on hydraulic results is masked by random effects. As such, further repeats of the dilation tests are suggested. It was not possible to complete these tests within the project timescale however. Finally, as with joint cohesion and friction, it is suggested that site specific dilation data should be acquired for future uses of the model.

6.8. EFFECTS OF CONVERGENCE RATIO

The termination criterion used in the UCG model is described in Section 5.5.1. As mentioned, convergence is achieved when the rate of change of displacement of all points on the ground's surface is less than a specified fraction of their accumulated displacement up to that time. This section investigates the influence of this criterion by varying the value of the fraction used. Smaller fractions imply a tighter criterion, which should increase model accuracy at the expense of a longer runtime. Table 6.15 shows the results of a number of models with varying convergence ratios.

Table 6.15 – Effect of varying convergence ratio on model results. The standard case is highlighted in bold.

Convergence Ratio (-)	Model Runtime (hrs)	Maximum Subsidence (cm)	Groundwater Inflow Rate (mL/day)	Thermal Penetration Length (m)
1×10^{-2}	13	3.18	0.25	10.36
1×10^{-3}	21	1.34	4.29	10.26
1×10^{-4}	31	0.82	26.3	10.36
1×10^{-5}	56	0.76	32.9	10.28

The results in Table 6.15 show the expected trends. Convergence ratio is shown to have little effect on thermal results as the termination criterion does not apply to the thermal model. As expected, runtime increases as convergence ratios are tightened. Maximum subsidence is seen to decrease as convergence is tightened, while groundwater flow rates are seen to increase.

The increase in subsidence for models with looser convergence ratios is caused by premature termination of the 'before' stage of the model. Given that subsidence results are found as the difference between the 'before' and 'final' stages, premature termination of the before stage acts to increase subsidence. Figures 6.8 and 6.9 show centreline displacement against iteration count for the 1×10^{-4} and 1×10^{-2} models respectively. It is seen that movement has definitely ceased at each stage of the 1×10^{-4} model before cycling continues in the following stage, justifying the use of 1×10^{-4} as the standard convergence ratio. The results for the 1×10^{-2} model show that motion is definitely still occurring when the before stage ends. This continuing motion then contributes to the deformation seen in the following stage, leading to an overestimation of final subsidence.

It is of note that in both models, the displacement during the 'before' stage is considerably greater than that of the other two stages. This displacement is caused by the rock mass settling as it reaches the initial equilibrium state. This settling process establishes the initial stresses and joint apertures of the rock mass. This process is the reason why UDEC models need to contain the 'before' stage. The fact that this stage tends to undergo an order of magnitude more displacement than the later stages is actually beneficial in the identification of premature termination errors. If models appear to have subsided considerably more than expected, especially away from the centreline, it is often found that the 'before' stage has terminated prematurely and the reason for this can then be sought out.

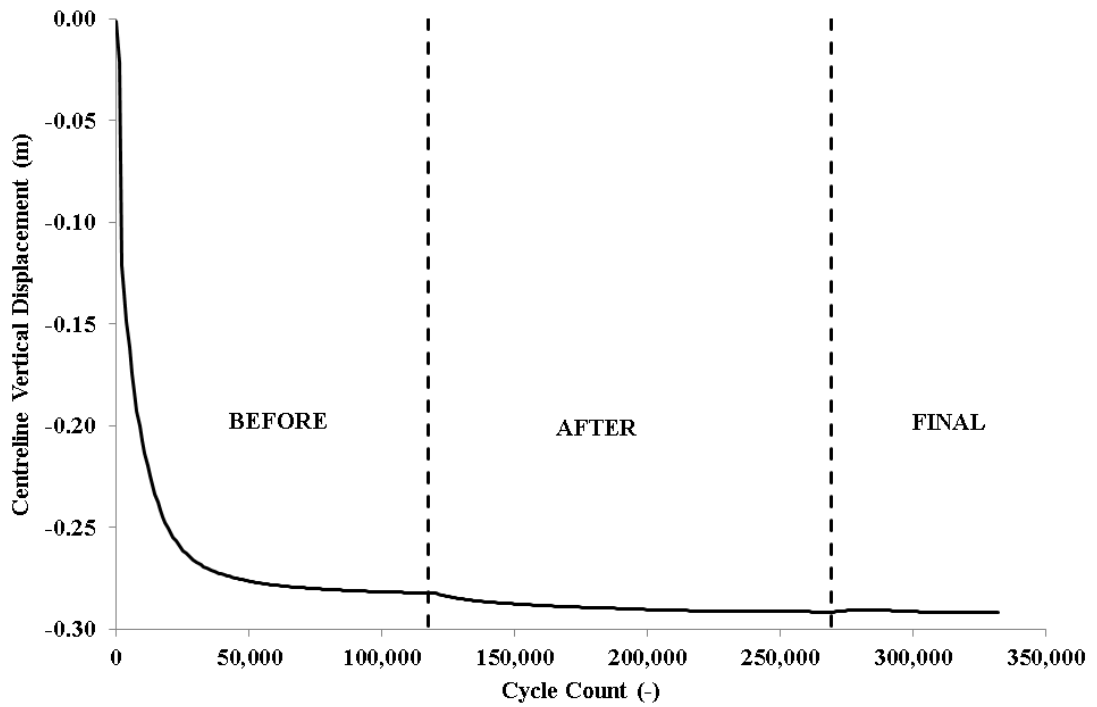


Figure 6.8 – Evolution of centreline vertical displacement during solution for a model with a convergence ratio of 1×10^{-4} .

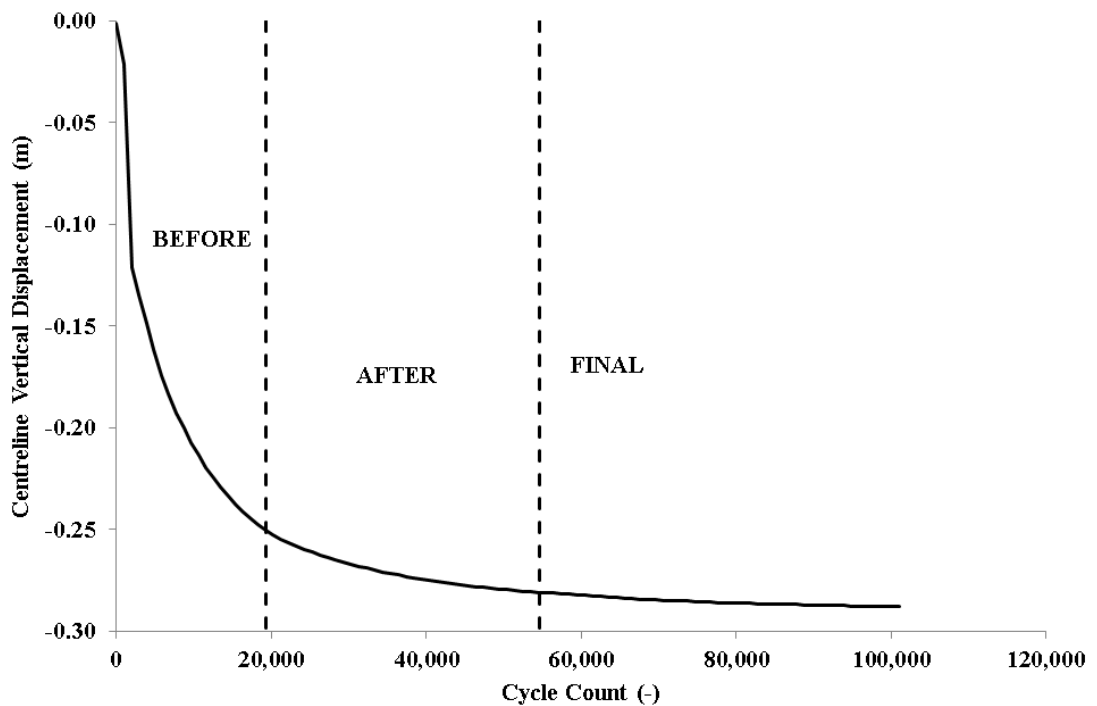


Figure 6.9 – Evolution of centreline vertical displacement during solution for a model with a convergence ratio of 1×10^{-2} .

Despite the termination criterion applying only to the mechanical aspect of the model, increasing the tightness of the convergence ratio is seen to lead to a gradual increase in groundwater flow rate. This is unsurprising, given the extent of coupling between the hydraulic and mechanical aspects of the model. As with the subsidence result, the effects of convergence ratio on flow rate are caused by premature termination of model stages. As shown previously, joints tend to open as the model progresses, increasing permeability and therefore flowrate. Premature termination stops this effect from concluding, reducing the flowrates seen in models with looser criteria.

As seen in Table 6.15, the mechanical and hydraulic results are still changing between the two tightest values of the convergence ratio. This suggests that a ratio of 1×10^{-5} is still not tight enough to ensure accurate results from the model. Although these results are still changing, their associated rates of change are seen to have slowed significantly. As such, results would not be expected to change a great deal if the ratio were reduced any further. Furthermore, it is seen in Table 6.15 that the increases in runtime associated with tighter criteria are accelerating. As such, tighter ratios are expected to give impractically long runtimes. For these reasons, it is believed that further tightening of the convergence ratio would not give a sufficient benefit to be justified. Given the scale of uncertainty in results caused by other factors (including arbitrary joint properties, the random nature of the DFN and the inherent uncertainty of real rock masses), it is believed that the differences between the 1×10^{-4} and 1×10^{-5} models are small enough to be considered insignificant by comparison. It is therefore believed that increasing tightness from 1×10^{-4} to 1×10^{-5} does not give enough of an increase in accuracy to warrant the associated increase in runtime. As such, a ratio of 1×10^{-4} is considered accurate enough for the intended end use of the model.

6.9. CONCLUDING REMARKS

The results presented in this chapter show how various parameters affect the behaviour of the UCG model. Two key limitations of the model have been identified: Firstly, hydraulic results are seen to vary greatly between trials. In some cases, variations are seen to be greater than an order of magnitude in scale. This variability is predominantly caused by the random nature of the DFN pattern, however it is exacerbated by the small absolute values of flow rate observed. It is therefore suggested that UDEC results be used only as a basis for further hydraulic modelling, using separate software. Plans for such a model are given in Appendix C.

Second, results are shown to depend heavily on a number of unphysical internal parameters. DFN dimensions, zone density and joint failure criteria are seen to have particularly strong effects. Extreme values of certain parameters may also stop models from solving at all, reducing model stability. The reliance on these parameters reduces model validity as results are shown to depend more on unphysical parameters than actual cavity design. In all cases however, these variables should be fixed in future predictive models, reducing their effect on the end results of the model.

Despite these limitations, the results of this chapter suggest that the model is sufficiently accurate for its intended end use. While the variability in results is large, this is considered acceptable compared with those seen for real rock masses. Chapter 7 aims to further prove model validity by comparing results against site measurements from UCG field trials. It is hoped that the outcome of these two chapters will thus be sufficient to ensure confidence in the future use of the model as a predictive tool.

7. FIELD TRIAL STUDIES

SUMMARY

This chapter presents comparisons between model results, empirical predictions and experimental measurements for a number of sites related to underground coal gasification (UCG). These comparisons provide a method of model validation, increasing confidence in the prediction of future UCG sites. Due to a relative lack of published data on UCG induced subsidence, only one UCG trial has been tested. Further testing is carried out based on the results of longwall mines, which have similar geometries to UCG cavities. Longwall mines are seen to provide a less competent analogue than previously thought however, due to significant differences in operating conditions. As such, the validation potential of these sites is limited.

Despite the lack of data available, the tests performed show reasonable agreement with UCG trials. Mean subsidence results for the UCG comparison agree to within 6% of the field measurements, however the standard deviation of this result is seen to be greater than 30% of the mean. Variations in hydraulic results are also seen to be large, while thermal results behave as expected. Later results show that multiple cavity modelling is also possible with the Universal Distinct Element Code (UDEC) model, however a number of alterations are required to give accurate results in these cases. Together with the observations presented in Chapters 6 and 8, the results presented herein suggest that the UDEC model is accurate enough for use as a first pass screening tool for prediction of the local environmental effects of underground coal gasification.

7.1. INTRODUCTION

Validation of results is a key step in the development of any numerical or analytical model of a physical system. Predictive results derived from such models are of little to no use if their validity cannot be proven. Throughout the creation of the UCG model, validation was performed continuously as new model functionality was developed. Much of this initial validation was performed by comparing model results with empirical models based on the Rocky Mountain 1 field trial (Lindblom & Smith, 1993). Parametric studies, such as those presented in Chapter 6, also act as initial methods of validation.

The work presented in this chapter aims to validate the behaviour of the entire model as a whole. One of the most effective methods for doing so is to simulate the full behaviour of previous field trials and compare model results with measurements performed at the field trial site. In the case of UCG however, such measurements are often difficult to obtain. As mentioned in Section 2.5.1, recent UCG field trials tend to be private commercial ventures. As such, information on site geology and cavity operating conditions is often considered commercially sensitive and is therefore unavailable to the public. While earlier trials tend to publish more information, measurements are often less accurate or are simply not performed for certain variables. For example, many early UCG trials did not take any measurements of ground subsidence, either because very little movement occurred or because it wasn't considered important at the time. The expense and negative public perceptions of UCG also limit the number of trials performed, and hence the data available.

One site which can be used for validation purposes is the Hoe Creek 3 UCG trial, performed in 1979 in Hanna, Wyoming. This trial was part of a series of experiments performed by the US Department of Energy in the late 1970's and early 1980s, and involved the gasification of a sub-bituminous coal seam (the Powder River Basin Felix No. 2 seam) interbedded between layers of sandstone (Burton *et al*, 2006). A large number of measurements were taken at the site and the majority of these are now publically available. The use of this site for validation purposes is problematic however, as exceptional behaviour was observed there.

As shown in figure 7.1, the target seam of the Hoe Creek 3 trial is overlaid by a second coal seam, separated by approximately 7m of interburden. During the trial, collapse of the interburden allowed heat and oxygen to transfer to this seam, resulting in its accidental ignition and gasification. This greatly increased the overall size of the cavity and reduced its depth below the ground's surface. These issues in turn led to considerable ground motion, including chimneying subsidence (see Section 2.2.1.1) which eventually produced an open sinkhole connecting the cavity with the surface. Furthermore, the enhanced fracturing of the overburden due to the extreme subsidence led to considerable pollution of the local groundwater. (Ganow, 1984). These issues combine to make the Hoe Creek 3 trial one of the most environmentally damaging UCG experiments on record. Because of this damage, and despite the anomalous behaviour observed, attempts have been made to model the subsidence at this site for validation purposes. A full description of these attempts is given in Section 7.2.

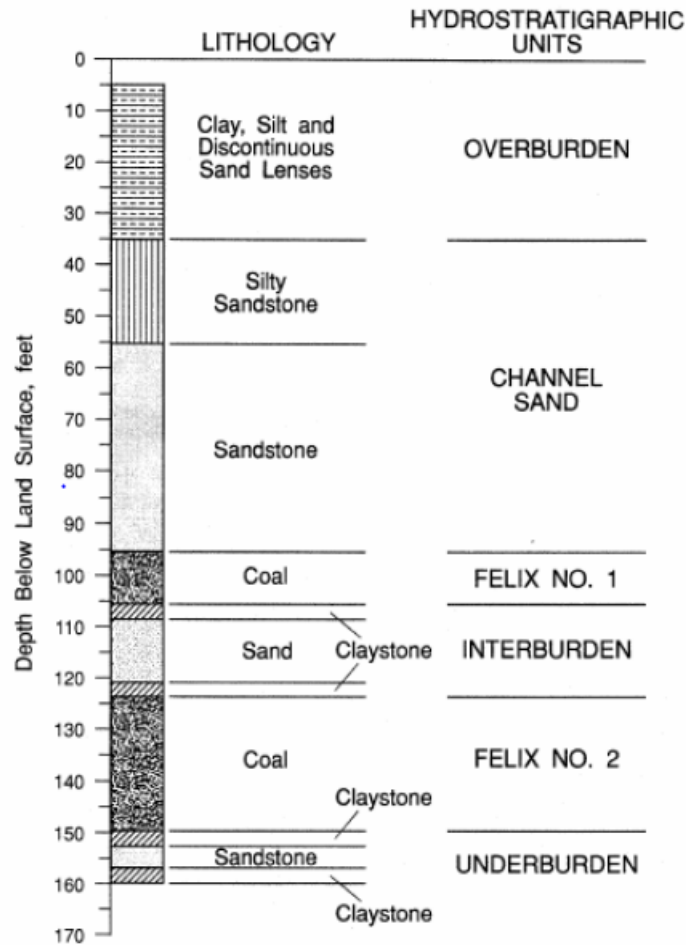


Figure 7.1 – Lithology of the Hoe Creek 3 UCG trial, showing the overlaid Felix coal seams which produced extreme subsidence at the site.

Other than the Hoe Creek 3 site, very little data are available for the validation of UCG subsidence models. In order to compensate for this lack of data, validation can be performed on other sites which are geometrically similar to UCG. Geometric similarity is based on a number of factors, including:

- Cavity length to width ratio – approx. 50 – 70 for linear CRIP UCG.
- Cavity depth on the order of 100m.
- No artificial support of overburden (e.g. rock bolting).
- Full overburden coverage (i.e. no large openings to the surface).

A site must conform to all of these criteria to be considered for validation. Sites which do not conform to one or more of the criteria cannot be used, as it is unknown to what extent this nonconformity will affect the behaviour of the rock mass. It is difficult to meet all of these criteria with a single excavation however. For example, many tunnelling projects satisfy the length and depth criteria, but are intentionally supported by artificial methods. Many underground mining techniques are unsupported, however these tend to have large surface openings (e.g. mine shafts) and lower length to width ratios.

One industry which often fulfils all of the above requirements is that of underground mining. Longwall mining in particular shares a number of similarities with UCG (Langland & Trent, 1981; Mallett 2006; Younger, 2011). Two particular sites are of interest as they both have a lot of data available for comparison with model results. The Jinchuan No 2 nickel mine in China and Angus Place Colliery in Australia have been used in this work in lieu of further comparisons with UCG sites. Validation studies based on these mines are presented in Sections 7.3 and 7.4 respectively.

7.2. HOE CREEK 3 UNDERGROUND COAL GASIFICATION

As mentioned above, the Hoe Creek 3 UCG site is one of very few trials where sufficient data are available on the post-burn geology of the site. As such, it is used here as a means of validating the behaviour of the UCG model. The use of this site for validation purposes is complicated however, by the exceptional subsidence behaviour which occurred there. As shown in Figure 7.2, this behaviour evolved over time. It is of note that a considerable change occurred after day 81. This is believed to be the point at which the interburden collapsed and gasification of the upper coal seam began. The considerable difference between the results of days 81 and 114 may be problematic, as the formulation of the model cannot accurately predict the effects which caused this behaviour.

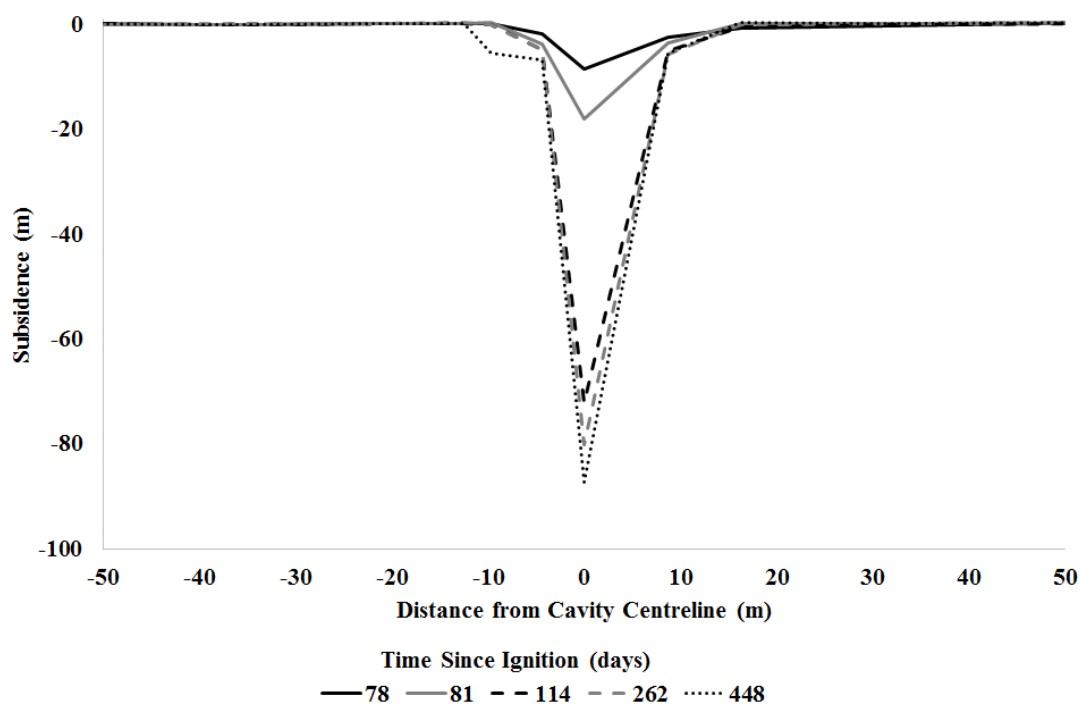


Figure 7.2 – Subsidence at Hoe Creek 3 UCG trial site as a function of time. After Ganow, 1984.

In order to validate the model against site measurements, an appropriate measurement time must be chosen. This must represent only the subsidence caused by stoping and stratal bending (see Section 2.2.1.1), as the UDEC model is incapable of resolving chimneying or plug failure. In order to choose an appropriate time, a simple empirical method is used to predict subsidence at the site. The measured time is then chosen as that which is closest to the empirical result. Empirical calculations are performed using an influence function method (Brauner, 1973), as given by Equation 7.1.

$$S_s = \sum_e \frac{3 S_{max}}{\pi r_{crit}^2} \left[1 - \left(\frac{x_s - x_e}{B} \right)^2 \right]^2 \quad \text{for} \quad 0 \leq r \leq r_{crit}. \quad (7.1)$$

$$S = 0 \quad \text{for} \quad r > r_{crit}.$$

$S_{max} = \alpha H_C$ is the maximum possible subsidence.

$r_{crit} = \frac{2D_C}{\tan(\gamma)}$ is the critical radius of subsidence.

Where:

- S Subsidence (m)
- α Subsidence factor (-)
- γ Angle of draw ($^{\circ}$)

Subscripts:

- e For a specified area of extraction.
- s At the specified point on the surface.

The subsidence factor α for UCG is given by Gregg (1977) as between 0.7 and 0.9, while the angle of draw is given by Younger (2011) as approximately 35° . Results in Chapter 6 suggest a subsidence factor of 0.59 and an angle of draw of 44° . Considering gasification of both cavities, Equation 7.1 predicts subsidence between 6.5 and 8.3cm using the literature values, and 10.21cm using the Chapter 6 result. The upper limit of the literature based prediction is close to the subsidence observed after 78 days at 8.6cm. As such, 78 days is used as the validation benchmark and all further empirical models assume a subsidence factor of 0.9 and an angle of draw of 35° .

The cavity geometry of the Hoe Creek 3 UDEC model is given in Figure 7.3. This geometry is based on the work of Hill (1981) and assumes full breakthrough of gasification into the upper coal seam.

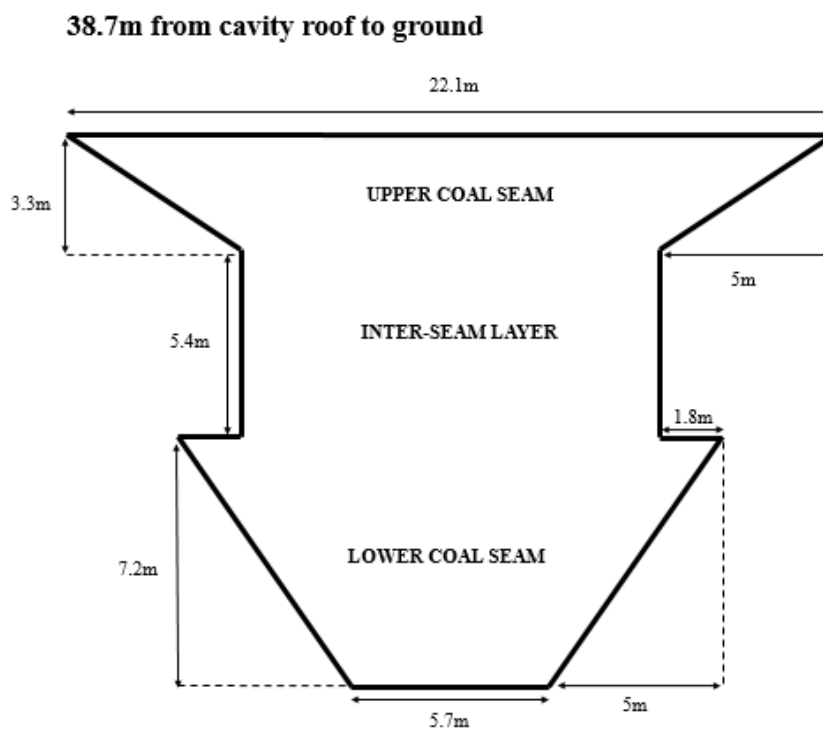


Figure 7.3 – Cavity geometry for the UDEC model of Hoe Creek 3 UCG site. After Hill (1981)

Figure 7.4 compares UDEC model results with empirical predictions and field trial measurements for the site. The UDEC result is presented as the mean subsidence taken over 10 executions, with error bars equal to the standard deviation of those executions. The graph has been cropped to show only the behaviour near the cavity, as negligible ground movement was observed at greater horizontal distances. It is of note that very little edge heave was seen in these models compared with those in Chapter 6. This is primarily due to the extent of subsidence at Hoe Creek compared with the benchmark model however, as the greater extent of ground motion dwarfs any movement at the model edges, making edge motion much harder to detect.

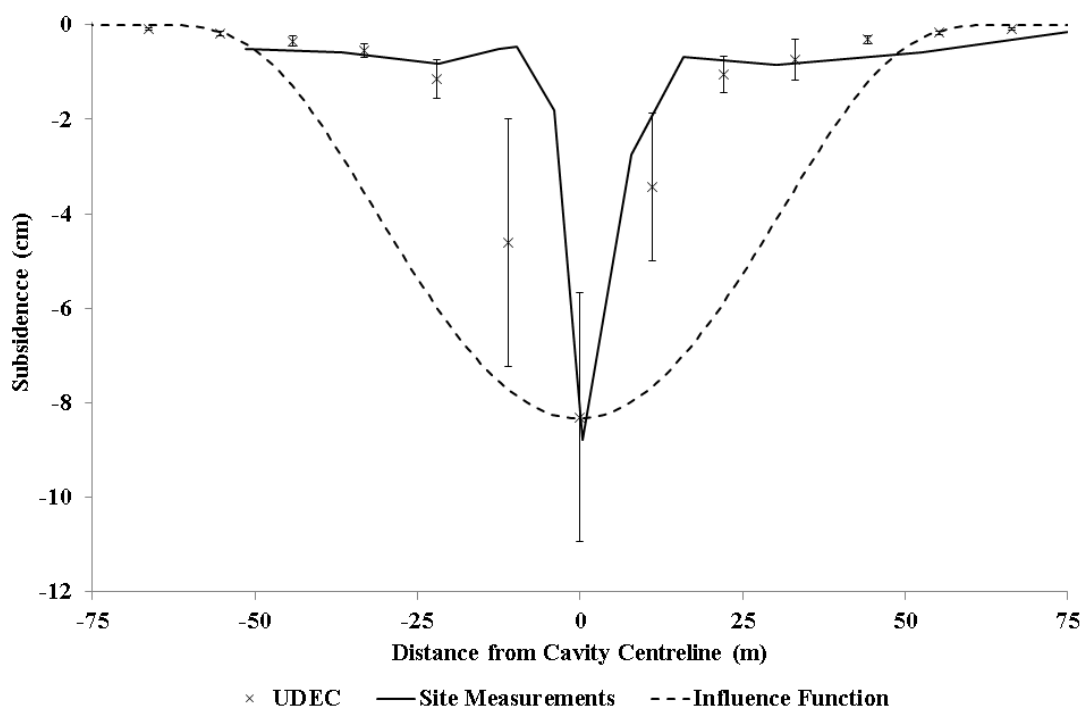


Figure 7.4 – Comparison of UDEC results, site measurements and influence function predictions (Brauner, 1973) for subsidence at the Hoe Creek 3 UCG site.

Figure 7.4 shows that the UDEC model accurately predicts the maximum subsidence seen at the Hoe Creek 3 site after 78 days. Measured subsidence is seen to fall well within the error margins of the UDEC model at the centreline, while the mean result differs from measurements by approximately 4mm. The standard deviation of centreline error predicted by UDEC is approximately 2.6cm, equal to 32% of the mean. While this is a large variance, it is within the expected range given by the natural variability of rock masses. It is of note that the UDEC model predicts a slightly shallower profile than that seen in reality, but the difference is small enough to consider the profile realistic. In comparison, the empirical method is seen to predict a profile which is much shallower still. This effect is predominantly caused by the assumption of rectangular cavity geometry, ignoring the effects of shape on subsidence. Such results therefore show that the UDEC model gives a considerable advantage over empirical methods, however the inability to predict chimneying greatly limits the reliability and applicability of the UDEC model.

Figure 7.5 shows the groundwater pressure distribution for the Hoe Creek 3 site during gasification (i.e. the “after” stage of the model). Results are taken from the run in which the subsidence results are closest to the mean. The water table at the Hoe Creek site was initially located at a depth of 24.5m below the ground (Wang *et al*, 1981). Permeability at the site is highly anisotropic, with a value of approximately 120mD in the horizontal direction and 22mD in the vertical direction (Buscheck *et al*, 2009; Snoeberger, 1976). In order to simulate this in the model, permeabilities are set at 22mD for joints between 60 and 120 degrees from the horizontal, and 120mD for all other joints. Cavity pressure was set equal to the local hydrostatic pressure at the roof of the lower seam, as in the field trial (US Department of Energy, 1997).

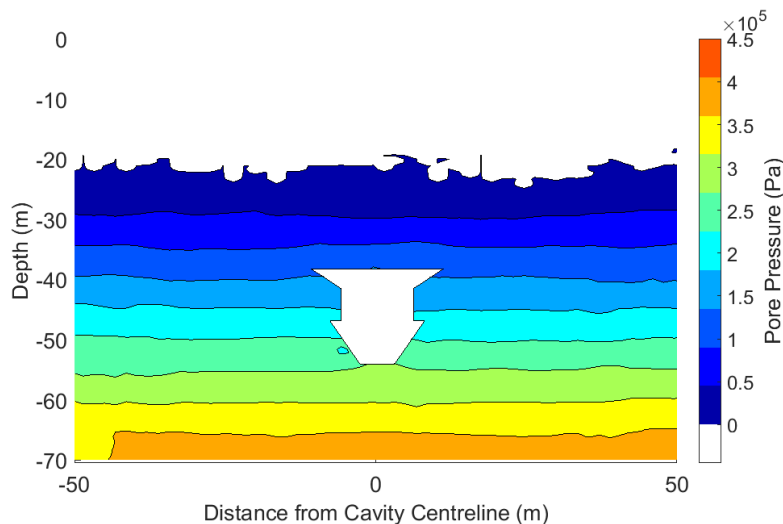


Figure 7.5 – Simulated pore pressure distribution during gasification at the Hoe Creek 3 trial site.

As seen above, the operation of the Hoe Creek 3 gasification site appears to have a negligible effect on the pore pressure distribution around the cavity. Given that overall cavity pressure is roughly equal to hydrostatic pressure, this is to be expected. Observed perturbations in pressure are predominantly caused by the random nature of the joint pattern and the interpolation process used to create the diagram.

Unlike modern UCG designs, the Hoe Creek 3 trial was not operated at sub-hydrostatic pressures. In addition, the accidental gasification of the upper coal seam actually led to cavity pressures exceeding local hydrostatic pressure in some regions. While these effects prevented lowering of the water table, they led to considerable groundwater contamination (Burton *et al*, 2008; Kapusta & Stanczyk, 2011). The results of the UDEC model predict both of these effects. As shown in Figure 7.5, the water table height remains unchanged. Groundwater is found to flow out of the cavity at a rate of $9.36 \times 10^{-8} \text{ m}^2\text{s}^{-1}$. Given a cavity length of 52m (Hill, 1981) this corresponds to 421 litres per day, more than sufficient to cause considerable pollution.

Figure 7.6 shows how the maximum temperature experienced by the rock mass varies with position in the Hoe Creek 3 trial. These results are taken from the same run as those shown in Figure 7.5. As seen, the maximum temperature profile initially follows the cavity wall, but begins to circularise as distance increases. Random fluctuations in the temperature contours are caused by the existence of large blocks in the discrete fracture network (DFN), as temperature transfers more slowly through blocks than joints. The temperature profile is seen to extend up to 15m from the cavity wall. This is longer than that suggested by the literature (Sarhosis *et al*, 2013; Yang, 2005). This discrepancy is believed to be due to the relatively large surface area of this cavity geometry compared with standard cavity shapes. Comparisons with field measurements for this site cannot be made as temperature measurements are not available for this trial.

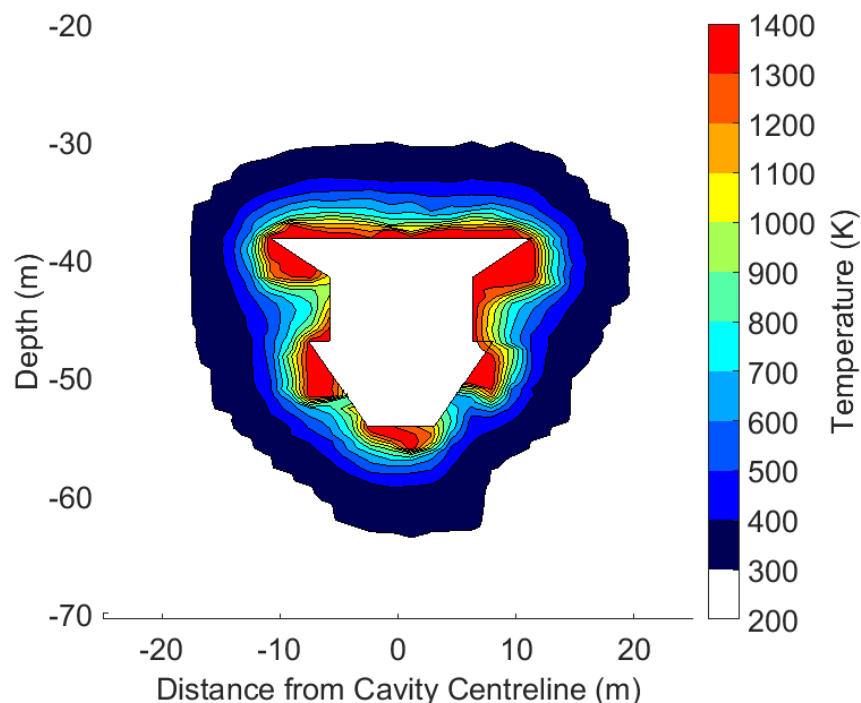


Figure 7.6 – Profile of maximum experienced temperature surrounding cavity at Hoe Creek 3 UCG trial site.

The above results show that the UDEC model agrees well with site measurements and historical predictions for the Hoe Creek 3 UCG site. It is important to note however that the model does not predict the increase in subsidence seen between days 81 and 114. As mentioned previously, this behaviour was caused by the accidental gasification of a second coal seam, followed by subsequent chimneying of the overburden. Despite the inclusion of this second seam in the model, subsidence results tend to agree with the original measurement taken at 78 days. The failure of the UDEC model to predict the secondary subsidence events considerably reduces the reliability of the model for the prediction of future UCG sites.

In order to better predict the secondary subsidence events mentioned above, several additions to the UDEC model would be required. These additions include full simulation of coal combustion, cavity growth mechanisms, fully realised roof collapse and transient hydraulic phenomena. The inclusion of these aspects would greatly increase the complexity and computational demands of the model. Given that the aim of the model is to act as a first pass screening tool rather than an in depth simulator, these complications are not considered important at this stage. It is imperative however, that any sites which the UDEC model deems as safe are further investigated using much more rigorous techniques before any experimental or commercial gasification operations are commissioned.

The agreement of model results with field trial data at day 78 is considered sufficient to confirm the validity of the model for use as a first pass screening tool for simple UCG designs. Further modelling should always be carried out using standalone models for particular sites before any experimental work begins however.

7.3. JINCHUAN NICKEL MINE

The Jinchuan No. 2 mine is a Chinese nickel mine operating on a steeply dipping seam. This site was chosen for model validation purposes as a great deal of data are available on the site (Li *et al*, 2004b; Ma *et al*, 2013; Zhao *et al*, 2012). Unlike UCG, underground mining does not involve any thermally driven processes. As such, the thermal aspect of the UDEC model is turned off for this analysis. In addition, no information is available on the local groundwater conditions at the mine, precluding hydraulic modelling.

Figure 7.7 shows a view along the length of the cavity in the UDEC model of Jinchuan nickel mine. The mine effectively consists of two identical cavities with a thin slice of material (the filling body) in between. This filling body would then be mined out at a later date. The model considers the mine with the filling body still in place as this is the geometry for which field measurements are available. Block, zone and DFN geometries depend on the total size of a rectangle circumscribed around both the cavities as well as the filling body. The material properties and boundary conditions at the site are based on those used by Zhao *et al* (2012). The UDEC model assumes that the entire modelled rock mass consists of migmatite as this is the most predominant rock type in the area. In the absence of information on local hydraulic conditions, the rock mass is assumed to be saturated with water. In reality, migmatite based geologies are likely to be dry, however the model considers a wet rock mass in order to maintain consistency with the UCG model.

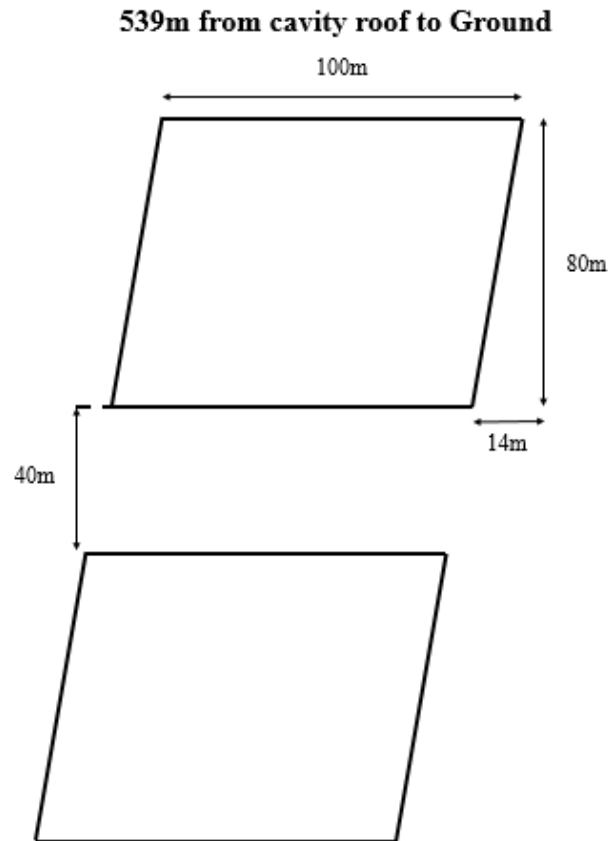


Figure 7.7 – View along the length of Jinchuan No. 2 nickel mine cavity.

Figure 7.8 compares the results of the UDEC model with site measurements and empirical predictions. UDEC results are given as the mean of 3 trials, with error bars given as the standard deviation of these trials. The influence function uses a subsidence factor of 0.9 and an angle of draw of 29° as suggested by the literature (Keilich *et al.*, 2006). As shape cannot be incorporated into the influence function, the cavities are assumed to be rectangles with the same area as the real cavities. The graph has been cropped to show only the behaviour near the cavity, as no ground movement was observed at greater horizontal distances. As with the Hoe Creek model, edge heave was negligible for the Jinchuan results.

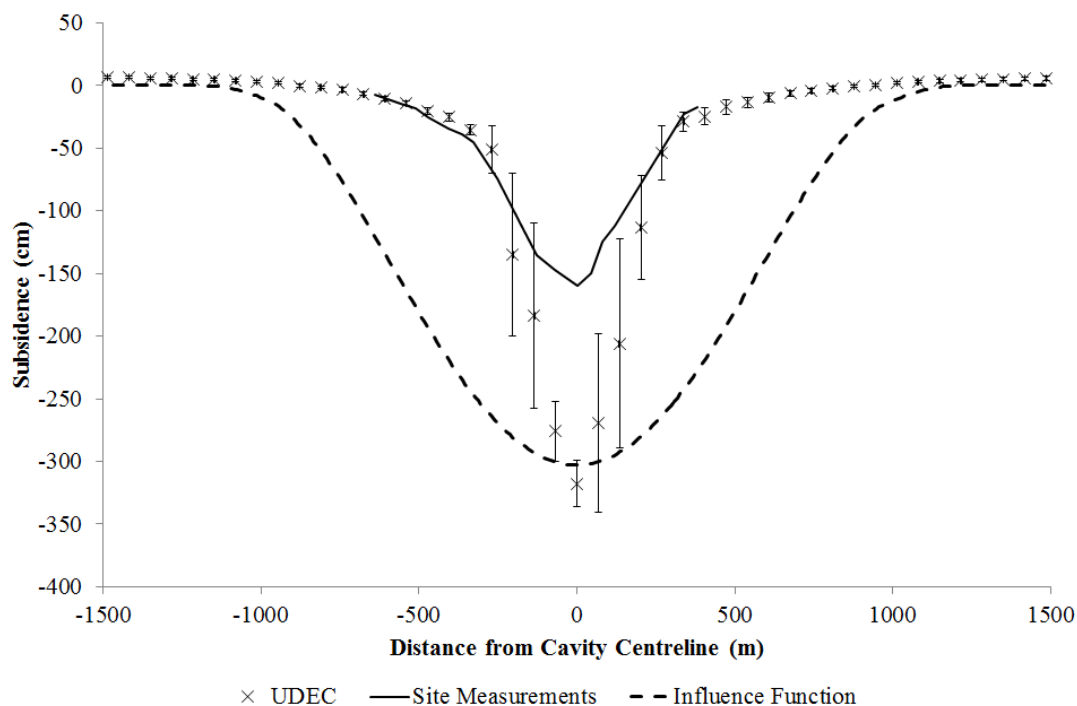


Figure 7.8 – Comparison of UDEC results, site measurements and empirical predictions (Brauner, 1973) for subsidence at the Jinchuan No. 2 nickel mine.

As seen above, both the UDEC model and the influence function greatly overpredict the subsidence seen at the Jinchuan mine. The UDEC model is seen to give a much more accurate representation of profile shape than the empirical function however. It is believed that the overprediction in both cases is due to the inability of the models to accurately represent the support given by the filling body, which acts in a similar manner to a spanning body. In the UDEC model the filling body is seen to sag into the lower cavity, as seen in Figure 7.9. This both removes the support of the filling body and increases the stress on the rocks surrounding the upper cavity, increasing subsidence. It is of note that a dry model would be likely to produce even greater subsidence, suggesting that the UDEC UCG model is not appropriate for modelling a mine such as this. Finally, the model does not consider temporal effects, such as the order of excavation. Including these effects may improve the accuracy of results, however it was not possible to test this within the timescale of the project.

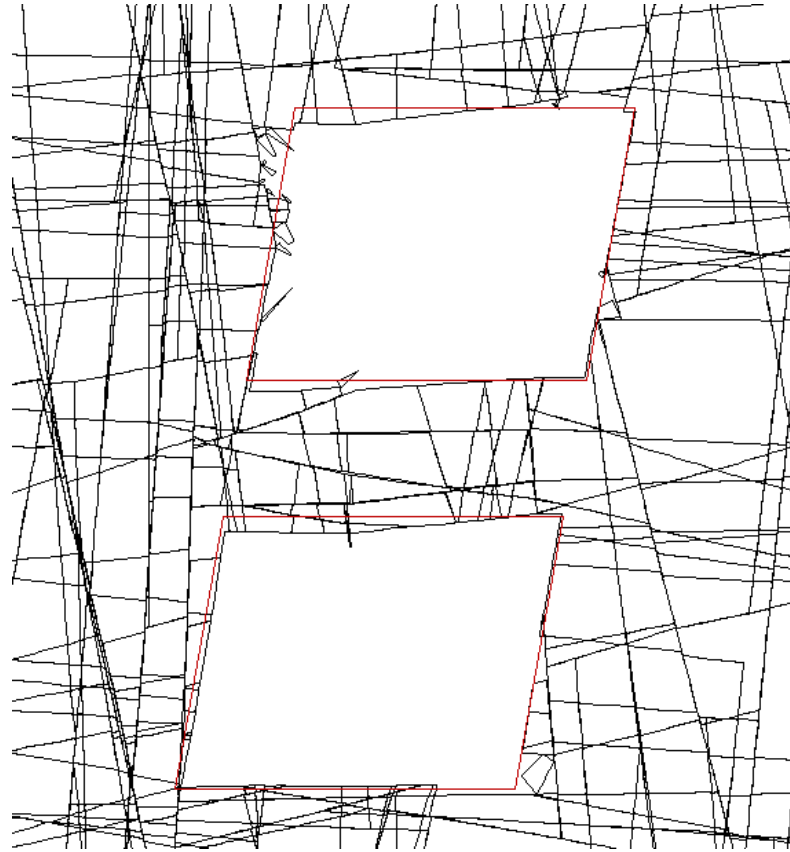


Figure 7.9 – Filling body failure observed in the UDEC model of the Jinchuan nickel mine. Red lines indicate the original location of the cavity boundaries. Fractures are generated via the discrete fracture network method (see Section 4.2.3).

The results above show that while the UDEC model is more accurate than the empirical model, it is generally incapable of predicting the subsidence seen at the Jinchuan site. Model realism could be improved by considering the order of excavation, however this was not attempted due to time constraints. Alternatively, results could be improved by altering design parameters to more closely fit the site; however this would preclude the use of the trial as a means of validation for the UCG model. These results therefore show that while the model can provide much information on the behaviour of diverse sites, its usefulness as a predictive tool may be limited to sites broadly similar to the Rocky Mountain 1 trial. The model is therefore seen to be generally valid for UCG trials, though care should be taken in its application to cases with notably different geometry from that presented in Chapter 5.

7.4. ANGUS PLACE COLLIERY – SINGLE CAVITY

Angus Place Colliery is a multiple panel longwall coal mine in Australia which was used as a test site for the validation of early numerical models in subsidence prediction (Coulthard, 1999; Kay *et al*, 1991). Because of this testing, a lot of information is available on the geology of the site and the subsidence observed there. As with the Jinchuan case study, Angus Place colliery does not involve any thermal or hydraulic modelling of the rock mass.

The geometry of this model is based on that of a single longwall panel (panel 11, as shown by Kay *et al* (1991)). This gives a rectangular cavity with the dimensions given in Table 7.1. A model based on the subsidence caused by multiple panels is presented in Section 7.5. In both models the rock mass material are the same as those presented in Chapter 5, as the rock masses at both Angus Place and the Rocky Mountain trial site are composed primarily of sandstone. As with the Jinchuan model, the rock mass is assumed to be fully saturated with water.

Table 7.1 – Dimensions of longwall panel 11, Angus Place Colliery.

Dimension	Length (m)
Length	1400.0
Width	211.0
Height	2.5
Depth	263.0

Figure 7.10 shows the results of the single cavity Angus Place UDEC model alongside site measurements and empirical predictions. As shown, the UDEC results overpredict subsidence by approximately 33%, with the subsidence measured at the site falling far outside the margin of error given by the models. Model results are seen to give a much better subsidence prediction than that given by the influence function however, with the empirical method under-predicting subsidence by more than a factor of 3. In addition, the shape of the profile given by the UDEC model is much closer to reality than that given by the empirical method.

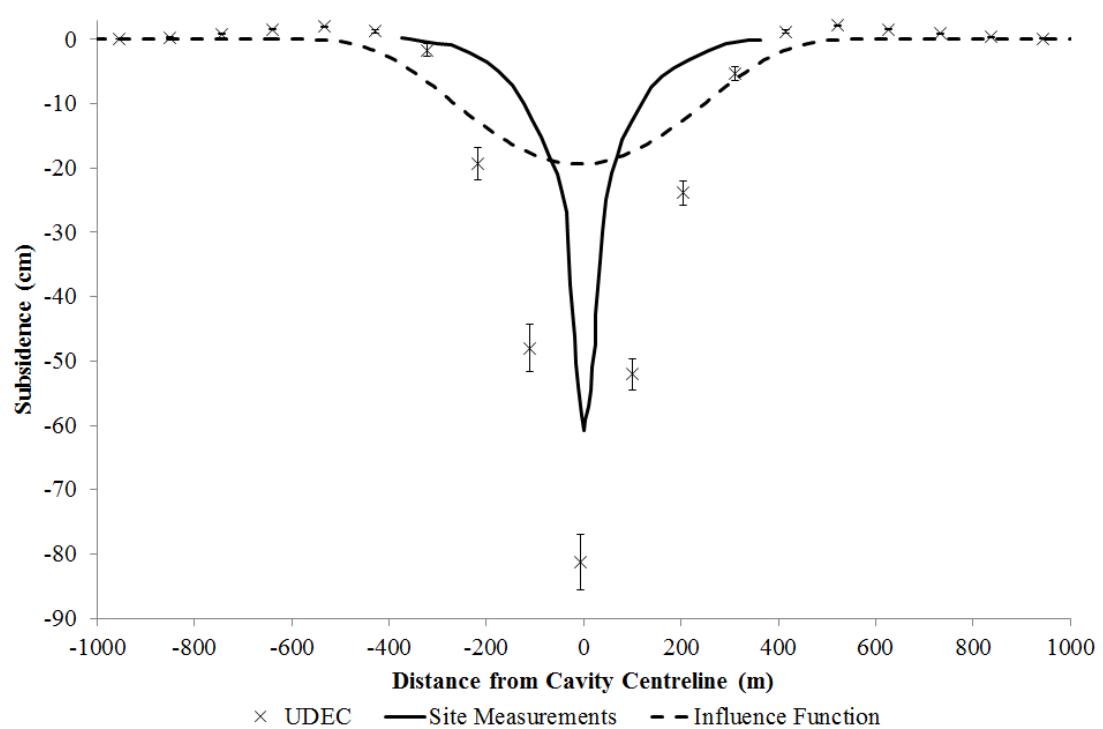


Figure 7.10 – Subsidence profiles for single cavity Angus Place Colliery Models. Influence function based on Brauner, 1973.

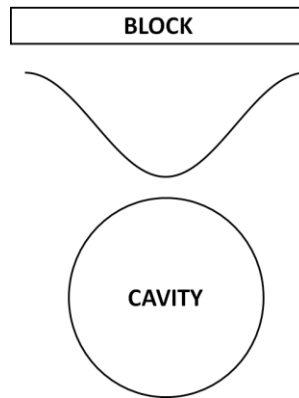
The inaccuracies shown in Figure 7.10 are believed to be caused by the extreme geometry of the site. The width to height ratio of 84.4 is much greater than that of the UCG benchmark case at 0.87. Such an extreme ratio of width to height greatly affects the geometry of the DFN region, as mentioned in Section 6.3. Such geometries have been shown to increase the subsidence predicted by the model, and therefore may contribute to the overprediction of subsidence in this case. In addition, the relatively small length to width ratio of 6.6 suggests that the plane strain geometry of UDEC may be unsuitable for this site.

In summary, the results show that while the UDEC UCG model cannot accurately predict subsidence for the Angus Place Colliery, it does give a distinct advantage over empirical methods in terms of both subsidence extent and profile shape. As with the Jinchuan site, the accuracy of the UDEC model could be improved by altering various design parameters for the site in question; however this would reduce its applicability for the validation of other sites, including UCG operations. As such, these results cast doubt on the usefulness of longwall mining trials as validation studies for the UCG model. Given the lack of available field trial data from UCG trials, this seriously limits the amount of validation which can be performed on the model and therefore limits the reliability and applicability of the model itself. As such, it is suggested that efforts should be made to acquire much more data on subsidence at UCG sites, either through collaboration with the operators of previous trials or by combined computational and experimental studies in the future.

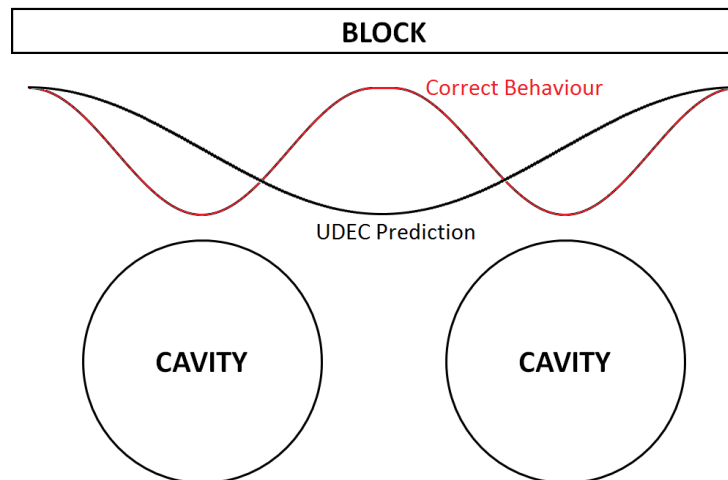
7.5. ANGUS PLACE COLLIERY – MULTIPLE CAVITIES

As mentioned above, the Angus Place Colliery site contains multiple parallel longwall panels. This section models the interaction between two such panels in an attempt to validate the future use of the UDEC model with multiple cavity UCG designs. The geometry of this model is based on that of two parallel longwall panels (panels 11 and 12). The panels have identical dimensions, which were previously given in Table 7.1. The panels are separated horizontally by a 50m thick coal pillar.

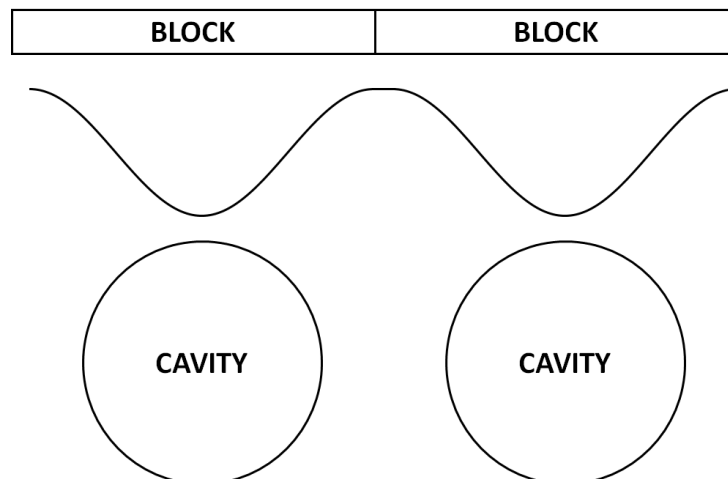
The standard UDEC UCG model is incapable of realising the subsidence profile produced by parallel cavities, because the stratified blocks can only produce first or second order bending. In order to predict the profile caused by two cavities, the blocks must be able to produce fourth order bending, which is impossible in UDEC due to the formulation of the discrete element method. This behaviour can be approximated however, by ensuring that block ends always rest in the space between the cavities. This allows a pair of blocks in second order bending to approximate the behaviour of a single block showing fourth order bending. This concept is shown in Figure 7.11. In order to achieve the desired profile for the Angus Place Colliery model, the stratified beams were shifted horizontally so that the interface between the beams always fell directly above the coal pillar. In addition, a greater number of subsidence measurement points were included to capture the full shape of the profile.



One block showing 2nd order bending – Standard UDEC Model



One block showing 4th order bending – Not possible in UDEC



Two blocks showing 2nd order bending, approximating an overall 4th order bending moment – Allowing multiple cavity modelling in UDEC

Figure 7.11 – Approximation of higher order bending modes through an increase in the number of stratified blocks, allowing for multiple cavity modelling in UDEC.

Figure 7.12 compares simulated subsidence profiles with measured field data and empirical predictions for the two cavity Angus Place Colliery site. As shown, the shape and extent of subsidence profiles were seen to depend heavily on the density of finite difference zoning used within the model. Low zone densities (approx. 11 zones per block) were seen to give a subsidence extent closer to that seen in reality, but failed to give an appropriate profile shape. Higher zone densities (approx. 95 zones per block) give the correct shape but greatly overestimate extent. In comparison, the empirical method is seen to both greatly underestimate the extent of subsidence and fail to capture the effects of the dual cavity geometry.

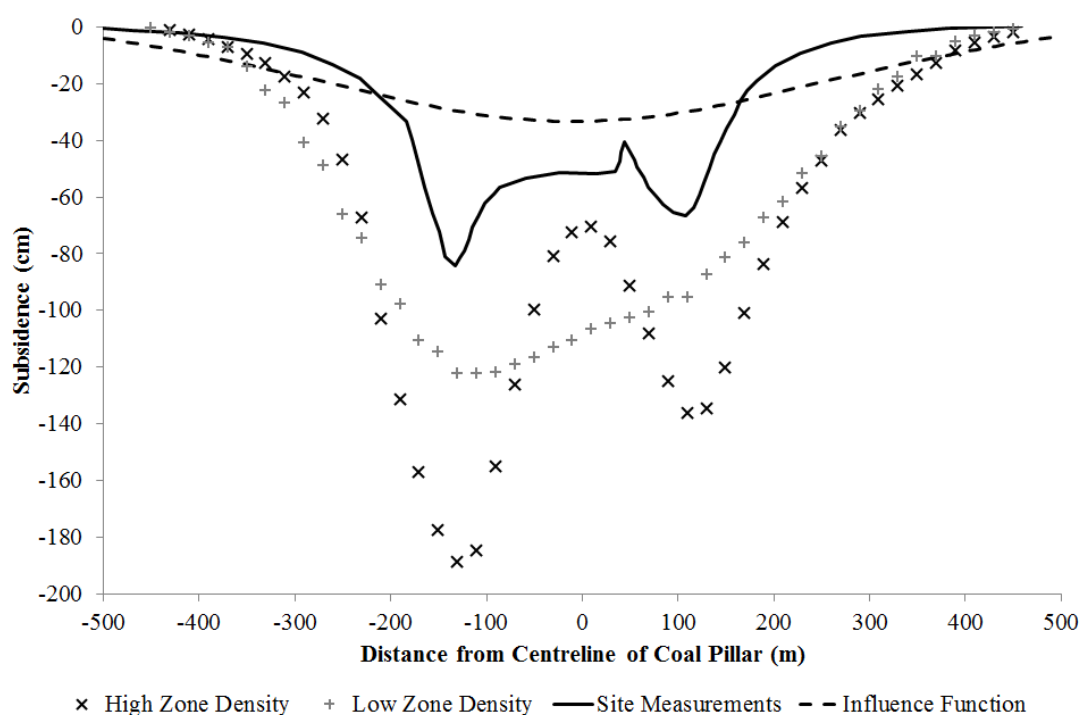


Figure 7.12 – Subsidence profile for two cavity Angus Place Colliery Model. Influence function based on Brauner, 1973.

Two principal conclusions can be drawn from Figure 7.12: Firstly, the shape of the high zone density profile proves that a UDEC model built in this way can predict the subsidence behaviour of multiple cavity systems. As such, appropriately designed models should be able to predict the behaviour of commercial scale UCG operations with several parallel CRIP channels. Second, the numerical results of both models suggest that they are not valid for this particular site. As with the single cavity model, the accuracy of results could be improved by altering the model design, though this would invalidate its use as a tool for the validation of UCG behaviour

Given the observations above, it is suggested that more accurate predictions of multiple cavity behaviour may be possible with the use of a model with a separate but similar design to that used for a single cavity. Such a model would need to use an increased zone density in order to capture the correct profile shape, but would need to be altered in other ways in order to counter the effect of an altered zone density on mechanical and hydraulic results. It is suggested that increasing the stiffness of joints could compensate for these effects. Such a method would greatly change results however, requiring the model to be calibrated against field trial data in order to produce a usable simulation. Such a method would require extensive testing to prove its validity across a number of geometries however, and may be limited to simulating sites which are already similar in shape to the calibration model. Such a process is beyond the scope of this project, but it is believed that it could be achieved relatively easily using similar techniques to those presented within this thesis.

7.6. CONCLUDING REMARKS

The studies in this chapter lead to four principal conclusions:

Firstly, the results of the Hoe Creek 3 tests show that the model is capable of predicting simple thermal, mechanical and hydraulic phenomena associated with single cavity UCG operations in hard rock. These results also show however, that the model is incapable of predicting complex subsidence phenomena such as chimneying, cavity collapse and overburden gasification. Such phenomena could be simulated by greatly increasing the complexity of the model, however the effect of doing so on runtime would preclude the use of the model as a first pass screening tool.

The second conclusion is that comparison with longwall mines may be less useful for predictive models of UCG than previously thought. Although the UDEC model is seen to be more accurate than empirical methods, the simulation is seen to consistently overpredict subsidence in these tests. While the accuracy of these models could be improved by better matching model designs to site parameters, doing so would greatly reduce their usefulness as validation studies for the UCG model.

Third, the results of the multiple cavity Angus Place study show that, with sufficient modification, the model is capable of simulating multiple cavity systems. Doing so requires a considerable increase in model complexity and runtime however. As such, it is suggested that an alternative model based on that presented in this chapter should be produced to simulate multiple cavity systems.

Finally, a key issue in the validation of the UCG model was the lack of available data on which to perform comparative work. Data are difficult to obtain in many cases due to commercial secrecy. As models are the primary tool for ensuring the safety of future UCG trials, and validation is the most important method of ensuring model validity, it is essential that a greater amount of data are acquired. Given the cost and political opposition to UCG experiments, it is suggested that these data would best be acquired by increasing access to existing trial results. This could be achieved through widening publication of these results or through closer collaboration between academic researchers and UCG operators.

Despite the above issues, the model produced in this work is considered to be sufficiently accurate for use as a first pass screening tool for UCG designs. As such, the following chapter applies the model to a range of varying UCG site designs in order to produce an initial set of predictive results and best practice guidelines for UCG operators. Further modelling of chosen sites should always be carried out using more detailed simulators before any experiments are performed, but this model should greatly reduce the demands of such modelling by allowing operators to quickly eliminate any unsuitable sites. Further work on the validation of the model should also be carried out using new data as it becomes available.

8. SITE DESIGN STUDIES

SUMMARY

This chapter presents the results of a series of tests in which the model is used to predict the local environmental effects of a range of potential underground coal gasification (UCG) sites with varying geometric, geological and operating conditions. These tests are used both to identify limitations in the applicability of the model and to provide initial predictive results for a range of UCG designs. These results are then used to produce a set of best practice guidelines for future UCG operations which allow operators to quickly assess the suitability of a range of site designs.

The majority of the results in this chapter show good agreement with expected trends in behaviour, providing further validation of the model and allowing for the derivation of robust guidelines for approximating the extent of subsidence and thermal penetration length. Hydraulic results are also seen to follow the expected trends, however the uncertainty in these results is significant, with many results showing a range of variation greater than 100% of the mean value. Further modelling work is suggested to improve the hydraulic results, as well as to extend the applicability of the model over a greater range of site designs. Despite the uncertainties observed, the results in this chapter suggest that the Universal Distinct Element Code (UDEC) model provides a sufficiently accurate prediction to satisfy its intended end use as a first pass screening tool for UCG site selection.

8.1. INTRODUCTION

This chapter applies the completed UDEC model to a number of cases with varying site conditions. This is performed both to test the limits of model validity and to produce initial predictive results. These results are then used to identify trends in how certain site parameters influence the local environmental impacts of underground coal gasification. Finally, these trends are used to produce a set of ‘best practice’ guidelines for UCG operators to minimise the future environmental risks of UCG.

The tests in this chapter were performed by making alterations to the initial model shown in Section 6.2. These alterations involved varying only those properties which can be set either through site selection (e.g. cavity depth) or operating decisions (e.g. operating pressure). As such, these results represent the effects of gasifier design and measurable physical properties rather than those of model specific variables.

Wherever possible, the models below use a consistent random seed. This allows for a direct comparison of results without the need to consider random effects, as well as reducing the number of tests which must be run. For the cavity geometry models, repeats must be performed as the random geometry of the discrete fracture network (DFN) depends on cavity geometry. In these cases, three repeats of each test are performed and the mean and standard deviation of the results are presented. Groundwater flow rates are given as the geometric mean of three trials and are expressed in mL/day calculated on the assumption of a 600m long channel, equal to that of the Bloodwood Creek trial (Mark & Mallett, 2008). Errors in flowrates are quoted as multiplicative rather than additive, indicated by prefixing with an “x”.

8.2. EFFECTS OF CAVITY GEOMETRY

The geometry of a UCG cavity has a considerable influence over the process. UCG geometry is defined by the width, length and depth of the cavity. As mentioned in Section 2.1.5, larger cavities are economically beneficial as they increase the amount of syngas obtained from a single pair of wells. Deeper cavities can also operate at higher pressures, increasing the quality of syngas. Deeper cavities have a disadvantage however, as they greatly increase the capital costs of UCG. Cavity geometry also has a strong influence over the local environmental impacts of UCG. This section uses the UDEC model to investigate how these properties affect these environmental issues. In cases where multiple cavity operations are performed, the separation between cavities is also important. As shown in Section 7.5 however, the current model is incapable of simulating multiple cavity systems. As such, it is recommended that an additional model should be produced to simulate these sites.

8.2.1. Cavity Height

The height of a UCG cavity is the vertical distance from the base of the injection well to the roof of the void, which usually extends a short distance into the overburden above the coal seam. While cavity height cannot be set by the operator, it can be approximated as the vertical distance between the base of the injection well and the roof of the coal seam. Table 8.1 shows the effects of cavity height on local environmental issues. Figure 8.1 compares model results with empirical predictions for subsidence across the range of heights modelled.

Table 8.1 – Effects of cavity height on local environmental issues. The standard case is highlighted in bold.

Cavity Height (m)	Model Runtime (hrs)	Maximum Subsidence (cm)	Groundwater Inflow Rate (mL/day)	Thermal Penetration Length (m)
3.55	35 ± 6	0.47 ± 0.14	91.1 ± x3.4	7.54 ± 1.42
7.10	33 ± 10	0.73 ± 0.03	35.3 ± x1.3	8.98 ± 1.77
14.2	37 ± 7	1.00 ± 0.29	28.2 ± x2.8	9.62 ± 1.36
20.0	57 ± 7	1.39 ± 0.29	119.9 ± x1.9	8.64 ± 1.05
28.4	53 ± 8	1.72 ± 0.66	36.0 ± x1.3	6.24 ± 3.60

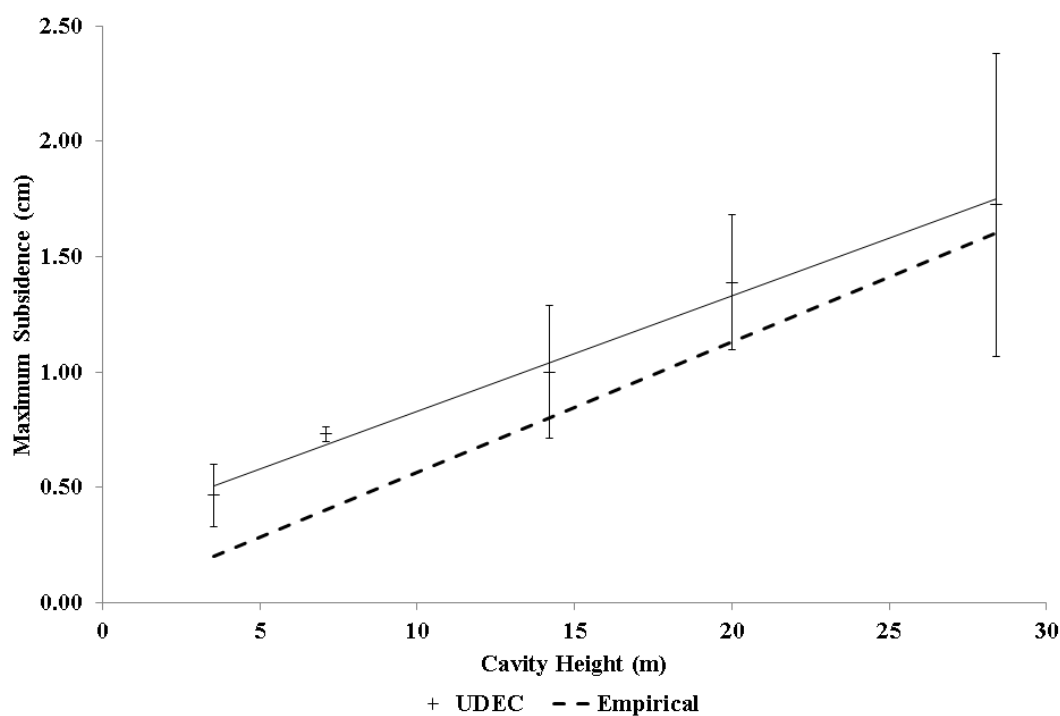


Figure 8.1 – Comparison of UDEC and influence function results (Brauner, 1973) for the effects of cavity height on subsidence, showing linear line of best fit for UDEC results.

Cavity height is seen to have a predictable influence on runtime and subsidence, and a less obvious effect on hydraulic or thermal results. Runtime is generally seen to increase with cavity height. This is to be expected, as taller cavities increase the length of joints in the DFN (see Section 6.3.1), producing more blocks and hence increasing the computational demands of the model.

Subsidence increases with cavity height as a larger void induces a greater stress on the cavity roof. In addition, taller cavities allow the stoping process (see Section 2.2.1.1) to continue to a greater extent, further increasing subsidence. As shown in Figure 8.1, modelled subsidence increases linearly with cavity height, agreeing with the empirical prediction. Model results are however seen to give consistently greater subsidence than empirical results. Given that the empirical model does not account for cavity shape, thermal or hydraulic effects, this suggests that the UDEC model is generally more accurate, as previously suggested in Chapter 7.

The hydraulic results shown in Table 8.1 suggest that cavity height has no overall effect on groundwater flowrate. This is unexpected, as one would expect a taller cavity to give higher flowrates due to the increase in differential pressure at the floor (cavity pressure is based on hydrostatic pressure at the roof). On the other hand, Section 6.3 shows that larger DFNs (associated with larger cavities) reduce flowrates as joint apertures tend to decrease with DFN size. Finally, given the scale of uncertainty in the results, it may also be that the effects of height are lost in the random variability of results. As such, it is suggested that further investigations be carried out to investigate the effects of cavity height on hydraulic behaviour.

The thermal results in Table 8.1 show the greatest thermal penetration length for the standard model, with shorter lengths observed as cavity height is either increased or decreased. As all results are within expected error margins, this effect is assumed to simply be a product of random variations. In addition, it is important to note that the thermal penetration length in the two shortest trials extends below the base of the model. This is a problem for any cavity with a height less than approximately 10m. This can be resolved simply by ensuring a minimum amount of rock is always simulated underneath the cavity. This was not performed in this work however, due to time constraints. Ensuring a minimum DFN height is also important to prevent this from occurring above the cavity roof.

Finally, the above tests highlight an issue with the relationship between DFN height and cavity depth. As shown in Section 5.2.1., the top of the DFN region extends to twice the cavity height above the cavity roof. If cavity depth is less than twice cavity height, the DFN would therefore extend above the ground's surface. Such a situation would invalidate model results as the model geometry would be too different from that used in validation studies. As such, simulated cavity heights should be limited to less than half the depth of the cavity.

8.2.2. Cavity Width

The effects of cavity width follow similar trends to those seen with cavity height. As with height, cavity width cannot be directly controlled, but can be approximated. Cavity width is usually found to be of a similar size to cavity height. Table 8.2 summarises the observations of a number of tests on varying cavity widths. Figure 8.2 shows the relationship between cavity width and subsidence for both model results and influence function predictions (Brauner, 1973).

Table 8.2 – Effect of cavity width on local environmental impacts of UCG. The standard case is highlighted in bold.

Cavity Width (m)	Model Runtime (hrs)	Maximum Subsidence (cm)	Groundwater Inflow Rate (mL/day)	Thermal Penetration Length (m)
3.10	Model failed due to block overlap error.			
6.20	57 ± 22	0.39 ± 0.08	63.3 ± x2.0	7.44 ± 1.63
8.80	35 ± 4	0.84 ± 0.06	4.14 ± x2.1	10.3 ± 0.71
12.4	37 ± 7	1.00 ± 0.29	28.2 ± x2.8	9.62 ± 1.36
17.5	29 ± 9	1.80 ± 0.39	1.61 ± x1.8	10.3 ± 0.84
24.8	49 ± 9	3.29 ± 1.08	2.72 ± x7.3	9.69 ± 1.36
49.6	Model failed due to block overlap error.			

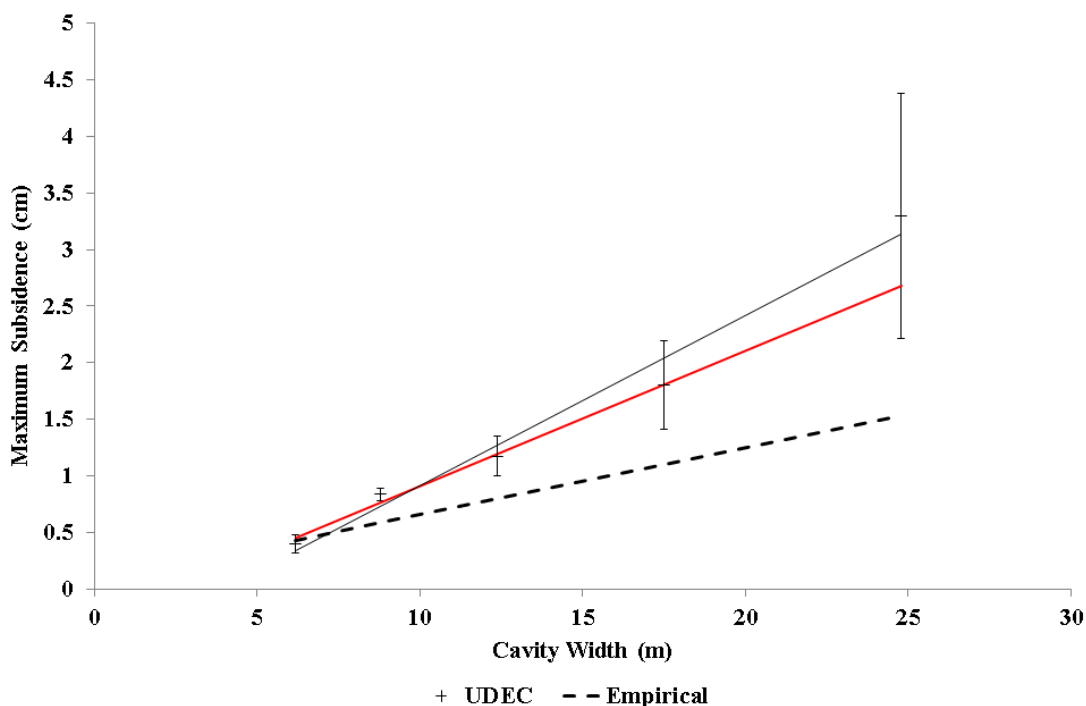


Figure 8.2 - Comparison of UDEC and influence function (Brauner, 1973) results for the effects of cavity width on subsidence, showing original (black) and corrected (red) trend lines.

As seen above, cavity width appears to have little effect on model runtime, with variations predominantly caused by the random nature of the DFN geometry. This is to be expected, given that DFN width has been previously shown (see Section 6.3.2) to have little influence on runtime. The lack of influence is predominantly due to the relationships between the size of the DFN and the length and number of joints it contains. These relationships imply that cavity width will only have an effect on runtime for designs with a high width to height ratio. As such, runtimes are expected to be approximately constant across the majority of practical site designs.

Groundwater inflow rate and thermal penetration length are also seen to be generally unaffected by cavity width. In reality, one would expect groundwater flow rates to increase with cavity width. As with height however, the effects of DFN size on flowrates prevent this effect. Thermal penetration lengths are constant within error across all cavity widths. This is to be expected, as cavity width should have no effect on heat transfer processes. It is of note however that the temperature profile extended outside of the DFN region in the two thinnest cases. This occurs simply because the DFN width is significantly reduced (as DFN width is set at three times cavity width). As with DFN height, this issue can be resolved in future by specifying a minimum width limit for the DFN region.

Cavity width is seen to have a considerable influence over the extent of surface subsidence above a UCG operation. Maximum subsidence is seen to increase in an approximately linear fashion with increasing cavity width, as shown in Figure 8.2. This behaviour agrees with that given by the empirical method, however the subsidence predicted by UDEC is seen to increase at a much faster pace than this method suggests. This difference in results is primarily caused by the large subsidence seen with the widest cavities. This large extent, and the accompanying large variability, were caused by a single data point with a much greater value than the others with that width. Removing this point from consideration gives a much closer agreement with empirical results, shown by the red trend line on Figure 8.2.

8.2.3. Cavity Depth

Cavity depth is defined as the vertical distance from the surface to the roof of the cavity. As with width and height, cavity depth is dependent more on the geometry of the coal seam than with operating conditions. Some control over depth is possible however, as the depth of the injection and production wells are set by the operator. Table 8.3 shows the results of a number of tests of the effects of cavity depth on environmental issues. Figure 8.3 compares model results and empirical predictions for the effects of cavity depth on surface subsidence.

Table 8.3 – Effects of cavity depth on UCG induced environmental impacts. The standard case is highlighted in bold.

Cavity Depth (m)	Model Runtime (hrs)	Maximum Subsidence (cm)	Groundwater Inflow Rate (m²s⁻¹)	Thermal Penetration Length (m)
24.6	Failed due to interaction between surface and DFN			
49.2	32 ± 2	2.26 ± 0.76	26.4 ± x1.7	10.49 ± 0.80
69.6	37 ± 13	0.86 ± 0.26	32.4 ± x1.5	8.84 ± 2.26
98.4	37 ± 7	1.00 ± 0.29	28.2 ± x2.8	9.62 ± 1.36
139.1	30 ± 7	0.70 ± 0.07	112.9 ± x1.5	3.66 ± 1.32
196.8	30 ± 7	0.69 ± 0.23	224.6 ± x1.6	3.66 ± 1.30
393.6	Failed – predicted upward motion across entire domain			

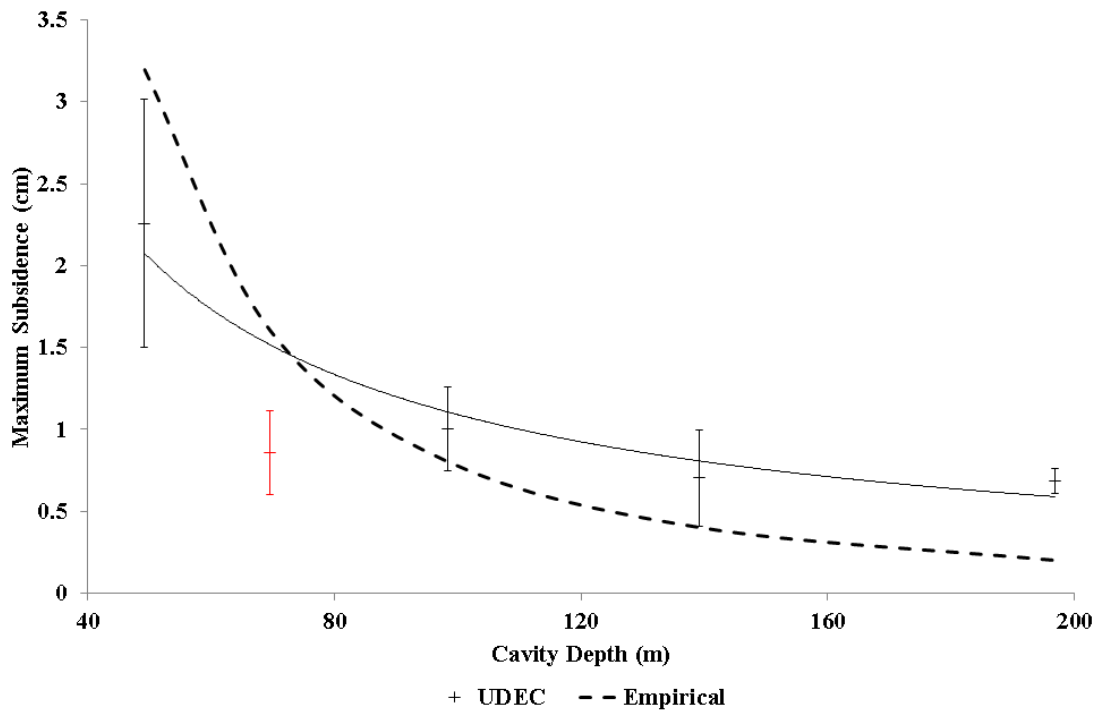


Figure 8.3 – Comparison of modelled and influence function (Brauner, 1973) predictions of the effects of cavity depth on surface subsidence.

Cavity depth is seen to have a negligible effect on runtime. This is expected as depth only affects the coarse region of the model. Subsidence is generally seen to decrease with depth, however the results at 69.6m do not follow this trend. It is believed that this error is simply due to random variations, and is exacerbated by the small number of trials performed. As such, the data at this depth (highlighted in red) is considered anomalous and is not included in the line of best fit. While subsidence decreases with depth as expected, the trend observed is much more gradual than that of the empirical method. It is of note however, that the results from both methods are close for all but the deepest data point. As such, it is believed that further trials should be performed in order to determine which method is more accurate. To further investigate these issues it is suggested that more data should be gathered, with a greater number of repeats for each point. Unfortunately, this was not possible within the timescale of the project.

As shown in Table 8.3, a model was produced for a depth of 393.6m (equal to four times the base case), however this model failed to solve. In two cases the model encountered block overlap errors, while the third predicted upward motion across the entire modelled domain. This failure was not unexpected however. As seen in Figure 8.3, subsidence is expected to decrease greatly with depth. For a depth of 393.6m, the empirical function predicts a maximum subsidence of 0.5mm. This is considerably smaller than the random variation seen in most executions of the model. As such, the model is shown to be incapable of accurately predicting such small ground movements. Given that such a small amount of subsidence is effectively harmless however (and would be difficult to detect in reality), the inability to predict this effect is not considered to be a problem. As such, the simulation of cavities at depths greater than approximately 250m is not considered necessary unless cavity width or height is greatly increased.

The effects of depth on hydraulic results behave as expected. Increases in depth lead to a steeper pressure gradient across the cavity wall as hydrostatic pressure increases. This in turn leads to an increase in flow rate which is observed in the results. Flow rate is seen to increase at a speed faster than the linear rate suggested by the cubic flow law. This difference caused by the effect of hydrostatic pressure on joints, as higher pressures force fractures open, increasing permeability. This is primarily seen with vertical joints, as the effect of pressure on horizontal joints is offset by the increased weight of the overburden. It is also of note however that the scale of statistical variations in hydraulic results also contributes to this effect.

Finally, cavity depth is seen to have an unexpected effect on thermal results. Penetration length is roughly constant across the shallower models, however the deep models give considerably shorter temperature profiles. After inspecting the outputs from the models it was found that the deeper trials had not successfully completed the thermal modelling stage. In these models the thermal stage ceased long before the desired end time of 100 days, however UDEC did not report any errors. It is not known why this occurred, as cavity depth should have no effect on either the thermal timestep or zone geometry. Given that this error occurred on every trial with a depth greater than 98.4m, there is evidently some unknown and potentially erroneous effect occurring. This issue, in combination with the limitations seen with the mechanical results, seriously challenges the validity of the model for assessing the effect of cavity depth on environmental issues. As such, it is suggested that a many more trials should be performed to identify the limits of the model with regards to depth. Given that many UCG operators would want to work at depths of several hundred metres, it is also suggested that separate models be produced (based on the current model) to simulate operations with much deeper cavities. Such simulations would only be necessary for larger cavities however, as small cavities at such depths would be expected to have a negligible influence on the local environment.

8.2.4. Combined Geometric Effects

As seen above, cavity height, width and depth all have a considerable influence on the extent of environmental damage caused by UCG. In the case of subsidence these properties are heavily interrelated, such that increases in one property could be offset by decreases in another. As such, directly setting limits for width, height or depth is not suitable. In order to overcome this issue, an attempt has been made to relate subsidence to a combined function of these measurements, as shown in Equation 8.1:

$$S_{max} = f\left(\frac{W_C H_C}{D_C}\right) \quad (8.1)$$

Where:

D_C	Cavity Depth	(m)
H_C	Cavity Height	(m)
S_{max}	Maximum Subsidence	(m)
W_C	Cavity Width	(m)

The above relationship was derived by considering the apparent relationships between subsidence and geometry, as shown in Figures 8.1 through 8.3. The factor of $\frac{W_C H_C}{D_C}$ was chosen in order to give the correct dimension (metres) for subsidence. Initial testing showed that this had a negligible effect on the accuracy of the combined predictor function, and was therefore considered to be justified. Figure 8.4 shows a plot of subsidence against the combined factor for every test performed in Section 8.2.

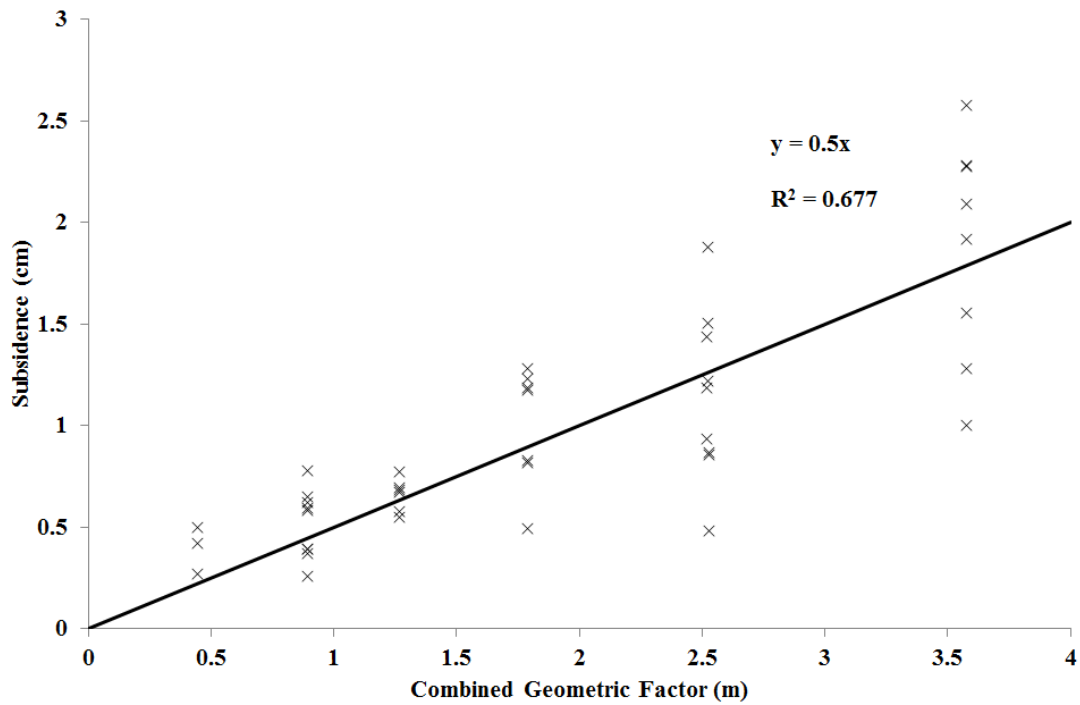


Figure 8.4 – Relationship between combined cavity geometric properties and subsidence. The datum point in red was considered anomalous and excluded.

The results in Figure 8.4 show a clear trend between subsidence and the factor proposed in Equation 8.1. From this trend, a predictive relationship has been proposed, as shown by the solid line on Figure 8.4. This relationship is given in Equation 8.2, where all variables are in units of m.

$$S_{max} = 0.005 \frac{W_c H_c}{D_c} \quad (8.2)$$

The linear relationship and factor of 0.005 were chosen for reasons of simplicity. Despite this, the function is seen to give a reasonable estimate for subsidence. While a slight improvement to accuracy is possible using a different coefficient, this was not considered worth the increase in complexity. As such, Equation 8.2 is presented as a simple and fast method for approximating subsidence from a UCG cavity. Further developments to the equation are presented in Section 8.3.1.

8.3. EFFECTS OF MECHANICAL PROPERTIES

Mechanical properties refer to the stiffness and strength of the rock mass in which UCG is to be carried out, as well as to the local in-situ stresses near the UCG cavity. As shown in Chapter 4, many of these properties depend on not only the physical composition of the rocks themselves, but also the geometry and material properties of the discontinuities between them. Given the complicated relationships between these properties, an independent analysis of each parameter is impractical. As such, this section investigates how variations in the properties of the overall rock mass (as found using the methods in Chapter 4) affect UCG induced environmental effects. In order to assess a real rock mass, the methods of Chapter 4 would be used to determine overall properties, and then the results of this section used to show how those properties affect behaviour.

8.3.1. Rock Mass Stiffness

Stiffness refers to a material's resistance to elastic strains, and is represented by Young's modulus. Increased stiffness allows rock strata to resist bending under their own weight and that of the strata above them. As such, stiffer rock masses tend to undergo much less strata bending, reducing subsidence. Stiffness has no effect on the plastic failure behaviour of the overburden however, as this depends on joint properties. Rock mass stiffness should have little effect on hydraulic results as flow occurs entirely within joints. Stiffness should also have no effect on thermal results. Table 8.4 shows the results of a number of tests using varying values of stiffness.

Table 8.4 – Effects of rock mass stiffness on local environmental issues. The standard case is highlighted in bold.

Young's Modulus (Pa)	Mechanical Timestep (μ s)	Model Runtime (hrs)	Maximum Subsidence (cm)	Groundwater Inflow Rate (mL/day)	Thermal Penetration Length (m)
1.58×10^8		Model failed due to block overlap errors.			
7.90×10^8	213	31	3.39	11.6	10.36
1.58×10^9	177	31	0.82	26.3	10.36
3.16×10^9	144	32	0.75	11.1	10.32
1.58×10^{10}	80	32	0.21	4.27	10.32

The results shown above behave as expected. Thermal penetration length and groundwater flow rate are seen to be generally unaffected by stiffness. Young's modulus is seen to have a negligible influence on runtime despite its effect on the mechanical timestep of the model. As stiffness increases, the timestep is decreased. Simultaneously, the increased stiffness reduces the amount of motion occurring in the model, reducing the total number of iterations needed. These effects are seen to cancel out, giving no overall effect on runtime. This is expected for a pseudo-steady state model such as this, but would not be true for dynamic models (e.g. of earthquakes).

In comparison with the above results, subsidence is seen to be heavily dependent on stiffness. Maximum subsidence is shown to be correlated with the reciprocal of the modulus, as expected. The strong dependence on rock mass stiffness suggests that the mechanical behaviour of the model is dominated by elastic deformation. This in turn suggests that strata bending is dominant mechanism driving subsidence. Stiffness can be included in Equation 8.2 to give Equation 8.3:

$$S_{max} = 8 \times 10^6 \frac{W_c H_c}{ED_c} \quad (8.3)$$

The constant value of 8×10^6 is chosen for simplicity, and has units of Pa. A slight increase in accuracy can be achieved using a more precise constant. Given the approximate nature of the equation however, this was not considered to be worth the increase in complexity. As such, Equation 8.3 presents a simple and fast method for estimating the subsidence caused by a UCG cavity of known dimensions in a rock mass of known stiffness. It is important to note that this is rock mass stiffness, rather than intact rock stiffness. As such, a method for estimating this stiffness, such as that presented in Chapter 4, should always be used in conjunction with this equation.

8.3.2. Intact Rock Strength

In the UDEC model, plastic failure of intact rocks is predicted by the strain softening Mohr-Coulomb yield criterion. The behaviour of this criterion depends on three properties: rock mass friction angle, cohesion and tensile limit. The effects of each of these parameters were tested at values of 0.1, 0.5, 2.0 and 10.0 times their base case values. In the case of friction angle, angles were set such that the tangent function of the angle was equal to the desired multiple of the base case value. In all cases, results showed that these properties had negligible influence effect on the runtime or mechanical, hydraulic or thermal behaviour of the simulation. These observations therefore show that plastic yielding of intact rocks is not occurring within the model, and that environmental effects are controlled entirely by the failure of joints and the elastic deformation of blocks.

8.3.3. Lateral Earth Pressure

Lateral earth pressure is a horizontal stress present in all rock masses. The stress can have a considerable influence over the behaviour of excavations by producing horizontal motion and/or providing a confining pressure effect. Lateral earth pressure varies from site to site and therefore its influence on the local environmental impact of UCG must be understood. Lateral earth pressure is usually referred to by means of the lateral earth pressure coefficient K_0 . This is given as the ratio of horizontal to vertical in-situ stress for a given site. Table 8.5 investigates the effect of K_0 on model results.

Table 8.5 – Effects of lateral earth pressure on local environmental impacts of UCG. The standard case is highlighted in bold.

Lateral Earth Pressure Coefficient (-)	Model Runtime (hrs)	Maximum Subsidence (cm)	Groundwater Inflow Rate (mL/day)	Thermal Penetration Length (m)
0.00	22	0.79	32.0	10.48
0.25	33	0.96	11.0	10.47
0.50	31	0.82	26.3	10.36
1.00	37	0.89	4.40	10.55
1.50	Model failed due to block overlap errors			
2.00	Model failed due to block overlap errors			

As shown above, lateral earth pressure has a negligible influence over the mechanical and thermal results of the model. Although results vary between trials there is no discernible trend, and all results are within expected error margins. Hydraulic results are also seen to be generally unaffected by lateral earth pressure. Finally, it is of note that increased earth pressures tend to increase model runtime. This is caused by the model requiring a greater number of steps to reach equilibrium as horizontal stresses increase. As such, the extra runtime seen in these models corresponds to an increase in the length of the “before” stage of the simulation. The overall results suggest that lateral earth pressure is not a critical parameter in model results. Given the relative difficulty of measuring this property in reality, it is therefore suggested that models continue to use the value of 0.5. Alternatively, K_0 could be set to zero in an attempt to speed model solution.

8.4. EFFECTS OF HYDRAULIC PROPERTIES

Hydraulic properties refer to parameters which control the flow of groundwater in the region of a UCG cavity. The most important of these are the local hydrostatic pressure (determined by the depth of the water table), the permeability of the overburden and the operating pressure of the cavity. These parameters are expected to have a considerable influence over the hydraulic results of the model, as well as some degree of coupling with mechanical results. Thermal results should be unaffected by these properties given the lack of thermal/hydraulic coupling in the model, however thermal behaviours would be somewhat affected by these properties in reality.

8.4.1. Water Table Depth

All of the models produced in this work initially contain a flat water table at a given depth below the surface. The height of this water table has a profound effect on UCG operations as it controls the value of the local hydrostatic pressure at the cavity. The height of the water table also has an effect on the material strength of the rock mass, as the action of groundwater pressure on the rocks acts to oppose the weight of the overburden. Table 8.6 shows the results of a number of tests which investigated the effects of water table height on model results. Tests were also produced with negative water table depths to represent offshore operations, but these failed due to overlap errors. Note that water table depths of 105.5, 119.7 and 200.0m represent the special cases in which the water table is inside the cavity, below the cavity, and below the model base respectively.

Table 8.6 – Effects of water table height on UCG induced local environmental issues. The standard case is highlighted in bold.

Water Table Depth (m)	Model Runtime (hrs)	Maximum Subsidence (cm)	Groundwater Inflow Rate (mL/day)	Thermal Penetration Length (m)
0.0	26	0.58	404.0	10.82
13.8	27	0.69	382.0	10.65
27.6	31	0.82	26.3	10.36
55.2	33	0.80	1.95	8.56
105.5 ^a	26	1.18	-0.24	11.02
119.7 ^b	27	1.31	0.00	10.94
200.0 ^c	15	1.19	0.00	9.64

a – Inside cavity. *b* – Below cavity. *c* – Below base of model (dry model).

Water table height is seen to have little effect on thermal results, with variations in penetration length seen to be within expected error. In addition, the effects of water table depth on runtime are seen to occur only with the deepest model. As mentioned above, this entire model was dry, leading to a considerable reduction in runtime as the hydraulic aspect of the model was effectively removed.

Water table height is seen to have the expected effect on hydraulic results. Deeper water tables reduce the pressure gradient across the cavity wall and thus reduce flow rates. The deepest sites behaved as expected, with zero flow observed in the driest models. The negative flow rate for the 105.5m model shows that groundwater is leaching out of the cavity. This is to be expected given that the cavity pressure in this model is effectively equal to hydrostatic pressure.

The only model in which a significant change in water table height was observed was the 105.5m model. The model is seen to form a small cone of depression and greatly exacerbate the variability in water table height near the cavity. This variability is partly caused by the generally low pressures in this model however, as the smaller range of variation makes minor effects stand out more clearly than in other models. No significant groundwater lowering was observed in any other trials.

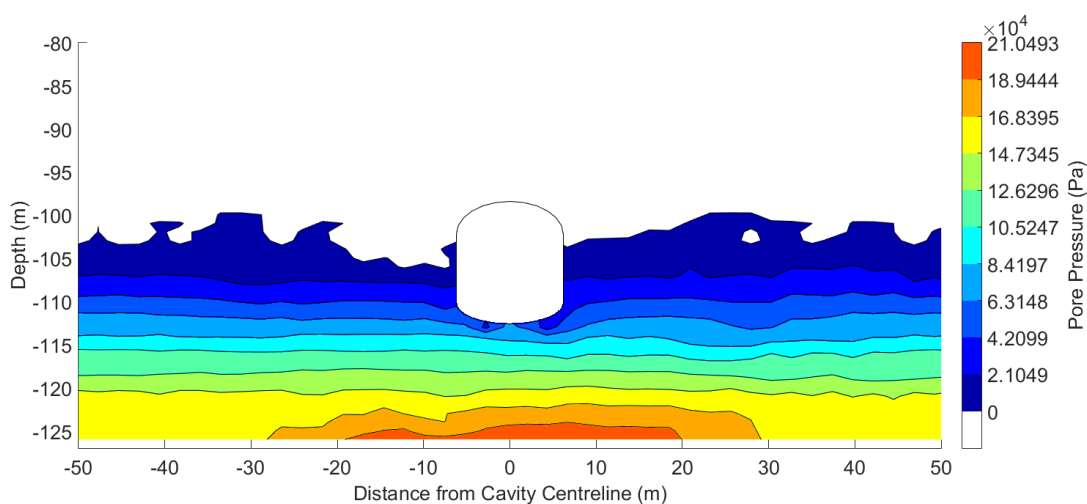


Figure 8.5 – Groundwater pressure distribution during operation of a UCG cavity initially sited within the water table at 105.5m.

Water table depth had the expected effect on subsidence, with deeper tables leading to increased ground deformation. As mentioned above, this occurs as reductions in pore pressure reduce the buoyancy forces opposing the weight of the overburden. As such, the net force on the rock mass is increased in models with deeper water tables, leading to greater subsidence. This trend is seen to reverse in the case of the completely dry 200m model; however it is believed that this is simply the result of random error. As such, further modelling of dry sites is recommended in order to confirm this.

The above results suggest higher water tables may benefit UCG by reducing subsidence. Increases in groundwater inflow rates caused by higher water tables also act to reduce the risks of groundwater contamination. Finally, the siting of UCG in offshore locations (i.e. with negative water table depths) may alleviate some of the social and legal concerns of UCG highlighted in Chapter 2. On the other hand the high groundwater inflow rates in these cases may act to quench gasification reactions, reducing syngas quantity and quality. Furthermore, although shallow water tables may reduce the risks of contamination, operating in completely dry sites eliminates it entirely. As such, operators should carefully consider the effects of water table height not only on environmental concerns, but also social and economic issues.

8.4.2. Site Permeability

Groundwater permeability is strongly related to hydraulic behaviour, although it is expected to also have an effect on subsidence due to the influence of pore pressure on mechanical results. The effects of permeability were tested at values equal to 0.01, 0.1, 10 and 100 times their base case values. The range of permeabilities tested is representative of many semi-pervious and impervious rock masses, including sandstone, limestone and typical oil reservoir rocks (Bear, 1972). Permeabilities outside this range were not considered relevant. Permeabilities lower than approximately 0.01mD are generally seen only in igneous rocks, which are not found near coal seams. Permeabilities greater than 1,000mD would generally be considered unsuitable for operations in which the control of groundwater flow is important. Table 8.7 shows the results of tests on site permeability.

Table 8.7 - Effects of rock mass permeability on local environmental issues of UCG. The standard case is highlighted in bold.

Permeability (mD)	Model Runtime (hrs)	Maximum Subsidence (cm)	Groundwater Inflow Rate (mL/day)	Thermal Penetration Length (m)
0.053	30	0.77	0.041	10.39
0.53	26	0.76	0.51	10.37
5.3	31	0.82	26.3	10.36
53	37	0.83	435.3	10.32
530	40	0.81	10049.9	10.32

As shown above, permeability is seen to have a negligible influence on thermal results. Subsidence is seen to increase slightly as permeability increases. This is due to slight increases in the suction force caused by groundwater flowing downwards into the cavity. Given the small changes however, this may also be due simply to random error. Runtime is seen to increase with permeability. This is partly due to increases in the amount of water flow to be modelled, however it is also affected by random variation.

As expected, permeability has a strong effect on the hydraulic results of the model. Figure 8.6 shows the relationship between permeability and flow rate. The exponent of 1.37 is close to the expected value of 1.5 found from the cubic flow law (with aperture proportional to the square root of permeability). This small difference in exponent is due to the opening and closing of joints around the cavity, altering their actual permeabilities from that of the input value.

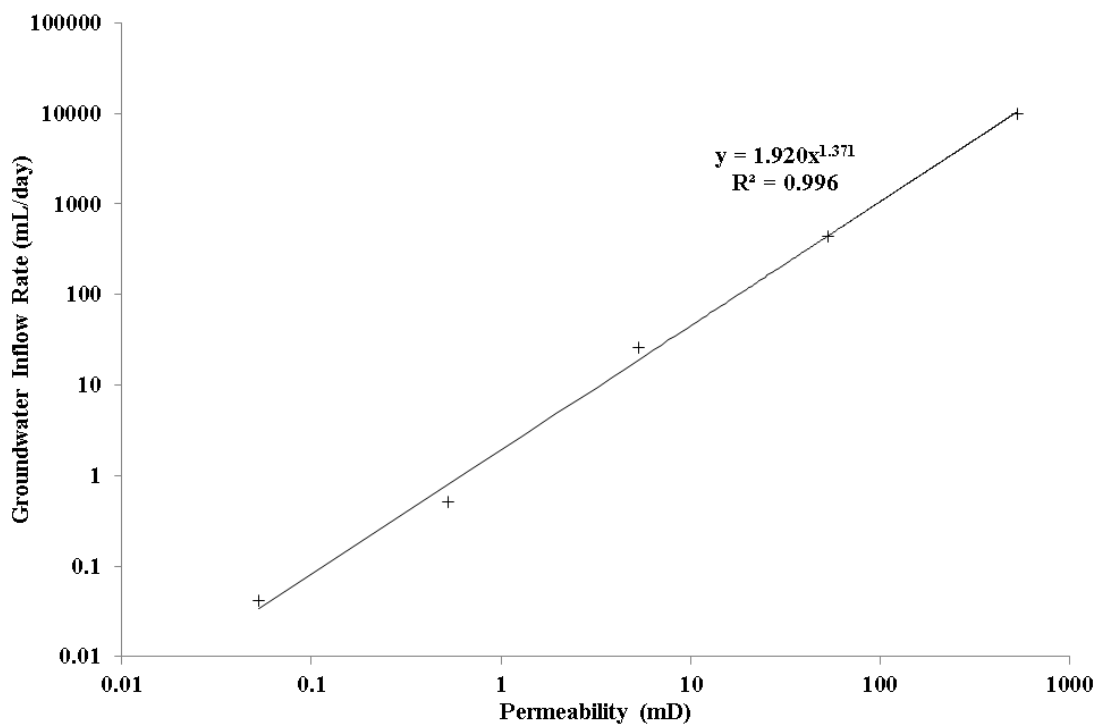


Figure 8.6 – Effect of site permeability on groundwater inflow rate.

Despite the considerable increases in flowrate, even at the highest permeability the level of the water table remains unchanged. As such, UCG operations would not be expected to cause water table lowering unless permeability is increased by a much greater amount. For example, consider an area of ground covering the entire cavity and extending to 100m beyond the cavity boundary (approximately equal to the size of the central subsidence trough). In England, the average annual rainfall rate is 855mm/year (Met Office, 2010). As such, the area above the cavity receives approximately 4×10^8 mL/day of rain on average. In order to increase water table depth, the overburden above the UCG cavity would therefore need a permeability on the order of 1×10^6 mD, similar to that of gravel (Bear, 1972). Note that dryer locations would produce a lowering effect at lower permeabilities however.

Despite the lack of influence on the water table, changes in permeability are seen to affect pressure distributions close to the cavity. As shown in Figure 8.7, models with decreased permeabilities lead to a greater degree of channelling and a less uniform pressure gradient around the cavity. These effects are caused by the reduction in permeability requiring a steeper pressure gradient to cause flow, therefore focusing groundwater flows in the area with the steepest pressure gradient. Despite the large variabilities seen between successive trials, the close agreement observed between theory and results for the effects of permeability gives good evidence for the veracity of the hydraulic model and its application to UCG cavity behaviour.

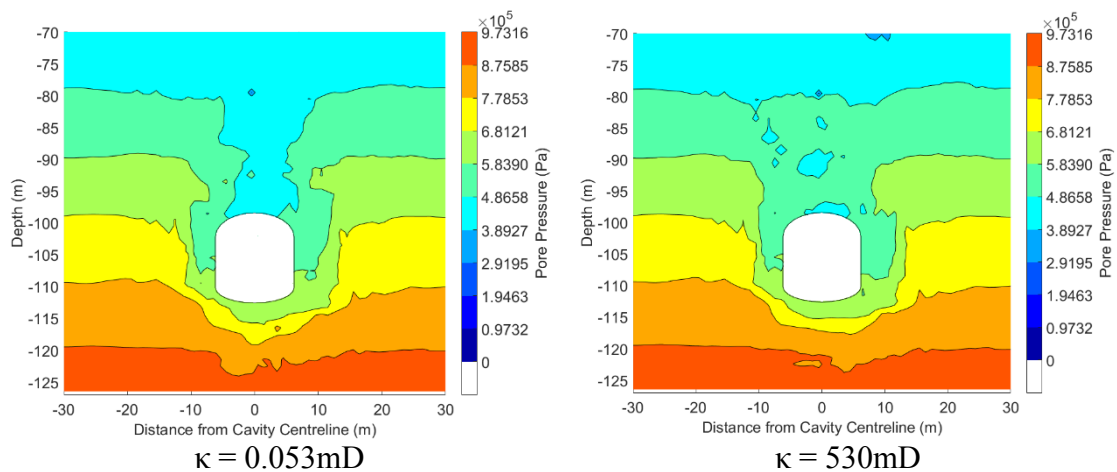


Figure 8.7 – Effects of permeability on pore pressure distribution.

8.4.3. Cavity Operating Pressure

Operating pressure has a considerable influence over UCG behaviour. Pressure is the primary means by which a UCG operator can control the gasification process. Higher pressures increase both gasification rates and syngas calorific value. Pressure is limited however by the need to prevent groundwater contamination. Operating at sub-hydrostatic pressures reduces the risk of pollution, but can lead to water table lowering and the quenching of the gasification process. Table 8.8 shows the results of a number of tests of the effects of operating pressure on the local environmental impact of UCG. Pressures are defined as a multiple of the local hydrostatic pressure at the roof of the cavity.

Table 8.8 – Effects of operating pressure on the local environmental impact of UCG. The standard case is highlighted in bold.

Pressure Multiple (-)	Model Runtime (hrs)	Maximum Subsidence (cm)	Groundwater Inflow Rate (mL/day)	Thermal Penetration Length (m)
0.00	Model failed due to overlap errors.			
0.50	38	0.79	51.9	10.15
0.80	31	0.82	26.3	10.36
1.00	41	0.73	0.16	10.15
1.25	41	0.71	-0.20	10.15
1.50	Model failed due to overlap errors.			

As shown above, operating pressure appears to have a negligible on many of the model results. Runtime and thermal penetration length are seen to be generally unaffected by operating pressure. In reality, decreased pressures would reduce thermal penetration lengths as increased flow rate would consume more energy to boil the groundwater. This is not seen in the model due to the lack of thermal/hydraulic coupling. Subsidence is seen to decrease slightly as pressure increases. This is expected, as an increase in pressure would reduce groundwater drawdown, leading to a reduction in the suction force on the overburden and reducing subsidence.

As expected, the greatest influence of operating pressure is seen with the groundwater inflow rate. For values equal to or lower than one, the relationship between pressure and flow rate is approximately linear. This is the expected relationship, as based on the cubic flow law. Theoretically, a pressure multiple of exactly unity should give zero flow. The small inflow rate observed in Table 8.8 is well within error however, confirming this behaviour. As expected, outflow is observed for pressures greater than the local hydrostatic value, confirming that sub-hydrostatic operation is a key requirement for the safe development of UCG. Extrapolating the above results to zero (i.e. a vacuum inside the cavity) gives a maximum possible inflow rate of approximately 105 mL/day for the base case cavity geometry. This is sufficiently low to prevent drawdown in all but the driest of locations, confirming the observations of unaltered water table heights throughout this chapter.

8.5. EFFECTS OF THERMAL PROPERTIES

Thermal properties refer to material properties which affect how heat transfers through rocks and how those rocks behave under high temperatures. The most important properties are thermal conductivity, specific heat capacity and thermal expansion coefficient. Other properties such as convective heat transfer coefficients are also important, but these cannot be simulated in UDEC.

8.5.1. Thermal Conductivity

Table 8.9 shows the effects of varying thermal conductivity on model behaviour. It is seen that conductivity has little influence on the runtime, mechanical or hydraulic results, with variations in all these properties within expected error..

Table 8.9 - Effects of thermal conductivity on the environmental impact of UCG. The standard case is highlighted in bold.

Thermal Conductivity (Wm⁻¹K⁻¹)	Model Runtime (hrs)	Maximum Subsidence (cm)	Groundwater Inflow Rate (mL/day)	Thermal Penetration Length (m)
0.139	24	0.77	18.0	5.38
0.695	31	0.85	18.5	8.53
1.39	31	0.82	26.3	10.36
2.78	31	0.84	18.5	13.84
13.9	31	0.84	17.8	21.27

As expected, thermal conductivity has a strong influence on thermal results. Thermal penetration length is seen to increase with conductivity to the power of approximately 0.3. This is close to the expected value of 1/3, given by Equation 8.4 (derived in Appendix B.5). It is of note that in the highest two cases, the thermal penetration length extends outside of the DFN in some directions. As such, penetration lengths can only be determined in certain directions. Given this observation it is suggested that any attempts to incorporate minimum DFN dimensions into the model, (such as suggested in section 8.1) should consider the thermal conductivity of the rock material. Despite this issue, the results shown in Table 8.9 behave almost exactly as expected, showing that the thermal model works as intended.

$$r_p \approx \left(\frac{12\lambda r_c t}{\rho C} \right)^{1/3} \quad (8.4)$$

Where:

C	Specific heat capacity	(Jkg ⁻¹ K ⁻¹)
r _c	Cavity radius	(m)
r _p	Profile radius / Thermal penetration length	(m)
t	Time	(s)
λ	Thermal conductivity	(Wm ⁻¹ K ⁻¹)
ρ	Density	(kgm ⁻³)

Equation 8.4 gives good agreement with model results for thermal properties and reasonable agreement for cavity geometry results, allowing it to be used as a simple tool to approximate the thermal influence of UCG cavities.

8.5.2. Specific Heat Capacity

Table 8.10 shows the effects of heat capacity on results. As with conductivity, this property has little influence over mechanical behaviour. It is of note however, that the model with the smallest heat capacity encountered less subsidence than other models. As shown in Section 5.3.3, rock mass strength increases at elevated temperatures. The larger thermal penetration length of this model therefore increases strength over a wider area, leading to a reduction in subsidence. Greater thermal penetration also drives rock mass expansion, further acting to resist subsidence as shown below.

Hydraulic results are seen to be affected by specific heat capacity, however no discernible trend is observed. Variations in flow rate are therefore predominantly caused by random effects. Unlike thermal conductivity, heat capacity is seen to be related to runtime. As shown in Equation A.34 (repeated below for comparison), the thermal timestep contains both a convective and a conductive term. The dependence of runtime on heat capacity but not conduction suggests that for a rock material, the convective term dominates. Given the low conductivity of rock, this is to be expected.

$$\Delta t = \min\left(\frac{B^2}{4\frac{\lambda}{\rho c}\left[1+\frac{UB}{2\lambda}\right]}\right) \quad (\text{A.34})$$

Where:

B	Zone edge length	(m)
U	Convective (boundary condition) heat transfer coefficient	(Wm ⁻² K ⁻¹)

Table 8.10 - Effects of rock mass specific heat capacity on model results. The standard case is highlighted in bold.

Specific Heat Capacity (Jkg⁻¹K⁻¹)	Model Runtime (hrs)	Maximum Subsidence (cm)	Groundwater Inflow Rate (mL/day)	Thermal Penetration Length (m)
92	49	0.62	40.2	21.27
460	40	0.82	3.48	13.83
920	31	0.82	26.3	10.36
4600	25	0.78	10.7	8.38
9200	27	0.84	21.7	5.44

As expected, thermal penetration length is seen to decrease greatly with increasing heat capacity. In addition, decreased values of C_P are seen to give highly circular temperature profiles. It can be seen that penetration length depends on specific heat capacity raised to the power of approximately -0.28. This is close to the expected value of $-1/3$, given by Equation 8.4. Finally, the temperature profile for the two lowest values of heat capacity were seen to extend outside the DFN, again suggesting that a minimum DFN size should be set based on thermal considerations. Despite this issue however, the close agreement between model and theory further verifies the behaviour of the UDEC thermal model.

8.5.3. Thermal Expansion Coefficient

Unlike thermal conductivity or heat capacity, the rock mass thermal expansion coefficient is expected to have a strong effect on the mechanical results of the model. On the contrary, this property is expected to have little to no effect on thermal model results. Table 8.11 shows the influence of this property on model behaviour.

Table 8.11 - Effects of thermal expansion coefficient on results. The standard case is highlighted in bold.

Thermal Expansion Coefficient (K⁻¹)	Model Runtime (hrs)	Maximum Subsidence (cm)	Groundwater Inflow Rate (mL/day)	Thermal Penetration Length (m)
1.16×10 ⁻⁶	36	0.93	13.8	10.67
5.80×10 ⁻⁶	31	0.88	19.6	10.60
1.16×10⁻⁵	31	0.82	26.3	10.36
2.32×10 ⁻⁵	35	0.80	10.1	10.63
1.16×10 ⁻⁴	Model failed due to overlap errors.			

As expected, the thermal expansion coefficient has a negligible effect on thermal penetration length. Groundwater inflow rate and model runtime are seen to be affected, but in both cases the variations are within the expected range of random variation. In addition, no clear trends can be discerned in either measurement. As such, these differences are simply caused by random effects.

Maximum subsidence is seen to decrease with increasing thermal expansion coefficient. This is to be expected, as the process of thermal expansion acts in opposition to that of cavity collapse and subsidence. As such, the situation of UCG in locations with more expansive overburden (e.g. overburden dominated by quartzite or sandstone) may act to prevent subsidence somewhat. Considering the relatively small change in subsidence over the range of measurements tested however, this effect may be minimal in comparison with other subsidence prevention techniques such as siting the cavity at greater depths.

8.6. BEST PRACTICE GUIDELINES FOR SITE DESIGN

The results of this and the previous chapters have identified several trends in how geometry, geology and operating conditions affect the environmental impact of UCG. From these trends, a set of best practice guidelines has been produced to suggest how future operations could avoid environmental damage. These guidelines are based on those given by Bhutto *et al* (2013), with additional suggestions based on model results. In order to avoid environmental damage while remaining economically viable, all future UCG operations should meet the following criteria:

- Coal seam thickness (and thus cavity height) should be at least 4m, in order to produce economically viable syngas quantities (Bhutto *et al*, 2013).
- Carbon capture and storage should be included on all UCG operations, regardless of the intended end use of the syngas. (Roddy & Younger, 2010)
- Wherever practical, cavity depths should be at least 800m, to allow storage of supercritical carbon dioxide within the reactor zone (Burton *et al*, 2006).
- UCG operations should be spaced at a horizontal distance of at least 5 times the critical radius (see Equation 2.1) from any other underground construction or resource extraction technology. The radius calculation should assume an angle of draw of 44° (see Section 6.2). The factor of 5 is double that used in the model, and accounts for the subsidence of the second construction.
- Cavity height, depth and width, should be chosen to produce a maximum surface subsidence of less than 2.0cm, as calculated by Equation 8.2. Equation 8.3 should be used when measurements of rock mass stiffness are available.

- Overburden Young's modulus should have a value of at least 1GPa and should be estimated using simulated axial compression wherever possible.
- UCG operations should be sited within a completely saline groundwater environment or completely dry rock mass if possible.
- If UCG must be sited near potable aquifers, the roof of the cavity should be vertically separated from the water table by at least 80m (see Table 8.6), or twice the coal seam thickness, whichever is greater. The height of the water table should be measured throughout operation.
- Operating pressure should be set below the local hydrostatic value at a depth equal to one cavity height above the cavity roof. The exact value to use depends on the local permeability of the rock mass which will change during operation. As such, continual monitoring of groundwater inflow is essential.
- UCG should not be attempted in saturated rock masses with local permeability greater than 1×10^6 mD, to avoid water table lowering. The avoidance of reaction quenching may require a tighter restriction.

The above guidelines should be followed by all UCG operations in order to prevent both local and global environmental damage whilst remaining economically competitive. Finally, it is important to note that these criteria provide a bare minimum level of safe operation. In reality, a safety factor should be applied to all of the above suggestions in order to further guarantee that operations will not produce environmental damage. With such a factor in place, it is believed that UCG could prove to be a viable energy source used as a bridging technology towards an eventual renewable economy. It is important to note however, that many of these criteria will be very difficult to meet in several nations, including the UK.

8.7. CONCLUDING REMARKS

This chapter aimed to investigate how a number of UCG design and operating conditions affect the local environmental damage caused by UCG. These investigations were performed in order to determine the limitations of the model and to produce the set of best practice guidelines presented in Section 8.6. The results of these investigations follow expected trends, showing the model to be capable of predicting effects over a range of designs, however several limitations are identified:

Firstly, an issue is identified with particularly deep models. For depths greater than approximately 200m, the UDEC model produces unphysical behaviour. Depths greater than 100m also cause erroneous thermal results. Given the suggestion that UCG should be carried out at depths greater than 800m, this greatly reduces the applicability of the model to many potential site designs. On the other hand, the lack of expected environmental effects for such deep sits is problematic for model design. It is therefore suggested that a second model should be developed to extend modelling capabilities into much greater depths. The simplest way to achieve this would be to produce a new model, based on this work, but in which designs are calibrated around a standard depth of around 800m, with a range of applicability from 400 – 1200m. Such a model would be produced by altering model geometric properties to allow operation in this range, while altering other parameters to ensure accurate results. A similar model is also suggested for the simulation of multiple cavity systems, as suggested in Section 7.5. Further modelling is also suggested for complex geometries, such as those containing geological faults or abandoned mine workings.

A second limitation refers to the dimensions of the DFN region. Cavities with widths or heights less than 10m often had distorted temperature profiles. This issue can be solved by setting minimum DFN region dimensions. Doing so may negatively affect other results however, as seen in Section 6.3. In addition, the model is seen to fail in cases where cavity height is greater than half cavity depth. This is due to an interaction between the surface and the DFN. Given that a depth to height ratio of 2 or less would almost certainly cause subsidence however, this is considered acceptable.

The final limitation of the model refers to the uncertainty in results. As mentioned previously, the model aims to account for the natural variability of rock masses. Results in this chapter however, show that variations between identical sites can be as high as 40% for mechanical results and greater than 200% for hydraulic results. It is believed that this mechanical uncertainty can be reduced simply by increasing the number of times a test is repeated, or by small variations to internal model parameters. Hydraulic uncertainty is a greater concern however. Given the importance of these results on groundwater contamination and water table lowering, it is suggested that further hydraulic modelling should be the top priority for further model development.

Despite the above limitations, the results in Chapters 6, 7 and 8 suggest that the model is a capable tool for predicting the environmental impacts of UCG. It is believed that, with the further developments suggested, the model could provide a valuable first pass screening tool for the initial development of UCG as a commercial energy source. The production of a set of best practice guidelines also allows for the fast selection of UCG sites, greatly reducing the extent of modelling required.

9. CONCLUSIONS AND FURTHER WORK

9.1. CONCLUSIONS

The principal aim of this project was to produce a model capable of accurate predictions of surface subsidence, groundwater pollution and water table lowering caused by underground coal gasification (UCG). The model was to be non-site specific and should produce results within 24 hours on a standalone desktop PC. The proposed end use of the model was to be a first pass screening tool for the selection of potential field trial sites and commercial scale operations. The model produced has successfully met most of these aims, giving accurate results for surface subsidence and water table lowering over multiple sites whilst retaining a low computational runtime of approximately 5 hours per result. Further modelling is required however for groundwater pollution effects. The results from the model have been used to produce a set of best practice guidelines for future UCG operations.

Initial field trial validation shows that the model is able to predict surface subsidence with sufficient accuracy, agreeing to within 6% of measured subsidence at a previous UCG field trial, and producing a considerably more realistic subsidence profile than that given by empirical methods. The variability in results is large, generally between 10 and 30% of the mean value, however this is considered to be consistent with the inherent variability of rock masses. Despite significant simplification, the thermal model produces reliable results, with thermal penetration lengths for all standard models within the bounds predicted in the literature. Suggestions for improvements to the thermal model are made, but given the intended end use of the model, the current state of thermal prediction is considered more than sufficient.

Hydraulic results show the expected behaviour, with groundwater flow rates seen to follow expected trends with up to 99% accuracy, however these results are seen to have considerable variability. Groundwater flow rates are seen to vary by over 125% between successive runs of identical models. This scale of variation means that groundwater contamination may be occurring in models where the mean result shows a net groundwater inflow. It is of note that in all cases, the absolute value of flow rate is very low (on the order of 10 mL/day). This exacerbates uncertainty, as very small changes in behaviour (e.g. the failure of single joints) can greatly change the magnitude of flow predicted. The accuracy and applicability of the hydraulic model are limited by the discrete element method (DEM) formulation used, and as such it is suggested that further work should be performed using an alternative method. Suggestions for how this could be achieved are given in Appendix C.

Given these observations, the model is considered to be sufficiently accurate for its intended use. Consistently fast runtimes of approximately 5 hours per simulation allow many designs to be considered in a short time. Two main challenges were identified during model development however. Firstly, fracture geometry is seen to have strong effects on rock mass behaviour, producing order of magnitude differences in subsidence for otherwise identical sites. The understanding of this issue was greatly improved however, by the development of a simulated rock mass compression testing methodology. This technique increases our understanding of the effects of fracturing on rock mass strength, and can be used to inform the choice of fracture patterns and reduced rock mass properties in the UCG model and other simulations. It is believed that the technique could improve the accuracy of many geotechnical simulations in addition to those of underground coal gasification.

The second challenge was the issue of proving the validity of results given a lack of field trial data. Due to commercial secrecy, very little data is published on UCG trials. Longwall mining has long been considered a good analogue for UCG, however the results in this work show that these comparisons are not as useful as previously thought. Despite these issues, the validation studies performed show that the model is capable of reasonable predictions of simple UCG cavity designs. In summary, a simple 2D DEM simulation is shown to be more than capable of predicting the environmental damage caused by a UCG site with sufficient accuracy to act as a first pass screening tool.

9.2. SUGGESTIONS FOR FURTHER WORK

This section gives recommendations for further work which could both increase the capabilities of the model and further develop the scientific understanding of UCG. The first suggestions presented are those which can be achieved in the short term through improvements to the model. The later suggestions require more work, either through further modelling, or through research into the phenomena in question.

9.2.1. Short Term Goals

Model validity is currently limited by the lack of field trial data available. While the performance of additional field trials may be difficult due to costs and political opposition, it may be possible to acquire data on past sites through collaboration with operators. Attempts should also be made to identify other sources of data which may be used as analogues for UCG, such as deep underground tunnelling projects or nuclear waste storage sites.

A second goal would be the improvement of the thermal model and the incorporation of thermal/hydraulic coupling within the Universal Distinct Element Code (UDEC). Model accuracy could be improved with a number of simple additions, such as an approximation of the energy stored in groundwater and the effects of flow rates on cavity temperature. Many of these effects may require the development of new techniques, as well as an increased understanding of thermal/hydraulic coupling. The lack of influence of temperature on other issues reduces the importance of these developments however.

A third goal of future work would be the application of the model to a wider range of UCG sites, in particular deep operations and sites with multiple cavities. At present, the UDEC model is incapable of simulating sites in which the geometry is considerably different from the initial Rocky Mountain 1 design. It is therefore suggested that additional models be produced for sites with extreme geometries. While some development and testing would be required, it is believed that the creation of these models should be relatively fast, as they would be predominantly based on the current model. The lack of overburden damage expected with the deep model may also act to simplify model development, but may make validation more difficult to the lack of measurable results.

The final suggestion for an improvement to the model is the development of the contaminant transport simulation. As mentioned previously, this model would be developed using the USGS MT3DMS code. This software uses the finite difference method to solve the coupled advection/diffusion equation of mass transport for groundwater contaminants. Additional processes such as adsorption, reaction and biological destruction can be included using add on modules. Coupling with UDEC would be achieved through the use of permeability and pressure distributions based on UDEC results. As such, a full representation of contaminant generation, transport and destruction could easily be achieved. The finite difference algorithm can be executed using parallel processing techniques, allowing the models to solve quickly and allowing both the UDEC and MT3DMS models to be used as first pass screening tools. A description of how this model could be produced is given in Appendix C.

9.2.2. Long Term Goals

The suggestions in the previous section should greatly improve the accuracy, validity and capabilities of the current UCG model without significant extra work. In order to further understanding of UCG induced environmental damage and improve the accuracy of modelling, a number of longer term goals have also been identified.

Several suggestions for future work involve the creation of more complex models of UCG. Extension of modelling efforts into the third dimension, the incorporation of cavity growth mechanisms and the coupling of environmental effects with gasifier chemistry and heat transfer would all greatly improve the efficacy of simulations. While many of these efforts have already been achieved in standalone models, very little has been achieved in terms of combining these efforts into a single simulation. Many of the issues above would not be possible using UDEC, requiring an entirely new model to realistically simulate these effects. Given the time dependent 3D nature of many of these issues, such a model would require a great deal of both programming effort and computational resources. As such it is envisioned that such a model would have to be built in a site-specific manner, and would need to run for a much longer time than the current model. Such a model would most likely be built out of many smaller submodels and would almost certainly require the use of high performance computing capabilities, which may be beyond the capability of some commercial operators. It is important to note however that the use of models with long runtimes would still be preferable to the propagation of expensive and publically opposed field trial experiments.

Other long term suggestions include the development of new techniques to improve the modelling of both UCG and other geomechanical problems. One of the key problems with geomechanical modelling in DEM is the need to predefine fracture patterns before model cycling begins. This introduces inaccuracies as these patterns are often be assumed or based on sparse data. The ability to generate fractures as the model proceeds would therefore greatly increase the accuracy and usability of large scale DEM models. The driving of new fractures is not currently possible in block based DEM however, due to issues with the conservation of element volume. It is thought that further developments of DEM may be able to overcome this issue and it is therefore recommended that efforts should be made to development potential fracture independent DEM methods.

The final suggestion for long term future work is an improvement of both the modelling and scientific understanding of coupled thermal/hydraulic/mechanical issues in underground construction. Efforts have already been made to incorporate convection into DEM, however these greatly increase model runtimes. More simplistic approaches may be possible in which convection effects are partly assumed rather than fully simulated. The effects of groundwater boiling within pore spaces also cannot be simulated, however these issues are also not well understood in reality. It is therefore suggested that a program of both computational and experimental work be performed to observe fluid boiling in the pore spaces of rocks and how these effects influence groundwater flows. Better understanding of these effects will lend itself to more realistic simulations of a range of problems in geotechnics, including many energy related applications such as carbon capture and storage and geothermal energy generation.

10. REFERENCES

- Abdallah, G., Thoraval, A., Sfeir, A., Piguet, J.P. 1995: Thermal convection of fluid in fractured media. *International journal of rock mechanics and mining sciences & geomechanics abstracts*. 32 (5) pp 481-490
- Ahola, M.P., Thoraval, A., Chowdhury, A.H. 1996: Distinct element models for the coupled T-H-M processes: Theory and implementation. *Developments in Geotechnical Engineering*, 79, pp 181-211
- Akbarzadeh, H., Chalaturnyk, R.J. 2013. Coupled Fluid-Thermal-Mechanical Analyses of a Deep Underground Coal Gasification Cavity. *Journal of Architecture and Civil Engineering*, 1(1), pp 1-14
- Andreev, G.E., 1995: *Brittle failure of rock materials: test results and constitutive models*. Taylor & Francis.
- Andrianopoulous, E., Korre, A., Durucan, S. 2015. Chemical process modelling of underground coal gasification and evaluation of produced gas quality for end use. *Energy Procedia*, 76, pp 444-453.
- Anthony, D.B., Howard, J.B. 1976: Coal devolatilisation and hydrogasification. *Journal of the American Institute of Chemical Engineers*. 22(4), pp 625-656
- Aspentech, 2016: *Aspen Hysys*. Retrieved 29/08/16 from <http://www.aspentech.com/products/aspen-hysys/>
- Australian Broadcasting Corporation. 2016. *UCG banned immediately in Queensland, laws to follow, mines minister Anthony Lynham says*.

Baghbanan, A., Jing, L. 2007: Hydraulic properties of fractured rock masses with correlated fracture length and aperture. *International journal of rock mechanics and mining sciences*, 44(5), pp 704-719.

Bandis, S.C., Barton, N.R., Christianson, M. 1985: Applications of a new numerical model of joint behaviour to rock mechanics problems. In *Fundamentals of rock joints (proceedings of the international symposium on fundamentals of rock joints, Bjorkliden, Sweden, September 1985)*, pp 343-356

Barreto, D., O'Sullivan, C. 2012: The influence of inter-particle friction and the intermediate stress ratio on soil response under generalised stress conditions. *Granular Matter* 14 (2012), pp 505-521

Barton, N., By, T.L., Chryssanthakis, P., Tunbridge, L., Kristiansen, J., Loset, F., Bhasin, R.K., Westerdahl, H., Vik, G. 1994: Predicted and measured performance of the 62m span Norwegian Olympic ice hockey cavern at Gjovik. *International journal of rock mechanics, mining sciences and geomechanics*, 31(6), pp 617-641

Bear, J. 1972: *Dynamics of fluids in porous media*. Elsevier, New York.

Bertrand, F., Leclaire, L.A., Levecque, G. 2005: DEM-based models for the mixing of granular materials, *Chemical Engineering Science*, 60(8-9), pp 2517-2531

Bhasin, R., Hoeg, K. 1998: Parametric study for a large cavern in jointed rock using a distinct element model (UDEC-BB). *International journal of rock mechanics and mining science*, 35(1), pp 17-29

Bhutto, A.W., Bazmi, A.A., Zahedi, G. 2013: Underground coal gasification: from fundamentals to applications. *Progress in energy and combustion science*. 39, pp 189-214.

Bidgoli, M.N., Zhao, Z., Jing, L. 2013: Numerical evaluation of strength and deformability of fractured rocks. *Journal of Rock Mechanics and Geotechnical Engineering*. 5(6), pp 419-430.

Bidgoli, M.N., Jing, L. 2014: Anisotropy of strength and deformability of fractured rocks. *Journal of Rock Mechanics and Geotechnical Engineering*. 6(2), pp 156-164.

Biezen, C.E.G. 1996: Modelling underground coal gasification. *PhD Thesis*, Delft University of Technology, Delft, The Netherlands.

Blinderman, M.S., Fidler, S. 2003: Groundwater at the underground coal gasification site at Chinchilla, Australia. Presented at the *water in mining conference*. 13-15 October 2003, Brisbane.

Blum, P., Mackay, R., Riley, M.S., Knight, J.L. 2005: Performance assessment of a nuclear waste repository: Upscaling coupled hydro-mechanical properties for a far-field transport analysis. *International journal of rock mechanics and mining sciences*, 42(5-6), pp 781 – 792

Blum, P., Mackay, R., Riley, M.S. 2009: Stochastic simulation of regional scale advective transport in fractured rock masses using block upscaled hydro-mechanical rock property data. *Journal of hydrology*, 369 (3-4), pp 318-325

Boon, C.W., Housby, G.T, Utili, S. 2014: Designing tunnel support in jointed rock masses via the DEM. *Rock Mechanics and Rock Engineering*, 48, pp 603-632

BP p.l.c. 2016: *BP Energy Outlook, 2016 edition*. London, 2016.

Brady, B.H.G., Brown, E.T. 2005: *Rock mechanics for underground mining*. Kluwer Academic Publishers, Berlin

Brand, J. 2014. Introduction and update to Africary's Theunissen UCG project. Presented at the *Theunissen UCG public participation meeting*. 18 March 2014, Theunissen, South Africa.

Brauner, G. 1973: *Subsidence due to underground mining (in two parts): 1 – Theory and practices in predicting surface deformation*. US Dept of the interior, Bureau of mines, Washington DC.

Bretas, E.M., Lemos, J.V., Lourenco, P.B. 2014: A DEM based tool for the safety analysis of masonry gravity dams. *Engineering structures*, 59, pp 248-260

British Standards Institution. 1990: BS 1377-7:1990 *Methods of test for soils for civil engineering purposes. Shear strength tests (total stress)*. London, British Standards Institute.

Britten, J.A., Thorsness, C.B. 1988: A mechanistic model for axisymmetric cavity growth during underground coal gasification. *Lawrence Livermore National Laboratory*, Livermore, California

Brown, K.M. 2012: In-Situ Coal Gasification: An Emerging Technology. *Journal of the American Society of Mining and Reclamation* 1(1)

Brownfield, M.E., Charpentier, R.R., Cook, T.A., Gautier, D.L., Higley, D.K., Kirschbaum, M.A., Klett, T.R., Pitman, J.K., Pollastro, R.M., Schenk, C.J., Tennyson, M.E., Wandrey, C.J., Whidden, K.J. 2012: *An estimate of undiscovered conventional oil and gas resources of the world, 2012*. United States Geological Survey.

Building Research Establishment, 2000: *Technical Data Sheet – Stanton Moor Sandstone*. Retrieved 03/02/17 from <http://projects.bre.co.uk/ConDiv/stonelist/stantonmoor.html>

Burton, E., Friedmann, J., Upadhye, R. 2006: Best practises in underground coal gasification. *Lawrence Livermore National Laboratory*, Livermore, California.

Burton, E., Friedmann, J., Upadhye, R. 2008: Environmental issues in underground coal gasification (with Hoe Creek example). *Lawrence Livermore National Laboratory*, Livermore, California.

Buscheck, T.A., Hao, Y., Morris, J.P., Burton, E.A. 2009: Thermal-hydrological sensitivity analysis of underground coal gasification. *Proc. 2009 International Pittsburgh coal conference*, Pittsburgh, PA, USA, 20-23 September 2009.

Cai, M. 2011: Rock mass characterisation and rock property variability considerations for tunnel and cavern design. *Rock mechanics and rock engineering*, 44, pp 379-399

Camp, D.W., Krantz, W.B., Gunn, R.D. 1980: A water influx model for UCG with spalling-enhanced drying. Presented at the *15th intersociety energy conversion engineering conference*. 18-22 August 1980, Seattle, Washington

Campbell, J.H., Dalton, V., Busby, J. 1978: *Effects of Underground Coal Gasification on Groundwater Quality*. Lawrence Livermore National Laboratory.

Carrington, D. 2009: No new coal without carbon capture, UK government rules. *The Guardian*, 23 April 2009.

Challener, C. 2013: Fraught Fracking Future. *Chemistry & Industry*. 77(2) pp 20-23

Chaudhuri, B., Muzzio, F.J., Silvina Tomassone, M. 2010: Experimentally validated computations of heat transfer in granular materials in rotary calciners. *Powder technology*, 198(1), pp 6-15

Chen, W., Konietzky, H., Tan, X., Frühwirt, T. 2016: Pre-failure damage analysis for brittle rocks under triaxial compression. *Computers and Geotechnics*, 74, pp 45-55

Cleary, P.W., Sawley. M.L. 2002: DEM modelling of industrial granular flow: 3D case studies and the effect of particle shape on hopper discharge. *Applied mathematical modelling* 26(2), pp 89-111

COMSOL. 2013. *Software prices*. Retrieved 02/12/13 from <https://www.comsol.com/>

Couch, G.R. 2009: *Underground Coal Gasification*. International Energy Agency Clean Coal Centre. 2009.

Coulson, J.M., Richardson, J.F., Backhurst, J.R., Harker, J.H. 2004: *Coulson & Richardson's chemical engineering, volume 1 – Fluid flow, heat transfer and mass transfer*. 6th Edition. Butterworth-Heinemann, Oxford. pp 395-400

Coulthard, M.A., Dutton, A.J. 1988: Numerical modelling of subsidence induced by underground coal mining. The 29th US Symposium on rock mechanics (USRMS), 13-15 June, Minneapolis, Minnesota

Coulthard, M.A. 1999: Applications of numerical modelling in underground mining and construction. *Geotechnical and geological engineering* 17 (1999), pp 373-385

Creedy, D.P., Garner, K., Holloway, S., Jones, N., Ren, T.X. 2001: *Review of underground coal gasification technological advancements*. UK Department of trade and industry. Report No. COAL R211, URN 01/1041. The stationery office, London.

Cuff, C. 2013: Hydrogeology and environmental risk assessment of UCG. Presented at the 8th International UCGA conference & workshop. 3 – 6 June 2013, London.

Cundall, P.A. 1980: UDEC – A generalised distinct element program for modelling jointed rock. Peter Cundall Associates, Report PCAR-1-80; European Research Office, U.S. Army.

Daggupati, S., Mandapati, R.N., Mahajani, S.M., Ganesh, A., Pal, A.K., Sharma, R.K., Aghalayam, P. 2012. Compartment modelling and flow characterisation in non-isothermal underground coal gasification cavities. *Journal of industrial and engineering chemistry research*, 50, pp 4493-4508.

Dennis, D.S. 2006: *Rocky Mountain 1 Underground Coal Gasification Test Project, Hanna, Wyoming. Final Technical Report for the Period 1986 to 2006*. US Department of Energy, National Energy Technology Laboratory, Morgantown, WV.

Department of Energy & Climate Change. 2012. *Electricity Generation Costs*. October 2012. London, The stationery office.

Department of Trade and Industry. 2004: *Review of the feasibility of underground coal gasification in the UK*. September 2004, London, The Stationery Office.

Dodson, S. 2014: *Wildhorse Energy exits Hungarian Underground Coal Gasification Sector*. Retrieved 18/07/16 from <http://www.worldcoal.com/>

[cbm/28102014/Wildhorse-Energy-sells-Hungarian-UCG-assets-131/](http://www.worldcoal.com/cbm/28102014/Wildhorse-Energy-sells-Hungarian-UCG-assets-131/)

ENN. 2014: *Underground Coal Gasification*. Retrieved 18/07/16 from http://www.enn.cn/wps/portal/ennen/jsugc!/ut/p/b1/04_SjzQyMDIyMLMwNDDUj9CPykssy0xPLMnMz0vMAfGjzOLNgpzcHZ0MHQ3cXXydDByD3d3MLYOcDI18jfRzoxwVAdNOB80!/?pageid=jsugc

Environment Agency. 2013: *Underground Coal Gasification*. Retrieved 29/08/16 from <https://www.gov.uk/government/publications/2010-to-2015-government-policy-low-carbon-technologies>

Fang, Y., Nguyen, B.A., Carroll, K., Xu, Z., Yabusaki, S.B., Scheibe, T.D., Bonneville, A. 2013: Development of a coupled thermo-hydro-mechanical model in discontinuous media for carbon sequestration. *International journal of rock mechanics and mining sciences*, 62, pp 138-147

Fergusson, K.J. 2011. Underground Coal Gasification: A clean, low cost, source of gas for power generation and chemical feedstock. Presented at *The Energy Institute East Midlands Meeting*. 27th September 2011, Loughborough, UK.

Fergusson, K.J. 2015: Underground Coal Gasification. UCG vs Shale gas – Chalk and Cheese. Presented at the *Coal Research Forum AGM and UCG Workshop*. 15 April 2015, Leeds.

Friedmann, S.J., Burton, E., Upadhye, R. 2006: *LLNL Capabilities in Underground Coal Gasification*. Lawrence Livermore National Laboratory, Livermore, California.

Friedmann, J., Burton, E., Upadhye, R. 2007: Underground Coal Gasification. Presented at *the potential for underground coal gasification meeting*. 5 June 2007, Washington, D.C.

Friedmann, S.J., Burton E., Ezzedine, S., Wagoner, J. 2008: *Report on phase 1 of the underground coal gasification simulation program: Environmental Management*. Lawrence Livermore National Laboratory, Livermore, California.

Ganow, H.C. 1984: Results of long term ground surface measurements at the Hoe Creek III site. Presented at the *10th Underground Coal Gasification symposium*, Williamsburg, Virginia, 12-15 August, 1984.

Green, D.W., Perry, R.H. 2007: *Perry's Chemical Engineer's Handbook, 8th Edition*. McGraw-Hill, New York, USA.

Green, M. 2013: Processing and utilisation of UCG syngas. Presented at *the 8th International UCGA conference & workshop*. 3 – 6 June 2013, London.

Green, M. 2013: How UCG works. Presented at *the 8th International UCGA conference & workshop*. 3 – 6 June 2013, London.

Green, M. 2014: Underground Coal Gasification: On the Road to Commercialisation. *Modern Power Systems*. Retrieved 15/08/16 from <http://www.modernpowersystems.com/features/featureunderground-coal-gasification-on-the-road-to-commercialisation-4198939>

Green, M. 2015: Underground coal gasification – practical experience with UCG trials. Presented at the *Coal Research Forum AGM and UCG Workshop*. 15 April 2015, Leeds.

Gregg, D.W. 1977: Ground subsidence resulting from underground gasification of coal. *Lawrence Livermore National Laboratory Report*, Livermore, California.

Hadda, N., Bourrier, F., Sibille, L., Nicot, F., Wan, R., Darve, F. 2015: A microstructural cluster-based description of diffuse and localised failures, *Proceedings of the TC105 ISSMGE International Symposium on Geomechanics from Micro to Macro*, Cambridge, UK, 1-3 September 2014, pp 169-174

Hammah, R.E., Yacoub, T., Corkum, B., Curran, J.H. 2008: The practical modelling of discontinuous rock masses with finite element analysis. Proceedings of the 42nd US rock mechanics symposium and 2nd US-Canada rock mechanics symposium. San Francisco, California. June 29 – July 2, 2008.

Hartman, H.L. ed. 1992: *Mining Engineering Handbook*, 2nd Edition. Society for mining, metallurgy and exploration, Englewood, Colorado.

Hebden, D., Stroud, H.J.F. 1981: Coal gasification processes. In: Elliott, M.A. ed. 1981: *Chemistry of coal utilisation. Second supplementary volume*. Chapter 24. Wiley, New York.

Heger, U. 2010. Underground Coal Gasification plant near Kingaroy shut down after cancer causing chemical found in bores. *The Courier Mail*, 16 July 2010.

Higman, C., Van der Burgt, M. 2008: *Gasification*. 2nd edition. Elsevier. Oxford.

Hill, R.W. 1981: Burn cavity growth during the Hoe Creek No. 3 underground coal gasification experiment. Presented at the 7th *Underground coal conversion symposium*, Fallen Leaf Lake, California, 8-11 September 1981.

Hoek, E. 2001: Rock mass properties for underground mines. In: Hustrulid, W.A., Bullock, R.L. ed. *Underground mining methods: Engineering fundamentals and international case studies*. Littleton, Colorado: Society for mining metallurgy and exploration, 2001.

Hoek, E., Carranza-Torres, C., Corkum, B. 2002: Hoek-Brown failure criterion – 2002 edition. Proceedings of the 5th North American Rock Mechanics Symposium and the 17th Tunnelling Association of Canada Conference, Toronto, Canada, July 7 – 10, 2002, **1** pp 267-273

Hoek, E. 2007: *Practical Rock Engineering, 2007 edition*. Retrieved 13/06/16 from <http://www.roscience.com/documents/hoek/corner/Practical-Rock-Engineering-Full-Text.pdf>

Humenick, M.J. 1984: Water pollution control for underground coal gasification. *Journal of energy engineering*, 110. pp 100 – 112.

International Energy Agency. 2010: *Power generation from coal. Measuring and reporting efficiency performance and CO₂ emissions*. International Energy Agency, Paris.

Itasca Consulting Group, Inc. 2004: UDEC - Universal Distinct Element Code (Version 4.01). Minnesota: Itasca Consulting Group, 2004. Software available at www.itascacg.com

Itasca Consulting Group, Inc. 2006: UDEC – Universal Distinct Element Code User’s Guide, Second edition (first revision). Minnesota: Itasca Consulting Group, 2006.

Itasca Consulting Group, Inc. 2014: PFC – Particle flow code version 5.0. Retrieved 13/01/16 from <http://www.itascacg.com/software/pfc>

Jing, L., Stephansson, O. 2007: *Fundamentals of discrete element methods for rock engineering. Theory and Applications*. Elsevier, Amsterdam.

Kapusta, K., Stanczyk, K. 2011: Pollution of water during underground coal gasification of hard coal and lignite. *Fuel*. 90(5) pp 1927-1934

Kapusta, K., Stanczyk, K., Wiatowski, M., Checko, J. 2013. Environmental aspects of a field scale underground coal gasification trial in a shallow coal seam at the experimental mine Barbara in Poland. *Fuel*. 113, pp 196-208.

Kapusta, K., Stanczyk, K. 2014: Underground Coal Gasification in Poland. Experiences, results and future prospects. Presented at the *Minerals Engineering 2014 UK Energy Symposium*, 15th May 2014, Kegworth, UK.

Kay, D.R., McNabb, K.E., Carter, J.P. 1991. Numerical modelling of mine subsidence at Angus Place Colliery, In: Beer, Booker & Carter (eds): *Computer methods and advances in geomechanics*, 1991.

Keilich, W., Seedsman, R.W., Aziz, N. 2006: Numerical modelling of mining induced subsidence. In: Aziz, N. ed. Coal 2006 – Coal operator's conference, university of Wollongong & the Australasian institute of mining and metallurgy, 2006, pp 313-326.

Klimenko, A.Y. 2009: Early Ideas in Underground Coal Gasification and their Evolution. *Energies*, 2009(2), pp 456-476

Klimentov, P.P. 1963. *Influence of ground water on the process of underground gasification of coal deposits*. Translated into English for Lawrence Livermore Laboratory, June 1975.

Köhne, J.M., Köhne, S., Šimůnek, J. 2009: A review of model applications for structured soils: a) water flow and tracer transport. *Journal of contaminant hydrology*, 104(1-4), pp 4 – 35.

Kratzsch, H. 1983: *Mining Subsidence Engineering*. Springer-Verlag, Berlin

Langland, R.T., Trent, B.C. 1981: Computer models to support investigations of surface subsidence and associated ground motion induced by underground coal gasification. Presented at the 7th Annual Underground Coal Conversion Symposium, Fallen Leaf Lake, California, 8-11 September 1981.

Lavis, S. 2013. Coalfield geology and site selection. *Presented at the 8th International UCGA conference & workshop*. 3 – 6 June 2013, London.

Lee, H., Cho, H., Kwon, J. 2010: Using the discrete element method to analyse the breakage rate in a centrifugal/vibration mill. *Powder Technology*, 198(13), pp 364-372

Lelyveld, M. 2015: China cuts coal mine deaths, but count in doubt. *Radio Free Asia*, 16 March 2015. Retrieved 29/06/16 from http://www.rfa.org/english/commentaries/energy_watch/china-coal-deaths-03162015103452.html

Li, H., McDowell, G., Lowndes, I. 2014: Discrete-element modelling of rock comminution in a cone crusher using a bonded particle model. *Geotechnique Letters*, 4(2), pp 79-82

Li, J., Langston, P.A., Webb, C., Dyakowski, T. 2004: Flow of sphere-disc particles in rectangular hoppers – a DEM and experimental comparison in 3D. *Chemical engineering science*, 59(24), pp 5917-5929

Li, X., Wang, S.J., Liu, T.Y., Ma, F.S. 2004: Engineering geology, ground surface movement and fissures induced by underground mining in the Jinchuan nickel mine. *Engineering Geology*, 76(1-2), pp 93-107.

Linc Energy. 2016: *Chapter 11 proceedings*. Retrieved 15/07/16 from http://lincenergy.listedcompany.com/newsroom/20160531_175533_BRE_2YU0YTE M7N026RX3.1.pdf

- Lindblom, S.R., Covell, J.R., Oliver, R.L. 1990: *Results of phase 1 post-burn drilling and coring, Rocky Mountain 1 underground coal gasification site, Hanna Basin, Wyoming*. Western Research Institute, Laramie, Wyoming
- Lindblom, S.R., Smith, V.E. 1993: Rocky Mountain 1 Underground Coal Gasification Test. Hanna, Wyoming. Groundwater Evaluation. Final Report, June 10 1988 – June 30 1993. *Western Research Institute*, Laramie, Wyoming.
- Lisjak, A., Grasselli, G. 2014: A review of discrete modelling techniques for fracturing processes in discontinuous rock masses. *Journal of rock mechanics and geotechnical engineering* .6(4) pp 301-314
- Liu, G., Rong, G., Peng, J., Zhou, C. 2015: Numerical simulation on undrained triaxial behaviour of saturated soil by a fluid coupled DEM model, *Engineering Geology*, 193, pp 256-266
- Lorig, L.J., Cundall, P.A. 1987. Modelling of reinforced concrete using the distinct element method. *Proceedings of the SEM-RILEM International conference on fracture of concrete and rock*. Houston, Texas. June 17th – 19th 1987, pp 276-287.
- Ma, F., Deng, Q., Cunningham, D., Yuan, R., Zhao, H. 2013: Vertical shaft collapse at the Jinchuan nickel mine, Gansu province, China: analysis of contributing factors and causal mechanisms. *Environmental Earth Sciences*, 69, pp 21-28.
- Mallett, C. 2006: Managing Ground Deformation in UCG. *Presented at the Underground Coal Gasification Workshop*, Kolkata, India, 12-15 November 2006.
- Mallett, C. 2013: Carbon energy UCG projects update. *Presented at the 8th International UCGA conference & workshop*. 3 – 6 June 2013, London.

Marinos, P., Marinos, V., Hoek, E. 2007: The geological strength index (GSI): A characterization tool for assessing engineering properties of rock masses. Proceedings of the International Workshop on Rock Mass classification for underground mining, Information circular 9498, NIOSH, Pittsburgh, PA, USA, pp 87-94

Mark, R., Mallett, C. 2008: Wyoming UCG trials at Hanna – a template for commercial UCG production modules in Queensland. Presented at *Clean Coal Technologies: Queensland and Wyoming – the case for cooperation*. 10-11 April 2008, Brisbane.

Mason, J.M., Oliver, R.L., Moody, C.G. 1987: *Geology and groundwater hydrology of the proposed Rocky Mountain 1 underground coal gasification site, Hanna, Wyoming*. Western Research Institute, Laramie, Wyoming.

McGlade, C., Speirs, J., Sorrell, S. 2012: *A review of regional and global estimates of unconventional gas resources*. UK Energy Research Centre.

Met Office, 2010. *Climate Statistics*. Retrieved 16/09/16 from <http://www.metoffice.gov.uk/public/weather/climate/>

Min, K.B., Jing, L., Stephansson, O. 2004: Determining the equivalent permeability tensor for fractured rock masses using a stochastic REV approach: Method and application to the field data from Sellafield, UK. *Hydrogeology Journal*, 2004, 12(5) pp 497 – 510

Mine Subsidence Engineering Consultants. 2007: *Introduction to longwall mining and subsidence*. Revision A. August 2007. Mine Subsidence Engineering Consultants, Chatswood, New South Wales.

Mocek, P., Pieszczyk, M., Swiadrowski, J., Kapusta, K., Wiatowski, M., Stanczyk, K. 2016: Pilot-scale Underground Coal Gasification (UCG) experiment in an operating mine “Wieczorek” in Poland. *Energy*. 111 pp 313-321.

Moran, C., da Costa, J., Cuff, C. 2013: *Independent Scientific Panel Report on Underground Coal Gasification Pilot Trials*. Queensland Independent Scientific Panel for Underground Coal Gasification (ISP).

Morris, J.P., Rubin, M.B., Block, G.I., Bonner, M.P. 2006: Simulations of fracture and fragmentation of geologic materials using combined FEM/DEM analysis. *International Journal of Impact Engineering*. 33 (1-12) pp 463 - 473

Morris, J.P., Buscheck, T.A., Hao, Y. 2009: Coupled geomechanical simulations of UCG cavity evolution. *Proceedings of the International Pittsburgh Coal Conference*, Pittsburgh, PA, USA, 20 – 23 September 2009

Morvan, H. 2013. ANSYS Licensing, University of Nottingham. *Personal Communication*.

Mostade, M. 2013: Surface and subsurface gasification process engineering. *Presented at the 8th International UCGA conference & workshop*. 3 – 6 June 2013, London.

Munjiza, A., John, N.W.M. 2002: Mesh size sensitivity of the combined FEM/DEM fracture and fragmentation algorithms. *Engineering Fracture Mechanics*, 69(2), pp 281-295.

Myongsook, S.O., Peters, W.A., Howard, J.B. 1989: An experimental and modelling study of softening coal pyrolysis. *Journal of the American institute of Chemical Engineers*. 35(5), pp 775-792.

Nathanail, C.P., Bardos, R.P. 2004: *Reclamation of contaminated land*. Wiley. Chichester.

Neavel, R.C. 1981: Origin, petrography and classification of coal. In: Elliott, M.A. ed. 1981: *Chemistry of coal utilisation. Second supplementary volume*. Chapter 3. Wiley, New York.

Ng, T.T. 2004: Shear strength of assemblies of ellipsoidal particles. *Geotechnique*. 54 (10), pp 659-669

Nitao, J.J., Camp, D.W., White, T.A., Burton, G.C. Wagoner, J.L., Chen, M. 2011. Progress on a new integrated 3D UCG simulator and its initial application. Presented at *The International Pittsburgh Coal Conference*, 22nd September 2011, Pittsburgh, PA.

Oliver, R.L. 1987: Geologic evaluation of the proposed Rocky Mountain 1 Underground Coal Gasification Test Site, Hanna, Wyoming. Western Research Institute, Laramie, Wyoming

O'Sullivan, C. 2015: Advancing geomechanics using DEM. *Proceedings of the TC105 ISSMGE International symposium on geomechanics from micro to macro*, Cambridge, UK, 1-3 September 2014, pp 21-32

Perkins, G.M.P. 2005: *Mathematical modelling of underground coal gasification*. PhD Thesis, University of New South Wales, Australia.

Perkins, G., Sahajwalla, V. 2008: Steady state model for estimating gas production from underground coal gasification. *Energy & Fuels*, 22, pp 3902-3914

du Plooy, A., Majoros, P., Paprika, D., Brand, J., van Vuuren, P. 2012. *Coal Exploration for Underground Gasification – It's all about planning*. Retrieved 31/07/13 from http://www.uni-miskolc.hu/~earthc/6old/A_9_duPlooy-et_al.pdf

Plummer, C.C., Carlson, D.H., Hammersley, L. 2012: *Physical Geology, Thirteenth Edition*. McGraw-Hill, New York, USA.

Queensland Government, 2016: *Underground Coal Gasification Banned in Queensland*. Retrieved 18/07/16 from <http://statements.qld.gov.au/>

Statement/2016/4/18/underground-coal-gasification-banned-in-queensland

Ranjith, P.G., Viete, D.R., Chen, B.J., Perera, M.S.A. 2012: Transformation Plasticity and the Effect of Temperature on the Mechanical Behaviour of Hawkesbury Sandstone at Atmospheric Pressure. *Engineering Geology*, 151, pp 120-127

Reid, C., Nitao, J., Camp, D. 2012. Modelling of underground coal gasification – from simple to simulation. Presented at *the 8th International UCGA conference & workshop*. 3 – 6 June 2013, London.

Reid, C., Nitao, J., White, J., Friedmann, J. 2012. Application of an integrated Multiphysics simulator to underground coal gasification. Presented at the *12th American Institute of Chemical Engineers Meeting*, October 28 – November 2 2012, Pittsburgh, PA.

Robertson, E.C. 1988: *Thermal Properties of Rocks*, United States Geological Survey Report.

Roddy, D.J., Younger, P.L. 2010: Underground coal gasification with CCS: A pathway to decarbonising industry. *Energy and Environmental Science*. 2010(3), pp 400-407.

Rong, G., Liu, G., Hou, D., Zhou, C-b. 2013: Effect of Particle Shape on Mechanical Behaviours of Rocks: A Numerical Study Using Clumped Particle Model. *Scientific World Journal*, 2013

Samdani, G., Aghalayam, P., Ganesh, A., Sapru, R.K., Lohar, B.L., Mahajani, S. 2016. A process model for underground coal gasification – part I: Cavity growth. *Fuel*. 161, pp 690-703

Samdani, G., Aghalayam, P., Ganesh, A., Sapru, R.K., Lohar, B.L., Mahajani, S. 2016. A process model for underground coal gasification – part II: Growth of outflow channel. *Fuel*. 181, pp 587-599

Sarhosis, V., Yang, D., Sheng, Y., Kempka, T. 2013: Coupled hydro-thermal analysis of underground coal gasification reactor cool down for subsequent CO₂ storage. *Energy Procedia*, 40, pp 428-436

Sarhosis, V., Lavis, S., Mostade, M., Thomas, H.R. 2016: Towards Commercialising Underground Coal Gasification in the UK. *Environmental Geotechnics*, 15.

Sarraf, A., Mmbaga, J.P., Gupta, Hayes, R.E. 2011: Modelling cavity growth during underground coal gasification. *Proceedings of the 2011 COMSOL conference*, Boston, MA.

Sato, A., Kano, J., Saito, F. 2010: Analysis of abrasion mechanism of grinding media in a planetary ball mill with DEM simulation. *Advanced Powder Technology*, 21(2), pp 212-216

Scottish Government. 2015: *Moratorium on Underground Coal Gasification*. Retrieved 30/06/16 from <http://news.scotland.gov.uk/News/Moratorium-on-underground-coal-gasification-1e1a.aspx>

Seebregts, A.J. 2010: *Energy technology systems analysis programme, technology brief E02 – Gas fired power*. International Energy Agency, Paris.

Seifi, M., Chen, Z., Abedi, J. 2011: Numerical simulation of underground coal gasification using the CRIP method. *The Canadian Journal of Chemical Engineering*, 89(6), pp 1528-1535

Self, S.J., Reddy, B.V., Rosen, M.A. 2012: Review of underground coal gasification technologies and carbon capture. *International journal of energy and environmental engineering*. 2012 3(16)

Shackley, S., Mander, S., Reiche A. 2006: Public perceptions of underground coal gasification in the United Kingdom. *Energy Policy*. 2006(34) pp 3423-3433

Shafirovich, E., Varma, A. 2009: Underground coal gasification: a brief review of current status. *Industrial and engineering chemistry research*, 48, pp 7865-7875

Shirsat, V.A. 1989. *Modelling of cavity growth in underground coal gasification*. MSc Thesis. Texas Tech University, Texas

Siemens, C.W. 1868: XXXIII – On the regenerative gas furnace as applied to the manufacture of cast steel. *Journal of the Chemical Society* 21(0), pp 279-310

Snape, C. 2013: An overview of CO₂ capture technologies and their application in UCG. Presented at *the 8th International UCGA conference & workshop*. 3 – 6 June 2013, London.

Snoeberger, D.F. 1976: Evaluation of the native hydraulic characteristics of the Felix coal (Eocene, Wasatch formation) and associated strata, Hoe Creek site, Campbell County, Wyoming. *Lawrence Livermore National Laboratory*, Livermore, California.

Solak, T. 2009: Ground behaviour evaluation for tunnels in blocky rock masses. *Tunnelling and underground space technology*, 24, pp 323-330.

Solomon, P.R., Serio, M.A. 1993: Progress in coal pyrolysis research. *Fuel*. 72(5), pp 587-597

Stuermer, D.H., Ng, D.J., Morris, C.J. 1982: Organic contaminants in groundwater near an underground coal gasification site in north-eastern Wyoming. *Environmental Science & Technology*, 16(9), pp 582-587.

Swan Hills Synfuels. 2012: *Swan Hills In-Situ Coal Gasification Technology Development. Final Outcomes Report*. May 2012.

Tan, X., Konietsky, H., Frühwirt, T. 2015: Numerical simulation of triaxial compression test for brittle rock sample using a modified constitutive law considering degradation and dilation behaviour. *Journal of Central South University*, 22(8), pp 3097-3107

Thambimuthu, K., Soltanieh, M., Abanades, J.C. 2005: Capture of CO₂ in: *IPCC special report on carbon dioxide capture and storage*, Cambridge University Press, Cambridge.

Thorsness, C.B., Rozsa, R.B., Wong, R. 1977. Two-dimensional modelling of in-situ coal gasification. Presented at *the 3rd annual underground coal conversion symposium*, California

Thorsness, C.B., Britten, J.A. 1986: A mechanistic model for axisymmetric UCG cavity growth. Presented at the *12th annual underground coal gasification symposium*. 24-28 August 1986, Saarbrücken, Germany.

Thorsness, C.B., Britten, J.A. 1989: Lawrence Livermore National Laboratory Underground Coal Gasification Project: Final Report. *Lawrence Livermore National Laboratory*. Livermore, California.

Tomac, I., Gutierrez, M. 2015: Formulation and implementation of coupled forced heat convection and heat conduction in DEM. *Acta Geotechnica*, 10, pp 421-433

Torres, V.N., Atkins, A.S., Singh, R.N. 2014. Assessment of an Environmental Sustainability Index for the Underground Coal Gasification Process by Using Numerical Analysis. Presented at the *Coal operators conference 2014*. 12 – 14 February 2014, Woolongong, New South Wales.

Tsory, T., Ben-Jacob, N., Brosh, T., Levy, A. 2013: Thermal DEM-CFD modelling and simulation of heat transfer through packed bed. *Powder technology*, 244, pp 52-60

UK Oil and Gas Authority, 2015: *Oil and Gas: Petroleum licensing guidance*. Retrieved 30/06/16 from <http://www.gov.uk/guidance/oil-and-gas-petroleum-licensing-guidance>

Underground Coal Gasification Association. 2011: *History of UCG*. Retrieved 20/02/15 from <https://web.archive.org/web/20150220174707/http://ucgassociation.org/index.php/ucg-technology/history-of-ucg>

US Department of Energy, 1997. Environmental assessment of Hoe Creek underground coal gasification test site remediation. *United States Department of Energy, Environmental, Safety and Health Division, Federal Energy Technology Center, Morgantown, WV 26507-0880*

US Energy Information Administration. 2016. *Carbon dioxide emission coefficients*. Retrieved 28/06/16 from http://www.eia.gov/environment/emissions/co2_vol_mass.cfm

US Geological Survey, 2005: *MODFLOW and Related Programs*. Retrieved 02/07/16 from <http://water.usgs.gov/ogw/modflow/>

Van Krevelen, D.W. 1993: *Coal – Typology, physics, chemistry, constitution*. 3rd Ed. Elsevier, Amsterdam.

Vardakos, S.S., Gutierrez, M.S., Barton, N.R. 2007: Back-analysis of Shimizu tunnel no. 3 by distinct element modelling. *Tunnelling and underground space technology*, 22(4), pp 401-413

Vorobiev, O., Morris, J., Antoun, T., Friedmann, S.J. 2008: Geomechanical Simulations Related to UCG Activities. Proceedings of the International Pittsburgh Coal Conference, Pittsburgh, PA, USA, September 29 – October 2, 2008

Vyazmensky, A., Elmo, D., Stead, D., Rance, J.R. 2007: Combined finite-discrete element modelling of surface subsidence associated with block caving mining. Proceedings of the 1st Canada-US Rock Mechanics Symposium, Vancouver, Canada, May 2007.

Walker, G. 2013. Itasca Software Quotes. *Personal Communication*.

Walter, K. 2007: Fire in the hole – Underground coal gasification may provide a secure energy supply and reduce greenhouse gas emissions. *Lawrence Livermore National Laboratory Science & Technology Review*, April 2007.

Wampler, S.P. 2012: *LLNL to work with Interior Department on underground coal gasification*. Retrieved 15/07/16 from <https://www.llnl.gov/news/llnl-work-interior-department-underground-coal-gasification>

Wang, F.T., Mead, S.W., Stuermer, D.H. 1981: Groundwater Contamination near the Hoe Creek UCG experiments. Presented at the 7th Annual Underground Coal Conversion Symposium, Fallen Leaf Lake, California, 7-11 September, 1981.

Wei, L., Hudson, J.A. 1998: A hybrid discrete-continuum approach to model hydro-mechanical behaviour of jointed rocks. *Engineering Geology* 49 (3-4), pp 317 – 325

Welsh Government. 2015: *Minister extends moratorium to underground coal gasification*. Retrieved 30/06/16 from <http://gov.wales/newsroom/environmentandcountryside/2016/160325-minister-moratorium/?lang=en>

Wildhorse Energy. 2013: *Wildhorse Energy Limited June 2013 Quarterly Report*

World Energy Council. 2013: *World Energy Trilemma, 2013 energy sustainability index*. World Energy Council, London, UK.

World Energy Council. 2013: *World energy resources, 2013 survey*. World Energy Council, London, UK.

Xu, Y., Xu, C., Zhou, Z., Du, J., Hu, D. 2010: 2D DEM simulation of particle mixing in rotating drum: A parametric study. *Particuology*, 8(2), 141-149

Yang, D., Sarhosis, V., Sheng, Y. 2014. Thermal-mechanical modelling around the cavities of underground coal gasification. *Journal of the Energy Institute*, 87, pp 321-329.

Yang, D., Sheng, Y., Green, M. 2014. UCG: Where in the world? *The Chemical Engineer*. 872, pp 38-41.

Yang, L. 2005: Theoretical analysis of the coupling effect for the seepage field, stress field and temperature field in underground coal gasification. *Numerical heat transfer, part A: Applications: An international journal of computation and methodology*, 48(6), pp 585-606

Yang, L., Zhang, X. 2009. Modelling of contaminant transport in Underground Coal gasification. *Energy & Fuels* 23(1), pp 193-201.

Yerostigaz, 2014: *About Us*. Retrieved 15/07/16 from <http://yerostigaz.com/about-us/>

Younger, P.L. 2011: Hydrogeological and geomechanical aspects of underground coal gasification and its direct coupling to carbon capture and storage. *Mine water and the environment*, 30, pp 127-140.

Zhao, H., Ma, F., Xu, J., Guo, J. 2012: In-situ stress field inversion and its application in mining induced rock mass movement. *International journal of rock mechanics and mining sciences*. 53, pp 120-128.

A. UNIVERSAL DISTINCT ELEMENT CODE THEORY

A.1. MECHANICAL FORMULATION

A.1.1. Mechanical Calculation Cycle

This section outlines the details of UDEC's mechanical calculation algorithm, as shown in figure 3.1 (section 3.2.1). The mechanical cycle is broken into the following six cyclic steps, which repeat until a convergence criterion is met. Each step is examined in detail below.

1. Calculate contact stresses at gridpoints
2. Find strains within zones
3. Find stresses within zones
4. Determine forces at gridpoints
5. Determine velocities of gridpoints
6. Find new gridpoint locations

STEP 1. Calculate contact stresses at gridpoints

In this step, stresses at contacts are calculated based on the degree of overlap of contacting blocks, as shown in equations A.1 through A.5. Tensile and shear strengths of joints are limited by the tensile limit and Mohr-Coulomb failure criterion respectively. If block overlap exceeds a set tolerance, UDEC produces an error message. If block separation exceeds a set limit, the contact is deleted and the two blocks are treated as independent.

Note that a positive value of separation implies detachment while a negative value implies overlap. Separation is initially defined as zero before cycling begins. By convention, stresses in UDEC are positive in compression and negative in tension.

$$\Delta\sigma = -k_N\Delta s_N \quad \text{For } \sigma > -\sigma_T \quad (\text{A.1})$$

$$\sigma = 0 \quad \text{For } \sigma \leq -\sigma_T \quad (\text{A.2})$$

$$\Delta\tau = -k_S\Delta s_S \quad \text{For } \tau < \tau_{max} \quad (\text{A.3})$$

$$\tau = \tau_{max} \text{sign}(s_S) \quad \text{For } \tau \geq \tau_{max} \quad (\text{A.4})$$

$$\tau_{max} = C + \sigma \tan(\theta) \quad (\text{A.5})$$

Where:

k	Stiffness	(Nm ⁻¹)
s	Separation	(m)
σ	Normal Stress	(Pa)
σ_T	Tensile Strength	(Pa)
τ	Shear Stress	(Pa)
τ_{max}	Shear Strength	(Pa)

Subscripts:

N	Normal
S	Shear

STEP 2. Find strains within zones

The strains within a zone are found simply as the difference between the cumulative displacements (in two dimensions) of the gridpoints which make up the zone.

STEP 3. Find stresses within zones

Zone stresses are determined by applying a constitutive model to the strains found in step 2. For example, the stress within an isotropic elastic material is found as:

$$\sigma_i = E \varepsilon_i \quad (\text{A.6})$$

Where:

E Young's modulus (Pa)

ε_i Strain in i^{th} direction (-)

σ_i Stress in i^{th} direction (Pa)

STEP 4. Determine forces at gridpoints

The forces on a given gridpoint are found as the sum of the following terms:

$$F_i = F_i^L + F_i^C + F_i^Z \quad (\text{A.7})$$

Where:

F_i^L Are any external applied loads (e.g. gravity).

F_i^C Are forces resulting from contacts, found in step 1. The force at any gridpoint is found as half of the sum of all forces incident on all edges connected to that gridpoint. The factor of two accounts for the fact that all edges are defined by two gridpoints.

F_i^Z Represents the contribution of the internal stresses (found in step 3) in all zones within the same block which are adjacent to the gridpoint in question.

STEP 5. Determine velocities of gridpoints

In this step, Newton's second law is applied to determine the velocity of each gridpoint. The central differencing scheme of numerical integration is used to eliminate first order error terms from the solution. Calculation of the new velocity is described in equation A.8:

$$v_i \left(t + \frac{\Delta t}{2} \right) = v_i \left(t - \frac{\Delta t}{2} \right) + F_i(t) \frac{\Delta t}{m_i} \quad (\text{A.8})$$

Where:

m_i	Mass of gridpoint i	(kg)
t	Time	(s)
v_i	Velocity of gridpoint i	(ms ⁻¹)

The mass m of a gridpoint is found as one third of the sum of the masses of all of the zones connected to that gridpoint. The factor of one third accounts for the fact that each triangular zone consists of three gridpoints.

STEP 6. Find new gridpoint locations

In step six, the new positions of each gridpoint are found using equation A.9:

$$u_i(t + \Delta t) = u_i(t) + v_i \left(t + \frac{\Delta t}{2} \right) \Delta t \quad (\text{A.9})$$

Where:

u_i Displacement of gridpoint i

After step six the timestep is iterated, the new positions of each gridpoint are used to calculate the separation/overlap of joints, and the cycle returns to step 1.

A.1.2. Mechanical Timestep Determination

The mechanical timestep in UDEC is controlled by the software in order to prevent block interpenetration by limiting the motion of blocks within a single step. Because the joints and gridpoints are controlled by different mechanical properties, UDEC finds an appropriate timestep for each and uses the smaller of the two in all calculations, as shown in equation A.10:

$$\Delta t = \min(\Delta t_J, \Delta t_G) \quad (\text{A.10})$$

The joint based timestep Δt_J is found as:

$$\Delta t_J = 2\beta \sqrt{\frac{m_{\min}}{k_{\max}}} \quad (\text{A.11})$$

Where:

m_{\min}	Mass of the smallest block in the model	(kg)
k_{\max}	Highest joint stiffness in the model	(Nm ⁻¹)
β	Contact coefficient.	(-)

The contact coefficient β is a user defined value (default 0.1) that accounts for the fact that a single block may be in contact with many others.

The gridpoint based timestep Δt_G is found as:

$$\Delta t_G = \min \left(2 \sqrt{\frac{m_i}{k_i}} \right) \quad (\text{A.12})$$

Where:

m_i	Mass of gridpoint i	(kg)
k_i	Effective stiffness of gridpoint i	(Nm ⁻¹)
\min	Implies the minimum value found over all gridpoints in the model	

The effective gridpoint stiffness k_i is a function of the stiffnesses of all of the zones and joints surrounding the gridpoint.

$$k_i = \sum k_{i,Z} + \sum k_{i,J} \quad (\text{A.13})$$

$$k_{i,Z} = \frac{8}{3} \left(K + \frac{4}{3} G \right) \frac{B_{max}^2}{H_{min}} \quad (\text{A.14})$$

$$k_{i,J} = \left(L_{i,i+1} + L_{i,i-1} \right)^2 \max(k_N, k_S) \quad (\text{A.15})$$

Where:

B_{max} Largest zone edge length (m)

G Shear Modulus (Pa)

H_{min} Smallest height of a triangular zone (m)

K Bulk Modulus (Pa)

$L_{i,j}$ Length of the edge between gridpoints i and j (m)

A.1.3. Adaptive Local Damping

Adaptive local damping works by reducing the force incident on each gridpoint within a UDEC model at every mechanical timestep. Under this scheme, the total force on a gridpoint is reduced with the use of a damping factor β (set to 0.8 by default). This alters step 4 of the mechanical cycle by reducing the total gridpoint forces as shown by equation A.16.

$$F_i^D = F_i - \beta |F_i| \text{sign} \left(v_i \left(t - \frac{\Delta t}{2} \right) \right) \quad (\text{A.16})$$

A.2. HYDRAULIC FORMULATION

A.2.1. Hydraulic Calculation Cycle

The hydraulic calculation cycle in UDEC couples joint apertures (driven by mechanical calculations) with fluid pressure and flow rate. This is achieved with the following steps, which occur alongside the mechanical cycle.

1. Find new gridpoint locations (mechanical step 6)
2. Determine joint apertures
3. Determine flow rates
4. Determine pressure distribution
5. Determine gridpoint forces (mechanical step 4)

Each step is examined in turn, below:

STEP 1. Find new gridpoint locations

This step is effectively identical to the final step of the mechanical cycle (see appendix A.1.1). The separation of each joint is read into the hydraulic algorithm for further calculation.

STEP 2. Determine joint apertures

Joint hydraulic apertures are controlled by separation. A minimum value is given for joint aperture to prevent complete closure of joints undergoing overlap. A maximum value is also given to improve the computational efficiency of the model when large apertures are present. Joint apertures are found relative to the initial aperture (found under zero stress conditions) as shown in equations A.17 through A.19:

$$a = a_{min} \quad \text{For} \quad a < a_{min} \quad (\text{A.17})$$

$$a = a_0 + s_N \quad \text{For} \quad a_{min} \leq a \leq a_{max} \quad (\text{A.18})$$

$$a = a_{max} \quad \text{For} \quad a > a_{max} \quad (\text{A.19})$$

Where:

a Joint Aperture (m)

s_N Joint Normal Separation (m)

STEP 3. Determine flow rates

The flow of fluid along joints is driven by pressure differentials between adjacent domains. Flow rates are found using the cubic flow law, shown in equation A.20:

$$q = -\frac{1}{12\mu} a^3 \frac{\Delta P}{L} \quad (\text{A.20})$$

Where:

L	Length of joint	(m)
P	Pressure	(Pa)
q	Flow rate per unit depth into page	(m ² s ⁻¹)
μ	Dynamic viscosity	(Pa s)

The length term in equation A.20 is found as the arithmetic mean of the distances to the nearest contacts in the upstream and downstream directions. The pressure term takes hydrostatic pressure into account, as shown in equation A.21:

$$\Delta P = P_2 - P_1 + \rho g(H_2 - H_1) \quad (\text{A.21})$$

Where:

H _i	Height of centre of domain i above datum	(m)
g	Gravitational acceleration	(ms ⁻²)

Note that equation A.21 can allow for flow out of regions with zero pressure. This could lead to fluid flowing out of a domain which is not fully saturated (i.e. a domain within the vadose zone), or to more fluid flowing out of a domain than is actually present within the domain (breaking conservation of mass). In order to account for this, equation A.20 is multiplied by a corrective factor f . This factor is based on the saturation S of the upstream domain, as shown in equation A.22:

$$f = S^2(3 - 2S) \quad (\text{A.22})$$

Where:

$$S = \frac{V_{fluid}}{V_{domain}} \quad (\text{A.23})$$

Where:

V Volume, per unit depth into page (m^2)

STEP 4. Determine pressure distribution

Pressure changes within a domain are driven by both the flow of fluid into and out of the domain and by the change in domain volume due to mechanical deformation.

Equation A.24 shows how pressure within a domain is found for the n^{th} timestep.

$$P_n = P_{n-1} + K_F q_{in} \frac{\Delta t}{V_n} - 2K_F \frac{V_n - V_{n-1}}{V_n + V_{n-1}} \quad (\text{A.24})$$

Where:

K_F Bulk modulus of fluid (Pa)

q_{in} Net inflow into domain (m^2s^{-1})

V Domain volume, per unit depth into page (m^2)

In the case where fluid is flowing out of the domain in question, or where that domain increases in volume, it is possible for equation A.24 to predict a negative pressure. In this case, pressure within the domain is set to zero and the calculation changes to a version based on saturation. This allows water to drain out of a domain and provides for a definition of saturation (as used in equation A.22):

$$S_n = S_{n-1} + q_{in} \frac{\Delta t}{V_n} - 2 \frac{V_n - V_{n-1}}{V_n + V_{n-1}} \quad (\text{A.25})$$

While saturation is less than one, the pressure in the domain remains at zero and A.25 is used. If a saturation greater than one is predicted, saturation is set to a value of one and control reverts to equation A.24. Initial saturation S_0 is set either at 0 or 1 for a given domain depending on the initial location of the water table within the model.

STEP 5. Determine gridpoint forces

This step is the same as mechanical step 4, with the addition of a term to equation A.7 to account for the forces exerted by fluid pressure on the solid rock block. F_i^P refers to the force exerted on a gridpoint due to the pressure of the fluid in each of the domains connected to that gridpoint. As with F_i^C , the force at a given gridpoint is found as half of the sum of all forces incident on all edges connected to that gridpoint. Each individual contributive force is found as the product of the domain pressure and length.

A.2.2. Hydraulic Timestep Determination

As with the mechanical timestep, the hydraulic timestep in UDEC is limited to maintain model stability. The value of the timestep is given by equation A.26:

$$\Delta t = \min \left(\frac{v}{K_F \sum_i \left[\frac{1}{12 \mu L} a^3 \right]} \right) \quad (\text{A.26})$$

Where:

min Implies the minimum value over all domains

i Refers to the i^{th} contact associated with the current domain

A.3. THERMAL FORMULATION

A.3.1. Explicit Thermal Algorithm

The explicitly time-stepped thermal algorithm in UDEC uses a four step cycle to determine rock mass temperature profiles at later times based on an initial temperature profile and any heat sources/sinks. The four steps of the algorithm are:

1. Find temperature gradients within zones
2. Find heat flow rates out of each zone
3. Find heat flow rate in to each gridpoint
4. Find new temperature at each gridpoint

Each step is outlined in turn, below:

STEP 1. Find temperature gradients within zones

Temperature gradients within each zone are found as the area normalised sum of the product of average temperature and length for each of the three edges making up the zone, as shown in equations A.27 and A.28

$$\frac{\delta T}{\delta x} = \frac{1}{A} \left[\frac{T_1+T_2}{2} |x_1 - x_2| + \frac{T_1+T_3}{2} |x_3 - x_1| + \frac{T_2+T_3}{2} |x_3 - x_2| \right] \quad (\text{A.27})$$

$$\frac{\delta T}{\delta y} = \frac{1}{A} \left[\frac{T_1+T_2}{2} |y_1 - y_2| + \frac{T_1+T_3}{2} |y_3 - y_1| + \frac{T_2+T_3}{2} |y_3 - y_2| \right] \quad (\text{A.28})$$

Where:

A Area of the zone (m²)

T_i Temperature of gridpoint i (K)

x_i Horizontal position of gridpoint i (m)

y_i Vertical position of gridpoint i (m)

STEP 2. Find heat flow rates out of each zone

The heat fluxes out of each zone are found according to equations A.29 and A.30:

$$Q_x = -\lambda_x \frac{\delta T}{\delta x} \hat{L} \quad (\text{A.29})$$

$$Q_y = -\lambda_y \frac{\delta T}{\delta y} \hat{L} \quad (\text{A.30})$$

Where:

\hat{L} Unit length in Z dimension (1m)

Q_i Heat flux in i direction (Wm⁻¹)

λ_i Two dimensional thermal conductivity in i direction (Wm⁻¹K⁻¹)

Note that for a thermally isotropic material, λ_x = λ_y = λ.

STEP 3. Find heat flow rate into each gridpoint

The heat flow from one zone into another must be allocated between the three gridpoints that make up the zone receiving the energy. This allocation is achieved by multiplying directional heat fluxes by the length of a line drawn normal to the heat flux between the perpendicular bisectors of the two zone edges connected the given gridpoint. This is illustrated by equation A.31 and figure A.1.

$$\Omega_{z,i} = Q_x H_i + Q_y W_i \quad (\text{A.31})$$

Where:

$\Omega_{z,i}$ Refers to the heat flow from zone z into gridpoint i (W)

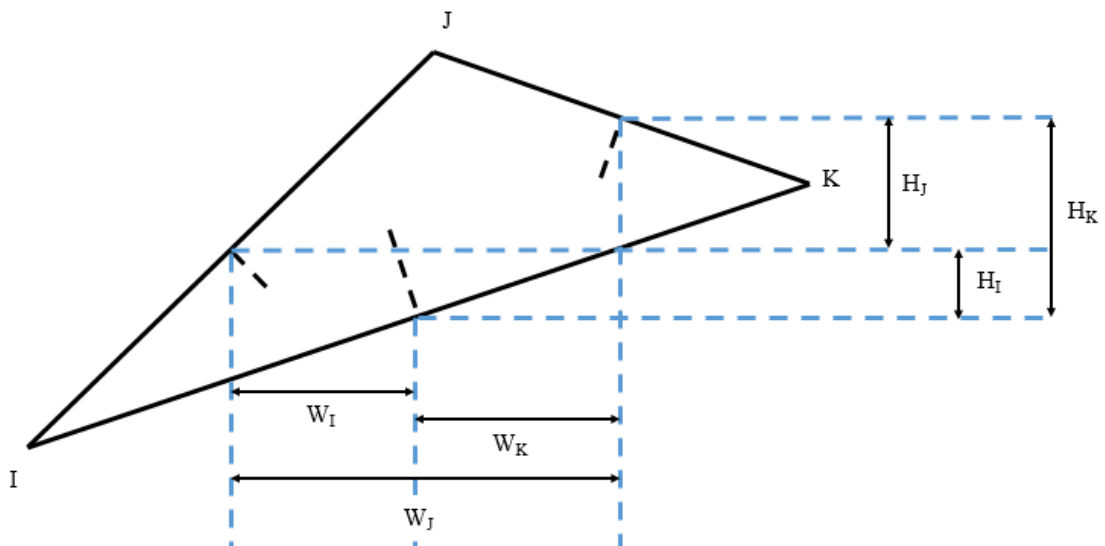


Figure A.1 – Definition of the lengths used in equation A.31

STEP 4. Find new temperatures for each gridpoint

The incremental temperature change at a gridpoint is found using equation A.32:

$$\Delta T = \frac{\sum_z \Omega_{z,i}}{mC_p} \Delta t \quad (\text{A.32})$$

Where:

C Specific Heat Capacity (Jkg⁻¹K⁻¹)

$\sum_z \Omega_{z,i}$ Implies a summation over all of the zones providing heat to gridpoint i.

A.3.2. Implicit Thermal Algorithm

UDEC's implicit thermal algorithm uses the Crank-Nicholson method to derive an expression for the finite difference representation of heat transfer. In one dimension, this is given by equation A.33. UDEC stores temperature data for all gridpoints in a matrix which is solved using a modified version of the Jacobi transformation method.

$$T_i(t + \Delta t) = T_i(t) + \frac{\lambda \Delta t}{\rho C_p} \left[\frac{T_{i+1}(t+\Delta t) - 2T_i(t+\Delta t) + T_{i-1}(t+\Delta t)}{(\Delta x)^2} + \frac{T_{i+1}(t) - 2T_i(t) + T_{i-1}(t)}{(\Delta x)^2} \right] \quad (\text{A.33})$$

A.3.3. Explicit Thermal Timestep Derivation

As with the mechanical and hydraulic aspects, an explicitly stepped thermal model has a maximum timestep above which model stability is not guaranteed. The definition of this timestep is given in equation A.34:

$$\Delta t = \min\left(\frac{B^2}{\frac{4\lambda}{\rho c} \left[1 + \frac{UB}{2\lambda}\right]}\right) \quad (\text{A.34})$$

Where:

B	Zone edge length	(m)
U	Convective (boundary condition) heat transfer coefficient	(Wm ⁻² K ⁻¹)
ρ	Material density	(kgm ⁻³)

A.3.4. Thermal Zone Generation

In an ideal case, the thermal mesh would be identical to the mechanical mesh (i.e. thermal zones would perfectly overlay mechanical zones). The need to conserve energy when heat transfers between blocks which are not perfectly aligned often leads to the requirement for extra thermal zones however. This concept is highlighted in figure A.2. In order to conserve energy, some heat must transfer between zones 1C and 2A, while some must transfer between 3C and 2A. The amount of heat transferred between any pair of blocks depends on the area of edge to edge contact between those blocks. In order to correctly determine this contact and thus model heat transfer between the blocks, new thermal zones (in red) are created. Heat can now transfer between zones 1Cb and 2Aa, and between zones 3Ca and 2Ab, satisfying the requirements of complete heat transfer and conservation of energy. Zones 1B and 3D are already perfectly aligned, so no new thermal zones are required. Note that joints are considered to have infinitesimal widths for the purposes of thermal calculations.

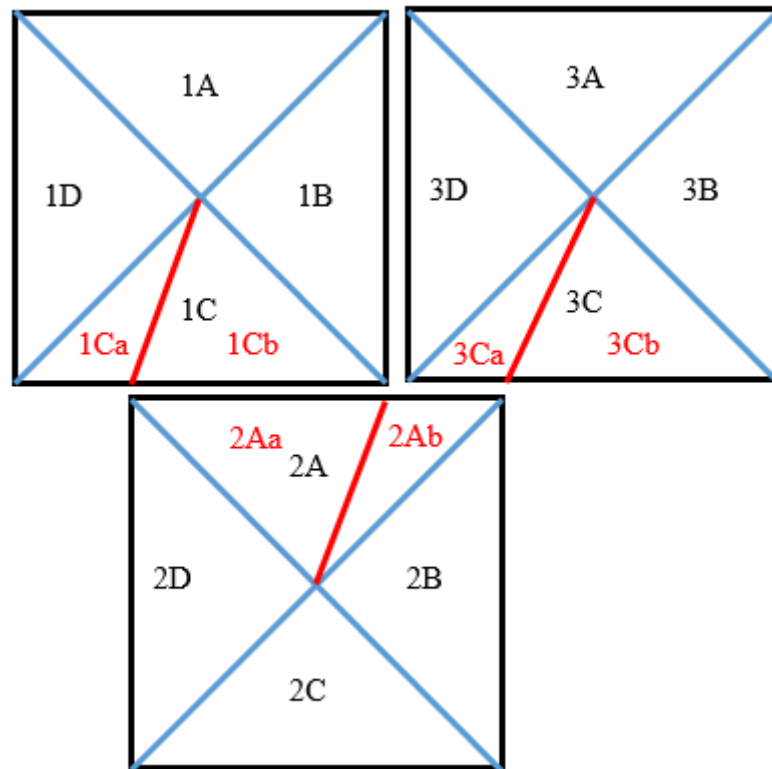


Figure A.2 – Discretisation of thermal/mechanical model into blocks (black), mechanical zones (blue) and thermal zones (red).

In some cases, slight block overlaps can cause the generation of excessively small and/or slender thermal zones. As with mechanical discretisation, these zones can lead to a considerable reduction in model timestep, greatly slowing model solution. In order to prevent this effect, a thermal tolerance parameter L^T can be defined. This forces any two gridpoints with a separation less than L^T to be treated as one for the purposes of the thermal calculation, preventing the generation of small thermal zones, as seen in figure A.3. Care must be taken in the use of the thermal tolerance parameter, as it effectively reduces the accuracy of the thermal model. Excessively high values of L^T can lead to the merging of zones in adjacent blocks, producing erroneous results.

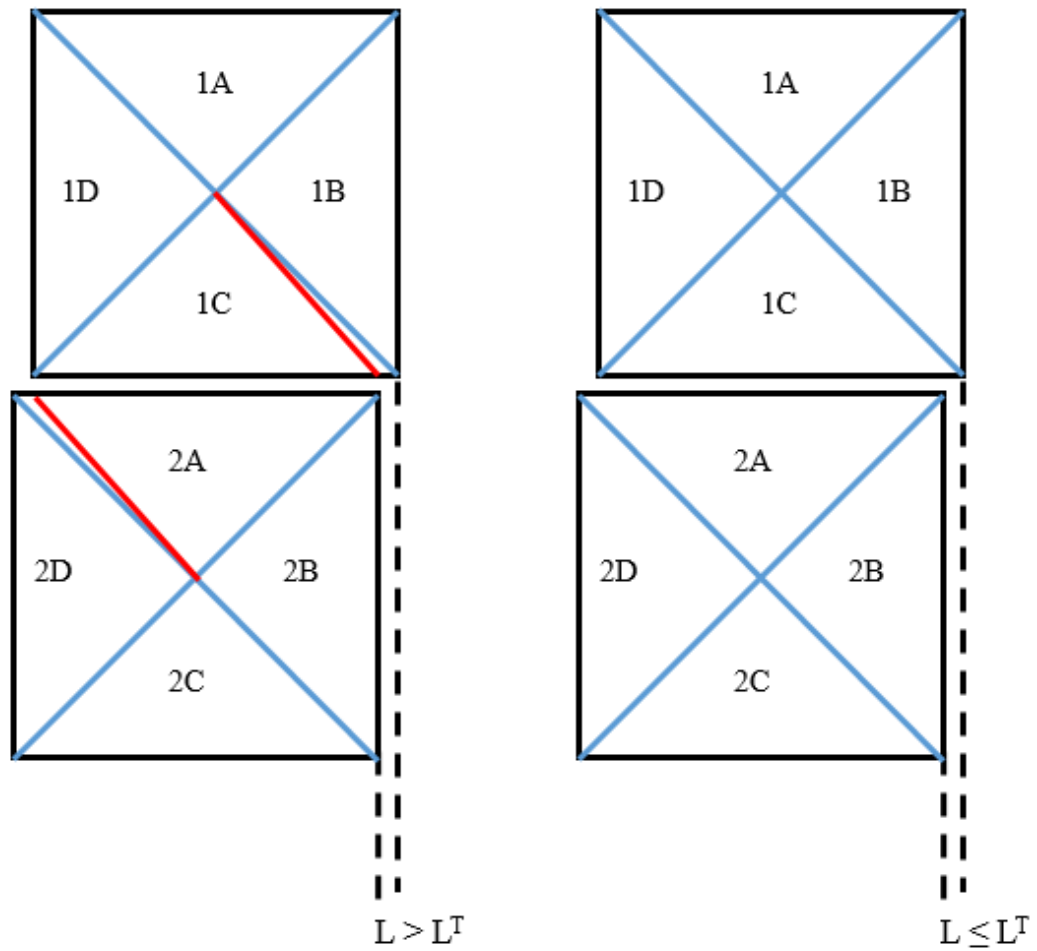


Figure A.3 – Effect of thermal tolerance parameter L^T on the generation of small thermal zones.

A.3.5. Thermal Expansion

UDEEC is capable of modelling thermally generated stresses within rock blocks, as shown in equation A.35. The temperature of a zone is defined as the arithmetic mean of the temperatures of the three gridpoints which constitute that zone.

$$\Delta\sigma_N = -3K\alpha\Delta T \quad (\text{A.35})$$

Where α is the linear thermal expansion coefficient (K^{-1})

A.3.6. Temperature Dependent Fluid Properties

The temperature dependence of fluid properties is simulated using a three step process:

1. Tables of property/temperature data are stored for fluid density and viscosity.
2. Fluid temperature is found as the arithmetic mean temperature of the gridpoints which define the fluid filled joint.
3. Property tables are linearly interpolated to find the values of density and viscosity at the given temperature.

B. DERIVATIONS

B.1. STRESS/DISPLACEMENT RELATIONSHIPS

This appendix covers the derivation of equations 4.2 and 4.3, which show the relationship between applied axial strain ϵ_a and horizontal and vertical displacements u_x and u_y respectively. Consider a single joint at an angle ϕ to the horizontal, as shown in figure B.1. This joint is part of a rock mass exposed to an applied axial compressive strain ϵ_a .

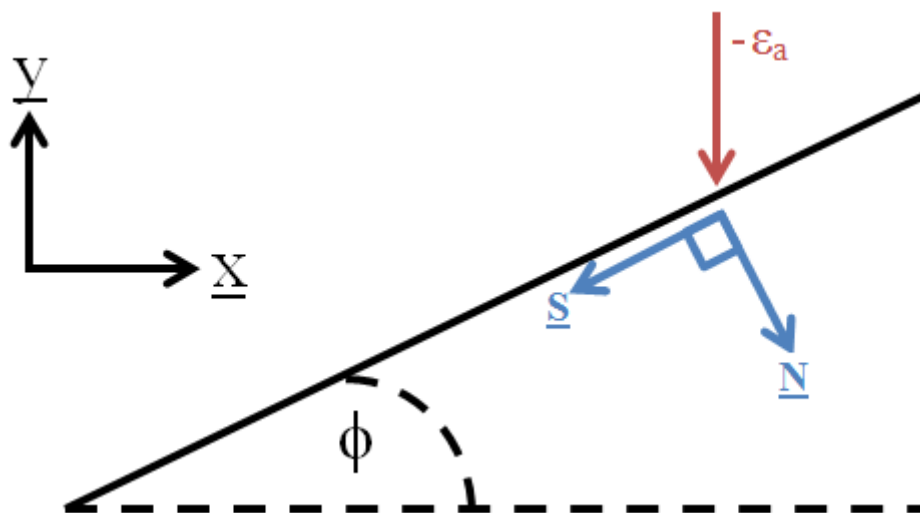


Figure B.1 – Schematic representation of the forces and motion on a single joint within a rock mass. N implies normal motion, S implies shear motion.

The force F on the joint due to the applied strain is:

$$F = -E\epsilon_a A$$

Where A is the surface area of the joint

We can find:

$$F_n = F \cos(\phi) = -E \varepsilon_a A \cos(\phi)$$

$$F_s = F \sin(\phi) = -E \varepsilon_a A \sin(\phi)$$

The displacement along a joint can be found as:

$$u_i = \frac{F_i}{k_i}$$

Therefore:

$$u_n = -\frac{E \varepsilon_a A}{k_n} \cos(\phi)$$

$$u_s = -\frac{E \varepsilon_a A}{k_s} \sin(\phi)$$

Convert into Cartesian co-ordinates:

$$u_x = u_{n,x} + u_{s,x}$$

$$u_y = u_{n,y} + u_{s,y}$$

Where:

$$u_{n,x} = u_n \sin(\phi) = -\frac{E \varepsilon_a A}{k_n} \cos(\phi) \sin(\phi) = -\frac{E \varepsilon_a A}{2k_n} \sin(2\phi)$$

$$u_{s,x} = -u_s \cos(\phi) = \frac{E \varepsilon_a A}{k_s} \sin(\phi) \cos(\phi) = \frac{E \varepsilon_a A}{2k_s} \sin(2\phi)$$

$$u_{n,y} = -u_n \cos(\phi) = \frac{E \varepsilon_a A}{k_n} \cos^2(\phi)$$

$$u_{s,y} = -u_s \sin(\phi) = \frac{E \varepsilon_a A}{k_s} \sin^2(\phi)$$

Therefore:

$$u_x = \frac{E \varepsilon_a A}{2} \left(\frac{1}{k_s} - \frac{1}{k_n} \right) \sin(2\phi) \quad \text{is equation 4.2}$$

$$u_y = E \varepsilon_a A \left(\frac{\cos^2(\phi)}{k_n} + \frac{\sin^2(\phi)}{k_s} \right) \quad \text{is equation 4.3}$$

B.2. TEMPERATURE DEPENDENT MATERIAL PROPERTIES

Ranjith *et al* (2012) present normalised relationships for the elastic modulus and uniaxial compressive strength of sandstone over a range of temperatures, as shown in figure B.2. In order to simulate temperature dependent materials in the UCG model, compressive strength must be converted into the model parameters of friction angle, cohesion and tensile limit. This section explains how this is achieved.

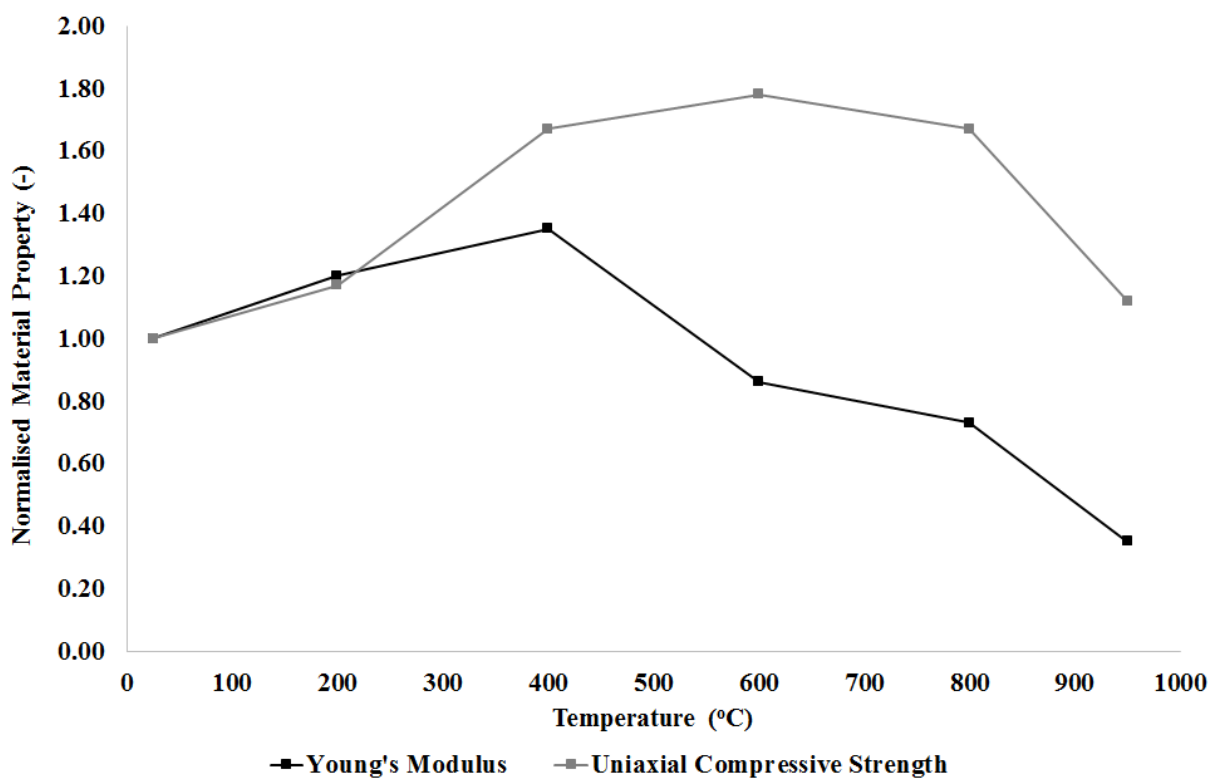


Figure B.2 – Temperature dependence of the Young's modulus and uniaxial compressive strength of sandstone over a range of temperatures. After Ranjith *et al*, 2012.

B.2.1. Friction Angle

In order to determine a temperature dependent friction angle, we must assume that normalised compressive strength is not a function of confining pressure. While there is no physical basis for this assumption, friction angle cannot be defined otherwise without further experiment. Given the relatively minor influence of both temperature and friction angle (relative to cohesion), the inaccuracies caused by this assumption are not considered critical. Using the assumption, we can plot strength/pressure curves for the material (based on axisymmetric brickwork results, see fig 4.12) over a range of temperatures. These values are found by multiplying the results found in the simulated triaxial tests by the normalised UCS given in figure B.2. The curves produced are shown in figure B.3.

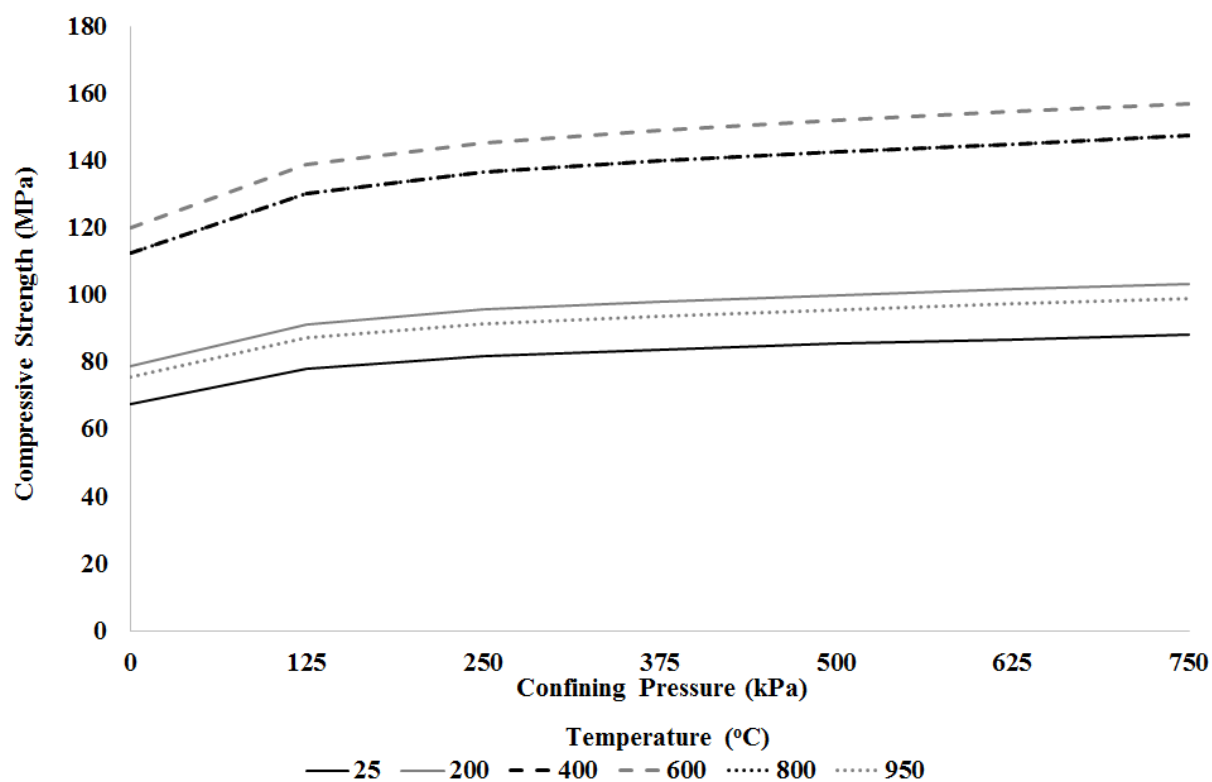


Figure B.3 – Strength/pressure curves as a function of temperature.

Friction angles are then found for each temperature as:

$$\theta_T = \frac{M_T - 1}{M_T + 1}$$

Where M_T is the gradient of the strength/pressure curve at temperature T.

B.2.2. Cohesion

Cohesion is found as:

$$C_T = \sigma_{c,T} \frac{1 - \sin(\theta_T)}{2 \cos(\theta_T)}$$

Where $\sigma_{c,T}$ is the unconfined compressive strength at temperature T.

B.2.3. Tensile Limit

Tensile limit is found as:

$$\sigma_T = \frac{C_T}{\tan(\theta_T)}$$

B.2.4. Normalised Properties

Normalised values of friction angle, cohesion and tensile limit are found by dividing their absolute values by their value at 25°C. The values found are plotted in figure 5.4.

B.3. CONDUCTIVE/CONVECTIVE HEAT TRANSFER RATIO

Consider a single joint in between a pair of blocks, as shown in figure B.4.

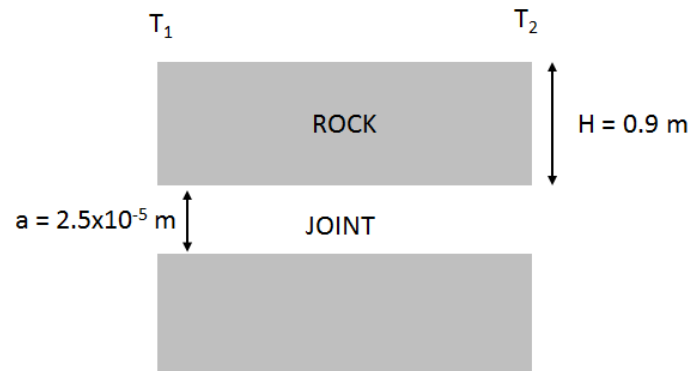


Figure B.4 – Schematic of a single joint between a pair of rocks.

Thermal conduction transfers heat from left to right (T_1 to T_2). This heat is partially negated by the inflow of cold fluid flowing from right to left (T_2 to T_1). Assuming fluid temperature is equal to rock temperature at all points along the joint, the magnitudes of heat transferred by each mechanism can be found as follows:

$$Q_R = \lambda H(T_1 - T_2)$$

$$Q_F = \dot{m}C(T_2 - T_1) = \rho avC(T_2 - T_1)$$

The ratio of conduction to convection can then be found as:

$$\frac{Q_R}{Q_F} = -\frac{\lambda H}{\rho avC}$$

Which is equation 5.8.

Where:

C	Fluid heat capacity	(Jkg ⁻¹ K ⁻¹)
v	Fluid velocity	(ms ⁻¹)
λ	Rock thermal conductivity	(Wm ⁻² K ⁻¹)
ρ	Fluid density	(kgm ⁻³)

B.4. CAVITY WALL TEMPERATURE DERIVATION

As shown in figure 5.10, the energy balance over the UCG cavity consists of 6 components:

- Energy stored in the coal E_C
- Energy stored in the oxidant gas E_O
- Energy stored in the injected steam E_S
- Energy stored in the groundwater E_W
- Energy stored in the product syngas E_P
- Energy lost to the rock mass E_L

For the thermal model, we are interested in the energy lost to the rock mass E_L . This can be found by an energy balance as:

$$E_L = E_C + E_O + E_S + E_W - E_P$$

The terms on the right hand side can be found by considering the stoichiometry of the reaction and the enthalpies of formation of the compounds involved. E_S and E_W also depend on the relative proportions of the water supplied by the injected steam and groundwater respectively.

Using coal as the basis for the calculation and assuming constant compositions we find the following stoichiometric relationships, where product gas composition is given by Perkins & Sahajwalla (2005):



Product gas composition, on a molar basis:

$$CO = 0.35$$

$$CO_2 = 0.29 \quad \therefore \quad \delta = 0.83\gamma$$

$$H_2 = 0.21 \quad \therefore \quad \varepsilon = 0.60\gamma$$

$$CH_4 = 0.06 \quad \therefore \quad \theta = 0.17\gamma$$

$$H_2O = 0.09 \quad \therefore \quad \mu = 0.26\gamma$$

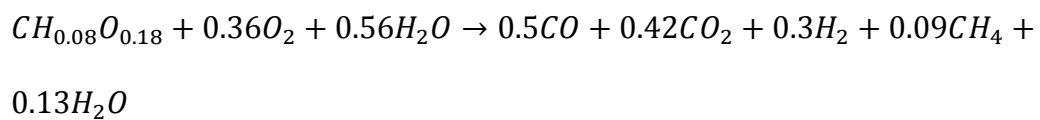
By performing an element balance over the stoichiometric equation, we find:

$$\alpha = 0.36$$

$$\beta = 0.56$$

$$\gamma = 0.50$$

We can now balance the equation as:



Combining with the relative molecular weights, we find the total mass fluxes associated with the process:

COMPOUND	kmol	kg	kg/kg coal	mass fraction
CH_{0.08}O_{0.18}	1 (basis)	14.97	1 (basis)	-
O₂	0.36	11.52	0.770	-
H₂O	0.56	10.09	0.674	-
CO	0.50	14.01	0.936	0.380
CO₂	0.42	18.48	1.234	0.501
H₂	0.30	0.61	0.041	0.017
CH₄	0.09	1.44	0.096	0.039
H₂O	0.13	2.34	0.156	0.063
Product Gas	1.44	36.88	2.463	-

The energy terms are found as:

$$E_i = -\Delta H_{f,i}^{\theta} + H^{T,P} - H^{\theta}$$

Where:

$$\Delta H_{f,i}^{\theta} = \text{Standard enthalpy of formation}$$

$$[\text{Jkg}^{-1}]$$

$$H^{T,P} = \text{Thermodynamic enthalpy at given temperature and pressure}$$

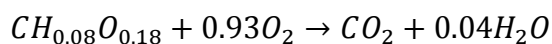
$$[\text{Jkg}^{-1}]$$

$$H^{\theta} = \text{Thermodynamic enthalpy at standard conditions}$$

$$[\text{Jkg}^{-1}]$$

All data is found from Green & Perry (2007). The H^θ term is required because the formation enthalpy is defined at 298K whereas the thermodynamic enthalpy is defined as zero at 0K. Differences in enthalpy can also be found via the constant pressure heat capacity in the case of solid and liquid compounds.

The enthalpy of formation for coal is difficult to define, due to its complex chemical nature. We can find this using Hess's law applied to coal combustion:



$$\Delta H_r^\theta = \Delta H_{f,CO_2}^\theta + 0.04\Delta H_{f,H_2O}^\theta - \Delta H_{f,coal}^\theta - 0.93\Delta H_{f,O_2}^\theta$$

$\Delta H_{f,O_2}^\theta$ equals zero, as oxygen is an element.

Therefore:

$$\Delta H_{f,coal}^\theta = \Delta H_{f,CO_2}^\theta + 0.04\Delta H_{f,H_2O}^\theta - \Delta H_r^\theta$$

From the literature:

$$\Delta H_{f,CO_2}^\theta = -393.51 \text{ kJmol}^{-1}$$

$$\Delta H_{f,H_2O}^\theta = -241.81 \text{ kJmol}^{-1}$$

$$\Delta H_r^\theta = -319.5 \text{ kJmol}^{-1}$$

Therefore:

$$\Delta H_{f,Coal}^{\theta} = -84.03 \text{ kJmol}^{-1} = -5613.4 \text{ kJkg}^{-1}$$

And:

$$E_C = -\Delta H_{f,Coal}^{\theta} + C_{P,Coal}(T_0 - 298) = 5615.2 \text{ kJkg}^{-1}$$

Where:

C_C Specific Heat Capacity of Coal (0.920 kJkg⁻¹K⁻¹)

T_0 Ambient Temperature at Cavity Depth (300 K)

E_O , E_S and E_W and E_P are found as:

$$E_O = 118.4 \text{ kJkg}^{-1} \quad (P = 555\text{kPa}, T = 429\text{K} = T_{\text{sat}})$$

$$E_S = 16074 \text{ kJkg}^{-1} \quad (P = 555\text{kPa}, T = 429\text{K})$$

$$E_W = 13435 \text{ kJkg}^{-1} \quad (P = 555\text{kPa}, T = 300\text{K})$$

$$E_P = 8249.9 \text{ kJkg}^{-1} \quad (P = 555\text{kPa}, T = 980\text{K})$$

We now express each term with respect to the basis of coal, giving:

$$E_C = 5615.2 \text{ kJkg}^{-1}$$

$$E_O = 91.2 \text{ kJkg}^{-1} \text{ (coal)}$$

$$E_S = 13435Q \text{ kJkg}^{-1} \text{ (coal)}$$

L_{burn}	Combustion zone length	(m)
R	Coal consumption rate	
	(kgs^{-1})	
ρ_W	Density of water	
	(kgm^{-3})	

Therefore:

$$Q = 6899q$$

And:

$$E_L = 5.48 \times 10^5 - 2.64 \times 10^9 q \text{ Wm}^{-1}$$

Is the total amount of power produced by the modelled region.

We can convert this into a wall temperature by equating the power produced with the heat lost to the surroundings:

$$E_L = \lambda P \frac{(T_w - T_0)}{L_T}$$

Where:

P Cavity Wall Perimeter (m)

L_T Thermal Penetration Length (m)

Assuming a thermal penetration length of 10m (this can be tested and updated in later versions of the model to increase accuracy) and a cavity geometry the same as that used in the Rocky Mountain 1 trial, we find:

$$T_w = 300 + \frac{E_L}{\lambda P L_T}$$

Substituting in the appropriate values gives:

$$T_w = 1153 - 4.1 \times 10^6 q \text{ Wm}^{-1} \quad \text{which is equation 5.12.}$$

B.5. THERMAL PENETRATION LENGTH

Consider a cavity with a circular cross section, surrounded by a temperature profile.

The amount of energy required to produce that profile is given as:

$$Q = 2\pi\rho C \int_{r_c}^{r_p} r(T - T_b)dr$$

If we assume a linear temperature profile, we find:

$$T = T_W + (T_B - T_W) \frac{r-r_c}{r_p-r_c}$$

Therefore:

$$Q = \frac{\pi\rho C(T_W - T_B)}{r_p - r_c} \int_{r_c}^{r_p} r_p r - r^2 dr$$

Where

T_b Background temperature (K)

T_w Cavity wall temperature (K)

r_c Cavity radius (m)

r_p Profile radius (m)

Assuming $r_p \gg r_c$, we find:

$$Q \approx \frac{\pi \rho C}{6 r_p} (T_W - T_B) r_p^3 = \frac{\pi \rho C}{6} (T_W - T_B) r_p^2$$

Note that the above assumption is not true in many cases. Given that this derivation is only intended to show an approximate relationship however, this error is considered acceptable.

The amount of heat transferred from the cavity over time t is found as:

$$Q = -2\pi\lambda r_c \frac{\delta T}{\delta r} t \approx -2\pi\lambda r_c t \frac{T_B - T_W}{r_p}$$

Therefore:

$$\frac{\pi \rho C}{6} (T_W - T_B) r_p^2 \approx -2\pi\lambda r_c t \frac{T_B - T_W}{r_p}$$

Rearranging terms gives:

$$r_p^3 \approx \frac{12\lambda r_c t}{\rho C}$$

Finally,

$$r_p \approx \left(\frac{12\lambda r_c t}{\rho C} \right)^{1/3} \quad \text{Which is equation 8.4.}$$

C. GROUNDWATER CONTAMINATION MODELLING

This appendix outlines a brief suggestion for how a model of UCG induced groundwater pollution could be created using the commercially available Modular 3 Dimensional Transport Model for Multiple Species (MT3DMS) (United States Geological Survey, 2005). The model would consider contaminant generation, transport and destruction and would be one-directionally coupled with the existing UDEC model. The model would effectively produce a two dimensional map of the spread of several contaminant species over time, both during and after gasification, using the results of the UDEC model as boundary conditions.

The model would simulate the behaviour of approximately 5 contaminant species, with each one chosen to represent several similar compounds. For example, benzene could be used to represent all low molecular weight aromatic hydrocarbons, while lead could be used to represent all heavy metals. The choice of species used would depend on their relative transport capabilities and environmental toxicity, with those which travel furthest or present the most danger used in the model to predict the worst possible pollution outcomes. A brief outline of the suggested model operation is given below:

1. An additional part of the UDEC model reads the “after” stage result and produces a 2D map of the permeability, pressure and flow distributions during gasification.
2. The data is mapped onto a grid of equally sized 2D elements.
3. The grid element(s) containing the cavity are set to produce contaminants at a fixed rate based determined from the literature.
4. Any other necessary boundary and initial conditions are set. Examples include background pollutant concentrations and far field pressure values.
5. MT3DMS is executed over the operational time of the gasifier to find the distribution of contaminant species at the end of gasification.
6. Steps 1 through 4 are repeated for the “final” stage of the model with appropriate contaminant generation rates.
7. MT3DMS is executed for a given period after gasification has ceased (years), with the distribution of contaminants output from the model at regular points in this time.

Given the relatively good scientific understanding of contaminant transport in groundwater, it is believed that the development of the pollution model should be much faster than that of the UDEC model. In addition, unlike subsidence, a great deal of field trial data is available for validation purposes. As such, it is expected that a valid, useful model could be developed within 12 months, based on the suggested methodology above. The creation of the model should therefore be considered a key priority in the further development of UCG modelling capabilities.